

UC Berkeley

UC Berkeley Electronic Theses and Dissertations

Title

Drilling on Mars - Mathematical Model for Rotary-Ultrasonic Core Drilling of Brittle Materials

Permalink

<https://escholarship.org/uc/item/6zq2x2d8>

Author

Horne, Mera F

Publication Date

2015

Peer reviewed|Thesis/dissertation

**Drilling on Mars – Mathematical Model for Rotary-Ultrasonic Core Drilling of Brittle
Materials**

by

Mera Fayez Horne

A dissertation submitted in partial satisfaction of the
requirements for the degree of

Doctor of Philosophy

in

Engineering - Mechanical Engineering

In the

Graduate Division

of the

UNIVERSITY OF CALIFORNIA, BERKELEY

Committee in charge:
Professor George Johnson, Chair
Professor Lisa Pruitt
Professor Khalid Mosalam

Fall 2015

Abstract

Drilling on Mars – Mathematical Model of Rotary-Ultrasonic Core Drilling

by

Mera Fayez Horne

Doctor of Philosophy in Engineering – Mechanical Engineering

In the

University of California, Berkeley

Professor George Johnson, Chair

The results from the Phoenix mission led scientists to believe it is possible that primitive life exists below the Martian surface. Therefore, drilling in Martian soil in search for organisms is the next logical step. Drilling on Mars is a major engineering challenge due to the drilling depth requirement. Mars lacks a thick atmosphere and a continuous magnetic field that shield the planet's surface from solar radiation and solar flares. As a result, the Martian surface is sterile and if life ever existed, it must be found below the surface. In 2001, NASA's Mars Exploration Payload Advisory Group proposed that drilling should be considered as a priority investigation on Mars in an effort of finding evidence of extinct or extant life.

On August 6, 2012, the team of engineers landed the spacecraft Curiosity on the surface of Mars by using a revolutionary hovering platform. The results from the Curiosity mission suggested the next logical step, which is drilling six meters deep in the red planet in search of life. Excavation tools deployed to Mars so far have been able to drill to a maximum depth of 6.5 cm. Thus, the drilling capabilities need to be increased by a factor or approximately 100 to achieve the goal of drilling six meters deep. This requirement puts a demand on developing a new and more effective technologies to reach this goal. Previous research shows evidence of a promising drilling mechanism in rotary-ultrasonic for what it offers in terms of high surface quality, faster rate of penetration and higher material removal rate.

This research addresses the need to understand the mechanics of the drill bit tip and rock interface in rotary-ultrasonic drilling of brittle materials. A mathematical model identifying all contributing independent parameters, such as drill bit design parameters, drilling process parameters, ultrasonic wave amplitude and rocks' material properties, that have effect on rate of penetration is developed. Analytical and experimental results are presented to show the effect of the variation of different parameters on rate of penetration performance.

Curriculum Vitae

Mera Horne

PhD in Mechanical Engineering at UC Berkeley / NASA Ames Research Center

merahorne@berkeley.edu

Summary

Risk Assessment and Management:

I am a PhD candidate in mechanical engineering at UC Berkeley with emphasis in materials design. I am passionate about human safety and ensuring proper mechanical designs used daily in our society. I am particularly interested in failure analysis that investigates past failures and improves upon current technology to prevent future ones. Equipped with "Risk Assessment and Management" training, I take a proactive approach ensuring all preventative measure in my operation system.

Teaching / Technical Training:

I am highly skilled in problem solving, critical thinking, and possess the ability to deliver technical information to wide range of audience, from laymen to scientists. I strive on interaction with clients ensuring smooth flow of operation and projects' plans to meet deadlines. Complex engineering problems intrigue me and ignite my determination in solving them. My ideal job will be the one to allow me to enjoy the utilization of most, if not all, of those skills.

Job Challenges:

Space applications are very intriguing where materials behave differently in extreme environment. My current research involves developing a mathematical model of drilling on Mars utilizing rotary-ultrasonic drilling mechanism. The research enhances my experience in dealing with materials in extreme condition and expands my knowledge in the area of failure analysis.

Experience

PhD Mechanical Engineer / Researcher at NASA Ames Research Center

August 2010 - Present (4 years 2 months)

A team of engineers behind the mission to Mars pulled off an audacious stunt by landing the Curiosity spacecraft on the red planet by using a revolutionary hovering platform. The results from curiosity mission paved the way to another engineering challenge, which is drilling six meters deep in the red planet in search for life. My research focuses on understanding the mechanics of the interaction between the drill bit and the rocks

interface applying the cutting edge drilling technology of rotary-ultrasonic. The plan is to develop a mathematical model of the fracture mechanics between the drill bit tip and rocks interface explaining the dual action of ultrasonic vibration coupled with rotary drilling. The mathematical model will be utilized to determine the effect of frequency Amplitude, force applied (WOB), and Rotary Speed (rpm) on Rate of Penetration (ROP). The model also will be validated by conducting experiments using multi-axial ultrasonic drill testing multiple types of rocks varying in materials properties (Young's Modulus, Piosson's Ratio, Fracture Toughness and Vickers Hardness) that is likely to be present on the red planet, Travertine, Limestone, Gypsum, Kaolinite, and Saddleback Basalt.

Graduate Student Instructor (GSI) - Mechanical Engineering Department at UC Berkeley

August 2010 - Present (4 years 2 months)

Teaching a course offers the fundamental techniques of engineering sketching and drawing, drawing conventions, computer graphics, and modeling. Also the course is addressing the classical descriptive geometry, and 3D drawing. Parametric and feature based solids modeling. Graphical analysis, and the documentation and presentation of engineering information are practices as well. This course introduces and emphasizes the use of CAD on the computer as the major graphical analysis and design tool.

Certificate Program in Teaching and Learning in Higher Education at UC Berkeley

August 2010 - Present (4 years 2 months)

As a national leader in preparing graduate students for teaching, UC Berkeley is one of the few universities in the country that have a comprehensive policy on GSI mentoring. The development activities that Berkeley GSIs undertake to fulfill the requirements of this policy — the Teaching Conference, the Online Ethics Course, and the 300-level pedagogy course in their disciplines — support GSIs in their teaching at UC Berkeley, but they also help form the foundation of their teaching and leadership skills in future academic and non-academic careers. The UC Berkeley Certificate Program in Teaching and Learning in Higher Education adds to these three basic requirements participation in workshops on teaching, teaching observation, creation of a teaching portfolio, and several other development activities. The following certificate requirements have been completed:

- Participation in the all-day Teaching Conference for First-Time GSIs at UC Berkeley
- Successful completion of a 300-level course on pedagogy that has been approved for the Certificate Program, in the relevant discipline
- Successful completion of the GSI Professional Standards and Ethics in Teaching Online Course Participation in six qualifying Workshops on Teaching
- Teaching as a GSI at UC Berkeley
- GSI classroom teaching observation by and consultation with a faculty mentor
- Development of a course syllabus

- Use of mid-semester teaching evaluations
- Teaching portfolio

Learning Support Specialist at Center for Access to Engineering Excellence (CAEE) UC Berkeley at UC Berkeley

January 2013 - June 2014 (1 year 6 months)

I facilitated the recruitment, training, and supervision of our peer tutors. In addition, I provided academic support to students who need more intensive tutoring. In addition to my passion for Engineering I also have a passion for Education, which led her to pursue an Education minor in her PhD program.

MS Mechanical Engineering at UC Berkeley

2010 - 2012 (2 years)

The results from the Phoenix mission to Mars in 2008 led scientists to believe it is possible that primitive life exists below the Martian surface. Therefore, drilling in Martian soil in search for organisms is the next logical step. Drilling on Mars is a major engineering challenge since Martian soil surprised Phoenix mission scientists with unexpected soil characteristics that nearly prevented the mission from being completed. Unexpectedly sticky soil initially prevented it from falling through one of the instrument's screens as planned. Therefore, further understanding of Martian soil mechanics is needed to better prepare engineers for proper drilling device design and methodology. Since soil is generated from rock disintegration (weathering), the most logical step toward drilling is to understand rock weathering on Mars in the presence of perchlorate salt. The results generated proved the hypothesis of rocks strength reduction that will be utilized in designing drilling bit parameters and developing drilling methodology for future missions to Mars.

Mentor/Instructor (Volunteer) - National Society of Black Engineers Jr. at National Society of Black Engineers (NSBE)

May 2012 - Present (3 years 4 months)

NSBE's mission is to increase the number of culturally responsible Black engineers who excel academically, succeed professionally and positively impact the community. NSBE Jr. is the pipeline to STEM disciplines for minority scholars in the East Bay. We offer workshops and experiences to enhance the education received by this population and expose them to STEM professionals who are role models in an effort to pique their interest in one of the STEM disciplines. We collaborate with companies and programs that offer STEM related experiences and/or hire STEM professionals.

Space Science Division - Research Associate at NASA Ames Research Center

May 2008 - August 2010 (2 years 4 months)

New data has come from the Cassini/Huygens mission related to Titan, the largest Moons of Saturn. We have an ongoing project looking at this data, developing numerical models to match the data, and contributing to the design of future missions to Titan. I worked on the temperature and methane data, comparing the results from the Huygens entry profile with the Voyager radio occultation data taken 23 years earlier.

BS Mechanical Engineering at UC Berkeley

January 2007 - May 2009 (2 years 5 months)

Completing undergraduate requirements for mechanical engineering BS degree.

NSTI Internship - Systems Engineer in Intelligent Systems Division at NASA Ames Research Center

May 2007 - August 2007 (4 months)

I served as the Systems Engineer on a project to design and integrate an experimental Unmanned Aerial Vehicle (UAV) test platform. Managed project from a systems engineering perspective, keeping track of various budgets, including payload weight, electrical consumption, and project costs. I worked with

AutoCAD to design thermal intake ducts and performed thermal analysis of a new avionics package. I analyzed propulsion system upgrades and designed upgraded structural engine mounts.

1 recommendation available upon request

Mechanical Designer at CDM

July 2005 - December 2006 (1 year 6 months)

Generated equipment mechanical designs for water treatment planes and HVAC systems. I also assisted in the production of architectural, structural and electrical drawings.

1 recommendation available upon request

Mechanical Designer at Chevron

May 2001 - August 2005 (4 years 4 months)

Generated isometric, as built drawings for Chevron Refinery PSM570 Inspection Project as well as generated P&ID drawings. Also generated and designed Intelligent P&ID, PFD, MOC, vessels, and column drawings for the research center. I also worked directly

for ConneXsys using Cyrax software generating as built 3D models for Chevron refinery plants in San Diego and Sacramento.

Mechanical Designer/Department Manager at Kraft Foods

May 1996 - December 2000 (4 years 8 months)

Designing and upgrading equipment and conveyor systems layout for variety of process lines such as: Coffee line, Green Beans, Neotec Roaster, General Food International Coffee (GFIC), 1&2LB Packaging Lines, ... etc. I was also responsible for updating the Architectural and Structural modification for all buildings in the plant (12). I also laid out the entire plant in 3D rendered model. The model shows the coffee process lines starting at the Green Bulk Dump Station to Clean and weight system. Coffee is pneumatic conveyed to be stored, roasted, grind and packed. The model covers thousands of square footage and four floor building equipment layout. At Kraft, after each project, I maintained drawings for the equipment as built for accuracy of the future projects.

Languages

Arabi

Dedication

To my son Kevin, my number one motivator

my first middle school math teacher, my inspirational

to my sister Mona,

for being my role model in striving for higher education,

and

to all my sisters and brothers, in memory of my mother and my father and to my
best friend Laura for supporting me throughout my endeavor

Contents

Abstract	1
Curriculum Vitae	i
Dedication.....	vi
Acknowledgments.....	xxvii
1. Introduction	1
1.1. Why Drilling on Mars?.....	1
1.2. Background of Extraterrestrial Drilling	2
1.3. Drilling Mechanisms for Extraterrestrial Bodies.....	3
1.4. Thesis Objectives and Layout.....	4
2. Design Constraints and Limitations on Martian Drill System.....	5
2.1. Environmental Constraints on Mars.....	5
2.1.1. Temperature.....	5
2.1.2. Pressure on Mars	5
2.1.3. Geology	6
2.1.4. Thermal flux.....	6
2.1.5. Water content	6
2.2. Technological Constraints on Martian Drill System	7
2.2.1. Drilling Power	7
2.2.2. Weight on Bit (WOB) (force exerted on workpiece during drilling)	7
2.2.3. Rotational Speed	7
2.2.4. Energy	8
2.2.5. Drill Bit Materials	8
2.2.6. Cutting Material Removal.....	10

2.2.7. Auger Design for Material Removal	10
2.2.8. Coring Vs. Drilling.....	11
2.2.9. Rotary vs. Percussive Drilling.....	11
3. History of Excavation Tools Deployed on Mars	13
3.1. From Viking to Curiosity	13
3.1.1. Viking 1 & 2, 1976:.....	13
3.1.2. Viking 1 & 2 Mission Excavation Plan and Tools.....	14
3.1.3. Mars Exploration Rovers Spirit and Opportunity 2003	15
3.1.4. Opportunity and Spirit Rovers Mission Excavation Plan and Tools.....	16
3.1.5. Phoenix Lander 2008.....	16
3.1.6. Phoenix Mission Excavation Plan and Tools.....	17
3.1.7. Mars Science Laboratory, Curiosity 2012	18
3.1.8. Mars Science Laboratory (MSL)/Curiosity Excavation Plan and Tools.....	18
3.1.8.1. Robotic Arm Mounted Powder Acquisition Drill System (PADS).....	19
3.1.8.2. Curiosity Robotic Arm Scoop	19
3.2. Mars 2020 Mission and Drilling System Requirements.....	20
3.2.1. Core Sample Mass, Length and Diameter	20
3.2.2. Number of Samples.....	21
4. Literature Review on Drilling Systems and Extraterrestrial Drilling.....	23
4.1. Rotary Drilling.....	23
4.2. Rotary-Percussive Drilling (RPD).....	23
4.2.1. European Space Agency (ESA) Implementing Drill with Hammering Mechanism (DHM)	26
4.3. Rotary-Ultrasonic Drilling (RUD)	30
4.3.1. Ultrasonically Assisted Drilling (UAD)	31

4.3.2. Pure Ultrasonic Drilling.....	32
4.3.3. Ultrasonic Core Drilling.....	33
4.3.4. Novel Ultrasonic Drill Designs Followed the USDC.....	34
4.3.5. Ultrasonic/Sonic Impacting Penetrator (USIP) Reaching 1 Meter in Depth	35
4.3.6. Ultrasonic/Sonic Drilling Corer (USDC) Advantages.....	36
5. Rotary-Ultrasonic Drilling Mechanics.....	39
5.1. Rotary and Oscillation Dual Action Mechanics.....	39
5.1.1. Axial oscillation dynamics.....	40
5.1.2. Rotary dynamics	41
5.2. Ultrasonic Wave Magnification Methods.....	41
5.2.1. Horns / Velocity Transformers	42
5.2.2. The most popular horn designs are shown in Figure 37.	42
5.2.3. Horns Suggested Materials	44
5.2.4. Actuators with Novel Horns	44
5.2.4.1. Dog-bone Shape Horn.....	44
5.2.4.2. Folded/Flipped Horn	45
5.2.4.3. Rotary-hammering Sample Actuated by a Single Piezoelectric Actuator.....	46
5.3. Ultrasonic Drilling Corer and Materials Removal Methods.....	47
5.3.1. USDC Based Rotary Hammer for Rapid Drilling.....	47
5.3.2. Subsurface Sampler	47
5.4. Rotary Ultrasonic Drilling Designs and Applications.....	49
5.4.1. Deep penetration of sub-surfaces using the Auto-Gopher	49
5.4.2. Percussive Augmenter of Rotary Drills (PARoD).....	50
6. Mathematical Model Development	51

6.1. Outline of Model Development.....	51
6.1.1. Effective cutting time and cutting length	51
6.1.2. Vickers indentation.....	51
6.1.3. Total force.....	52
6.1.4. Material removal rate for single particle.....	52
6.1.5. Total material removal rate.....	52
6.2. Model Introduction.....	53
6.3. Fracture Concept and Assumptions.....	53
6.4. Mathematical Model Parameters	54
6.4.1. Abrasive Particle Position and Velocity.....	54
6.4.2. Effective Time (Δt)	56
6.4.3. Effective Cutting Length (L_s)	57
6.4.4. Helix Path Pitch (b)	59
6.4.5. Maximum Depth (δ).....	59
6.4.5.1. Indentation Fracture Mechanics.....	60
6.4.5.2. Sharp Indenter Fracture Mechanics.....	63
6.4.6. Maximum Depth (δ) in Terms of Materials Hardness.....	64
6.4.7. The relationship between WOB/cutting force on the workpiece (F) and force on one abrasive particle (F_n).....	66
6.4.8. Number of Abrasive Particles (N_a)	67
6.4.9. Material Removal Rate for One Abrasive Particle (MRR_p).....	68
6.4.10. Material Removal Rate for Core Drill (MRR_d)	70
6.4.11. Lateral Cracks Length (C_L) and Depth (C_h)	70
6.4.12. Rate of Penetration (ROP)	71
7. Experiment Design.....	76

7.1. Experiments Parameters.....	78
7.2. Rock Type Selection	78
7.2.1. Travertine.....	79
7.2.2. Marble.....	80
7.2.3. Basalt.....	80
7.3. Rock Samples.....	81
7.4. Rocks Type and Materials Properties	85
7.4.1. Rock Specimens Preparation	85
7.4.2. Material Property Tests	88
7.4.2.1. Uniaxial Compression Test	88
7.4.2.2. Vickers Hardness Test	97
7.4.2.3. Fracture Toughness Test.....	102
7.4.3. Material Properties Summary	107
7.5. Experimental Setup.....	107
7.6. Ultrasonic Wave Amplitude	110
7.7. Drill Bits	115
7.8. Core Drill Bit Design Parameters	116
7.8.1. Cutting Force Plots.....	116
7.8.2. Core Drill Bit Outside and Inside Diameters.....	117
7.8.3. Abrasive Particles Concentration (C_a).....	118
7.8.4. Abrasive Particle Size (S_a).....	119
7.9. Drill Process Parameters.....	119
7.9.1. Rate of Penetration (ROP).....	119
7.9.2. Speed	120
7.10. Ultrasonic Wave Parameters	121

7.10.1. Wave Amplitude	121
7.10.2. Ultrasonic Frequency	121
8. Mathematical Model Validation	122
8.1. Volume Proportionality Parameter K	122
8.1.1. Volume Proportionality K for Marble	123
8.1.2. Volume Proportionality K for Travertine.....	124
8.1.3. Volume Proportionality K for Basalt.....	125
8.2. Core Drill Bit Parameters Change Effect on WOB.....	128
8.2.1. Drill Bit Outside and Inside Diameters / Drill Bit Cross Section Area (A_o).128	
8.2.2. Abrasive Particles Size (S_a).....	130
8.2.3. Abrasive Particles Concentration (C_a).....	131
8.3. Process Parameter Change Effect on WOB	132
8.3.1. Rate of Penetration (ROP).....	132
8.3.2. Speed (S)	134
8.3.3. Ultrasonic Amplitude (A).....	135
8.4. Summary	137
9. Conclusion and Future Work.....	138
9.1. Challenges of Drilling on Mars and Future Missions Requirements	138
9.2. Drilling Parameters and Their Effect on Rate of Penetration Performance.....	139
9.3. Predicted Versus Experimental Results	140
9.3.1. Results for Basalt	141
9.3.2. Results for Marble	142
9.3.3. Results for Travertine.....	143
9.4. Discussion	144
9.4.1. Speed (S)	144

9.4.2. Feed Rate / ROP	144
9.4.3. Particle Size (S_a)	145
9.4.4. Particle Concentration (C_a)	145
9.4.5. Drill Bit Cross Section Area (A_o)	145
9.4.6. Ultrasonic Amplitude (A).....	145
9.5. Direction of Future Research.....	145
10. Education: Activity Design Utilizing Knowledge Integration.....	148
10.1. Eliciting and Building on a Repertoire of Ideas.....	149
10.2. Adding New Ideas	151
10.3. Help Student Develop Criteria: Prediction vs. Observations	157
10.4. Sort Out Ideas	157
10.5. Develop Cohesive and Coherent Understanding of Mars Exploration	158
11. Appendix A.....	165
Mathematical Model Development	165
Rate of Penetration Expression Derivation	165
12. Appendix B.....	173
13. Appendix C	175
14. Appendix D.....	181

List of Figures

Figure 1:	Diamond pull out due to weak mechanical locking inside the matrix.....	6
Figure 2:	Scanning electron micrograph of a diamond-impregnated segment in good condition. (Zacny and Cooper, 2006)	8
Figure 3:	Coring bit with four diamond impregnated blocks placed in so-called 4-wing configuration. (Zacny and Cooper, 2007)	9
Figure 4:	Size comparison between three generations Mars rovers landed on Mars between 1997 and 2012, Mars Exploration Rovers, JPL.....	13
Figure 5:	Separation of the Viking descent module from the Orbiter, NASA Mars Exploration Site: http://mars.nasa.gov	14
Figure 6:	Viking soil sampler (SSA), Smithsonian Institution photograph (left), a close up view of SSA (right)	14
Figure 7:	An artist's concept portrays a NASA Mars Exploration Twin Rovers, Spirit and Opportunity, landed on the surface of Mars in 2003, Mars Exploration Rovers, JPL site: http://www.jpl.nasa.gov/missions/mer/	15
Figure 8:	Rock Abrasion Tool (RAT) on Spirit & Opportunity Rovers (left) and an exposed fresh rock surface (right), Mars Exploration Rovers, JPL	16
Figure 9:	Phoenix Mars Lander during testing at Lockheed Martin Space Systems in 2006, JPL	17
Figure 10:	Phoenix Robotic Arm	17
Figure 11:	Curiosity Rover 2012, JPL	18
Figure 12:	Mars Hand Lens Imager (MAHLI) camera on NASA's Curiosity Mars rover shows the first sample-collection hole drilled in Mount Sharp, JPL.....	19
Figure 13:	Mechanisms for scooping, sieving and portioning samples of powdered rock and soil samples, JPL.....	19
Figure 14:	Honeybee Robotics Bit	20
Figure 15:	To bring back 500 g of sample of a particular size, particular packaging geometry are possible, Mars 2020 SDT	22
Figure 16:	Rock damage process for rotary drilling.....	23
Figure 17:	Rock damage process for rotary-percussive drilling	23

Figure 18:	Honeybee Robotics percussive scoop tests (Zacny et al., 2009).....	25
Figure 19:	Apollo 16 astronaut trains in lunar soil drilling, NASA	26
Figure 20:	The ExoMars Drill, ESA Robotic Exploration of Mars.....	26
Figure 21:	Schematics of TE at Galileo Avionica, ESA and Galileo Avionica.....	27
Figure 22:	Test equipment with integrated drill/core tool that is 70 cm long. ESA and Galileo Avionica.....	27
Figure 23:	Schematics and pictures of commercial drill tools, ESA and Galileo Avionica	28
Figure 24:	The drill tools used during the DHM test campaign. ESA and Galileo Avionica	28
Figure 25:	New thin corer after test in granite. Arrows indicate the points where the external parts of the tool were hitting the materials. ESA and Galileo Avionica.....	29
Figure 26:	Test No. 2 into granite: hole and sample. (a) Granite hole with powder. The sample was removed and placed on the blue sheet. (b) Granite hole with powder removed. ESA and Galileo Avionica	30
Figure 27:	Rotary Ultrasonic Motion, DMG.....	30
Figure 28:	UAD system configuration, Ba-Cohen and Zacny, 2008	31
Figure 29:	UAD excitation, Bar-Cohen and Zacny, 2008	32
Figure 30:	A photographic view of the USDC showing its ability to core with minimum axial force (left); a schematic cross-section view (right). Courtesy of NASA/JPL (Bar-Cohen and Zacny, 2008)	33
Figure 31:	Analytical drilling rates in rocks with various hardness levels using 10 W of average power. The rocks are classified by their compression strength, where: Soft: 0 – 50; Medium: 50 – 100; Hard: 100 – 200; and Very hard: > 200 (MPa) (Bar-Cohen et al., 2012)	35
Figure 32:	A schematic view of the USIP, (Bar-Cohen, Sherrit, Badescu, & Bao, 2012)...	36
Figure 33:	Particle simulation of down-hole percussive drilling. (a) Propagation of the drill bit; (b) detail of (a)., Universities of Aberdeen and Leicester.....	37
Figure 34:	Concept of an ultrasonic drill for planetary applications. ESA and Universities of Aberdeen and Leicester	37

Figure 35:	Ultrasonic device schematic of the operation concept, Decoup site	39
Figure 36:	Ultrasonic device schematic of the components and amplitude magnification, Decoup site (http://www.decoup.com/en/content/how-does-it-work).....	41
Figure 37:	Different horn designs, (a) Linear taper, (b) Exponential taper, and (c) Stepped taper, sonicsystems.co.uk	42
Figure 38:	Various horn/transducer arrangements, Sonic Systems.....	43
Figure 39:	Stress and amplitude of different horn designs (a) Linear, (b) Exponential and (c) Stepped taper	44
Figure 40:	Gopher design with dog-bone horn.....	45
Figure 41:	Photograph of the folded horn (16 kHz) and a comparison of a straight horn with approximately the same frequency (20 kHz). A substantial decrease in the resonance if found.	45
Figure 42:	Photographs of (a) the drill bit with the flutes and (b) the bit in the formed borehole and the extracted powdered cuttings. Courtesy of NASA/JPL.....	47
Figure 43:	Subsurface sampler. Clockwise from left: full assembly; coring drill string; core sample; regolith sample; regolith sampling drill string. Courtesy of Honeybee Robotics	48
Figure 44:	Subsurface sampler core break-off and ejection. Courtesy of Honeybee Robotics.....	49
Figure 45:	Schematic view of the ultrasonic/Sonic Gopher inside the borehole.	50
Figure 46:	Using the Auto-Gopher, the first core (57.25 mm diam. and 97.25 mm long) that was produced of limestone (photo courtesy of K. Zacny, Honeybee Robotics).....	50
Figure 47:	Percussive Augmenter of Rotary Drills Component Details (PARoD), JPL	50
Figure 48:	Modified illustration of Rotary Ultrasonic Milling (RUM) process for downhole drilling and core drill bit.	53
Figure 49:	Abrasive particle simplified as an octahedron shape, http://paulscottinfo.ipage.com/polyhedra/platonic/octahedron/1octahedronL.gif 54	54
Figure 50:	Ultrasonic Wave Superimposed on rotary motion of an abrasive particle mounted on the cutting surface of a drill bit	54
Figure 51:	Rotary Cutting Direction.....	55

Figure 52:	Effective time (Δt) during one ultrasonic cycle	56
Figure 53:	Helix path pitch "C"	57
Figure 54:	Core Drill Schematic	58
Figure 55:	Drill bit helix path.....	59
Figure 56:	Coordinate system for indentation stress field, (Lawn and Wilshaw, 1975).	60
Figure 57:	Half-surface view (top) and side view (bottom) of stress trajectories in Boussinesq field. Plotted for $\nu=0.25$, Lawn and Wilshaw, 1976	61
Figure 58:	Contours of principal normal stresses, (a) σ_{11} , (b) σ_{22} , (c) σ_{33} , in Boussinesq field, shown in plane containing contract axis. Plotted for $\nu = 0.25$. Unit of stress is p_0 , contact "diameter" (arrowed) is $2a\sqrt{\alpha}$. Note sharp minimum in σ_{11} and zero in σ_{22} ,	62
Figure 59:	Parameters of the median vent configuration. Broken lines represent stress contours, heavy line represents crack profile, and shading represents inelastic deformation zone.	63
Figure 60:	Vickers Hardness Test.....	64
Figure 61:	Vickers Hardness indentation shape formed by indenter tip	65
Figure 62:	Abrasive particle octahedron shape showing relevant dimensions.....	66
Figure 63:	Schematic diagram of material removal in brittle fracture mode induced by the abrasive particle process (Zhang et al., 2013).....	68
Figure 64:	Scanning electron micrograph of Knoop impression quartz (0001) surface. Section shows inelastic deformation zone immediately below surface impression, and associated vent pattern. Indenter load 2N. Width of field 100 μm (left) and In situ photograph of Vickers indentation in soda-lime glass taken in transmitted light with an indenter load of 250N and width of field of 11mm (right) (B. Lawn and R. Wilshaw, 1975).....	69
Figure 65:	Fracture zone theoretical volume calculation (V_0)	69
Figure 66:	The expression $\pi^2 - \arcsin^2 - \delta A_{18} \approx 1$	74
Figure 67:	Ultrasonic amplitude vs. max. depth.....	74
Figure 68:	Drill, abrasive particle and ultrasonic wave parameters.....	77
Figure 69:	Rotary ultrasonic dual action of rotation in a helix path and oscillation vertically	78

Figure 70:	Natural Travertine rocks, http://www.collecting-rocks-and-minerals.com/image-files/turkish-travertine.jpg	79
Figure 71:	Natural marble rocks, http://www.creativeincounters.com/wp-content/uploads/2012/03/white-marble-blocks.jpg	80
Figure 72:	Basalt and lava rock, http://meteorites.wustl.edu/id/basalt_0885l.jpg	80
Figure 73:	Natural Basalt rocks, http://farm4.staticflickr.com/3077/2517111350_051e520c92.jpg	81
Figure 74:	Top view of travertine Rock Sample with overall dimensions of 38x60x2.5 cm	82
Figure 75:	Size view of travertine sample close up image showing an estimated grain size and porosity level	82
Figure 76:	Top view of marble Rock Sample with overall dimensions of 25x152x2.54 cm	83
Figure 77:	Side view of marble sample close up image showing an estimated grain size and porosity level	83
Figure 78:	Top view of basalt rock sample with overall dimensions of 30x58x3.8 cm...	84
Figure 79:	Side view of basalt sample close up image showing an estimated grain size and porosity level	84
Figure 80:	Property tests and experiments allocations for Travertine.....	85
Figure 81:	Travertine rock sample	86
Figure 82:	Property tests and experiments allocations for Marble	86
Figure 83:	Marble rock sample	87
Figure 84:	Property tests and experiments allocations for Basalt.....	87
Figure 85:	Basalt rock sample	88
Figure 86:	Typical Uniaxial Compression Strength test setup (UCS), National Technical University of Athens	89
Figure 87:	Travertine specimens (3) prepared for compression test	89
Figure 88:	Marble specimens (3) prepared for compression tests	90
Figure 89:	Basalt specimens (3) prepared for compression tests.	90

Figure 90:	Milling a flat surface for basalt specimens ensuring parallel surfaces for the compression tests (left). Strain gage mounted on travertine specimen for elongation and compression strength measurements (right).....	90
Figure 91:	Photo of test specimens	91
Figure 92:	Loading was conducted with the same speed (test data for travertine specimen Sp4 is shown here)	92
Figure 93:	Average modulus of linear portion of axial stress-strain curve	93
Figure 94:	Travertine Young’s modulus estimate (specimen Sp4 is presented as an example)	93
Figure 95:	Format of Graphical Presentation of Data	94
Figure 96:	Travertine Poisson’s ratio (specimen Sp4 is presented as an example).	94
Figure 97:	Rock specimen in UTM (spherical swivel at the bottom)	95
Figure 98:	Failure mode of Travertine specimen	95
Figure 99:	Failure mode of Marble specimen.....	96
Figure 100:	Failure mode of Basalt specimen	96
Figure 101:	Vickers hardness diamond tip indenter, https://upload.wikimedia.org/wikipedia/commons/d/d2/Vickers_anvil_diamonds.jpg	98
Figure 102:	Vickers hardness test method, NASRUL Design http://nasruldesign.weebly.com/uploads/7/4/1/9/7419180/8927090_orig.jpg	98
Figure 103:	Vickers hardness tester, IDI lab	99
Figure 104:	Specimens prepared for Vickers hardness tests	100
Figure 105:	Discs used to polish the specimens providing very smooth surfaces (left). Casting specimens in the epoxy for Vickers hardness tests (right)	100
Figure 106:	Basalt Vickers hardness test results	101
Figure 107:	Marble Vickers hardness test results	101
Figure 108:	Travertine Vickers hardness test results	102

Figure 109:	The CCNBD specimen geometry with recommended test fixture (Zhao et al., 1994)	103
Figure 110:	Marble K_{IC} value validation obtained from experiment using Brazilian disk method.....	105
Figure 111:	Travertine K_{IC} value validation obtained from experiment using Brazilian disk method	106
Figure 112:	Basalt K_{IC} value validation.....	107
Figure 113:	Schematic of Rotary Ultrasonic Machine (RUM) at KSU, (Cong et al., 2014)	108
Figure 114:	Dynamometer measuring applied force (left), ultrasonic frequency display unit by Sonic-Mill (right)	109
Figure 115:	A/D converter received signal from dynamometer of the applied force	109
Figure 116:	Rotary Ultrasonic Machine (RUM) located at KSU	110
Figure 117:	a) Amplitude measuring device, dial gage, b) Typical drill bit showing tuning length (Weilong Cong, 2013)	111
Figure 118:	Dial gage placed under the drill bit and in contact with the surface as it operates and measure the wave amplitude	111
Figure 119:	Five different tools used in the study, Cong et al, 2011	111
Figure 120:	Effects of ultrasonic power on vibration amplitude (measure with the dial indicator method) for five tools (#1, #2, #3, #4, and #5), Cong et al, 2011.	112
Figure 121:	Hardware dialog between acquisition cycles set for A/D board multichannel amplifier type 5070	112
Figure 122:	A/D board multichannel amplifier has Ch1 is assigned for torque and ch2 is assigned for applied force (AKA, Weight on Bit).....	113
Figure 123:	Documentation dialog allows for storing document under desired title, and set up to record cutting force and be displayed between acquisition cycles	113
Figure 124:	Experimental core rock samples drilled at various drilling parameters.....	114
Figure 125:	Rock samples drilled at various input parameters close up view showing the labeling system applied to identify each core sample.....	114
Figure 126:	Drill bits with varies design parameters	115

Figure 127:	Sharpening (dressing) stick refreshing the core drill bit cutting surface after each test exposing a fresh layer of abrasive particles.....	116
Figure 128:	Typical plot of cutting force measured for travertine at a given value set of S, A, S _a , C _a , D _i , and D _o parameters	116
Figure 129:	Typical plot of cutting force measured for marble at a given value set of S, A, S _a , C _a , D _i , and D _o parameters	117
Figure 130:	Typical plot of cutting force measured for basalt at a given value set of S, A, S _a , C _a , D _i , and D _o parameters	117
Figure 131:	Experimental results of the cutting force vs drill bit average diameter	118
Figure 132:	Experimental results of the cutting force vs cross abrasive particles concentration.....	118
Figure 133:	Experimental results of the cutting force vs cross abrasive particles size ...	119
Figure 134:	Experimental results of the cutting force vs ROP	120
Figure 135:	Experimental results of the cutting force vs Speed.....	120
Figure 136:	Experimental results of the cutting force vs ultrasonic amplitude.....	121
Figure 137:	Volume proportionality K for marble for various parameters	123
Figure 138:	Average K for marble	124
Figure 139:	Volume proportionality K for travertine for various parameters	124
Figure 140:	Average K for travertine	125
Figure 141:	Volume proportionality K for Basalt for various parameters.....	125
Figure 142:	Average K for basalt	126
Figure 143:	Distance between two particles compared to particle size as the particle size vary	127
Figure 144:	Distance between two particles compared to particle size as the particles concentration vary	127
Figure 145:	Distance between two particles compared to particle size as the drill bit cross section area vary.....	128
Figure 146:	Predicted effect of drill bit diameters on WOB.....	129
Figure 147:	Experimental results of drill bit diameters on cutting force/WOB	129

Figure 148:	Predicted effect of abrasive particle size on WOB.....	130
Figure 149:	Experimental results of the abrasive particle size effect on cutting force/WOB	131
Figure 150:	Predicted effect of abrasive particle concentration on WOB	131
Figure 151:	Experimental results of the abrasive particle concentration effect on cutting force/WOB	132
Figure 152:	Predicted effect of applied force on ROP performance for basalt rock.....	133
Figure 153:	Experimental results of the feed rate/ROP effect on cutting force/WOB	133
Figure 154:	Predicted effect of spindle speed on WOB.....	134
Figure 155:	Experimental results of the speed effect on cutting force/WOB	135
Figure 156:	Predicted effect of ultrasonic wave amplitude on ROP performance for basalt rock.....	136
Figure 157:	Experimental results of the ultrasonic wave amplitude effect on cutting force/WOB	136
Figure 158:	Mathematical model validation of RUM parameters effect on WOB performance for basalt.....	141
Figure 159:	Mathematical model validation of RUM parameters effect on WOB performance for marble.....	142
Figure 160:	Mathematical model validation of RUM parameters effect on WOB performance for travertine.....	143
Figure 161:	Size comparison between Earth, Mars and the Moon, http://www.astro.virginia.edu/class/skrutskie/images/mars_earth_moon.jpg	148
Figure 162:	http://bc.outcrop.org/images/earthquakes/press4e/figure-19-13b.jpg ...	149
Figure 163:	Earth structure, http://upload.wikimedia.org/wikipedia/en/1/1b/Earth_layers_NASA.png 150	
Figure 164:	Earth's magnetic field, http://www.todayifoundout.com/wp-content/uploads/2014/04/magnetic-field-earth.jpg	150
Figure 165:	Planet Mars, http://i.dailymail.co.uk/i/pix/2012/08/21/article-2191399-14A3025500005DC-839_964x1035.jpg	151

Figure 166:	Planet Earth, http://images-gededah.in/wp-content/uploads/5517167-planet-earth-isolated.jpg	152
Figure 167:	Artist perspective of Plant Mars if it has water, http://www.lpi.usra.edu/education/timeline/gallery/images/019.jpg	153
Figure 168:	Gullies on Mars, http://www.desktopexchange.net/plog-content/images/space-pictures/mars-wallpapers/fresh-crater-with-gullies.jpg	154
Figure 169:	Mars Curiosity, http://mars.jpl.nasa.gov/msl/images/msl20110526_MSL_Artist_Concept_PI_A14165-full.jpg	155
Figure 170:	Remote controlled plane, http://rc.org.uk/images/CoxEasyFlyer.jpg	156
Figure 171:	Communication system between Earth and Mars, http://planete-mars.com/wp-content/uploads/2014/07/mars20140723-full.jpg	157
Figure 172:	Marble Sp1 Young modulus	175
Figure 173:	Marble Sp1 Poisson ration	176
Figure 174:	Marble Sp2 Young modulus	176
Figure 175:	Marble Sp2 Poisson ratio	176
Figure 176:	Travertine Sp4 Young modulus	177
Figure 177:	Travertine Sp4 Poisson ratio	177
Figure 178:	Travertine Sp4.0 Young modulus	178
Figure 179:	Travertine Sp4.0 Poisson ratio	178
Figure 180:	Basalt Sp7 Young modulus	179
Figure 181:	Basalt Sp7 Poisson ratio	179
Figure 182:	Basalt Sp8 Young modulus	180
Figure 183:	Basalt Sp8 Poisson ratio	180
Figure 184:	Change of frequency has no effect on the effective time and ROP performance	181

List of Tables

Table 1: Main characteristics of TE available at Galileo Avionica, ESA.....	29
Table 2: Acoustic power transmitted by various horn/transducer arrangements in Fig. 38.....	43
Table 3: List of the resonance frequencies for the various horn types, Sherrit et al., 2002.....	46
Table 4: Input variables, definitions, symbols, and units.....	55
Table 5: Experiments value range for each drill bit design and process parameters.....	78
Table 6: Mechanical properties of rock materials.....	79
Table 7: Specimens dimensions and quantities for materials properties tests.....	81
Table 8: List of rock samples available for the material testing.....	91
Table 10: A summary of test results.....	96
Table 11: Material properties average values used in this research.....	97
Table 12: IDI and Struers Vickers hardness test results.....	100
Table 13: Standard CCNBD and geometrical dimensions.....	103
Table 14: Marble K_{Ic} test dimensions using Brazilian disk method, (Zhao, Fowell, Roegiers, & Xu, 1994).....	104
Table 15: Travertine K_{Ic} test dimensions using Brazilian disk method, (Zhao, Fowell, Roegiers, & Xu, 1994).....	105
Table 16: Basalt K_{Ic} test dimensions using Brazilian disk method did not yield result and analytical method was used.....	106
Table 17: Rocks Materials Properties Tests Summary.....	107
Table 18: Drill bits specifications.....	115

List of Equations

Equation 1:	Position (S_p).....	55
Equation 2:	Velocity (V_p).....	55
Equation 3:	Effective time in terms of t_2 and t_1	57
Equation 4:	Z at first contact point (t_1).....	57
Equation 5:	Time (t_1).....	57
Equation 6:	Time (t_2).....	57
Equation 7:	Effective Time Expression.....	57
Equation 8:	Effective length L_s	58
Equation 9:	Vickers hardness indentation area (A_s).....	65
Equation 10:	Vickers Hardness.....	65
Equation 11:	Maximum depth δ	66
Equation 12:	Impulse of one abrasive particle I_1	66
Equation 13:	Impulse of one abrasive particle I_2	66
Equation 14:	Normal force on one abrasive particle.....	67
Equation 15:	Number of abrasive particles.....	67
Equation 16:	Theoretical volume V_o	69
Equation 17:	Actual volume V	69
Equation 18:	Abrasive particle material removal rate MRR_a	70
Equation 19:	Material removal rate of core drill MRR_d in terms of number or particles N_a	70
Equation 20:	Material removal rate for core drill MRR_d	70
Equation 21:	Product of lateral crack length C_L and lateral crack height C_h	71
Equation 22:	Material removal rate of drill bit in terms of b and A_o	71
Equation 23:	Rate of penetration ROP.....	72

Equation 24: Material properties parameters	72
Equation 25: Final ROP mathematical model expression.....	73
Equation 26: Simplified ROM mathematical model expression.....	75
Equation 27: The mathematical model is expressed in terms of WOB in a simplified form.....	122

Acknowledgments

I would like to acknowledge the support of the National Science Foundation (NSF) of awarding me a fellowship for my graduate work for the first three years of my PhD in mechanical engineering. I was also awarded NASA - Harriet Jenkins Pre-doctoral Fellowship Project (JPFP) for the following two years and NASA Graduate Students Researcher Program Fellowships. My current research is conducted with the assistance of the NASA chief scientist, Dr. Chris McKay, at NASA Ames Research Center and the advice of Kris Zacny, VP at Honeybee Robotics. I also like to acknowledge Kansas State University Professors and employees for assisting in the research experiments and using the RUM on campus. Particularly, I would like to acknowledge Professor Bradley Kramer, the head of the IMSE department, Professor Pei ZJ, Visiting Assistant Professor Meng Zhang, and graduate student Palamandadige Fernando for assisting with the experiments using the rotary ultrasonic machine. I also like to acknowledge Professor Kevin Lease and his graduate student John Herman for assisting with conducting the tests and providing the rock materials properties.

Chapter 1

1. Introduction

1.1. Why Drilling on Mars?

Are we alone in the universe? This question will keep scientists restless until an answer is found. As a result, searching for extraterrestrial life has launched several research and space missions, and numerous innovations such as the Kepler telescope in search of earth-like planets. Compelling evidence from a spacecraft flying in orbit around Mars suggests that the planet was once much like Earth is today, with a hot dynamo at its core, intense magnetism in its crust and possibly massive continental plates adrift on its surface [Mitchell, 1999].

In the effort to understand more about our own planet, it is often necessary to study another planet that is at a different development stage than ours. Mars and Earth share many similarities - hard crust, dense cores and similar materials composition [ESA, Mars Express, 2006]. To better understand our planet, one of the best comparative laboratories that exists is planet Mars. The study of Mars provides Earth scientists invaluable information as they examine the processes of climate change, geophysics, and the potential for life beyond our own planet. Mars took center stage as a primary planet where life may have existed in the past when the recent Phoenix Mars Mission revealed indisputable evidence of water and perchlorate existence in Martian soil. Presence of water strengthens the possibility of that life once existed on Mars since it is one of the major sources for life, and it is reinforced by the presence of perchlorate since it can be used as an oxidizer to derive energy organisms [Phoenix Mars Mission, 2008].

Mars, however, correctly lacks a thick atmosphere and continuous magnetic field that shields Earth from solar radiation and solar flares. As a result, the Martian surface is now sterile and if life ever existed, it must be found below the surface. In 2001, NASA's Mars Exploration Payload Advisory Group [MEPAG, 2001] proposed that drilling should be considered as a priority investigation on Mars in the effort of finding evidence of extinct or extant life [Zancy PhD thesis, 2005]. The results from the Phoenix mission also support these findings and led scientists to believe it is possible that primitive life exists below the Martian surface. Therefore, drilling in Martian soil in search for organisms is the next logical step.

While drilling on Mars is a major engineering challenge, on August 6 of 2012, a team of engineers assigned to send the spacecraft Curiosity to Mars pulled off an audacious feat and landed on the red planet by using a revolutionary hovering platform. The results from Curiosity mission revealed the ultimate engineering challenge, the need to drill six meters deep in the red planet in search for life. This depth was determined by Curiosity scientists to ensure avoiding the effect of radiation on living organisms at lesser depth.

In January 2013, NASA appointed the Mars 2020 Science Definition Team (SDT) composed of 19 scientists and engineers from universities and research organizations to develop the scientific objectives for the mission as stated in the report: *“Outlined a mission concept for a science-focused, highly mobile rover to explore and investigate in detail a site on Mars that likely was once habitable”* (2020 SDT Report).

1.2. Background of Extraterrestrial Drilling

The initial objectives of the space exploration involved orbital spacecraft since it started in 1957 when the Soviet Union launched Sputnik 1 and it was followed by United States launch of Explorer 1 in 1958. Soon after, the objectives scope expanded to in-situ investigation of extraterrestrial bodies started in 1964 with the crashing the US Ranger 7 on to the Moon while sending pictures to Earth. Several missions of soft landings on the moon by United States and Russia followed successfully. Those missions paved the way for greater space exploration objectives, and to physically explore other planets. That led to landing astronauts on the moon for first time on July 20th, 1969. A total of six successful Apollo missions, 11-17, with the exception of the failure of Apollo 13, contributed great scientific findings that were based on the analysis of rocks and drill cores that astronauts collected from the moon and returned to Earth. The last human landing on the moon was on December 14, 1972 and human exploration of extraterrestrial bodies has not resumed. Due to budget cuts, the remaining planned missions of Apollo 18, 19, and 20 were cancelled and Saturn V rockets were placed on display at the Johnson Space Center, the Kennedy Space Center and the U.S. Space & Rocket Center in Huntsville, Al (Zacny et al., 2009).

Despite the discontinuation of human space exploration, the desire to learn the geological history of other planets and the search for signs of past or present life continued to grow. Today, robotic missions to Mars and other planets is the approach taken to conduct in-situ sampling and analysis that acquires subsurface samples. To achieve this goal, drilling in extraterrestrial bodies is required and due to the harsh environment, such as extremely low temperature and vacuum space, engineers are faced with the complex task of developing drilling techniques and methodology (Briggs and Gross, 2002; Zacny et al., 2008b).

In 1970, the Soviet Luna 16 lander, with an extendable arm, was the first drill rig to land on the moon surface. It collected 101 grams of lunar soil sample and brought it back to Earth. United States followed with Apollo 15 mission in 1971 drilling a continuous core sample of 2 cm diameter and approximately 2.4 m in length using Apollo Lunar Surface Drill (ALSD) and applying the rotary-percussive drilling technique. The drill design contained an auger as the method for drilled materials removal bringing it up to the surface (Zacny et al., 2009).

Due to planetary protection regulations, additional measures have been added to extraterrestrial drilling such as preventative measures of contamination for

example. Forward contamination refers to organic materials brought from Earth and introduced to the extraterrestrial body, and backward contamination refers to organic materials brought to Earth from the extraterrestrial body. Therefore, and particularly when sampling in search for life, it is essential that the data acquisition tools have high level of cleanness to prevent potential forward contamination.

Also sampling depth is another point that needs to be taken into consideration in the case of drilling on Mars. Since the planet does not have an atmosphere, it is important to consider the high level of radiation and the continuous surface exposure to galactic cosmic rays and radiation. This exposure causes the top surface layer to be oxidized with no potential presence of any life signs. It is estimated to be at least 2 meters deep and it is named the oxidized zone. Beneath the oxidized zone is the sterilized zone that extends from 2 to 10 meters deep depending on the type of formation and it also does not have potential for life. As a result, rock samples need to be collected at a depth is below both oxidized and sterilized zones, which makes drilling a complex engineering task (Zacny et al., 2009).

1.3. Drilling Mechanisms for Extraterrestrial Bodies

Extraterrestrial drilling methods have to overcome numerous challenges that limit the drilling mechanisms used. The most widely used drilling techniques are the mechanical technique. Utilizing such a technique requires applying stresses on the drilled medium that exceeds the rock's tensile or shear strength. In such an event, brittle failure or plastic yielding occurs allowing drill bits to penetrate through rock. This technique is used in rotary drilling, the most widely used drilling method. However, upon the introduction of percussive drilling coupled with rotary motion, it was proven that drilling performance was enhanced significantly and the rate of penetration increased substantially. Chapter 3 describes these two types of drilling mechanisms in detail. Increasingly there is recognition that ultrasonic drilling has exceptional features and it could be very beneficial to consider for future missions and it is also the subject of my research.

All the aforementioned drilling methods have limitations in their ability to operate on extraterrestrial bodies. Careful design and a robust operation are required due to the condition and remote location of other planets and moons. One of the challenges is the drilled materials removal method. While drilling, the cuttings need to be removed and the methods of removal are limited. Fluid for example could not be used due to low temperature and pressure. Instead, an auger or compressed gas is considered as cuttings removal options. Additional limitations apply to the drill bit operation condition. For example, the drill bit might experience bending during the initiation of drilling a hole if the mount or drilled object is unstable. In extreme cases, the drill bit might fail if it subjected to excessive bending. Finally, drilling generates heat that may be undesirable in some cases where it can damage or melt collected samples (Zacny et al., 2009).

1.4. Thesis Objectives and Layout

Drilling in a harsh environment and extreme conditions such as planet Mars subjects the drill system to a number of constraints. These types of constraints affect a variety of the drill system parameters from the drill bit design and materials to the drilling method implemented. Chapter 2 addresses the design constraints and limitations on the drill system. To better understand the defined research problem, it is essential to know the history of the excavation tools deployed to Mars and how much they have achieved. Chapter 3 covers every excavation tool deployed to Mars from Viking to Curiosity. It also addresses the drilling system requirements defined by the Mars 2020 team based on Curiosity mission findings.

To better understand the proposed drilling mechanism of rotary-ultrasonic drilling and the advantages and disadvantages of utilizing such a drilling technique, other types of drilling are described in detail in Chapter 4. Those techniques namely are rotary and rotary-percussive drilling. Chapter 5 dives deeper in the ultrasonic operation of the rotary and oscillation dual action mechanics and drill bit tip and rocks interaction mechanics. Chapter 6 presents mathematical model for rotary ultrasonic material removal rate based on fracture mechanics and addressing each parameter contributing in the drilling performance.

In order to validate the mathematical model developed in Chapter 6, experiments were conducted and the major drilling system components are identified in Chapter 7. Major drilling system parameters are described in detail on how they were designed and operated also in Chapter 7 for drill bit design, drill process, ultrasonic wave, and rock types and material properties. Chapter 8 provides a detailed comparison between the effect of the ultrasonic wave amplitude, weight on bit (WOB) and drill speed on the rate of penetration analytically and experimentally. Finally, Chapter 9 provides conclusions based on the research findings. Chapter 10 provides a way to demonstrate the major points of this research in a form of class activity for middle and high school students introducing science and space exploration in an interesting form.

Chapter 2

2. Design Constraints and Limitations on Martian Drill System

To have a better understanding of the complexity of drilling on Mars and the challenges engineers have to face in order to design an effective drill system, the major environmental and technological constraints need to be addressed. Environmental constraints such as low pressure, low temperature, thermal flux, water content, and geology that requires drilling in wide range of terrain. Technological constraints such as limits on available weight on bit (the force exerted on rocks resulting in cutting if it exceeds the rock's tensile strength), drilling power, rotational speed, energy, drill bit materials, cutting removal rate, and coring vs. drilling. Each constraint individually imposes a limitation on the design options, and to better understand the drilling mechanism, technical issues, as well as overcoming obstacles that may hinder the drilling process during testing, the following constraints need to be taken in consideration during the design phase.

2.1. Environmental Constraints on Mars

2.1.1. Temperature

The temperature on Earth's surface is controlled through heat exchange with the atmosphere, whereas on Mars, it is controlled by solar heating and infrared cooling to space. As a result, Martian atmospheric temperatures can be as low as $-133\text{ }^{\circ}\text{C}$ at the poles during winter (Clancy et al., 2000; Martin et al., 2003) and thermal fluctuations of over $100\text{ }^{\circ}\text{C}$ within 6 h can occur (Martin et al., 2003). The effect of this environment on drilling is significant and limits the choices of materials used for drill bits. For example, materials such as ferritic steel, with BCC structure that becomes brittle at low temperatures are unsuitable to be used for drill bits on Mars (Dutta, 1988).

2.1.2. Pressure on Mars

The water triple point is at 0.63 kPa and 0°C . If the atmospheric pressure is above this value, and ice is present in subsurface materials, the heat generated from the drilling process due to friction with ice will cause the ice to melt forming water in the borehole. Due to low temperature, the melted water will be followed by freezing that may lock the drill. If the pressure is lower than the triple point however, the ice will immediately sublime turning to vapor (Zacny & Cooper, 2006). Also due to the low pressure, the normal drill bit cooling by convection heat transfer is drastically reduced. Therefore, a drilling strategy has to be carefully chosen with moderate rotary speed and force minimizing bit heating and allowing for cooling (Zacny & Cooper, 2006).

2.1.3. Geology

The drill bit has to be designed to drill in a range of terrain that includes both hard and soft formations, as well as be able to resist choking if it encounters ice or ice-bound materials. The geology of the surface of Mars is not completely understood. However it is believed that some parts of the surface consist of hard rocks such as basalt, and other parts may contain evaporites (a water-soluble mineral sediment that results from concentration and crystallization by evaporation from an aqueous solution) (Soderblom et al., 2000). Material consistent of evaporites is expected to be much softer and more uniform, which makes it easier to penetrate than basalt. Therefore, designing a drill bit that is capable of handling a wide range of materials from very soft, to very hard rocks and everything in between is a critical, yet challenging feature.

2.1.4. Thermal flux

Large and rapid temperature change, a drop of over 100 °C, could occur within 6 h (Martin et al., 2003), and cause thermal fatigue in drill bit materials. This is particularly problematic for composite materials with large thermal expansion coefficient difference between their different components. For example, the cutting segment in a diamond impregnated bit is made of diamonds embedded inside a metal matrix. The thermal expansion coefficient of diamond is much smaller than that of metals.



Figure 1: Diamond pull out due to weak mechanical locking inside the matrix

When the thermal flux results in continuous expansion and contraction of the metal around the diamond, materials debonding will occur (Figure 1). If the diamonds are secured in the matrix by mechanical, and not chemical, bonding (Konstanty, 2000; de Chalus, 1994; Dwan, 1998), the gaps between the diamonds and the matrix eventually become large enough where the diamonds could easily fall out and the cutting edge become dysfunctional prematurely (Zacny & Cooper, 2006).

2.1.5. Water content

Mellor (1971) found that the rock strength is not only a function of temperature but also of water content. The unconfined compressive strength of Berea Sandstone when water saturated and tested at -80 °C was three times greater than the same dry sandstone tested under the identical condition. This finding was also supported by Honeybee drilling experiments which found that the power required to achieve the same rate of penetration (ROP of 80 cm/hr) also tripled for water-saturated frozen rocks versus dry rocks (30 W vs. 100 W). Since ROP depends on rock strength, it is concluded that the water-saturated frozen rocks strength is three times larger than dry rocks, which an observation that is consistent with Mellor's earlier findings.

2.2. Technological Constraints on Martian Drill System

2.2.1. Drilling Power

The baseline 2020 rover will likely use a Multi-Mission Radioisotope Thermoelectric Generator (MMRTG) nuclear power source that would provide 110-115 W of continuous power (2020 SDT Report). MMRTG is the nuclear power system of choice for a variety of reasons. Among the main advantages is that it has a long life that is only constrained by the drop of about 0.8%/year based on the rate of decay of the Pu- 238 fuel. It operates in harsh environment from high radiation to extreme temperature and severe dust storms. It also, unlike solar powered power supply systems, operates independently from the sun location and position. In addition, it is highly reliable. RTGs have proven to be the most reliable power systems ever flown on U.S. spacecraft where the two Pioneer spacecraft, for example, operated for more than two decades before being shut down, and NASA is planning on an extended Voyager mission that could last up to 40 years using RTG power supply (Furlong and Wahlquist, 1999).

2.2.2. Weight on Bit (WOB) (force exerted on workpiece during drilling)

The general principle is that the maximum force that can be applied on the drill bit is the total weight of the drill system. In the case of drilling on Mars, the maximum force applied on drill bit is a function of the weight of the Martian Lander or Rover. As reported by SDT, NASA is sending a near-clone of the Curiosity rover to Mars in 2020. The 2009 Mars Science Laboratory Rover has a mass of approximately 900 kg (Mars Science Laboratory, 2005). Therefore, calculating the maximum force that could be applied on the bit while testing the drill bits on Earth considering the reduction in Martian gravity force that is one third of Earth's gravity: maximum WOB = $(0.37)(9.8 \text{ m/s}^2)(900 \text{ kg}) \approx 3200 \text{ N}$.

It is critical to note that the above equation is valid, and the entire weight of the Lander considered in the equation, only if the drill is situated directly under the Lander center of gravity. Typically, the drill will be located on the side of the Lander, which reduces the weight considered in the equation by a factor of ($f = 0.5$). Therefore, the above calculated force value is reduced to become WOB = $0.5 \times 3200 \text{ N} = 1600 \text{ N}$.

2.2.3. Rotational Speed

The rock damage/fracture does not significantly change with a change of the rotary speed for most rocks. Therefore, the drilling torque is approximately constant, resulting in a proportional relationship between rate of penetration (ROP) and power required for rock destruction. However, additional factors constrain the drill rotational speed such as drill bit material. Too high a speed resulting from an increase of the input power

generates heat that increases bit wear and alters the bit core temperature. Too low a speed on the other hand causes excessive vibrations that might lead to bit fracture (Zacny & Cooper, 2005). Optimum rotational speed for different materials is critical and needs to be identified based on the bit material.

2.2.4. Energy

Energy balance is evaluated based on the heat and data noise generated from the power required for drilling. Since noise is insignificant compared to heat ($\ll 1\%$), the noise effect is disregarded in the energy balance. Heat, however, is used to warm up the drill bit material, warm up the drilled formation materials and if the formation contained water, energy also is used to melt, or possibly vaporize (based on the atmospheric pressure level) water content (Zacny & Cooper, 2005).

2.2.5. Drill Bit Materials

Considerable research has been conducted to examine the most critical elements in constructing drill bits: materials. The following is a summary of the findings, as well as advantages and disadvantages of the materials of choice. Taking into consideration the environmental and technological constraints mentioned previously such as thermal flux, low temperature, rock materials variation, water saturation vs. dry and materials mechanical behavior, the following three major drill bit designs are considered:

- Diamond Impregnated,
- Polycrystalline Diamond Compact (PDC)
- Hybrid

Materials Design / Behavior and Advantage vs. Disadvantage:

1) Diamond Impregnated Bits are constructed of cutting element blocks consisting of a matrix of a relatively soft metal such as bronze, impregnated with small diamond particles dispersed throughout the block's body. As drilling progresses, the bronze is worn away, exposing the diamonds that cut the rock. Eventually, the bronze matrix erodes away at a rate that allows the surfaced diamond to be lost exposing the sharp diamond layer beneath (See Fig. 2). For optimal performance, the hardness of the bronze matrix must be matched to the hardness of the rock to be drilled,

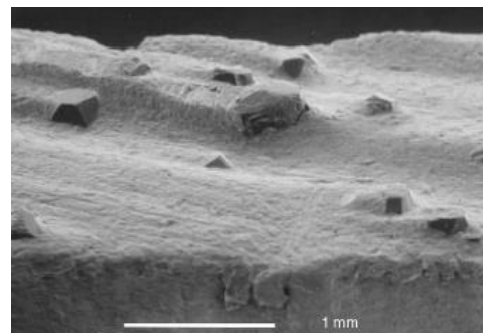


Figure 2: Scanning electron micrograph of a diamond-impregnated segment in good condition. (Zacny and Cooper, 2006)

the hardness of the bronze matrix must be matched to the hardness of the rock to be drilled,

with harder rocks being matched to softer bronze matrix. If the matrix is made too hard, the diamonds can be worn down to a condition in which they no longer cut (See Figure 3). If matrix is too soft, the overall wear rate of the bit will be high. Thus, the total drilled depth may be limited (Zacny & Cooper, 2005)

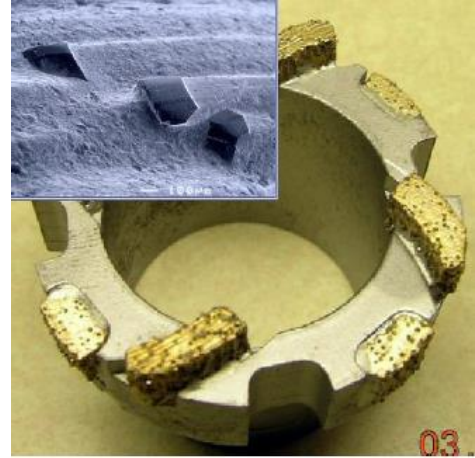


Figure 3: Coring bit with four diamond impregnated blocks placed in so-called 4-wing configuration. (Zacny and Cooper, 2007)

- 2) Polycrystalline Diamond Compact (PDC) Bits are constructed of relatively few, large teeth usually made of cemented tungsten carbide (WC) coated with a layer of polycrystalline diamond on the forward edge of the cutter. These types of bits are generally much more aggressive than diamond impregnated bits with an order of magnitude greater ROP for equivalent WOB and rotary speed. One of the disadvantages, however, is that the cutters sharp edges can be worn down cutting through hard and abrasive rocks. They also can get chipped due to sudden cutting in hard rocks that are hidden in uneven terrains. Also, unlike diamond-impregnated cutters, once the cutting segments are worn or chipped, they have to be replaced. In addition, both bit types have difficulty drilling in ice and icebound soils due to melting and re-freezing process that results in the formation of an ice-glazed surface on the bit. Bits design solutions could possibly involve making the bit teeth extremely sharp with positive rake angle with respect to the cutting direction. A disadvantage of this design is that the sharp teeth could easily get damaged or chipped. Typically, and for normal rock drilling, the cutters are usually set with a negative rake angle to reduce the chance of cutter fracture (Zacny & Cooper, 2005).

3) Hybrid Bits

Since the previous two bit types have been shown not to perform successfully on all types of rock formations under Mars condition, researchers considered a hybrid type that combines PDC and diamond-impregnated types that might be able to drill in a wide range of terrain (Tomlinson and Clark, 1992; Sheppard and Dolly, 1993). The hybrid bits are designed to cut into soft rocks while protected if they encountered hard rocks. One of the disadvantages of the hybrid bits is that they are not suitable to drill into soils, ice, ice and soil mixtures and rocks of variable strength, since they tend to choke and clog with drilling debris when run in very soft materials. Drill bit optimization also takes into

account rock's water saturation level. When drilling in rocks that contain water, the cutting materials will be removed in the water vapor and the exposed cutting tip will erode rapidly. Therefore, it is critical that the bit matrix has to be erosion-resistant. In dry rocks, the cutting tip will soon become dull. If the bit is designed to cut through dry rocks, the matrix has to be soft. If saturated rocks are encountered, the drill depth will be much shorter than anticipated (Zacny & Cooper, 2006).

2.2.6. Cutting Material Removal

Due to low temperature and low pressure combined, liquids are not suitable choice for cutting removal from the hole. Zacny and Cooper (2006) found that using a gas blast has many factors that affect the material removal performance such as removed materials particle size distribution, the hole bottom geometry, the hole surface roughness and the geometry of the hole itself. Therefore, it is difficult to develop an accurate model for the material removal and it is critical to test the gas flushing method under an actual operation condition on Mars (Zacny, 2005).

2.2.7. Auger Design for Material Removal

Auger is historically the method of materials removal considered in rock drilling. It is typically designed as a hollow-stem auger allowing the cutting and recovery of a core, with a drive tube surrounding the coring assembly. The use of augers in drilling is well known, although there is still a lot of empiricism in their design (Carleton et al., 1969). The major auger design criterion is for the cuttings to flow freely up the auger, preventing them from choking the auger flights. The best performance occurs when the conveyed material is dry and powdery. If the material is moist or sticky, however, augers get choked.

Experiments conducted by Honeybee Robotics, they showed that auger design produced very poor performance and it is extremely difficult to clear. Under Martian conditions however, it might be easier than it is on Earth for materials removal since the materials are known to be either dry, or ice cemented, in which the materials will be removed along with the sublimated ice upon drilling. They also found in their experiments that were conducted under Martian conditions, once the auger has choked and become clogged with cuttings, it is almost impossible to clear despite of the variety of maneuvers such as lifting off bottom while rotating or applying reverse rotation. Therefore, it is crucial to determine the maximum lifting capacity of the auger under the anticipated operating conditions, and then to limit the rate of penetration of the drill to not exceed this value.

2.2.8. Coring Vs. Drilling

A sub-discipline of geology known as petrology focuses on integrating chemistry, mineralogy, and textures on the rock's grain size scale in order to determine the origin and evolution of rocks. The instruments necessary to make measurements at this scale now exist, and measurements of this kind benefit from a smoothed surface, obtained from core sample, for which the technology has been well established by Mars Exploration Rover (MER). Using the principles of petrologic analysis would be especially powerful for the scientific objectives of the proposed Mars mission, which is interpreting habitability and the preservation of the evidence of that habitability (Mars 2020 SDT Report).

2.2.9. Rotary vs. Percussive Drilling

Of the three primary limiting parameters (WOB, Power, and Energy) the WOB has the largest limitation due to the desired spacecraft low payload. One way to solve the WOB problem is to employ a rotary-percussive rather than a pure rotary drilling technique. Rotary-percussive systems are used every day in industry to efficiently drill through hard rocks and concrete without applying large forces. The reduction in WOB is attributed to a stress wave generated by a hammering device within the drill head itself. When a hammer hits the top of a drill pipe, it induces an elastic wave that propagates down the drill pipe and eventually to the bit at the end of the drill pipe. Once the stress wave reaches the tip of the drill bit, it momentarily increases the force the bit exerts against a rock. Thus, a modest WOB combined with percussive system creates a large WOB for a short period of time. Since a rotary-percussive drill fractures and breaks off large chunks of rocks, it is also more energy efficient than a pure rotary drill that shears and to some extent crushes a rock. However, because it also requires another mechanism (percussor), the drilling power is higher than for a pure rotary system and the mass and complexity of the drill system is also higher. Thus, while rotary-percussive systems can solve the WOB problem, they will require batteries that can provide higher power (higher current at a set voltage) and also a large actuator or an additional actuator (if it is desirable for one actuator to turn the drill while another actuator to drive the percussive system). Either way, the mass of a drill head would be larger than for a rotary drill. Having an additional mechanism would also lead to an increased complexity of the drill head. These two disadvantages (increased mass and complexity) must be weighed against the two advantages (reduction of WOB and Energy). Finding the optimum point in the rotary-percussive drilling system is also a challenge (Paulsen et al., 2010).

Paulsen et al., (2010) also found that when using a rotary-percussive system, the stiffness of the drill string greatly affected the drilling efficiency. From the tests described in this paper, it was determined that using a steel drill

string as opposed to an aluminum drill string would increase the rate of penetration by a factor of 2.5. This equivalently reduced the drilling energy by a factor of 2.5. However, note that steel has higher density (7.8 g/cc) than aluminum (2.7 g/cc) and in turn a steel drill string would weigh almost three times more than an aluminum drill string.

Chapter 3

3. History of Excavation Tools Deployed on Mars

Over the years and after several historic rovers landing on Mars, the trend was of rovers getting larger, more efficient, and carrying more sophisticated excavation. Figure 4 shows replicas of three rovers that have landed on Mars: the *Sojourner*, the smallest rover that was a part of the Mars Pathfinder Project (1997); the medium sized Spirit and its twin Opportunity rover (2003) is the medium size, and Curiosity (2012), the largest rover ever sent to Mars.



Figure 4: Size comparison between three generations Mars rovers landed on Mars between 1997 and 2012, Mars Exploration Rovers, JPL

3.1. From Viking to Curiosity

The absence of atmosphere on Mars, and the intense exposure to radiation that basically sterilized the Martian surface of any form of life, makes excavation on Mars the only viable approach in the efforts to find life there. Six missions have been deployed to Mars with excavation instruments onboard the spacecraft.

3.1.1. Viking 1 & 2, 1976:

Viking 1 and Viking 2 are two identical NASA spacecraft that launched a few days apart to land on the surface of Mars at two different landing sites (Figure 5). The spacecraft each consisted of an orbiter and a lander where each orbiter-lander pair flew together and entered Mars orbit. Each lander has a mass of 576 kilograms. On August 20, 1975, Viking 1 was launched to arrive on June 19, 1976 and the lander then separated and descended,

landing on Mars's surface on July 20, 1976. On September 9, 1975, Viking 2 was launched to arrive on August 7, 1976 and the lander then separated and descended to Mars's surface on September 3, 1976. Viking 1 landed on the western slope of Mars at a site named Chryse Planitia, or the Plains of Gold, while Viking 2 landed at a site named Utopia Planitia. (NASA Mars Exploration Site: <http://mars.nasa.gov>).

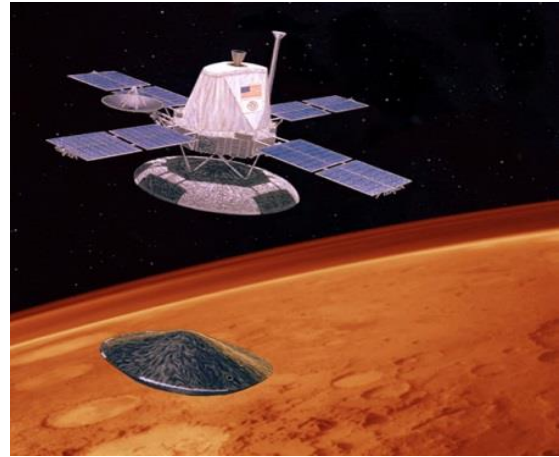


Figure 5: Separation of the Viking descent module from the Orbiter, NASA Mars Exploration Site: <http://mars.nasa.gov>

3.1.2. Viking 1 & 2 Mission Excavation Plan and Tools

One of the Viking lander's major tasks was to take surface samples and analyze them to determine their composition and to search for signs of life. To accomplish this task, onboard Viking 1 and 2 was the Surface Sampler Assembly (SSA) excavation tool (Figure 6). It was designed to acquire the top Martian regolith for tens of centimeters in depth, sift it, and then deliver it to other lander-mounted instruments for further analysis. One of these instruments is the gas chromatograph-mass spectrometer (GCMS), which is a device designed to detect small concentrations of organic compounds in samples of Martian soil. These experiments allowed scientists to conclude that Mars is a self-sterilizing planet. They determined that the solar ultraviolet radiation penetrating through Martian dry soil and the oxidizing nature of the soil chemistry prevented living organisms from forming. Future missions were able to support this finding, considering that the scooping device of the SSA was limited to scoop tens of centimeters in depth. As a result, further depth was considered for future missions requiring soil sample acquisition (NASA Mars Exploration).

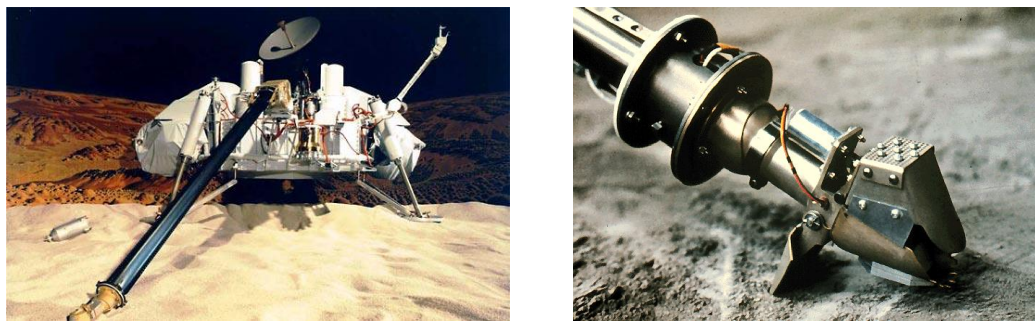


Figure 6: Viking soil sampler (SSA), Smithsonian Institution photograph (left), a close up view of SSA (right)

The results from the Viking life experiments were inconclusive. The experiment did not find evidence of life, but did not rule out the possibility of life existing below the surface. Therefore, future exploration continue, with the objective of searching for evidence of ancient organisms. Subservent spacecraft have been designed to assess the habitability of the red planet.

3.1.3. Mars Exploration Rovers Spirit and Opportunity 2003

The twin Mars Exploration Rovers Spirit and Opportunity are referred to as NASA's twin robot geologists (Figure 7). This mission is a part of NASA's Mars Exploration Program, which is a long-term effort of robotic exploration of the red planet. They launched on June 10 and July 7, 2003. The primary mission goal was to investigate the history of water on Mars. They landed on Mars on January 3 and January 24 PST, 2004 (January 4 and January 25 UTC, 2004). To accomplish the mission goal in search for water, scientists equipped the rovers with instruments that were designed to search for and characterize a wide range of rocks and soils that may hold clues to past water activity on Mars. The landing sites were chosen based on the appearance of being affected by liquid water in the past. The two sites, located on the opposite sides of Mars, were the Cusev Crater and the Meridiani Planum Cusev Crater was thought of as a possible former lake in a giant impact Crater, while Meridiani Planum contains hematite mineral deposits which suggest that Mars had a liquid form in the past (Mars Exploration Rovers, JPL site: <http://www.jpl.nasa.gov/missions/mer/>).



Figure 7: An artist's concept portrays a NASA Mars Exploration Twin Rovers, Spirit and Opportunity, landed on the surface of Mars in 2003, Mars Exploration Rovers, JPL site: <http://www.jpl.nasa.gov/missions/mer/>

3.1.4. Opportunity and Spirit Rovers Mission Excavation Plan and Tools

A Rock Abrasion Tool (RAT) on the end of each rover's robotic arm was designed and operated by Honeybee Robotics (Figure 8). The RAT was the first grinding tool to gain access to the interior of Martian rocks. The RAT uses grinding wheels of diamond dust and resin to gently abrade the surface of Martian rocks helping scientists understand the past and current environment on Mars. The RATs on both rovers have performed hundreds of grinds and the system on Opportunity remains functional about 10 years after its first use (Honeybee Robotics site: <http://www.honeybeerobotics.com/>).



Figure 8: Rock Abrasion Tool (RAT) on Spirit & Opportunity Rovers (left) and an exposed fresh rock surface (right), Mars Exploration Rovers, JPL

The goal is that as scientists examine the abraded area in detail with the help of other instruments onboard designed for organic molecule detection, they may be able to determine the rock history, how it was formed and how it was altered in time. These changes the rocks exhibit may reveal clues on whether or not life evidence found on Mars. Although, past research revealed invaluable information on Mars' rock types and formation history, evidence of life has yet to be found.

3.1.5. Phoenix Lander 2008

Phoenix mission was also a part of NASA's Mars Exploration Program. The mission objective was to study the history of water on Mars and search for complex organic molecules in the ice-rich soil of the Martian arctic. In 2002, Mars Odyssey Orbiter made discoveries showing large amounts of potential subsurface water-ice in the northern arctic plains. Phoenix lander mission's objective was targeting this region to collect and analyze soil and water ice. To accomplish this goal, a robotic arm onboard the Phoenix lander was designed to dig through the protective top soil layer to the water-ice below in order to collect samples (Figure 9). The soil and water-ice samples were then brought to the lander platform for scientific analysis. Analysis of the

chemistry of the soil and ice with robust instruments enabled scientists to better understand the history of the Martian arctic (Phoenix Mars Mission).

One of the major goals of Phoenix mission was to characterize the geology on Mars. Phoenix also explored the habitability of the Martian environment by conducting sophisticated chemical experiments assessing the soil's composition of life-giving elements such as carbon, nitrogen, phosphorus, and hydrogen. The aforementioned mission goals require digging into the soil protected from harmful solar radiation in search for organic life signature.



Figure 9: Phoenix Mars Lander during testing at Lockheed Martin Space Systems in 2006, JPL

3.1.6. Phoenix Mission Excavation Plan and Tools

Phoenix robotic arm (RA) is the tool of choice onboard the lander that is over two meters long and it was built by the Jet Propulsion Laboratory (Figure 10). At the end of the robotic arm, Honeybee Robotics built the Icy Soil Acquisition Device (ISAD), also called the Phoenix Scoop that was designed to excavate Mars dirt and ice. The RA coupled with the ISAD were critical tools for the mission operations and the unit operated successfully as designed to dig trenches, scoop up soil and water-ice samples, and deliver them to other onboard instruments such as Microscopy, Electrochemistry and Conductivity Analyzer (MECA) and Thermal and Evolved Gas Analyzer (TEGA) for detailed chemical and geological analysis (Honeybee Robotics).



Figure 10: Phoenix Robotic Arm

3.1.7. Mars Science Laboratory, Curiosity 2012

The Curiosity mission launched on November 26, 2011 and landed on August 5, 2012 (Figure 11). Known as the Mars Science Laboratory mission, the effort, was again part of NASA's Mars Exploration Program designed to explore the red planet. The primary purpose of the Curiosity mission was to determine the planet's "habitability." To enable the mission to achieve such a goal, a rover was equipped with the most advanced suite of instruments for scientific experimentation. The Curiosity rover is capable of determining the soil and rocks formation, structure and chemical composition by analyzing soil and drilled powdered rocks allowing scientist to determine the planet's climate and geology. Furthermore, scientists were able to detect the chemical building blocks of life, such as forms of carbon, on Mars and whether or not Mars environment was habitable in past.

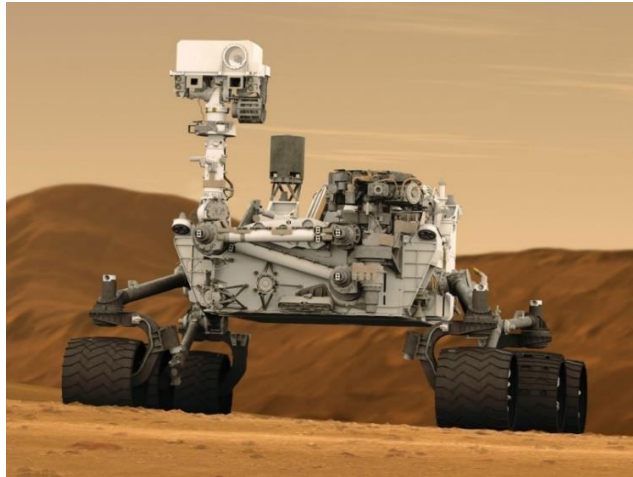


Figure 11: Curiosity Rover 2012, JPL

3.1.8. Mars Science Laboratory (MSL)/Curiosity Excavation Plan and Tools

The Curiosity mission is the most recent of a series of expeditions to the red planet with four main objectives to be achieved: Determining whether life ever existed on Mars, characterizing the climate of Mars, characterizing the geology of Mars, and preparing for human exploration. The theme of the exploration missions before Curiosity was "Follow the Water" in search for evidence of habitability. However, scientists changed the theme to "Seek Signs of Life" using the Curiosity rover. Therefore, instead of choosing a landing site with evidence of water, the landing site was chosen based on evidence of possible organics, the chemical building blocks of life, and ultimately habitability.

3.1.8.1. Robotic Arm Mounted Powder Acquisition Drill System (PADS)

A 2.1 m long, 36 kg titanium robotic arm on the Curiosity rover has five instruments installed at the end of it. Two of these instruments are designed for sample acquisition, a rotary percussion drill and a scoop delivering powdered rock and soil samples to the analysis instruments Sample Analysis at Mars (SAM) and Chemistry and Mineralogy (CheMin), onboard the rover. The drill has a diameter of 1.6 cm (0.63 in) and can penetrate up to 5 cm (2.0 in) deep. The drilled materials in a powder form are delivered to the instruments using the scoop (Figure 12).



Figure 12: Mars Hand Lens Imager (MAHLI) camera on NASA's Curiosity Mars rover shows the first sample-collection hole drilled in Mount Sharp, JPL

3.1.8.2. Curiosity Robotic Arm Scoop

The scoop is an instrument located at the end of the robotic arm that can collect loose soil material from depths of up to 3.5 cm (Figure 13). The rover wheel-dug trenches could reach a depth of approximately 20 cm below the original surface. The scoop can also collect unconsolidated samples from those trenches depending on the trench geometry. The scooped soil sample volume could be as much as 3000 mm³.



Figure 13: Mechanisms for scooping, sieving and portioning samples of powdered rock and soil samples, JPL

3.2. Mars 2020 Mission and Drilling System Requirements

Obtaining a “Mars returned sample” has been the top of the planetary exploration program priorities since exploration on Mars began. In addition to the Mars 2020 Science Definition Team (SDT), the Mars Exploration Program Analysis Group (MEPAG) also requested a “Mars returned sample” report from the International Science Analysis Group (iSAG). The iSAG would conduct careful *in situ* science and use that scientific information to select and cache samples. This process ensures samples collected meet the mission sample requirement and establishes a successful mission planning and concept from end to end for Mars 2020 (E2E-iSAG).

Both the Mars 2020 Science Definition Team and the International Science Analysis Group conducted extensive independent analysis of potential future Mars mission before specifying the mission requirements. In their final reports (Mars 2020 report), the drilling system requirements were determined in accordance with the mission objectives and with consideration for the planetary protection rules. The requirements and the importance of the drilled sample to be in a solid shape of a core sample and not a powdered form, the limitation of WOB of the drill system, and the drill speed limitation were addressed in details in chapter 2. The following are the major points influencing the drill system design:

3.2.1. Core Sample Mass, Length and Diameter

The sample length and diameter specifications, which determine the drill bit dimensions, sample mass and volume requirements are considered. Analysis was conducted by Next Decade Science Analysis Group (ND-SAG) guided by Mars Exploration Program Analysis Group (MEPAG) report. The analysis report by the MEPAG ND-SAG (2008) concluded “A full program of science investigations would likely require samples of >8 g for bedrock, loose rocks and finer-grained regolith. To support required biohazard testing, each sample requires an additional 2 g, leading to an optimal size of 10 g.” (E2E-iSAG 2012)

ND-SAG stated: “For core samples: length vs. diameter. This report recommends that a mini-corer be utilized to acquire rock samples and these samples must be larger than about 10 grams. However, the ND-SAG team did not attempt to evaluate the optimal combination of length and diameter of these core samples. Preliminary thought within the ND-SAG team was that a mini-core length of about 5 cm would be desirable, but more systematic analysis is required” (ND-SAG 2008). Thus, while the drill bit length is desired to be 5 cm, the inner and outer diameters must be determined in order to meet the required sample volume of 8 cc addressed below.



Figure 14: Honeybee Robotics Bit

The SDT suggests the baseline/threshold for the sample volume of approximately 8 cc of material per sample. The 8 cc value is established based on the desired mass of 15-16 g (500g total returned sample mass) of material and assumes an average sample density value of 2 g/cc. The diversity of sample materials varies drastically depending on the materials type and whether it is regolith, sedimentary rock or igneous rock. Also, another critical point needs to be taken into consideration, which is the possibility of core fracture during collection leaving large voids within the sample. Therefore, the 8 cc volume is only an approximate volume. The SDT suggests that the value be further examined by the 2020 project office to determine what volume best meets the requirement to obtain 15-16 g of material per sample (Mars 2020 SDT Final Report). See (Figure 14) of Honeybee Robotic drill bit design that meets the SDT core sample requirement.

3.2.2. Number of Samples

Scientists estimated/determined the number of samples necessary required a deeper understanding of rock formation structure as the basis for their selection. In ND-SAG report, they explained that natural materials are heterogeneous at scales ranging from atomic to planetary. It is assumed that the mineralogical, geochemical, biogeochemical, and morphological properties would vary among samples based on the temporal and spatial distribution of processes active on Mars. It is well known from previous studies that the characterization of heterogeneities could provide as much information about processes as the specific characteristics of a given sample. Therefore, Mars sample return missions would need to collect as many of these diverse samples as reasonable to optimize the mission scientific benefits. Such a goal could be accomplished through a careful selection of both landing sites and samples from each site.

For purpose of comparison, during the first year of Spirit rover sample analysis in Gusev crater, a suite of 30 samples were deemed sufficient to characterize the diversity of materials encountered on Mars's surface. The sample cache is a core sample storage unit onboard Curiosity spacecraft. Therefore, the baseline and threshold of 31 core sample cache size is an adequate number of samples to address the mission objectives. The 2020 SDT supports the previous proposals of baseline and threshold values of 31 core samples in the cache (E2E-iSAG, 2011, JSWG, 2012). The cache packaging geometry for different arrangements is showing in (Figure 15).

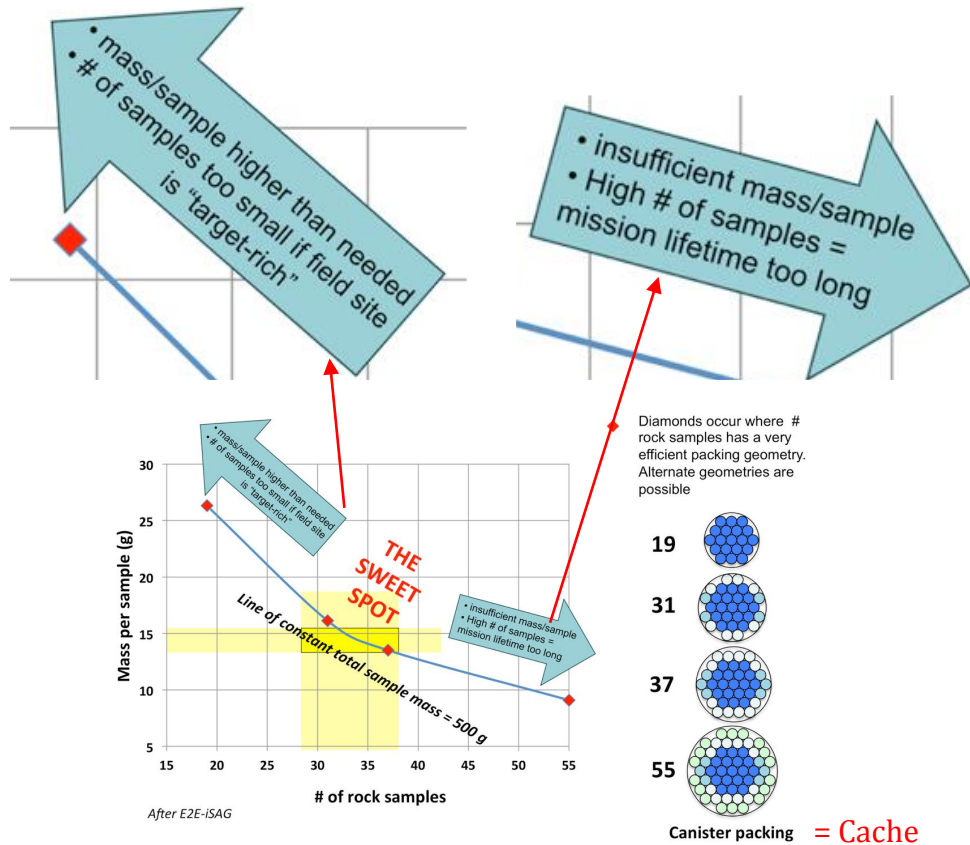


Figure 15: To bring back 500 g of sample of a particular size, particular packaging geometry are possible, Mars 2020 SDT

To better understand the local Martian environment and geological history, it is important to acquire sufficiently diverse samples that allow scientists to evaluate a specific research question/objective. Diverse samples would allow the evaluation of whether or not a specific result is representative and extrapolate processes interpretations from variations among and within samples. A careful sample selection will allow scientists to evaluate “1) how representative each sample may or may not be of the geologic unit; 2) the consistency of processes creating and altering the samples; and 3) abundances of specific attributes such as minerals and geochemical signatures.” (ND-SAG 2008).

Chapter 4

4. Literature Review on Drilling Systems and Extraterrestrial Drilling

Drilling systems with application to extraterrestrial exploration have been developed and have shown progressively improved performance aiming to achieve optimum drilling capabilities under extreme conditions. The following is a review of the historic development of the drilling techniques utilized thus far and their limitations of rate of penetration and maximum depth they can reach. Recent Curiosity findings revealed the need of drilling six meters deep that requires more of an aggressive drilling technique investigated in this research, rotary ultrasonic drilling.

4.1. Rotary Drilling

The rotary drilling mechanism is based on the drill bit rotation that produces two different types of forces on the workpiece, impact force as the drill bit presses vertically on the workpiece and shearing forces as the drill bit rotates. As the bit rotates, penetration occurs normal to the direction of rotation as a result of the thrust on bits breaking the bond holding the rock particles together. The built up stress is relieved through tension or shear fractures along the thrust direction. As the impact creates compression, a cutting force that is perpendicular to the penetrating direction causes tensile fractures that extend from the bit tip to the rock surface at about 80°. Chip formation occurs discontinuously ahead of the bit, and the penetrating and cutting forces oscillate during cutting as shown in (Figure 16) (Bruno, Han, & Honeger, 2005).

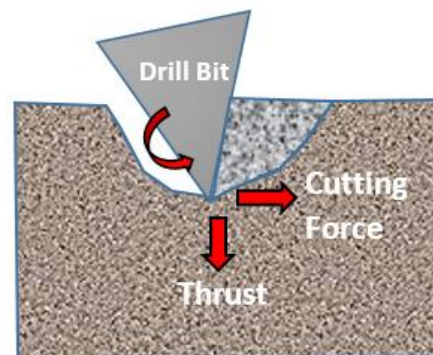


Figure 16: Rock damage process for rotary drilling

4.2. Rotary-Percussive Drilling (RPD)

Rotary-percussive drilling mechanism is based on the rotary mechanism coupled with applying a repeated large impulsive force ranging from 1500 – 3000 blows/minute from the impact of a pneumatically-operated piston (hammer) to a rotating bit. The kinetic energy conveyed by the piston is transformed into compressive stress waves that propagates through the drill bit down to the workpiece (rock) causing rock destruction by indentation, crushing and chipping as shown in (Figure 17) (Bruno et al., 2005).

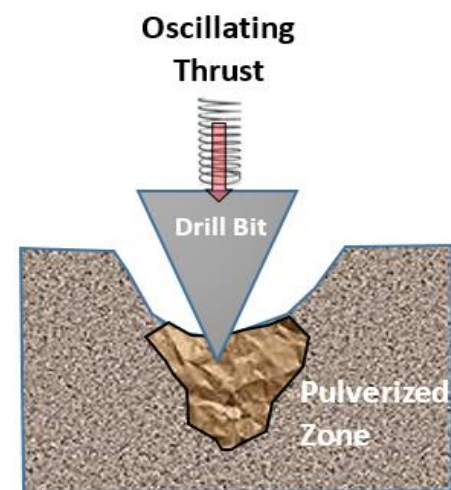


Figure 17: Rock damage process for rotary-percussive drilling

The energy and gas industry have invested heavily in research that leads to advances in simulation technology to help the industry economically and efficiently recover vast untapped gas resources contained in deep, hard rock environments. This extensive research revealed evidence that the combination of the percussive and rotary drilling technique offers significant improvement in the rate of penetration in hard rock environments (see Samuel, 1996 for a review). In addition to a higher rate of penetration than either rotary or percussive alone, the rotary-percussive drilling technique demonstrated other benefits such as achieving same results using less weight on bit, less contact time with rock and therefore less abrasion and a longer bit life, improved control of hole deviation and producing large cuttings that resulted in an improved geologic interpretation. Although the aforementioned rotary-percussive drilling advantages were demonstrated theoretically, the results in the field varied (Bruno et al., 2005).

Bruno et al (2005) shed some light on the comprehensive research that took place in the industry to advance the fundamental understanding of the physical mechanisms of combining the percussion and rotary drilling. Zachny et al (2009) show much lower force required for drilling with percussion compared to without (Figure 18). Terralog Technologies led a team of researchers, and supported by TerraTek, that had extensive experience and distinct capabilities in fundamental rock mechanics, geo-mechanical simulation, and conducting full-scale rock mechanics and drilling experiments. The research program included three primary goals:

- 1) Analysis: extensive analytical investigations were conducted to develop a deeper and improved understanding of the fundamental rock mechanics processes with respect to percussion drilling.
- 2) Simulation: advanced simulation technology was developed for the percussion drilling process taking into account coupled structural, particle and fluid flow mechanics.
- 3) Experiments: the results from the analytical investigation and simulation modeling validation of these improved characterizations were validated with full-scale laboratory experiments (Bruno et al., 2005).

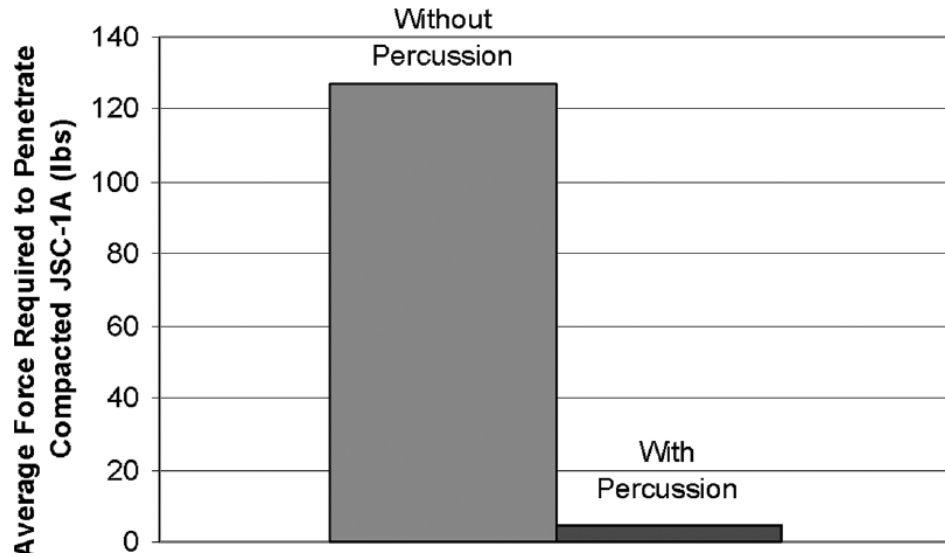


Figure 18: Honeybee Robotics percussive scoop tests (Zacny et al., 2009)

In the area of planetary drilling, most of the drills that have been used in the previous missions and even the one that are being considered for future missions are rotary drills. Recently the significant benefit of combining the percussive action to the rotary drilling has been recognized. The Mars Science Lab (MSL) mission in 2011 used a rotary-percussive drill that required two independent actuators to generate rotation and impact motions that are synchronized using a specialized control system. The utilization of such synchronization produces the most effective penetration rates and highest efficiency (Zacny et al., 2009). Subsequently, the self-excitation systems that combined the driving and synchronization of the striker from the rotation were developed and the two independent actuators were eliminated (Batako, Babitsky and Halliwell, 2003).

In the 1970's the Apollo mission drill system was a rotary-percussive drill that applied approximately (8) blows per revolution. One of the disadvantages of the applying only rotary drilling is the uncontrolled stick-slip events that could cause damage to the drill bit, and in extreme cases, it could damage the entire drill string. Using a rotary-percussive drill on the Apollo mission not only introduced favorable impulsive events, but it also reduced the uncontrolled stick-slip events (Figure 19). An additional advantage to the rotary-percussive drilling system is that it is self-regulating where it intensifies its impulse if it encounters resistance. Therefore, it is most effective drilling method thus far where the media is hard and brittle, yet higher efficiency is needed to reach a greater depth. It has higher performance in both increased penetration rates and reduced weight on bit than the conventional rotary drills (Bar-Cohen and Zacny, 2008, p.347).



Figure 19: Apollo 16 astronaut trains in lunar soil drilling, NASA

4.2.1. European Space Agency (ESA) Implementing Drill with Hammering Mechanism (DHM)

The European Space Agency (ESA) has a research program that is considering the implementation of hammering mechanism in rotary drills in the efforts of increasing the drilling performance efficiency when drilling hard rocks. ESA started with the ExoMars drill as a reference drill on which the hammering device would be mounted (Figure 20). The ExoMars drill research was completed in 2008 and it was conducted by a team of researchers from Galileo Avionica in Milan and Helsinki University of Technology (Bar-Cohen and Zacny, 2008, p.393).

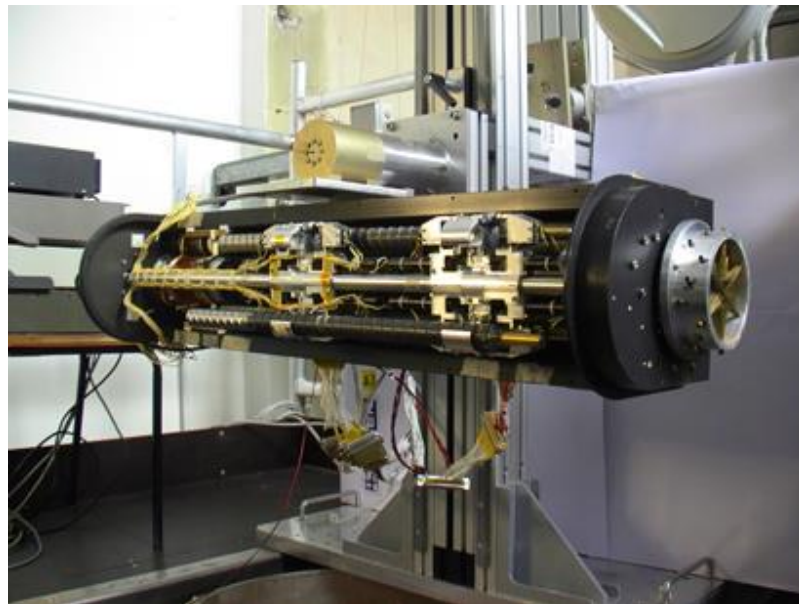


Figure 20: The ExoMars Drill, ESA Robotic Exploration of Mars

To implement the hammering mechanism, ESA considered two different systems concepts, a spring-loaded impactor released by a cam and various resonant systems. Both concepts were preliminarily tested to determine the final system choice for full prototyping. The cam-hammer mechanism was the system of choice to be developed and designed to use the sudden release of a previously loaded cam-compressed spring to produce 1 joule of impact energy at a nominal frequency of 1 Hz. A challenge to the overall system design was the drill bit's small diameter, a maximum 24 mm, to accommodate the mechanism implementation.

The cam-hammer mechanism is based on a rotary cam that is driven by an electric motor to move up and down. The cam works against a compressed spring and when it is released, the spring provides the hammering energy. A striker attached to the cam that hits a coupling interface holding the drill bit mounted to the hammering mechanism. A rod of 505 mm length, 24 mm inner diameter, and 27 mm outer diameter without auger, and 29 mm diameter with auger for chip removal, holds the drilling mechanism. The prototype used a Maxon EC22 motor provides 55 watts and a gearbox of 22 mm in diameter (Bar-Cohen and Zacny, 2008, p.394).

The drill system prototype was manufactured and tested on a variety of hard materials as well as tested in different operating conditions. The drill systems (Figure 22 and Figure 21) and the mock up commercial and specifically designed drill tools and their specifications (Figure 23, Figure 24, Figure 25, and Table 1) were used for tests showing some design options and process characteristics.



Figure 22: Test equipment with integrated drill/core tool that is 70 cm long. ESA and Galileo Avionica

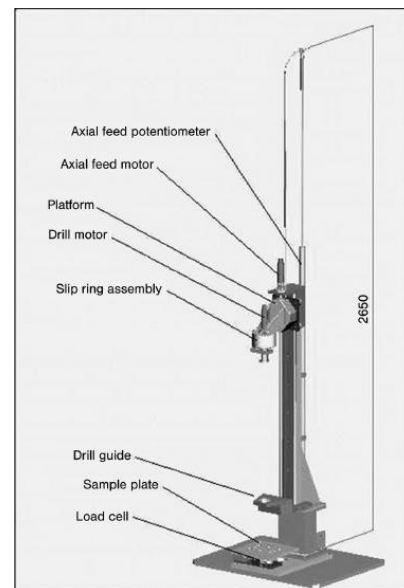


Figure 21: Schematics of TE at Galileo Avionica, ESA and Galileo Avionica

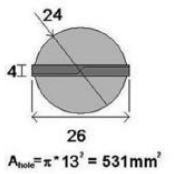


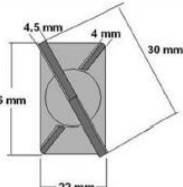


 <p>$A_{area} = \pi \cdot 13^2 = 531 \text{ mm}^2$</p>	 <p>Commercial tool 26 mm – top view (2 cutting bits are present)</p>	 <p>Commercial tool 26 mm – lateral view</p>
 <p>Area = 22 * 26 = 572 mm²</p>	 <p>Commercial tool 30 mm – top view (4 cutting bits are present)</p>	 <p>Commercial tool 30 mm – lateral view</p>

Figure 23: Schematics and pictures of commercial drill tools, ESA and Galileo Avionica

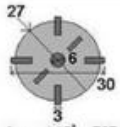


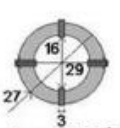


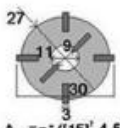


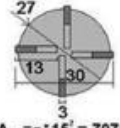


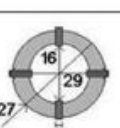


 <p>$A_{area} = \pi \cdot 15^2 = 707 \text{ mm}^2$</p>	 <p>Pure drill type A - top view</p>	 <p>Pure drill type A - lateral view</p>
 <p>$A_{area} = \pi \cdot ((14.5)^2 - 8^2) = 460 \text{ mm}^2$</p>	 <p>Thin corer - top view</p>	 <p>Thin corer - lateral view</p>
 <p>$A_{area} = \pi \cdot ((15)^2 - 4.5^2) = 643 \text{ mm}^2$</p>	 <p>Thick corer - top view</p>	 <p>Thick corer - lateral view</p>
 <p>$A_{area} = \pi \cdot 15^2 = 707 \text{ mm}^2$</p>	 <p>Pure drill type B - top view</p>	 <p>Pure drill type B - lateral view</p>
 <p>$A_{area} = \pi \cdot ((14.5)^2 - 8^2) = 460 \text{ mm}^2$</p>	 <p>New thin corer – top view (new cutting bits)</p>	 <p>The new cutting bits have a shape similar to the ones of the commercial tool diameter 26 mm.</p>

Figure 24: The drill tools used during the DHM test campaign. ESA and Galileo Avionica

Table 1: Main characteristics of TE available at Galileo Avionica, ESA

Drill rotation speed	25 - 250 rpm
Drill motor nominal power	50 W
Drill rotation speed measure	Encoder
Linear translation speed	0 - 55 mm/min
Linear stroke	1 m
Linear stroke measure	Linear potentiometer
Electrical slip ring	12 tracks
Load cell for thrust measure (implemented at the base of TE)	0 - 2400 N
End stops	Microswitches

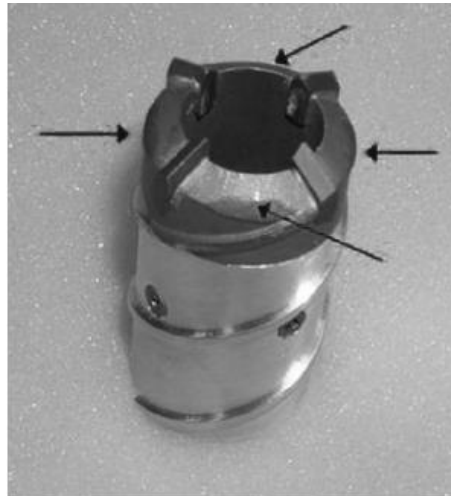


Figure 25: New thin corer after test in granite. Arrows indicate the points where the external parts of the tool were hitting the materials. ESA and Galileo Avionica.

The DHM prototype was most effective in drilling into granite compared to previous research results that has a compressive strength of 160 MPa and obtaining samples of granite. It used a relatively low applied load of 100 N and low power consumption of between 5-10 W at in order to achieve a rate of penetration of about 0.2 mm/min. The new thin corer (Figure 25) was used for the test on marble and granite types of rocks (Figure 26). A thrust of 98 N was applied at a rotational speed of 6 rpm. First choice of frequency of DHM was at 1 Hz and the second part of the test the frequency was doubled to 2 Hz while the power consumption range was from 5.5 to 7.5 W depending on the chosen frequency (Bar-Cohen and Zacny, 2008, p. 394).

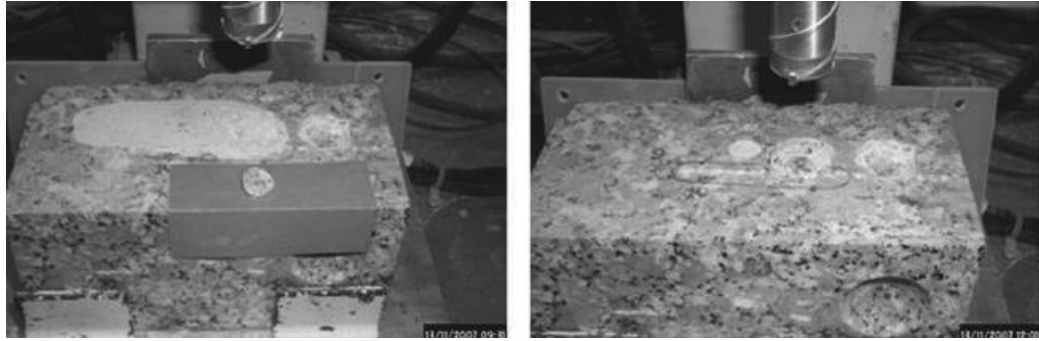


Figure 26: Test No. 2 into granite: hole and sample. (a) Granite hole with powder. The sample was removed and placed on the blue sheet. (b) Granite hole with powder removed. ESA and Galileo Avionica

Another test was conducted on granite also at frequencies of 1 and 2 Hz and at a slow rotation speed of 0.26 rpm. It was concluded from the tests conducted on granite that it is critical to drive the tool rotation with proper indexing speed rather than a random speed relative to the cutting bit's position when the shock is transmitted in a synchronized way to the material. As a result, a circular sample was obtained. It was also noted that, in the case of drilling in granite, a higher thrust was not beneficial to the rate of penetration while the hammer is activated. Best results were achieved at a thrust of 100 N (Bar-Cohen and Zacny, 2008, p. 397).

4.3. Rotary-Ultrasonic Drilling (RUD)

An alternative to rotary-percussive drilling is a technique that uses much lower amplitude axial motion with much higher frequency known as rotary-ultrasonic drilling.

The drill's movement mechanisms in RUD are rotational due to the rotary motion of the drill bit superimposed with a axial oscillation (ultrasonic wave) (Figure 27). Literature show the following major advantages to the rotary ultrasonic drilling over traditional rotary or rotary-percussive drilling:

- Reduction in the applied force required for drilling.
- Higher surface quality.
- Higher level of accuracy.
- High chipped materials removal rate.
- Faster penetration rates.
- Less contact time with the workpiece and therefore less of tool wear.

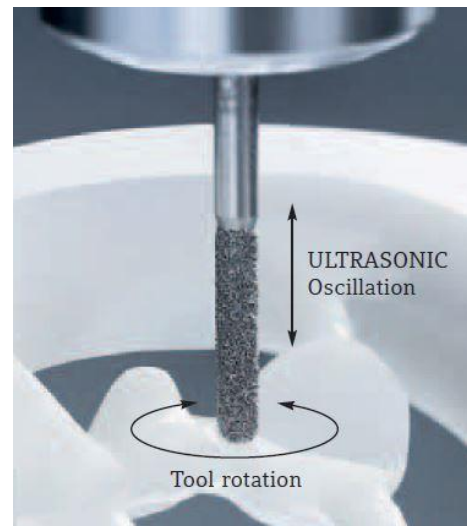


Figure 27: Rotary Ultrasonic Motion, DMG

- In ductile materials, the reduction or even elimination of burrs on both the entrance and exit faces of plates. As a result, ultrasonic drilling leads to improved surface quality and tool life.

Rotary component mechanism as discussed in section 4.1: the Weight On Bit (WOB)/force applied to the drill bit as it rotates produces two different forces, impact and shearing forces exerted on the workpiece (rock). The impact force causes the rock to be crushed, while the shearing (cutting) force causes the rock to fracture.

Ultrasonic component mechanism: the axial oscillation is generated from very rapid percussive impact or ultrasonic vibrations in the sonic or ultrasonic frequency range (> 20 kHz). This component of the motion has three different mechanisms; 1) hammering force generated upon the impact of the percussive/vibrational oscillation slowly builds up between the drill bit cutting edge and the rock point of contact and gradually fracture and compact rock's irregular surface; 2) force rapidly increases and subsurface cracks are developed in the rock radially outwards from the stress concentration lines at the bit cutting edge outer boundaries; 3) rock fatigue due to cyclic loading is an additional dynamic that has effect on percussive/vibrational (sonic/ultrasonic) drilling mechanism (Han & Bruno, 2005) (Bruno et al., 2005) and (Terralog Technologies Inc: <http://www.terralog.com/>).

4.3.1. Ultrasonically Assisted Drilling (UAD)

Ultrasonic-assisted drilling is based on superimposing high frequency (ultrasonic) vibrations on the cutting motion of the conventional rotary drill (Toma and Babitsky, 2007). The typical configuration for UAD involves mounting a conventional drill bit on an ultrasonic transducer that consists of a backing section, two piezoceramic rings, waveguide/concentrator, and a tool holder (Figure 28). The concentrator's function is to amplify the piezoceramic rings' vibration, with respect to the displacement amplitude, and through the tool holder it delivers it to the drill bit. In order to achieve high displacement amplitude at the tip of the drill bit, the entire ultrasonic system must be tuned to resonate at a suitable frequency (usually between 20 and 40 kHz) (Bar-Cohen and Zacny, 2008, p.377).

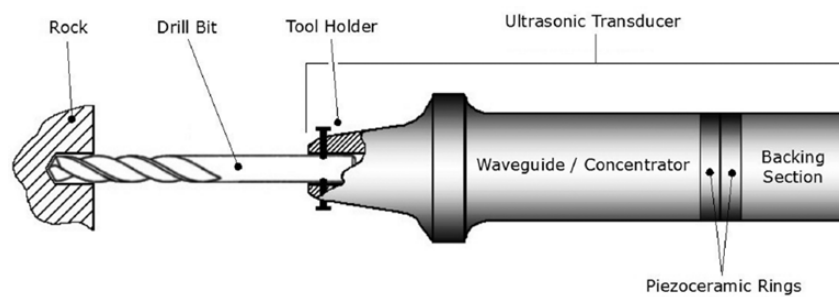


Figure 28: UAD system configuration, Ba-Cohen and Zacny, 2008

The drilling process is conducted with dual motion of the drill bit. One is in the axial direction, which is the ultrasonic vibration (Figure 29, a), and the other motion is in the conventional twist direction that is applied by the rotary motor (Figure 29, b).

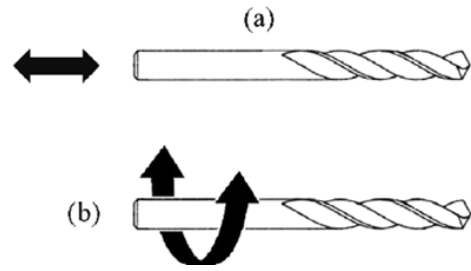


Figure 29: UAD excitation, Bar-Cohen and Zaczny, 2008

4.3.2. Pure Ultrasonic Drilling

Drilling holes or core holes in rocks and hard brittle materials could be achieved using pure ultrasonic drilling (no rotation) using frequencies of about 20 kHz and above. It is required that the stress applied exceed the rock strength to achieve compressive rock fracture. Therefore, it is presumed that erosion is the mode of cutting using purely ultrasonic cutting tools. The erosion process takes place as the broken small particles are forced against the mass of the rock's surface causing more particles to break off perpetuating the drilling or coring process. If the broken particles are not removed, a large portion of the energy in the system is consumed in reducing the size of the very small loose particles. Eventually, the very small loose particles cause a reduction in material removal rate resulting in an inefficient drilling process.

The purely ultrasonic drilling tool operates on the principle of the traditional ultrasonic machining techniques where either an abrasive slurry or particle impregnated metal matrix composites (MMC) abrasion tools is used. The cutting action is achieved by using harder abrasive particles in the abrasive slurry than the materials being drilled. Ultrasonic drilling using fluid/slurry has been used to drill rocks where the hard and sharp particles in the fluid abraded the rocks (Maurer, 1968). Fluid circulation ensures the fresh supply of abrasive particles to the tool removing rock particles. Due to the usage of external fluid purely ultrasonic drilling technique, it is unsuitable for most extraterrestrial drilling applications since external fluid is considered contamination.

Another factor that affects the drilling efficiency is whether a full face bit is used for drilling or a coring bit. Drilling with a full face drill bit is inefficient since the entire cutting surface of the drill bit is in contact with the workpiece. However, using a coring bit increases the efficiency significantly due to the reduction of the drill bit cutting area that is in contact with the workpiece requires breakage. JPL jointly with Cybersonic, Inc. were the first to develop a drill called Ultrasonic/Sonic Driller/Corer (USDC) where sonic frequency oscillations to the ultrasonic actuation (Bar-Cohen and Sherrit, 2001). This design was followed by numerous modifications since it was

developed in 1999 with the goal in mind to make the drilling method applicable to as many future missions as possible as it is addressed in the following sections.

4.3.3. Ultrasonic Core Drilling

The limitations of the rotary drilling techniques were the main driver behind investigating new drilling approaches. Rotary drilling techniques require high drilling force on the drill bit and inability to duty cycle efficiency. To overcome these limitations the JPL's Advanced Technologies Group and engineers from Cybersonics, Inc. joined efforts to develop the Ultrasonic/Sonic Driller/Corer (USDC) (Bar-Cohen et al., 2001, 2007; Bao et al., 2003; <http://ndeaa.jpl.nasa.gov/nasa-nde/usdc/usdc.htm>). A low frequency hammering action produced by a conversion of high-frequency vibration drives the USDC penetration mechanism (Figure 30). The initial purpose of the USDC drill was to support NASA's search for existing or past life on the extraterrestrial planets with the capabilities of sampling of rocks, ice, and soil. The drilling mechanism is driven by an ultrasonic piezoelectric actuator impacting the drill bit at sonic frequencies using an intermediate free mass (Bar-Cohen and Zancy, 2008, p. 380).

The USDC overcame one of the rotary drill limitations by requiring low axial force applied on the drill bit. This feature is a significant benefit for planetary sampling in low gravity environment. It is also a great advantage to be able to perform drilling and coring in hard rocks, ice, and packed soil, which are considered difficult drilling and coring tasks by utilizing low axial force and lightweight hardware. The USDC capability to operate with low axial force allows it to be utilized on lightweight rovers and robots. It is also designed to produce core and powder cuttings, which is an advantage for a variety of research purposes.

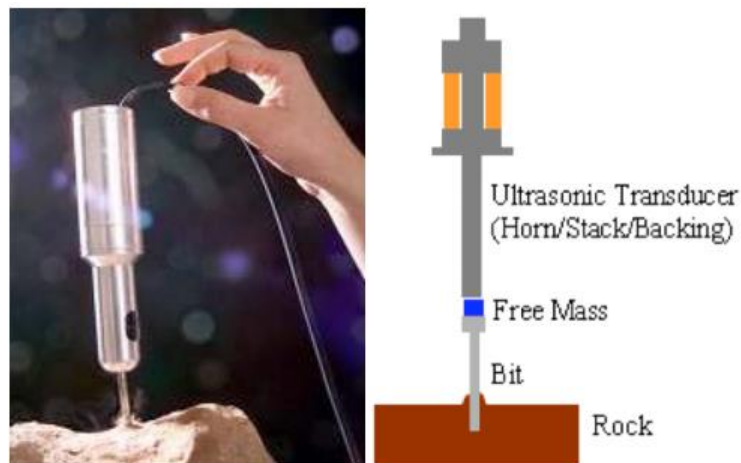


Figure 30: A photographic view of the USDC showing its ability to core with minimum axial force (left); a schematic cross-section view (right). Courtesy of NASA/JPL (Bar-Cohen and Zancy, 2008)

The USDC consist of three components: actuator, free mass, and drill bit (Figure 30) (Bao et al., 2003). An ultrasonic vibration mechanism through the actuator delivers energy to the free mass that as a result impacts the drill bit producing a stress impulse. Rock fracture occurs when the rock ultimate strain is exceeded by the stress impulse at the rock/bit interface. The actuator consists of a piezoelectric stack with a backing layer for forward power delivery and a horn to amplify the induced displacement. The actuator is driven in resonance and is held in compression position by a stress bolt to prevent fracture during operation.

The basic design of the piezoelectric stack is to have resonance frequency around 20 kHz, the long limit of the range of ultrasonic vibration. To ensure maximum input current to the actuator, and in return maintaining the resonance frequency, the driver electronics are designed to utilize either software or hardware to maintain the actuator tuning. This tuning is essential due to the presence of various factors that affect the resonance frequency. One of those factors is the action of drilled medium reducing the Q of the resonator and slightly shifts frequency. USDC particularly requires tuning in cases of impacts that cause time variations in the current signal (Aldrich et al., 2006). The conventional ultrasonic drills have the drill bit ultrasonically coupled to the horn, while the actuator in the USDC drives a free mass and converting the ultrasonic impulse to hammering impacts at sonic frequencies.

4.3.4. Novel Ultrasonic Drill Designs Followed the USDC

The development of the USDC opened the doors to a variety of research areas such as analytical modeling and field testing of improved design that apply to a different application types. USDC performance optimization was also pursued in developing an improved analytical capabilities, while additional research was conducted to enhance its ability in drilling at a higher range of power and speed. One approach to utilize the benefit of the USDC does not require rotation was mounting sensors were mounted on the drill bit to examine the borehole while drilling. Following these efforts, a variety of novel design and improvements were made on the drill bit, horn, and other USDC components to be able to conduct autonomous sampling in extreme environments and in dealing with the challenging requirements. The analytical results enabled scientists to predict the performance capabilities of the drill and allowed further development improving the design effectiveness by optimizing performance configurations (Bar-Cohen et al., 2005).

After the development of the USDC, NASA's New Technology group generated a series of novel designs that were published in their reports and patents (e.g., Aldrich et al., 2006; Badescu et al., 2006; Bao et al., 2004; Bar-Cohen et al., 2001, 2002, 2005; Bar-Cohen, Sherrit, and Herz, 2003; Bar-

Cohen and Sherrit, 2003; Chang et al., 2004; Dolgin et al., 2001a; Dolgin et al., 2001b; Sherrit et al., 2001, 2002, 2003). To name a few of the known ultrasonic drills that were developed include the ultrasonic/sonic rock abrasion tool (URAT), and the ultrasonic/sonic gopher for deep ice drilling, and the lab-on-a-drill. The developed ultrasonic drills were designed with the main goal of planetary exploration applications. The USDC was effective in drilling in a variety of media such as ice and different types of rocks such as granite, limestone, basalt, and diorite (Bar-Cohen and Zacny, 2008, p. 357) (Figure 31).

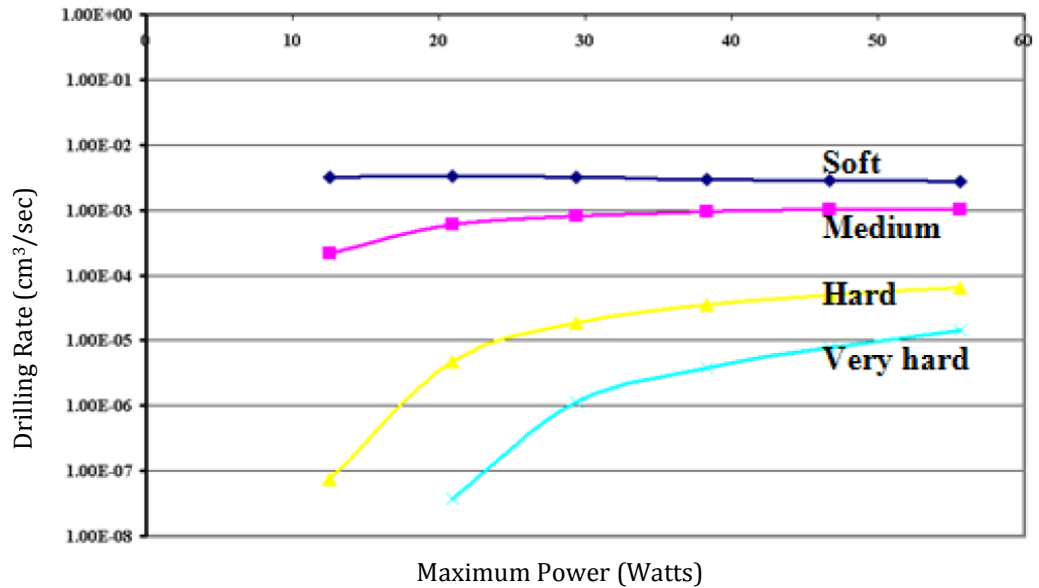


Figure 31: Analytical drilling rates in rocks with various hardness levels using 10 W of average power. The rocks are classified by their compression strength, where: Soft: 0 - 50; Medium: 50 - 100; Hard: 100 - 200; and Very hard: > 200 (MPa) (Bar-Cohen et al., 2012)

4.3.5. Ultrasonic/Sonic Impacting Penetrator (USIP) Reaching 1 Meter in Depth

Attaching a drill bit of 3.18-4.76 mm in diameter to a USDC-based penetrator (USIP) made it capable of reaching a depth of 1 meter in packed soils (Figure 32). It would have required several hundred pounds using conventional pushing force alone that may subject the drill bit to failure due to buckling. It was shown that the force applied was reduced to 31 N using USIP versus 890 N using pushed force alone (Bao et al., 2004).

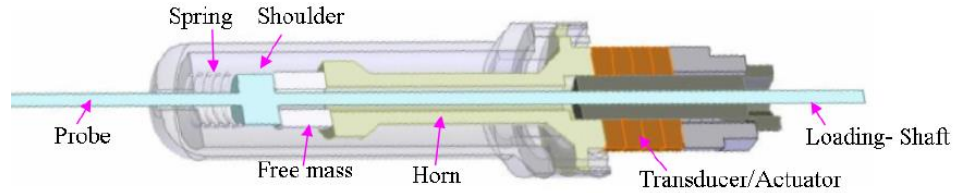


Figure 32: A schematic view of the USIP, (Bar-Cohen, Sherrit, Badescu, & Bao, 2012)

To achieve effectiveness and high performance, the design involved three different types of analysis. Two were conducted on the actuator, the modal analysis and harmonic analysis. The modal analysis was used to guide the actuator design and the harmonic analysis used to predict the actuator performance. The third was the system impact analysis that guided the effectiveness of the penetrator design. It determined the interaction between the USIP components, free mass, ultrasonic horn, and the drill bit to derive the free mass optimal weight, determining the actuator design parameter required that the actuator neutral plane to coincide with the mounting location.

4.3.6. Ultrasonic/Sonic Drilling Corer (USDC) Advantages

The following features were concluded to be the major benefits of the USDC based on analysis and field tests:

- 1) Low force that allowed for low-mass platforms.
- 2) Power efficiency
- 3) Mass-efficient drilling
- 4) Relatively, simple drill bits that don't require sharpening eliminating possible contamination and increasing reliability.
- 5) Simple mechanical bit interface utilizing the option of using multi-function bits accomplishing variety of tasks.

ESA also put on great efforts in investigating the ultrasonic rock corer performance for planetary missions by putting together a team of scientists and researchers from the Universities of Leicester and Aberdeen (Sims et al., 2002). Leicester was heavily involved in the spacecraft Beagle 2 activities while Aberdeen specialized in ultrasonic tools development for terrestrial applications.

Literature showed, and it was accepted, that the main mechanism of the ultrasonic drilling is dynamic fracture. The dynamic interactions between the drill bit and the drilled materials were analyzed utilizing the concept of the dynamic fracture propagation under percussive loading. Material fracture during drilling was simulated using the particle dynamics method where the model of the drilled materials was based on a set of particles representing grains. The simulation of a wide range of material properties were achieved based on advanced interparticle interactions laws. Particle

dynamics simulation methods were developed as a result to an established research program at the University of Aberdeen examining the application of percussive drilling of hard rock formations novel nonlinear dynamic methods. The drill bit propagation dynamic simulation is shown in (Figure 33)(Bar-Cohen and Zacny, 2008, p. 391).

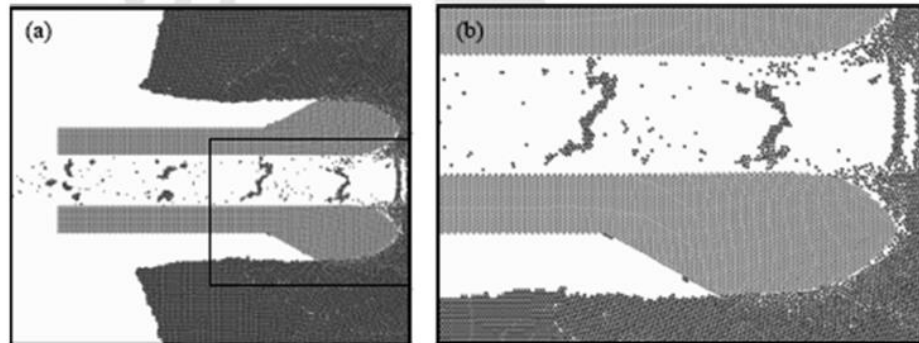


Figure 33: Particle simulation of down-hole percussive drilling. (a) Propagation of the drill bit; (b) detail of (a)., Universities of Aberdeen and Leicester.

A novel design was developed to overcome the issue of lower efficiency showed in other potential designs. It is a drive electronics design that operates based on utilizing bidirectional switching amplifier control by control logic possibly using a digital signal processor that allowed, if required, waveform synthesis to be performed. Utilizing this design, a corer tool of 3 mm drill bit diameter could operate around ultrasonic frequency of 28 kHz with an amplitude of 10 μm , with as low power as 20 W or less and a mass less than 0.5 kg, achieving drilling depth of 30 mm. The concept of sample collection and retention were investigated to arrive to the result that a separate collection mechanism is less risky development option. A similar design of Beagle 2 instrument arm was integrated to the new drill as it was recognized to be an adequate design for the tasks. The following is the proposed concept outline design of the ultrasonic rock corer (Figure 34). As the design may reveal some of drilling appealing features, the effect of each design and process parameter on the drilling rate of penetration performance yet to be investigated in this research.

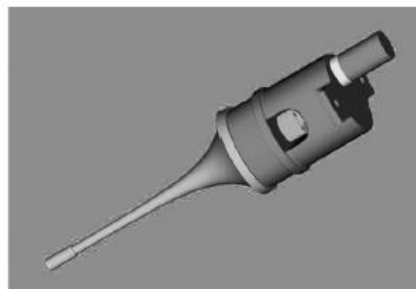


Figure 34: Concept of an ultrasonic drill for planetary applications. ESA and Universities of Aberdeen and Leicester

It is evident that the previously developed drilling devices and techniques have made a great improvement in achieving more efficient drilling and reaching a greater depth. However, they are still unable to achieve the desired depth of six meters that scientists concluded is necessary based on the Curiosity mission's results. A new technique is investigated in this research utilizing the rotary-ultrasonic drilling (RUD) mechanism. As discussed in Section 4.3, RUD offers the possibility of particularly high rate of penetration (ROP). A detailed explanation to the drilling mechanism is presented in Chapter 5 along with a discussion of the latest devices developed utilizing the RUD technique.

Chapter 5

5. Rotary-Ultrasonic Drilling Mechanics

While purely ultrasonic drilling showed great promise in the laboratory, field tests using such drilling tool, including the ultrasonic/sonic gopher in Antarctica, have shown significant limitation on the powdered cuttings removal rate necessary to achieve rapid deep-hole drilling (Badescu et al., 2006). This limitation was the main motivation behind the consideration of superimposing the ultrasonic mechanisms in drilling with the rotary action to achieve higher material removal rate and reach greater depths. A rotary percussion was designed to introduce the rotation capability and the ultrasonic vibration combined (Badescu et al., 2007). To ensure a robust mechanisms, the actuations of the rotation and hammering functions were decoupled, using one as a backup system in a case of the failure of the other. The dual action mechanics enhanced the drilling process significantly. In addition, various ultrasonic drilling parameters need to be handled with special care in the effort to reach optimum drilling process such as, matching resonance of the drilling device and using the proper horn design to achieve the desired amplitude magnification as described below.

5.1. Rotary and Oscillation Dual Action Mechanics

To achieve rotary and oscillation dual action, the drilling system will consist of the major following components (<http://www.decoup.com/en/content/how-does-it-work>):

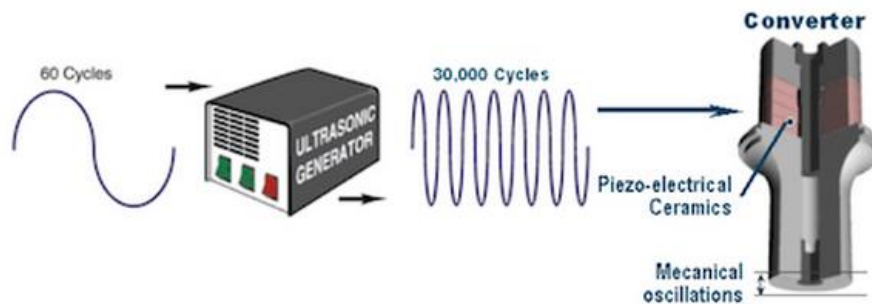


Figure 35: Ultrasonic device schematic of the operation concept, Decoup site

1) Ultrasonic spindle system

- a. Power supply (converts 60 Hz electrical supply to high frequency (>20 kHz) AC electrical output fed to the piezoelectric transducer)
- b. Ultrasonic spindle
 - i. Piezoelectric transducer that converts electrical input from the power supply into mechanical vibrations.
 - ii. Motor attached atop the ultrasonic spindle that supplies the rotating motion of the core drill (not shown in the figure).

- c. Motor speed controller that can be adjusted to obtain different motor speeds.
- d. Specimen fixture that holds the specimen and it is mounted on a dynamometer that is attached to the machine table.

2) Data acquisition system

- a. Piezoelectric dynamometer (measures the cutting force along feed direction producing an electrical signal and fed to A/D converter)
- b. A/D converter (converts electrical signals from the dynamometer into numerical signals that are displayed and saved on a computer system).
- c. Computer is typically equipped with a device that displays and saves the numerical signals coming from the A/D converter.

3) Coolant system

5.1.1. Axial oscillation dynamics

Axial oscillation is generated from vibrations in the range of sonic or ultrasonic range (> 20 kHz frequency) (Terralog Technologies Inc.) The oscillation effect takes three major states during the process of drilling. Hammering force is generated upon the impact of the percussive/vibrational oscillation slowly builds up between the drill bit cutting edge and the rock point of contact and gradually crushes and compact rock's irregular surface. The rapidly increased force develops subsurface cracks in the rock radially outwards from the stress concentration lines at the bit cutting edge outer boundaries. Finally, rock fatigue due to cyclic loading is an additional dynamic that has effect on percussive/vibrational (sonic/ultrasonic) drilling mechanism. Rock fatigue is not a part of the mathematical model developed in this research.

The rock workpiece during percussion drilling is exposed to uniaxial compression type of loading at the bit-rock interface. Literature shows that the rock uniaxial compressive strength (UCS) is weakened by approximately 75% in percussive drilling (Bar-Cohen and Zacny, 2008). Although this result was not closely examined by the oil industry until late the 1970s due to its high level of uncertainty, it is an invaluable finding as the fundamental mechanisms for rock damage during percussive /ultrasonic drilling. The fact of the UCS drop in percussive drilling may explain the fact that the process is faster than traditional rotary drilling since the rock is weakened and easily fractured due to the developed microfractures in the materials. In this research, the main goal is to determine the rotary ultrasonic drilling performance in brittle material (rock) as a drilling mechanism.

5.1.2. Rotary dynamics

As the materials are already fractured due to the vertical oscillation, the built up stress in the plane due to the rotary motion is relieved through the shear fractures along the thrust direction allowing the cuttings to be removed. The clearance of the cutting materials allows the drill bit to penetrate further achieving greater depth and overcoming the purely ultrasonic limitation mentioned previously.

Literature shows evidence of higher performance of rotary ultrasonic compared with the traditional rotary drilling where the static and lower WOB applied. For example, ROP of 3.3m/h was achieved with the 8.75 inch bit when WOB is 44.84 kN. While in rotary drilling mode, 184.33 kN of WOB is needed to achieve the same ROP (Melamed, 2000). Also, the less contact time with rock that lead to less drill bit abrasion and longer bit life where only 1 – 2% of total operational drilling time (Bates, 1965; Melamed et al, 2000).

5.2. Ultrasonic Wave Magnification Methods

To increase vibration amplitude, the drilling tool is designed to operate in the resonance mode (i.e. its length is equal to an integral number of half-wavelengths at a given frequency) (Ubartas). The piezoelectric rod is driven with an alternating voltage at a frequency corresponds to its resonance. As a result, the rod dimensions are set depending on the voltage used.

The power handling capacity for the piezoelectric materials, generally ceramics, is low due to its poor thermal conductivity and low tensile strength. Therefore, the amplitude of the vibrating motion generated by the transducer is normally too small for practical use and it is critical to amplify this motion (Figure 36).

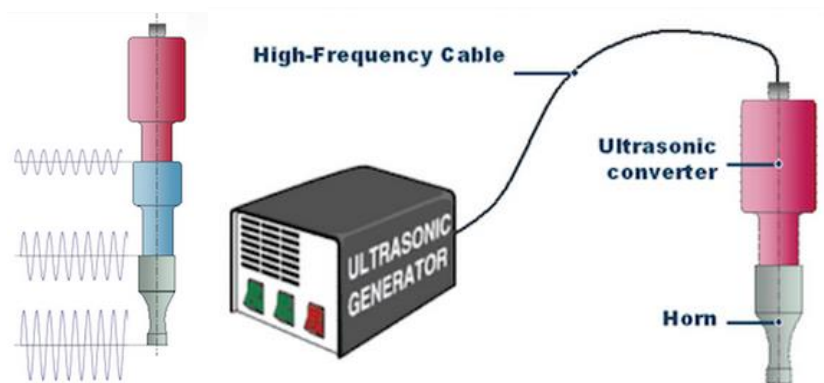


Figure 36: Ultrasonic device schematic of the components and amplitude magnification, Decoup site
(<http://www.decoup.com/en/content/how-does-it-work>)

5.2.1. Horns / Velocity Transformers

To overcome the inherent limitations of the piezoelectric's low power capacity, a variety of horn designs have been connected to the ultrasonic assembly between the transducer and the drill bit. It is critical, however, to maintain the overall assembly length at one half-wave. The horn function is to magnify the motion generated from the piezoelectric transducer. It is also a resonant element in the compression mode that is half a wavelength long. So, if the distance between the transducer and the workpiece needs to be increased, the horn is designed in multiples of half wavelengths or screwing one horn into the other thereby building up the overall length (<http://sonicsystems.co.uk/page/power-ultrasonics-a-guide/39/>).

5.2.2. The most popular horn designs are shown in Figure 37.

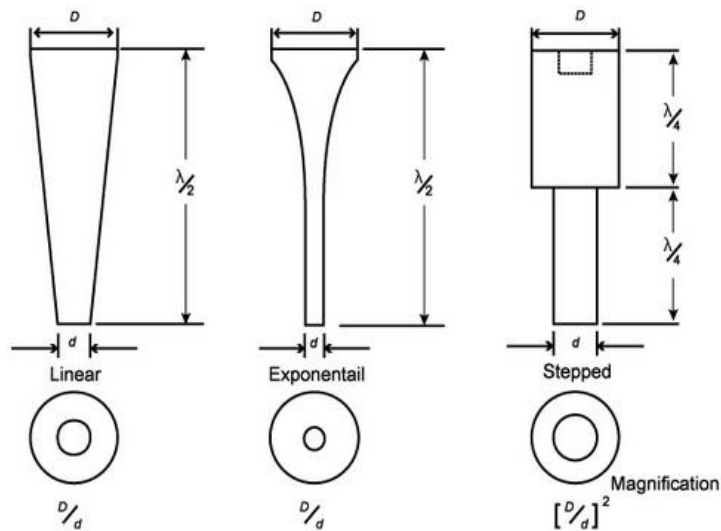


Figure 37: Different horn designs, (a) Linear taper, (b) Exponential taper, and (c) Stepped taper, sonicsystems.co.uk

Linear Taper: It is a simple design to manufacture, but it has magnification limitation to approximately four times (Figure 37, a and Table 2).

Exponential Taper: This design has the advantage of a higher magnification than the linear taper but it has the disadvantage of being difficult to manufacture due to its shape. Another attractive feature of this design is that its length coupled with the small diameter at the working tip makes it very suitable for micro applications (Figure 37, b and Table 2).

Stepped Taper: The magnification factor of this design is the ratio of the end areas $(D/d)^2$. The magnification limitation is

depending on the dynamic tensile strength of the horn material. The design attractive features are it is easy to manufacture, and it is easy to achieve 16 times magnification (Figure 37, c and Table 2).

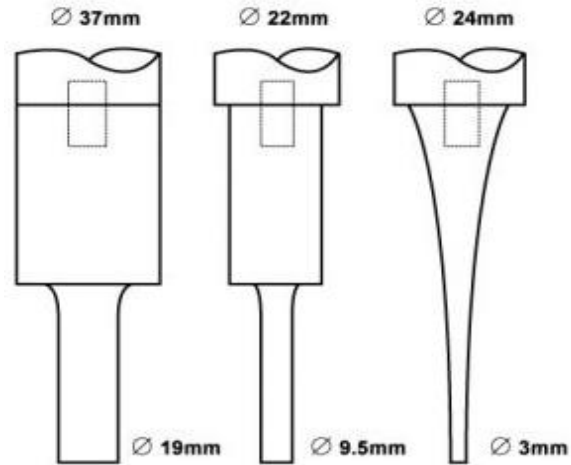


Figure 38: Various horn/transducer arrangements, Sonic Systems

Table 2: Acoustic power transmitted by various horn/transducer arrangements in Fig. 38

	<u>Stepped</u>	<u>Stepped</u>	<u>Exponential</u>
Amplitude ($\mu\text{m p.p}$)	46	72	96
Horn magnification	3.8	6	8
Radiating area (cm^2)	2.86	0.64	0.07
Transmitted acoustic power (W)	69	28	9.5
Power density (W/cm^2)	24.4	44	135

Magnification and stress curves distribution are shown below for the three different horn designs (Figure 39). The design of the stepped horn shows discontinuity in the stress curve and extra care needs to be taken in machining this design. The nodal region might be subject to metal fatigue in high magnification horns if it contains any marks that create “stress raisers” in the region.

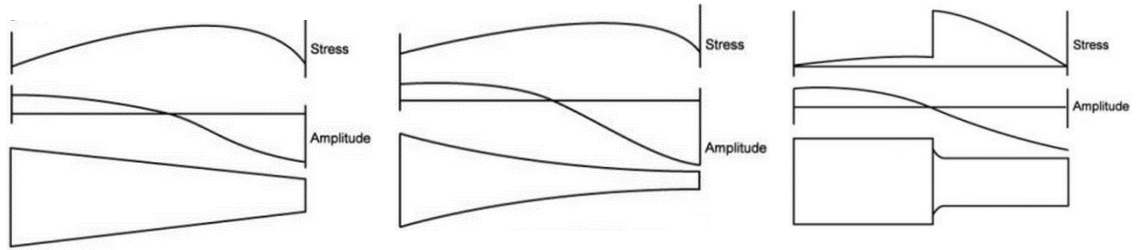


Figure 39: Stress and amplitude of different horn designs (a) Linear, (b) Exponential and (c) Stepped taper

5.2.3. Horns Suggested Materials

Ultrasonic horn materials are highly recommended to have the following characteristics:

- 1) High dynamic fatigue strength
- 2) Low acoustic loss
- 3) Resistance to cavitation erosion
- 4) Chemical inertness

Suitable materials that fit the above criteria are:

- 1) Titanium alloy
- 2) Aluminum
- 3) Aluminum bronze
- 4) Stainless steel

5.2.4. Actuators with Novel Horns

The most important component in the ultrasonic / sonic drill / corer (USDC) is the horn that amplifies the vibration amplitude generated by piezoelectric transducer. The most common horn design used is the stepped taper that gains amplitude due to the related reduction in the end surface areas.

5.2.4.1. Dog-bone Shape Horn

The dog-bone design shape was introduced and demonstrated a significant improvement to the drilling performance (Chang et al., 2004; Sherrit et al., 2001). Attractive features of the design are allowing the drill bit to be mounted to the actuator, and two separate free masses allowed forward and reverse hammering motions. Various designs were investigated analytically and then compared to the conventional solid shape horns. It was proven analytically that the dog-bone design significantly outperformed the conventional ones (Figure 40). A finite element modeling was conducted to demonstrate the dog-bone horn design performance to determine

the control parameters. The FEM showed the superior tip displacement and velocity (Bar-Cohen et al, 2007).

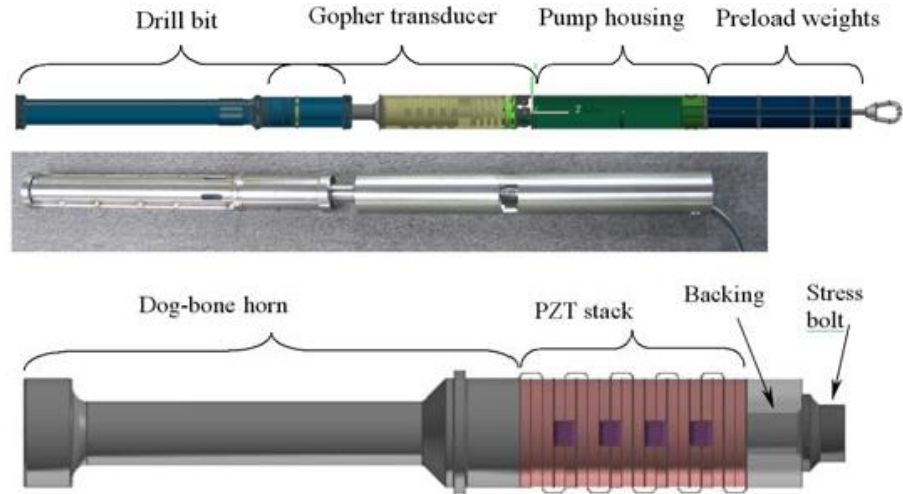


Figure 40: Gopher design with dog-bone horn

5.2.4.2. Folded/Flipped Horn

In some applications, the horn length is a critical factor of the operation where it has to be shortened due to volume constraints. This fact was the main motive behind the design of the folded and flipped horns that utilize hollow configuration that amplifies vibrations of high power actuation mechanisms (Figure 41) (Chang et al., 2004; Sherrit et al., 2001).

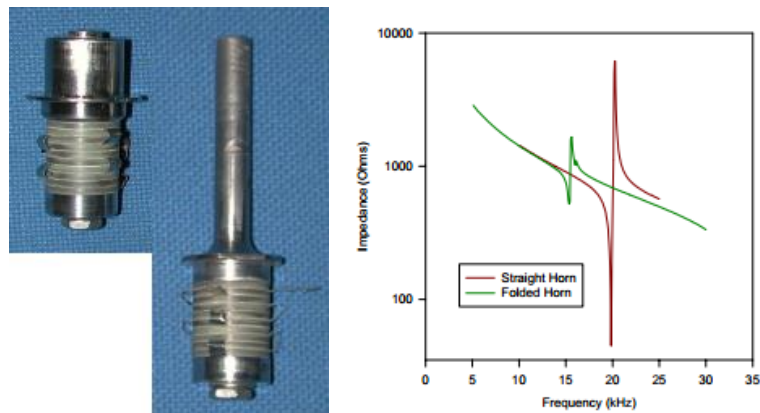


Figure 41: Photograph of the folded horn (16 kHz) and a comparison of a straight horn with approximately the same frequency (20 kHz). A substantial decrease in the resonance is found.

Varieties of manufacturing options are possible through the horns design of axis-symmetric and planar shapes configuration. The design contains reflectors at the folds that allow the reflected strain wave phase to be controlled introducing constructive bending vibrations leading to the enhancement of the actuation amplification (Sherrit et al., 2002).

The table below shows a list of the resonance frequencies for the various horn types. Acoustic length and cross sectional area are kept constant to the first order, where the frequency is shown as a function of the fold's thickness (Table 3).

Table 3: List of the resonance frequencies for the various horn types, Sherrit et al., 2002.

Horn Type	Resonance Frequency (kHz)
Regular R	18.3
Inverted no folds IF ₀	18.3
Inverted one folds IF ₁ (2 mm thick fold)	14.7
Inverted one folds IF ₁ (4 mm thick fold)	16.0
Inverted one folds IF ₁ (6 mm thick fold)	16.0
Inverted two folds IF ₂ (2 mm thick fold)	14.1
Inverted two folds IF ₂ (4 mm thick fold)	16.2
Inverted two folds IF ₂ (6mm thick fold)	16.4

5.2.4.3. Rotary-hammering Sample Actuated by a Single Piezoelectric Actuator

Due to the dual functionality of the rotary hammering drills, multiple actuators might be required that adds to the complexity of the design. Therefore, in the efforts to simplify the design, a single piezoelectric stack actuator was developed and demonstrated to derive a solid-state rotary-hammer drill (Sherrit et al, 2009). The actuator consists of a horn with a helical slots configuration applying rotation forces leading to the turning of the drill bit, which is the function of the rotor, while free to vibrate longitudinally (**Error! Reference source not found.**). A portion of the axial vibrations supply the helical slots with the twisting motion on the horn surface producing tangential force. This tangential force turns the drill bit while pressing against it via a compressive force from the bolt through a bearing, and a high stiffness spring. As a result of the impact and the shear forces, the drilled medium fracture as the aforementioned forces exceed the medium tensile and/or shear strength. The shear forces from the twisting and rotation actions play a significant role in enhancing the fracturing process.

5.3. Ultrasonic Drilling Corer and Materials Removal Methods

The drilling process produced powdered cutting due to the induced vibration and as a result of the vibrating bit. As the powdered cutting accumulate the drilling efficiency drops unless it cleared. To achieve a greater depth of penetration, pressurized gas was introduced from the drill bit center. Applying this technique allowed for extracting a basalt core sample of approximately 10 cm long. However, this method is not an option in the planetary drilling since pressurized gas is considered contamination to the collected core samples. Therefore, another approach has to be used to increase the rate of penetration even further and eliminate the usage of pressurized gas.

5.3.1. USDC Based Rotary Hammer for Rapid Drilling

The rotary-hammering capability was developed and the drill bit was designed with flutes allowing the cutting materials to be augered up the outer core shaft. The auger design helped the cutting materials to travel upward along the bit side to the surface of the drilled medium (Figure 42). A drill bit of a 14 mm diameter was used to drill through limestone rock for demonstration. A significant rate of penetration was found as the USDC operated with a continuous power of 100 W, and a WOB of 29 N where it reached an approximate depth of 8.5 cm in 5 minutes of continuous drilling time (Bar-Cohen and Zacny, 2008).

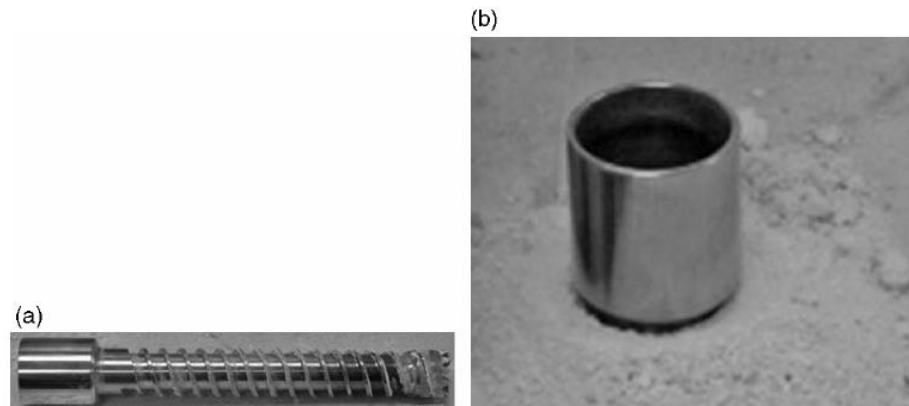


Figure 42: Photographs of (a) the drill bit with the flutes and (b) the bit in the formed borehole and the extracted powdered cuttings. Courtesy of NASA/JPL.

5.3.2. Subsurface Sampler

The rotary hammer design seems to overcome the rapid penetration challenge in a few centimeters depth range. To reach a depth of approximately 0.5 m in regolith, a new design had to be developed. Honeybee Robotics and JPL jointly took on this task and developed the subsurface sampler (Figure 43).

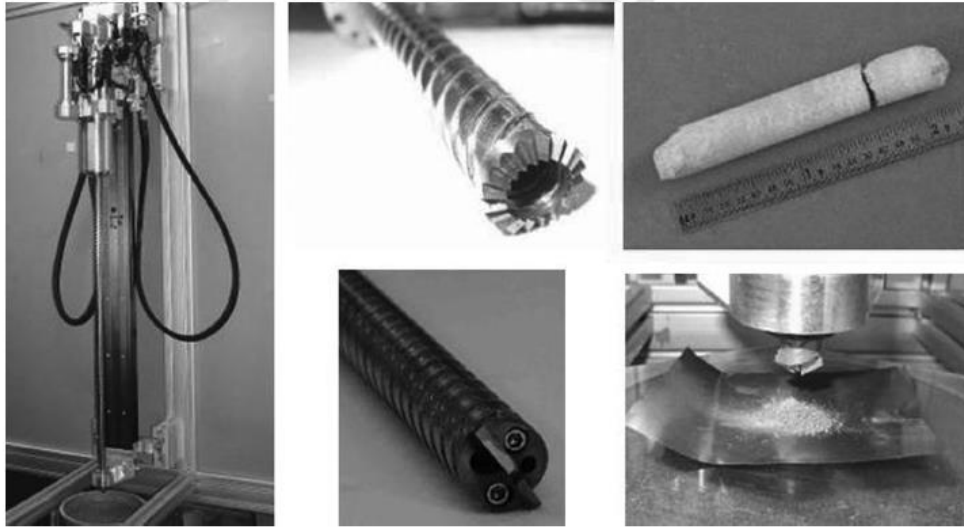


Figure 43: Subsurface sampler. Clockwise from left: full assembly; coring drill string; core sample; regolith sample; regolith sampling drill string. Courtesy of Honeybee Robotics

The sampler objective is to combine the USDC mechanism and drill bit rotation producing an all-in-one type of bit with the capability to produce, retain, and transfer samples. They created the coring and powder/regolith sampling drilling mechanisms where the coring drill is capable of producing 9 mm diameter and up to 51 mm long cores, and the regolith sampling has a sample chamber allowing the capable of 0.25 cm³ of materials. Both drill configurations are capable of creating a borehole up to 14.5 mm in diameter. A closed-loop control of feed rate and WOB are obtained through the preload sensor in the integrated load cell (Bar-Cohen and Zacny, 2008).

An additional important feature is added to the design allowing the separation of the core sample from the base materials using a core break-off tube. The break-off tube is located inside the primary drill tube and it separate the core sample using a rotary shear action. At the core sample end near the cutting tip of the drill bit, the relative rotation of two non-concentric components create a shearing force achieving the task. In the break-off configuration, the two components also act to retain a consolidated core (Figure 44, b). The center axes of the two tubes are aligned during core drilling and core ejection operations (Figure 44, a, c).

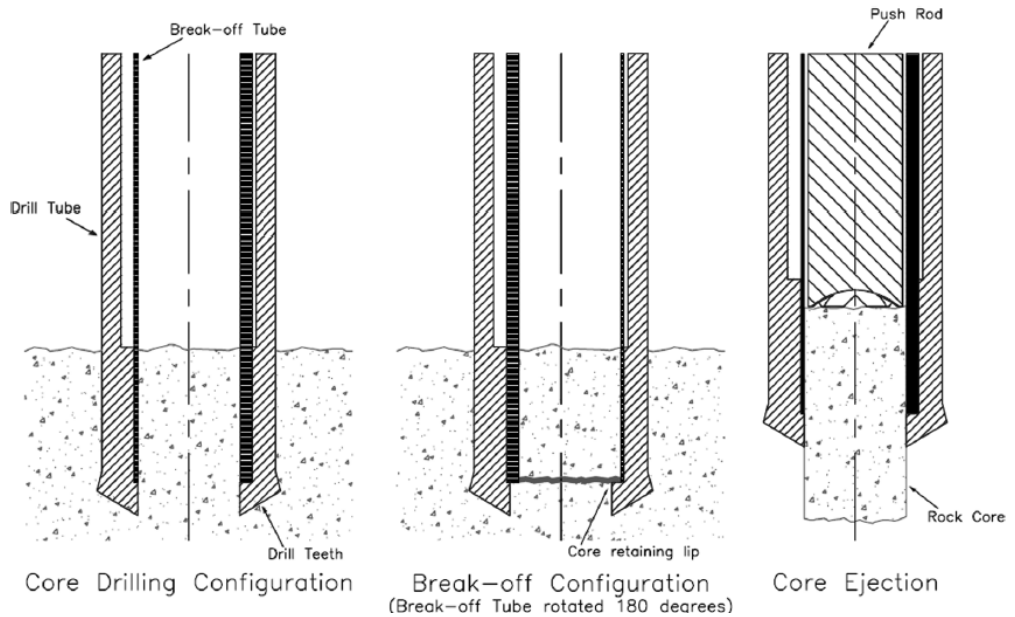


Figure 44: Subsurface sampler core break-off and ejection. Courtesy of Honeybee Robotics

5.4. Rotary Ultrasonic Drilling Designs and Applications

5.4.1. Deep penetration of sub-surfaces using the Auto-Gopher

NASA's future space exploration missions depend heavily on the deep penetration capabilities of the sub-surface of extraterrestrial planets to acquire samples in-situ. As the Curiosity mission to Mars revealed the necessity to penetrate thru several meters of the subsurface beyond the sterilized and oxidized zones in order to acquire pristine samples, this design feature became ever more important. JPL and Honeybee jointly developed an Auto-Gopher that operates based on rotary ultrasonic drilling and coring mechanism. The piezoelectric actuated percussive mechanism producing rock fracture while the rotary motion removes the cuttings. An anchoring mechanism is used to provide a preload for the rotary mechanism. In order to reach optimal penetration rate, the Auto-Gopher's percussive and rotary motions are activated simultaneously. The USDC-based mechanism generates the percussive action that is duty cycled to maintain low power operation. Also, the Auto-Gopher is a wireline mechanism that allows thru cyclic coring and coring removal reaching greater subsurface depth. The Auto-Gopher is designed to reach as deep as 3 to 5 meters in rocks and regolith (Figure 45, Figure 46)(Bar-Cohen et al., 2012).



Figure 46: Using the Auto-Gopher, the first core (57.25 mm diam. and 97.25 mm long) that was produced of limestone (photo courtesy of K. Zacny, Honeybee Robotics).

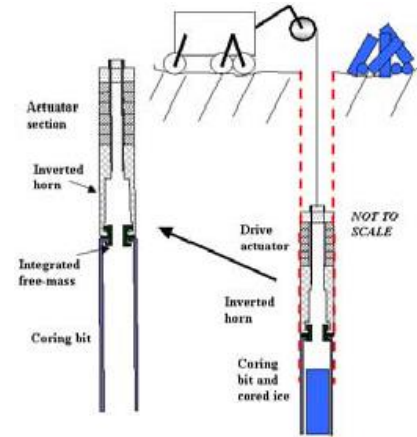


Figure 45: Schematic view of the ultrasonic/Sonic Gopher inside the borehole.

5.4.2. Percussive Augmenter of Rotary Drills (PARoD)

JPL utilized the best features of both rotary and hammering action developing the RPARoD. The rotary drill is widely used in commercial application due to its capability of offering an effective cutting removal method, while the hammering action is superior in formation fracture. As an objective of the new design to enhance the rotary hammers performance, a piezo-actuated mechanism was utilized in developing a percussive augments (Aldrich et al., 2008). There are two types of operation in the design, one is vibrating free-mass (sonic impacts) and one operates without a free mass. In order to transfer electric power while freely turning the bit, the design employs electric and mechanical slip-rings used to apply the mechanism. The design enhanced the rate of penetration significantly where it demonstrated to increase it as much as 10 times using 6.4 mm bit diameter and a fixed total power of 160 W by comparison to conventional pure rotary drilling (Aldrich et al, 2008).

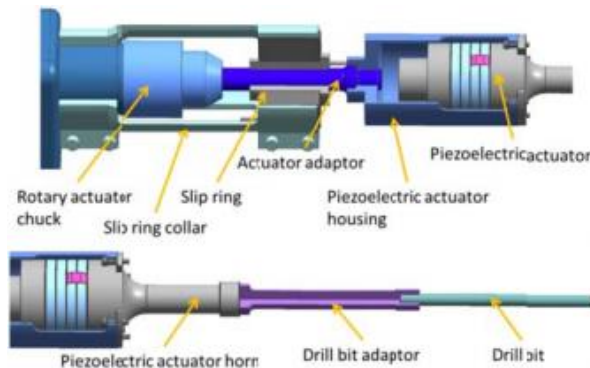


Figure 47: Percussive Augmenter of Rotary Drills Component Details (PARoD), JPL

Chapter 6

6. Mathematical Model Development

6.1. Outline of Model Development

The analysis begins with a consideration of the motion of a single abrasive particle due to the rotation of the bit and the superimposed ultrasonic vibration. This leads to an expression for the position and velocity of the particle as functions of time. The expression contains the following parameters, with the units used given in parentheses:

- Distance from the axis to the abrasive particle (m) r
- Amplitude of the ultrasonic excitation (m) A
- Angular velocity of drill bit (rad/s, Hz, rpm) ω_r, f_r, S
- Ultrasonic frequency (rad/s, Hz) ω_u, f_u
- Rate of advance of bit into the workpiece (m/s) b

6.1.1. Effective cutting time and cutting length

Next, the effective cutting time and effective length are introduced in terms of the (unknown) maximum depth of penetration that the abrasive particle experiences as it travels below the surface of the workpiece. The expressions developed contain the following parameters:

- Maximum Depth that the abrasive particle travels (m) δ
- Time right before the particle cuts into workpiece (s) t_1
- Time the particle reaches the maximum depth (s) t_2
- Time the particle ends cutting (s) t_3
- Effective total time the particle is cutting (s) Δt
- The distance traveled during the effective time (m) L_s

6.1.2. Vickers indentation

An analysis of Vickers indentation of brittle materials is then used to relate the maximum depth of penetration δ to the force necessary to achieve this depth. This gives an explicit function relating δ and the force or vice versa. The expressions introduce the following parameters:

- Vickers hardness of the rock (Pa) H_v
- Force applied to a single particle (N) F_n

- Angle between faces of abrasive particle (rad) α_o

6.1.3. Total force

Total force applied to the drill bit (or weight-on-bit) is determined by relating it to the sum of F_n applied to total number of particles that involved in cutting process and the time spent each particle spends cutting (Δt). The expressions introduce the following parameters:

- Force applied to drill bit (WOB) (N) F
- Number of abrasive particles take part in cutting (-) N_a
- Particle concentration (-) C_a
- Abrasive particle size (m) S_a
- Drill bit face area (m²) A_o

6.1.4. Material removal rate for single particle

The next step involves determining the material removal rate for a single particle in terms of the fracture characteristics of a brittle material under an indenter as it cuts into the material. Of particular interest are the length and depth of the lateral cracks that form under the indenter as these two lengths, along with the distance traveled by the particle during the cutting process, provide an estimate of the volume of material that is chipped out of the workpiece during a single ultrasonic cycle. The model expressions used introduces the following parameters:

- Lateral crack length (m) C_L
- Lateral crack height (m) C_h
- Volume proportionality (-) K
- Young's modulus of the workpiece (Pa) E
- Poisson's ratio of the workpiece (-) ν
- Fracture toughness of the workpiece Pa \sqrt{m} K_{IC}

6.1.5. Total material removal rate

Finally, the total material removal rate is determined in two ways: as the material removal rate of all of the particles and as the product of the area times the rate of penetration, which then leads to equations giving ROP as a function of both F and δ . At this point, the solution depends on going back to the relations between F and δ , or alternatively δ and F .

6.2. Model Introduction

A variety of research has been conducted on rotary-ultrasonic machining of brittle materials relating the material removal rate and cutting force. However, none of them addressed the process for hole drilling in brittle materials. In this research, a rate-of-penetration mathematical model is developed utilizing a previously published mathematical model for cutting force in rotary-ultrasonic milling of brittle materials (Zhang, Zhang, & Feng, 2013). The basis for this model involves the material brittle fracture removal mechanism. In the previous research of Zhang et al (2013), the essential approach to the cutting force model was developed by analyzing a single abrasive particle as the basic component of cutting forces in a diamond drill bit. The model was derived by summing up all forces exerted by all diamond particles taking part in cutting, which was published in many papers for the cutting force models of variety of abrasive particles.

First, I will address the fracture concept and assumptions shared in both research, as well as the common parameters of both equations and how some of them are different for drilling versus milling.

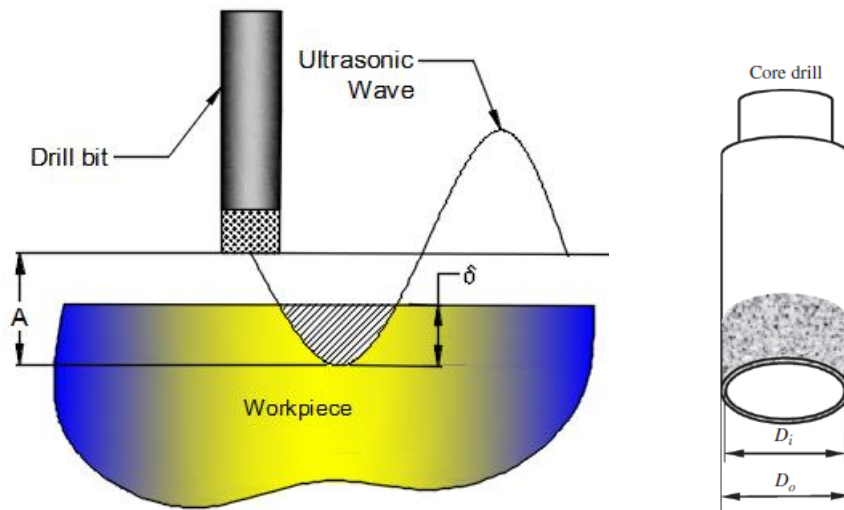


Figure 48: Modified illustration of Rotary Ultrasonic Milling (RUM) process for downhole drilling and core drill bit.

6.3. Fracture Concept and Assumptions

The following is a list of assumptions developed particularly for the materials in consideration in this research, which are brittle materials.

- a) While the material removal modes may vary, brittle material removal is the primary mode.

- b) All workpieces used in this study are ideal brittle materials. Therefore, the brittle fracture removal mechanism applies to the removed materials on the workpiece surface in brittle fracture mode (F. Zhang, 2004, Arif M, et al, 2011).

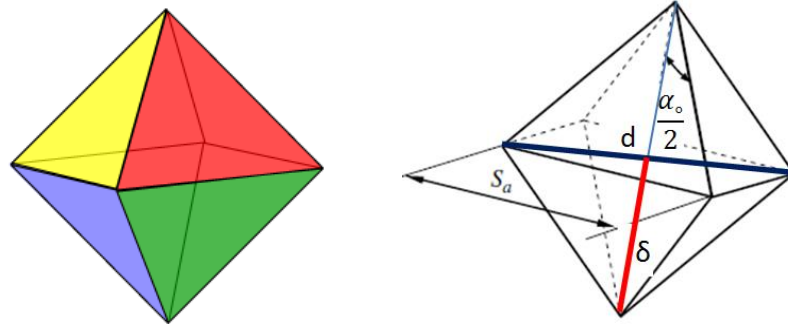


Figure 49: Abrasive particle simplified as an octahedron shape, <http://paulscottinfo.ipage.com/polyhedra/platonic/octahedron/1octahedronL.gif>

- c) All cutting particles (diamond) in the drill bit cross section take part in cutting.
 d) All diamond particles are rigid octahedrons shape of the same size with equal side length for the twelve sides (S_a) (Figure 49).
 e) Each diamond particle has one sharp corner of the octahedron shape (one corner for each particle) that acts on the workpiece surface with the same mechanics as a Vickers indenter.

6.4. Mathematical Model Parameters

6.4.1. Abrasive Particle Position and Velocity

The kinematic motion of one abrasive particle can be expressed in terms of the position and velocity of the particle. Considering the dual motion of the drill bit that combines rotational motion of counterclockwise rotation in the x-y plane, coupled with vertical vibration of the ultrasonic wave in the tool axis / feed direction.

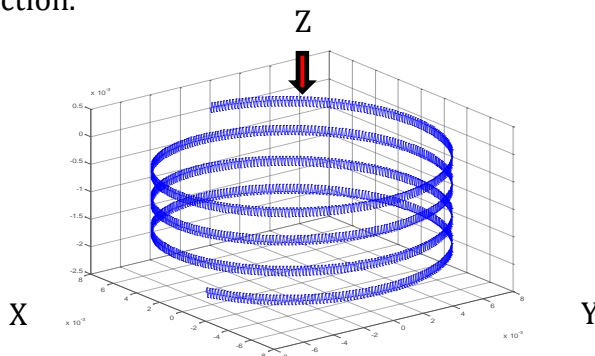


Figure 50: Ultrasonic Wave Superimposed on rotary motion of an abrasive particle mounted on the cutting surface of a drill bit

Variables used in developing the mathematical model, definitions, symbols and measuring units are listed in Table 4 as follow:

Table 4: Input variables, definitions, symbols, and units

Input variables	Definitions and symbols	Units
Drill bit / diamond variables	1. Drill bit outer diameter, D_o	mm
	2. Drill bit inner diameter, D_i	mm
	3. Abrasive concentration, C_a	unitless
	4. Abrasive size, S_a	mm
Machining process variables	5. Spindle speed, S	rpm
	6. Applied force (WOB), F	N
	7. Feed rate, f_r	mm/s
Ultrasonic vibration variables	8. Amplitude, A	μm
	9. Frequency, f_u	Hz
Workpiece material properties	10. Elastic modulus, E	GPa
	11. Poisson's ration, ν	unitless
	12. Fracture toughness, K_{Ic}	$\text{MPa}\sqrt{\text{mm}}$
	13. Hardness, H_v	MPa

Starting with a helix path in the drilling process of a drill bit with rotational speed ω_r , in the x-y plane and speed b downwards in the z-direction, the position S_p of one abrasive particle is:

Equation 1: Position (S_p)

$$S_p = \begin{bmatrix} r \cdot \sin(\omega_r t) \\ r \cdot \cos(\omega_r t) \\ A \cdot \sin(\omega_u t) + bt \end{bmatrix}$$

The velocity (V_p) is then:

Equation 2: Velocity (V_p)

$$V_p = \frac{dS_p}{dt} = \begin{bmatrix} r \cdot \omega_r \cdot \cos(\omega_r t) \\ -r \cdot \omega_r \cdot \sin(\omega_r t) \\ A \cdot \omega_u \cdot \cos(\omega_u t) + b \end{bmatrix}$$

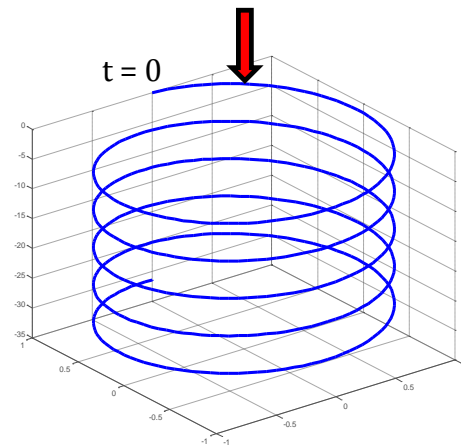


Figure 51: Rotary Cutting Direction

6.4.2. Effective Time (Δt)

Let the effective time be the time it takes for one abrasive particle to cut through the workpiece during one ultrasonic cycle as shown in Figure 52.

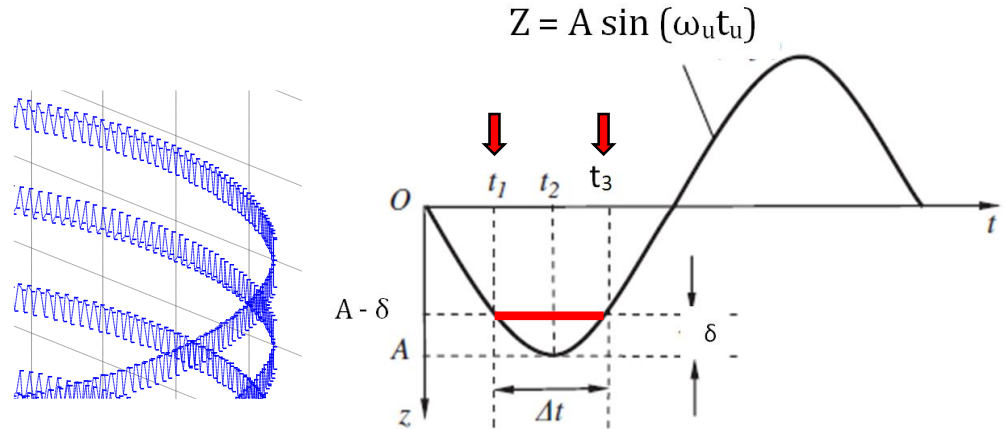


Figure 52: Effective time (Δt) during one ultrasonic cycle

- Where
- $Z \equiv$ ultrasonic wave equation
 - $A \equiv$ ultrasonic wave amplitude
 - $\delta \equiv$ maximum penetrated depth in the workpiece
 - $t_1 \equiv$ time that the abrasive particle begins to cut into the workpiece.
 - $t_2 \equiv$ the time the abrasive particle reaches the maximum depth.
 - $t_3 \equiv$ ending time for the abrasive particle to cut through and leaves the workpiece.
 - $\Delta t \equiv$ effective time = $t_3 - t_1$

As the abrasive particle moves downwards during the first half of the ultrasonic sine wave, it starts cutting through the materials at t_1 . It keeps cutting downwards until at time t_2 , the abrasive particle reaches the maximum cutting depth in the workpiece. The abrasive particle progresses in cutting the material until it exits the workpiece at time t_3 . The time duration between t_1 and t_3 is what is defined as the effective time (Δt).

Therefore,

Equation 3: Effective time in terms of t_2 and t_1

$$t_2 - t_1 = \frac{t_3 - t_1}{2} = \frac{\Delta t}{2}$$

The Z values at time t_1 , and t_2 are:

Equation 4: Z at first contact point (t_1)

$$\begin{aligned} Z(t_1) &= A - \delta \\ &= A \sin(\omega_u t_1), \end{aligned}$$

Where $\omega_u = 2\pi f_u$

Solving for (t_1) gives

Equation 5: Time (t_1)

$$t_1 = \frac{1}{2\pi f_u} \arcsin\left(\frac{A - \delta}{A}\right)$$

At the time of maximum depth, $Z(t_2) = A$ so

Equation 6: Time (t_2)

$$t_2 = \frac{1}{4f_u}$$

Manipulating the above equations and solving for Δt :

Equation 7: Effective Time Expression

$$\Delta t = \frac{1}{\pi f_u} \left[\frac{\pi}{2} - \arcsin\left(1 - \frac{\delta}{A}\right) \right]$$

6.4.3. Effective Cutting Length (L_s)

The effective cutting length L_s is the distance one abrasive particle travels during the effective time (Δt) from time t_1 to time t_3 . To calculate the effective length, the integral of the abrasive particle's velocity (V_p) (Equation 2) is taken over the range from t_1 to t_3 as follow:

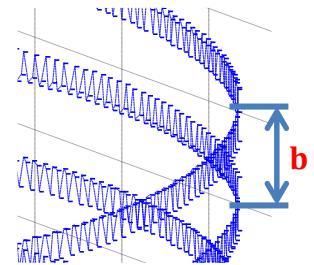


Figure 53: Helix path pitch "C"

$$L_s = \int_{t_1}^{t_3} \sqrt{V_p \cdot V_p} dt$$

$$L_s = \int_{t_1}^{t_3} \sqrt{X'^2 + Y'^2 + Z'^2} dt$$

$$L_s = \int_{t_1}^{t_3} \sqrt{R^2 \cdot \omega_r^2 \cos^2(\omega_r t) + R^2 \cdot \omega_r^2 \sin^2(\omega_r t) + (\omega_u A \cos(\omega_u t) + b)^2} dt$$

The ultrasonic superimposed term $\omega_u A \cos(\omega_u t)$ is not included in calculating L_s in the Z-axis because $A \ll R$. That is only the $Z = bt$ component where $Z' = b$.

$$L_s = \int_{t_1}^{t_3} \sqrt{R^2 \cdot \omega_r^2 + b^2} dt$$

$$L_s = \sqrt{R^2 \cdot \omega_r^2 + b^2} \Delta t$$

However, $b^2 \ll R^2 \cdot \omega_r^2$ and L_s simply becomes:

$$L_s = R \cdot \omega_r \Delta t$$

Where $R = \frac{D_o + D_i}{4}$; $\omega_r = \frac{2\pi S}{60}$

$$L_s = \left(\frac{\pi S (D_o + D_i)}{120} \right) \Delta t$$

$$L_s = \left(\frac{\pi S (D_o + D_i)}{120} \right) \frac{1}{\pi f_u} \left[\frac{\pi}{2} - \arcsin \left(1 - \frac{\delta}{A} \right) \right]$$

Equation 8: Effective length L_s

$$L_s = \left(\frac{S (D_o + D_i)}{120 f_u} \right) \left[\frac{\pi}{2} - \arcsin \left(1 - \frac{\delta}{A} \right) \right]$$



Figure 54: Core Drill Schematic

6.4.4. Helix Path Pitch (b)

The pitch value is the direct rate of penetration of the process. In one revolution a depth of the value of h is reached as shown in Figure 55. Therefore, the overall rate of penetration is expression is:

$$ROP \left[\frac{mm}{sec} \right] = h \left[\frac{mm}{rev} \right] f_r \left[\frac{rev}{sec} \right]$$

$$ROP = h f_r$$

$$h = (b dt)$$

$$h = \left(b \frac{2\pi}{\omega_r} \right); \quad \omega_r = 2\pi f_r$$

$$ROP = b$$

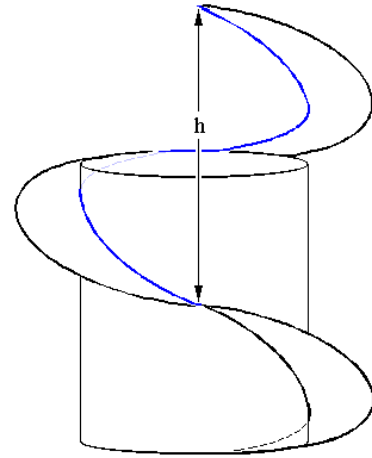


Figure 55: Drill bit helix path

This result could also be directly observed in the particle velocity given in Equation 2.

6.4.5. Maximum Depth (δ)

Indentation fracture technique is used in this drilling process for what it has to offer particularly when it is applied to brittle materials. Point-indentation approach generates high stress intensity region applying shear and hydrostatic compression producing irreversible deformation on the specimen. It is a stable fracture processes that allows the examination of its effect as it apply to brittle solids. For the same reasons the point-indentation techniques are used for hardness testing such as Vickers and Knoop tests (Lawn and Swain, 1975). Additional details on the point-indentation microfracture patterns in brittle solids are addressed in the following sections providing a clearer picture of the fracture mechanics beneath the point-indentation zone.

As discussed in section 6.4.2, δ is the maximum depth one abrasive particle, an indenter, penetrates into the workpiece in one ultrasonic cycle. It occurs at the maximum downward amplitude (A) of the ultrasonic.

To determine (δ), the stress analysis of an indenter that is well established in the literature is addressed in this section with the focus on a sharp indenter as the type of indentation to accurately represent the abrasive particles' octahedron shape. At this point, it is important to address the development of the indentation fracture mechanics.

6.4.5.1. Indentation Fracture Mechanics

Lawn and Wilshaw (1976) in their review of the indentation fracture mechanics analysis identified the detailed stress field within the loaded system to develop a theory of indentation fracture. The nature of the contact zone must be well understood, which makes the indenter shape a critical factor in determining the resulting behavior see (Figure 56 and Figure 57). The stress is expected to exhibit high gradients, or even a singularity, at the contact point of a sharp indenter in an ideally elastic substrate. This stress will be relieved as localized inelastic deformation occurs. Lawn and Wilshaw defined convenient scaling parameters for the general stress field that involved spatial contact scales with characteristic dimension “a” being the crack size (Figure 59). The stress at a point in the stress field (P_o) is expressed in terms of the crack size (a), the applied load (P) and the indenter geometry (α) as follow (Lawn & Wilshaw, 1975). Axially symmetric indenters, $\alpha = 1$.

$$P_o = \frac{P}{2\alpha a^2}$$

Indentation fracture mechanics’ main objective of the investigation was the stress distribution responsible for the fracture processes, which is the tensile stress. The stress field directions of the principal stresses, σ_{11} , σ_{22} , and σ_{33} were investigated by applying stress trajectory such that $\sigma_{11} \geq \sigma_{22} \geq \sigma_{33}$ almost everywhere (Figure 57).

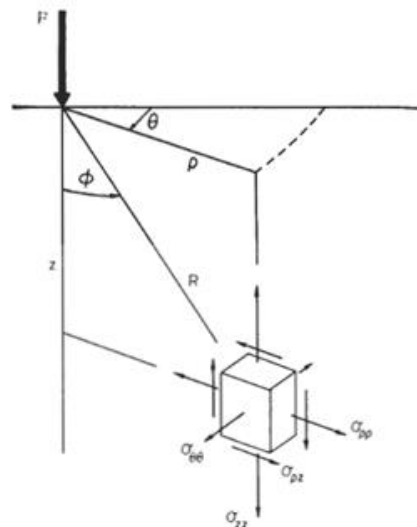


Figure 56: Coordinate system for indentation stress field, (Lawn and Wilshaw, 1975)

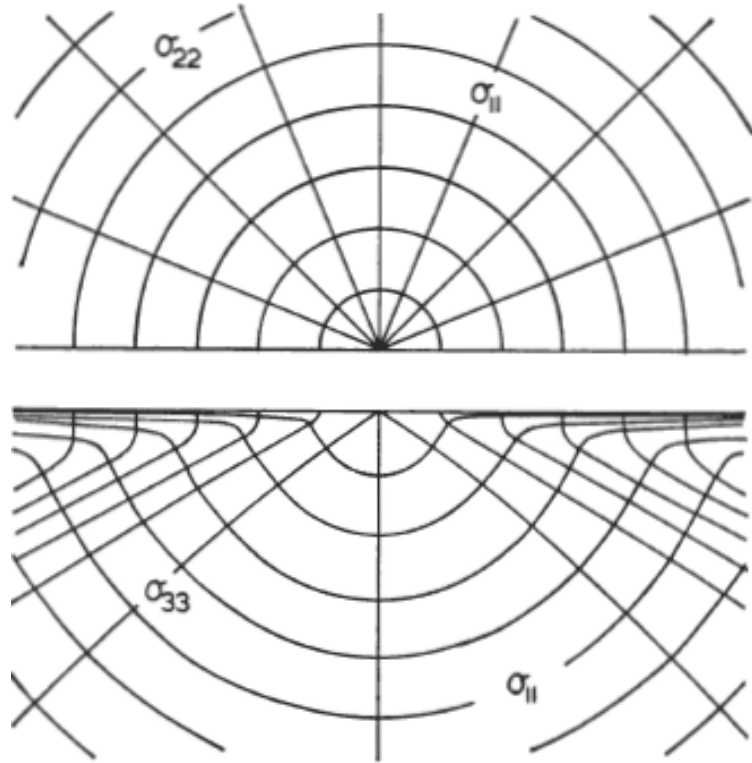


Figure 57: Half-surface view (top) and side view (bottom) of stress trajectories in Boussinesq field. Plotted for $\nu=0.25$, Lawn and Wilshaw, 1976

Another approach to visualizing the stress distribution involves contour plots as shown in Figure 58. The symmetrical stress to the planes through the load axis, σ_{11} and σ_{33} where identified to be wholly tensile and compressive respectively. The “hoop stress” σ_{22} holds both types of stresses where it is tensile in the region below the indenter and compressive near the surface. It is notable that the tensile stresses maxima is at $\Phi=\pi/2$ (σ_{11}) and at $\Phi=0$ ($\sigma_{11}=\sigma_{22}$). Upon the evaluation of the principal shear and hydrostatic compressive stresses from three principal stresses were determined as follow; both stresses exceed the tensile stresses by several times where the maxima occur at the contact axis.

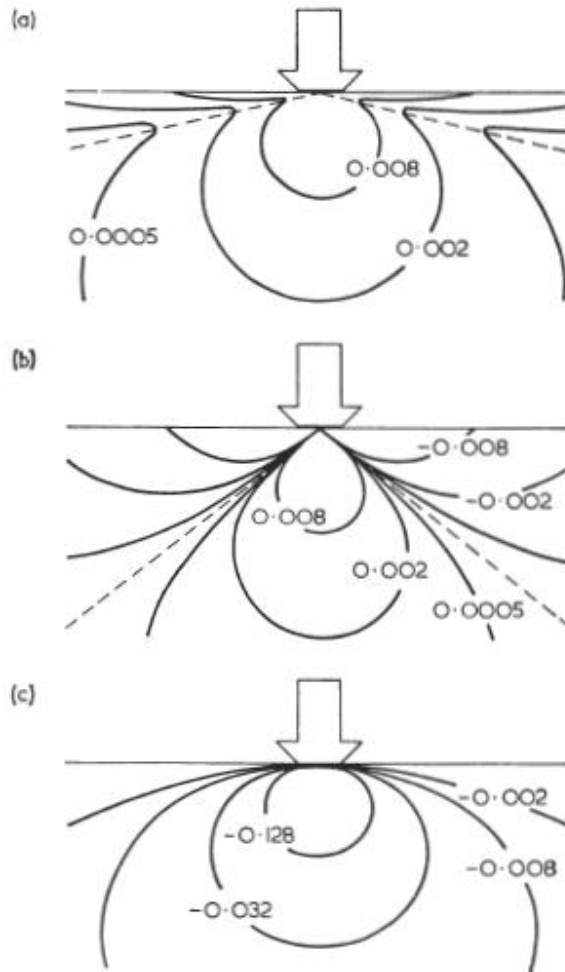


Figure 58: Contours of principal normal stresses, (a) σ_{11} , (b) σ_{22} , (c) σ_{33} , in Boussinesq field, shown in plane containing contact axis. Plotted for $\nu = 0.25$. Unit of stress is p_0 , contact "diameter" (arrowed) is $2a\sqrt{\alpha}$. Note sharp minimum in σ_{11} and zero in σ_{22} ,

The focus area of stress field investigation is beneath the indenter where the fracture configuration can be determined. According to Griffith's pioneering paper (Griffith, 1920) on the rupture of brittle solids, two types of crack actions are taking place. First is the crack initiation which identifies where and how the crack starts. Second is the crack propagation where once the crack starts, the path it takes and the extent of the growth is determined.

Examining crack initiation closely it was found that it possibly begins from materials "flaws" that are either pre-existing or induced by the indentation process itself. The mechanical, thermal, and chemical material histories determine the nature and distribution of the pre-existing flaws that typically occur as micro-scale microcracks. However, materials flaws nature and distribution are

related most commonly to the brittle surfaces susceptibility to contact and handling damage.

6.4.5.2. Sharp Indenter Fracture Mechanics

Utilizing the hardness test to provide a systematic description of the crack pattern of the impression of the sharp indenters is fundamentally related to a great diversity of the patterns generated due to minor variations in the test system. Variations include the indenter shape, testing environment, load rate, etc. However, the major features of the fracture behavior remained general and provided the basis of the model of Lawn and Wilshaw (1976).

As the starting flaw's probable location is defined, which gradually starting a crack, one can make use of the tensile stresses maxima at the workpiece surface and contact axis for the Boussinesq field addressed earlier in this section (Figure 57). It is reasonable to predict the crack will tend to initiate at one of those favored locations where the stresses exceeds a critical tensile stress.

Defining the indentation fracture geometry makes it possible to quantify the crack growth in terms of the important system variables, particularly the applied load (P) and the crack dimensions (a) (Figure 59). Linear fracture mechanics provides the mathematical basis for the evaluation of the mechanical-energy release rate function ($G = G(P, a)$) or other stress intensity factor equivalent function that is appropriate to a given crack configuration. However, there is no exact solution for the complex geometries present in the indentation problems and some approximations had to be made in the analysis (Lawn and Wilshaw (1976)).

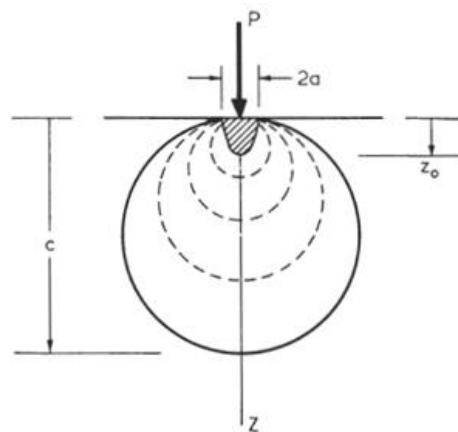


Figure 59: Parameters of the median vent configuration. Broken lines represent stress contours, heavy line represents crack profile, and shading represents inelastic deformation zone.

Now it is essential to determine whether or not the value of the energy release rate (G) is sufficient to propagate the crack based on a fracture criterion. It is not adequate to assume crack propagation based on the maximum tensile stress exceeding the critical level alone. Therefore, generally two basic crack propagation conditions were distinguished. The first condition is equilibrium: on an atomic level, a brittle crack grows as the cohesive bonds across the crack plane rupture and create two surfaces. The condition of the bond rupture process is assumed to operate under thermodynamics equilibrium (Griffith) (Griffith et al., 1920).

$$G = 2 \Gamma$$

Where Γ the second condition is kinetic: the bond rupture process is a sequence of discrete events where an energy barrier to crack motion exists at the atomic level. This behavior is expressed in an atomic periodicity in the term (Γ) and the crack may grow in a rate-dependent manner by thermal fluctuations over the barrier (Lawn and Mater, 1975). Finally, the crack may propagate according to the kinetic equation:

$$v_c = v_c(G)$$

where $v_c(G)$ is the crack velocity function appropriate to the system under consideration.

6.4.6. Maximum Depth (δ) in Terms of Materials Hardness

Considering the Vickers hardness test (Figure 60 and Figure 61), the maximum depth achieved by one abrasive particle can be estimated:

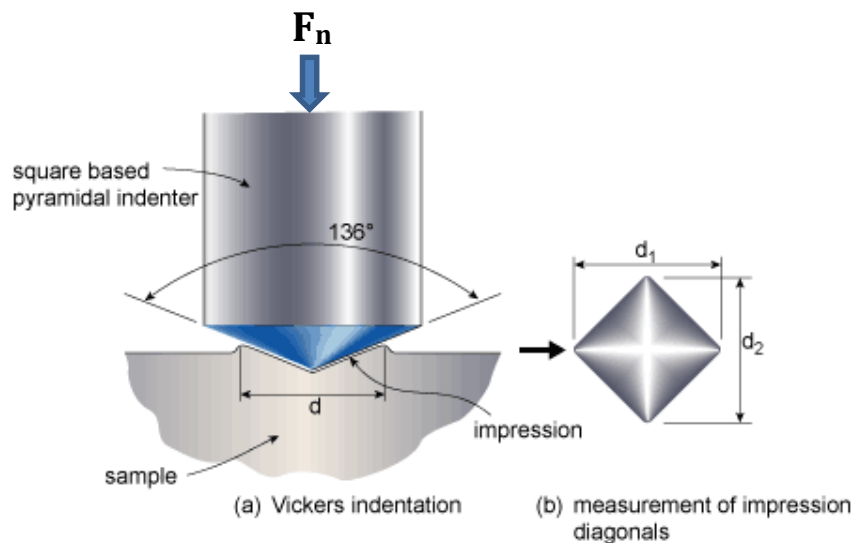


Figure 60: Vickers Hardness Test

H_v \equiv Vickers hardness
 F_n \equiv applied force on one abrasive particle
 $d_{1,2}$ \equiv indentation diagonal average length

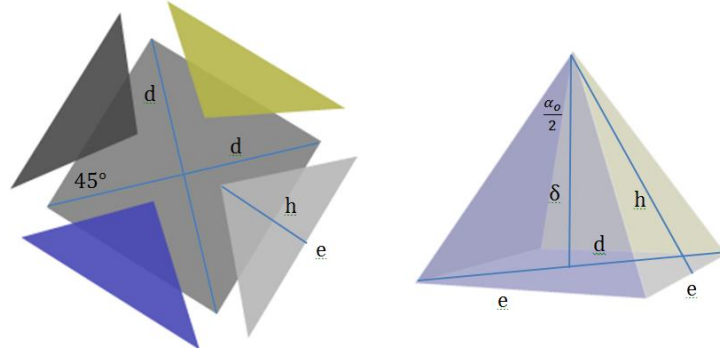


Figure 61: Vickers Hardness indentation shape formed by indenter tip

The Vickers hardness indentation area (A_s) consists of four equal triangles with base length of (e) and a height, slanted height, of (h) (Figure 61). A detailed derivation is provided showing the following expression (Appendix B):

Equation 9: Vickers hardness indentation area (A_s)

$$A_s = \left(2 \tan\left(\frac{\alpha_o}{2}\right) \sqrt{\left[\tan\left(\frac{\alpha_o}{2}\right)\right]^2 + 2} \right) \delta^2$$

Vickers hardness is defined as the ratio of the applied force (F_n) to the indented area.

Equation 10: Vickers Hardness

$$H_v = \frac{\text{Applied Force}}{\text{Indented Area}} = \frac{F_n}{A_s}$$

Substituting for the expression of A_s into equation (8) and solving for A_s in terms of F_n and H_v gives:

$$A_s = \frac{F_n}{H_v} = \left(2 \tan\left(\frac{\alpha_o}{2}\right) \sqrt{\left[\tan\left(\frac{\alpha_o}{2}\right)\right]^2 + 2} \right) \delta^2$$

Finally, solving for δ ,

Equation 11: Maximum depth δ

$$\delta = \left(\frac{F_n}{2 \tan\left(\frac{\alpha_o}{2}\right) \sqrt{\left[\tan\left(\frac{\alpha_o}{2}\right)\right]^2 + 2 H_v}} \right)^{1/2}$$

6.4.7. The relationship between WOB/cutting force on the workpiece (F) and force on one abrasive particle (F_n)

To establish the relationship between the cutting force (F) on the entire drill bit and the force exerted on one abrasive particle (F_n), we will take in consideration that the particle is a rigid body and impulses during one ultrasonic cycle are the same (Liu, Cong, Pei, & Tang, 2012b).

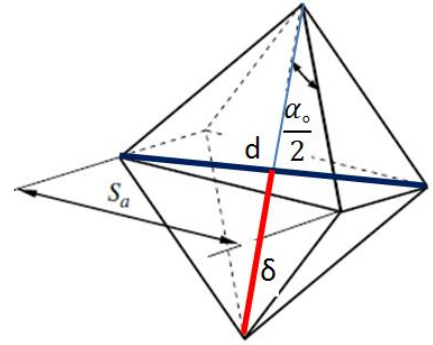


Figure 62: Abrasive particle octahedron shape showing relevant dimensions

Let

- F_m \equiv maximum impact force between core drill and workpiece
- F_n \equiv force applied on one abrasive particle
- F \equiv force measured during the experiment/force applied = WOB
- I_1, I_2 \equiv impulse during one ultrasonic cycle

The impulse of one abrasive particle as a rigid body in terms of maximum impact force F_m during one ultrasonic vibration can be calculated as:

Equation 12: Impulse of one abrasive particle I_1

$$I_1 = \int_{cycle} F_m dt \approx F_m \Delta t$$

Impulse in terms of total cutting force F can be calculated as:

Equation 13: Impulse of one abrasive particle I_2

$$I_2 = \frac{1}{f_u} F$$

and $F_m = N_a F_n$

By equating impulses equations (12) and (13) and solving for the cutting force F :

$$F = f_u F_m \Delta t = f_u F_n N_a \left(\frac{1}{\pi f_u} \left[\frac{\pi}{2} - \arcsin \left(1 - \frac{\delta}{A} \right) \right] \right)$$

$$F = F_n \left(\frac{N_a}{\pi} \left[\frac{\pi}{2} - \arcsin \left(1 - \frac{\delta}{A} \right) \right] \right)$$

Finally, the force exerted on one abrasive particle (F_n) in terms of cutting force on the workpiece (F) is:

Equation 14: Normal force on one abrasive particle

$$F_n = \frac{\pi F}{N_a \left[\frac{\pi}{2} - \arcsin \left(1 - \frac{\delta}{A} \right) \right]}$$

6.4.8. Number of Abrasive Particles (N_a)

The number of active abrasive particles taking part in cutting on the drill bit cross section depends upon the abrasive concentration (C_a). The usual measure for this concentration is defined in terms of abrasives weight. If $C_a = 100$, then there is $0.88 \times 10^{-3} \text{ g/mm}^3$ of abrasive in matrix material (Liu et al., 2012a). Assuming uniform particles distribution in the abrasive portion of the core drill, the number of abrasive particle (N_a) can be calculated as:

$$N_a = \left[\left(\frac{0.88 \times 10^{-3} \text{ g}}{\text{mm}^3} \right) \left(\frac{C_a}{100} \right) \frac{1}{\left(\frac{\sqrt{2}}{3} S_a^3 \right) \rho} \right]^{2/3} A_o$$

Where

$\rho =$ is the abrasive particle mass density

$$\text{Octahedron's volume} = \frac{\sqrt{2}}{3} S_a^3$$

Let

$$C_1 = \left(\frac{3 \times 0.88 \times 10^{-3}}{100 \sqrt{2} \rho} \right)^{2/3};$$

Equation 15: Number of abrasive particles

$$N_a = C_1 \left(\frac{C_a^{2/3} A_o}{S_a^2} \right)$$

Where

- $S_a \equiv$ abrasive particle length (equal for 12 sides of the octahedron shape)
- $C_a \equiv$ abrasive particles concentration
- $A_o \equiv$ area of core drill end face / cross section
- $C_1 = 3 \times 10^{-2}$ Dimensionless constant (ρ is the density of abrasive material, g/mm^3 , $\rho = 3.52 \times 10^3 \text{ g}/\text{mm}^3$ for diamond)

6.4.9. Material Removal Rate for One Abrasive Particle (MRR_p)

To calculate the material removal rate for one abrasive particle, first we define the fracture zone at the indenter/abrasive particle cutting point or tip. Upon exerting force on the abrasive particle, a fracture zone is formed that consists of a plastic zone, median crack and lateral crack. The material removed is primarily influenced by the lateral crack that has a length of (C_L) and a height of (C_h) as shown in Figure 63.

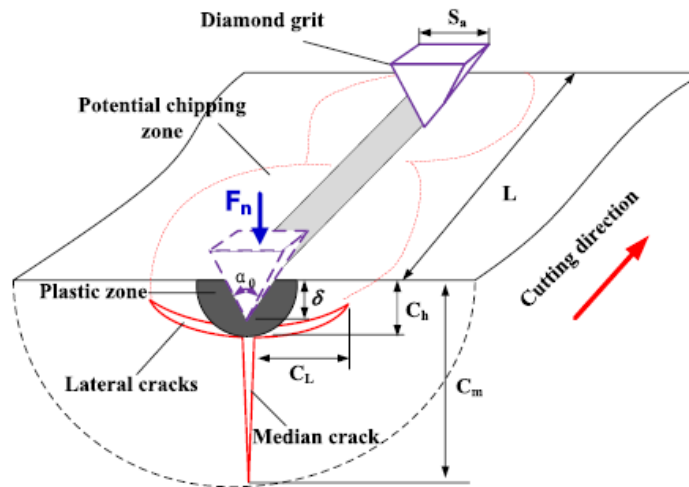


Figure 63: Schematic diagram of material removal in brittle fracture mode induced by the abrasive particle process (Zhang et al., 2013)

The material removal volume is based on the fracture zone developed using hardness tests. To further understand the fracture zone, one of the hardness tests applying an indenter is The Knoop hardness test that is presented for clarity. It is a micro-hardness test and it is a particularly used to test brittle materials that makes a small indentation that is used for testing purposes. The Knoop indenter is an octahedron diamond shaped particle that is pressed against a polished surface of the tested materials with a load of 100N and applied for a period of time. A microscope is used to measure the

resulting indentation from Knoop and Vickers hardness tests shown in Figure 64 (Lawn and Wilshaw, 1975).

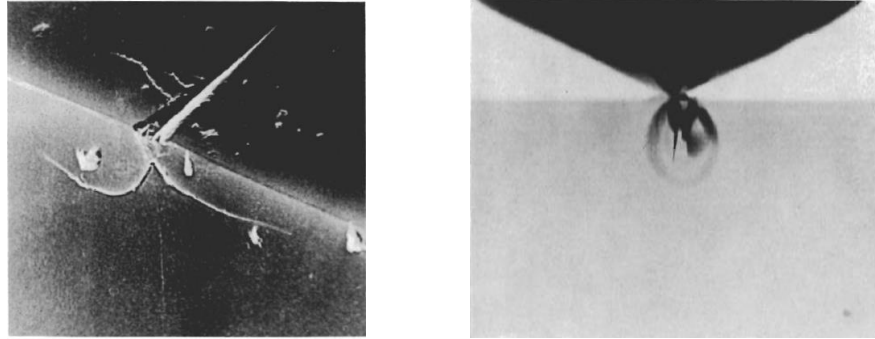


Figure 64: Scanning electron micrograph of Knoop impression quartz (0001) surface. Section shows inelastic deformation zone immediately below surface impression, and associated vent pattern. Indenter load 2N. Width of field 100 μm (left) and In situ photograph of Vickers indentation in soda-lime glass taken in transmitted light with an indenter load of 250N and width of field of 11mm (right) (B. Lawn and R. Wilshaw, 1975)

To calculate the material removal rate for one particle (MRR_p), first we calculate a theoretical volume (V_o) which will then be compared with actual volume (V) of the fracture zone. As the abrasive particle comes in contact with the workpiece and start cutting at t_1 , the cutting depth increases from zero to the maximum depth δ at t_2 and then decreases again to zero at t_3 while moving the distance L_s on the workpiece surface, see Figure 65.

As a result to the aforementioned cutting process, the lateral crack length C_L and height C_h will increase and decrease accordingly forming the fracture zone volume. This volume is simplified to two tetrahedron volume of ABCD as shown in Figure 65 as follow (Liu et al., 2012a).

Equation 16: Theoretical volume V_o

$$V_o = 2 V_{ABCD} = \frac{1}{3} L_s C_L C_h$$

Abrasive particles' theoretical volume (V_o) of the fracture zone may overlap and interrelations between it and the actual volume (V) is expressed through the volume proportionality (K) as follow:

Equation 17: Actual volume V

$$V = K V_o = \frac{K}{3} L_s C_L C_h$$

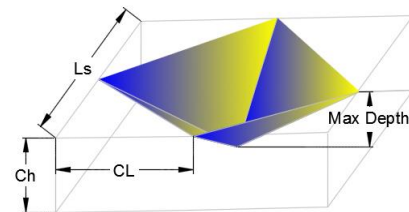


Figure 65: Fracture zone theoretical volume calculation (V_o)

Where

$K \equiv$ constant proportionality due to interrelations among abrasive particles (Liu et al., 2012a).

The particle material removal rate (MRR_a) is the product of the fracture zone actual volume times the ultrasonic frequency. By substituting the values of L_s (Equation 8) in actual volume (V) (Equation 17) above, the particle material removal rate could be calculated as:

Equation 18: Abrasive particle material removal rate MRR_a

$$MMR_a = f_u \cdot V = \frac{K}{3} \left(\frac{S(D_o + D_i)}{120} \right) \left[\frac{\pi}{2} - \arcsin \left(1 - \frac{\delta}{A} \right) \right] C_L C_h$$

6.4.10. Material Removal Rate for Core Drill (MRR_d)

The material removal rate for the core drill bit is calculated based on the product of the material removal rate of one abrasive particle MRR_a (Equation 18) times the number of abrasive particles takes part in cutting as:

Equation 19: Material removal rate of core drill MRR_d in terms of number or particles N_a

$$MMR_d = N_a MRR_a$$

Substituting for N_a (Equation 15) and MRR_a (Equation 18)

Equation 20: Material removal rate for core drill MRR_d

$$MMR_d = \frac{K C_1}{360} \left(\frac{C_a^{2/3} A_o (D_o + D_i)}{S_a^2} \right) (S) \left[\frac{\pi}{2} - \arcsin \left(1 - \frac{\delta}{A} \right) \right] C_L C_h$$

6.4.11. Lateral Cracks Length (C_L) and Depth (C_h)

The brittle fracture mechanism of materials has been investigated in previous literature using indentation fracture mechanics (Lawn, Wilshaw, 1975; Ostojic, Mcpherson, 1987; Lawn, Evans, Marshall, 1980 and Marshall, Lawn, Evans, 1982). As shown in Figure 63, the indentation of an abrasive

particle generates cracks in brittle materials. The lateral crack length C_L and lateral crack depth C_h were determined by Marshall et al, (1982) to be:

$$C_L = C_2 \left(\cot \frac{\alpha_o}{2} \right)^{5/12} \left(\frac{E^{3/4}}{H_v K_{IC} (1 - \nu^2)^{1/2}} \right)^{1/2} (F_n)^{5/8}$$

$$C_h = C_2 \left(\cot \frac{\alpha_o}{2} \right)^{1/3} \left(\frac{E^{1/2}}{H_v} \right) (F_n)^{1/2}$$

Substitute for F_n (Equation 14)

Equation 21: Product of lateral crack length C_L and lateral crack height C_h

$$C_L C_h = \frac{C_2^2}{\left(\tan \frac{\alpha_o}{2} \right)^{3/4}} \left(\frac{E^{7/8}}{H_v^{3/2} K_{IC}^{1/2} (1 - \nu^2)^{1/4}} \right) \left(\frac{\pi F}{N_a \left[\frac{\pi}{2} - \arcsin \left(1 - \frac{\delta}{A} \right) \right]} \right)^{9/8}$$

Where

- E \equiv Workpiece Young's modulus
- K_{IC} \equiv Workpiece fracture toughness
- ν \equiv Workpiece Poisson's ratio
- C_2 = 0.226 Dimensionless constant that is dependent on the material/indenter system (B.R. Lawn, A.G. Evans, 1982)

6.4.12. Rate of Penetration (ROP)

It was previously shown that

$$MMR_d = N_a MRR_a \quad (\text{Equation 19})$$

Also, MMR_d could be expressed in terms of feed rate (b [mm/s]) and the area of drill core end face (A_o) as:

Equation 22: Material removal rate of drill bit in terms of b and A_o

$$MMR_d = b A_o$$

$$\text{Since } b = ROP \quad \text{and} \quad A_o = \frac{\pi(D_o^2 - D_i^2)}{4}$$

By equating Equation 19 and Equation 22 of MMR_d , the following result is obtained:

$$MMR_d = N_a MRR_a = b A_o$$

OR

$$N_a MRR_a = ROP A_o$$

Equation 23: Rate of penetration ROP

$$ROP = \frac{N_a}{A_o} MRR_a$$

Substituting for the values of N_a ([Equation 15](#)), A_o , and MRR_a ([Equation 18](#)), we obtain the following equation for the rate of penetration ROP:

$$ROP = \frac{N_a}{A_o} MRR_a$$

$$ROP = \frac{N_a K}{A_o 3} \left(\frac{S(D_o + D_i)}{120} \right) \left[\frac{\pi}{2} - \arcsin \left(1 - \frac{\delta}{A} \right) \right] C_L C_h$$

$$C_L C_h = \frac{C_2^2}{\left(\tan \frac{\alpha_o}{2} \right)^{3/4}} \left(\frac{E^{7/8}}{H_v^{3/2} K_{IC}^{1/2} (1 - \nu^2)^{1/4}} \right) \left(\frac{\pi F}{N_a \left[\frac{\pi}{2} - \arcsin \left(1 - \frac{\delta}{A} \right) \right]} \right)^{9/8}$$

To simplify the derivation, let the material properties in $C_L C_h$ equation = Q as follow (see Appendix B for derivation):

Equation 24: Material properties parameters

$$Q = \left(\frac{E^{7/8}}{H_v^{3/2} K_{IC}^{1/2} (1 - \nu^2)^{1/4}} \right)$$

Then

$$ROP = \left(\frac{K C_2^2 4^{9/8}}{360 C_1^{1/8}} \right) \left(\frac{S^{1/4} (D_o + D_i)}{C_a^{1/12} (D_o^2 - D_i^2)^{9/8} \left(\tan \frac{\alpha_o}{2} \right)^{3/4}} \right) (Q) \left(\frac{S F^{9/8}}{\left[\frac{\pi}{2} - \arcsin \left(1 - \frac{\delta}{A} \right) \right]^{1/8}} \right)$$

Let $D_{avg} = \frac{D_o + D_i}{2}$; then $D_o + D_i = 2D_{avg}$

Also, $D_o^2 - D_i^2 = (D_o + D_i)(D_o - D_i)$

Let the thickness $t = \frac{(D_o - D_i)}{2}$

$$D_o^2 - D_i^2 = (2D_{avg})(2t)$$

$$D_o^2 - D_i^2 = 4 t D_{avg}$$

Substituting the values of $(D_o + D_i)$ and $(D_o^2 - D_i^2)$ in the above equation yield the final ROP expression:

$$ROP = \left(\frac{K C_2^2 4^{9/8}}{360 C_1^{1/8}} \right) \left(\frac{S_a^{1/4} 2 D_{avg}}{C_a^{1/12} (4 t D_{avg})^{9/8} \left(\tan \frac{\alpha_o}{2} \right)^{3/4}} \right) \left(\frac{S F^{9/8}}{\left[\frac{\pi}{2} - \arcsin \left(1 - \frac{\delta}{A} \right) \right]^{1/8}} \right) (Q)$$

Substitute for the material properties Q (Equation 24) and finally the ROP equation is:

Equation 25: Final ROP mathematical model expression

$$ROP = G_1 \left(\frac{S_a^{1/4}}{C_a^{1/12} (t)^{9/8} (D_{avg})^{1/8} \left(\tan \frac{\alpha_o}{2} \right)^{3/4}} \right) \left(\frac{S (F)^{9/8}}{\left[\frac{\pi}{2} - \arcsin \left(1 - \frac{\delta}{A} \right) \right]^{1/8}} \right) \left(\frac{E^{7/8}}{H_v^{3/2} K_{IC}^{1/2} (1 - \nu^2)^{1/4}} \right)$$

Drill bit design

Process design

Material Property

Where $G_1 = \frac{K C_2^2}{180 C_1^{1/8}}$

The above ROP expression can be approximated to even a simpler form by recognizing that $\left[\frac{\pi}{2} - \arcsin \left(1 - \frac{\delta}{A} \right) \right]^{1/8} \approx 1$. As the ultrasonic amplitude A changes and the corresponding maximum depth δ also changes the data generated from experiments as well as the mathematical model supports this results.

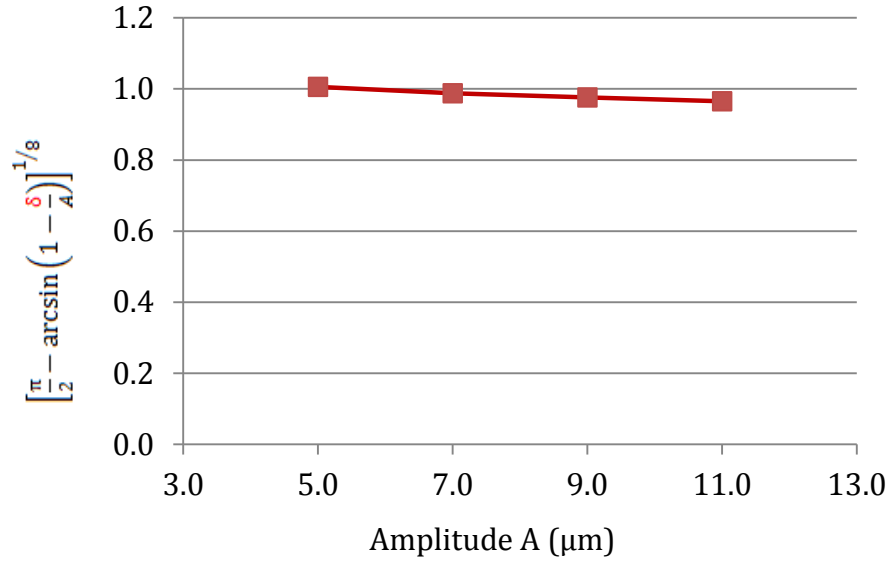


Figure 66: The expression $[\frac{\pi}{2} - \arcsin(1 - \frac{\delta}{A})]^{1/8} \approx 1$

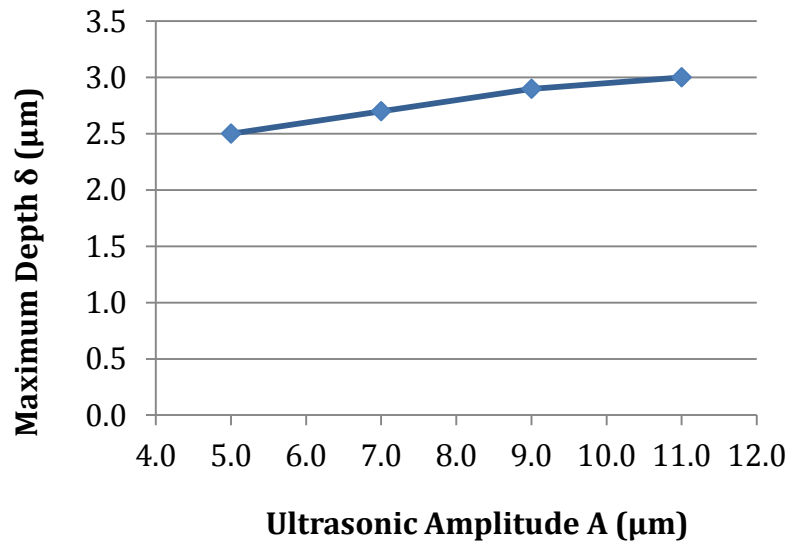


Figure 67: Ultrasonic amplitude vs. max. depth

Also, the semi-angle is constant in this study and it is roughly $\alpha_0=120^\circ$, and the drill bit thickness $t=1$ mm.

Then, the expression $(\tan \frac{\alpha_0}{2})^{3/4} = 1.51$, and $(t)^{9/8} = 0.000422$

Now,

$$\text{Let } G_2 = \frac{G_1}{(1.51)(0.000422)} = \frac{K C_2^2}{0.11 C_1^{1/8}}$$

Finally,

Equation 26: Simplified ROM mathematical model expression

$$ROP = G_2 (WOB)^{9/8} \left(\frac{S S_a^{1/4}}{C_a^{1/12} (D_{avg})^{1/8}} \right) \left(\frac{E^{7/8}}{H_v^{3/2} K_{IC}^{1/2} (1 - \nu^2)^{1/4}} \right)$$

Chapter 7

The performance of a number of the key parameter in the developed rate of penetration mathematical model is predicted in this chapter. In the efforts of validating the mathematical model, the predicted results are compared to experimental results and presented in Chapter 8.

7. Experiment Design

The rotary-ultrasonic drill utilizes the dual action of rotational and axial motion of the bit in the core drilling process. The ultrasonic drill uses a power supply that converts conventional line voltage (60 Hz) to a high frequency electrical energy of 20 kHz AC output. A piezoelectric converter receives this high frequency electrical signal and changes it into a mechanical motion. The ultrasonic mechanical motion gets amplified and transmitted to the horn and cutting tool. The resulting motion is a vertical oscillation of the cutting tool acting predominantly on the workpiece. The motor located on top of the ultrasonic spindle rotates it in the plane where the rotation speed can be controlled. The final cutting action is takes a helical path as the drill bit rotates in the plane due to the rotary motion and moves down at ROP and it also oscillates vertically due to the ultrasonic vibration (Figure 68).

As shown in chapter 6, the rate of penetration depends on a number of parameters associated with the drill bit design, the material being drilled, and the overall process variables such as rotation speed, ultrasonic amplitude and applied force. For ease of this discussion, equation (Equation 25) is restated here, with the various parameters grouped according to type. The first set of parameters contains the drill bit design variables; the second contains the process variables, while the third contain he material parameters.

The following equation was developed determining the effect of the input variables on the ROP performance.

$$ROP = G_1 \left(\frac{S_a^{1/4}}{C_a^{1/12} (t)^{9/8} (D_{avg})^{1/8} \left(\tan \frac{\alpha_o}{2}\right)^{3/4}} \right) \left(\frac{S (F)^{9/8}}{\left[\frac{\pi}{2} - \arcsin \left(1 - \frac{\delta}{A}\right)\right]^{1/8}} \right) \left(\frac{E^{7/8}}{H_v^{3/2} K_{IC}^{1/2} (1 - \nu^2)^{1/4}} \right)$$

$$\text{Where } G_1 = \frac{K C_2^2}{180 C_1^{1/8}}$$

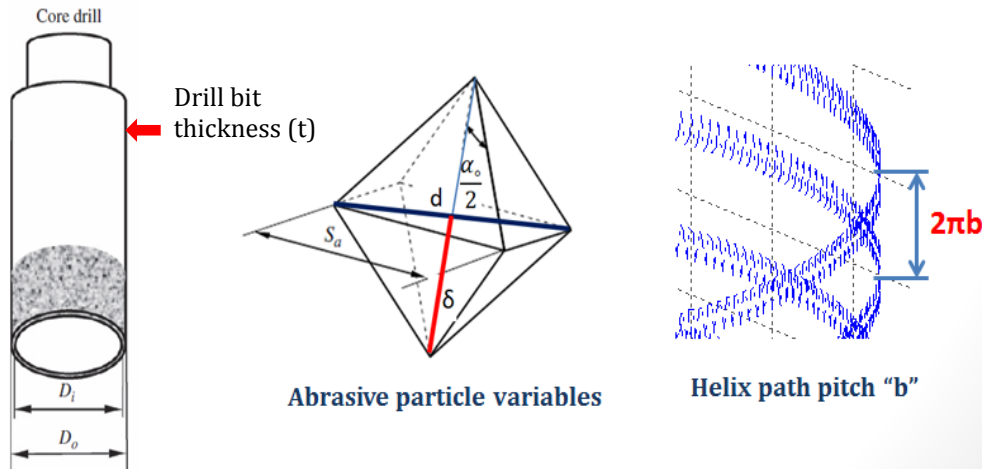


Figure 68: Drill, abrasive particle and ultrasonic wave parameters

According to this model, there are twelve parameters that affect the rate of penetration: five associated with the drill bit design, four with the material being drilled and three process parameters. (Recall that δ and F are related through equation (Equation 14)).

As shown in

Figure 69, as the cycles progress in depth reaching maximum depth of “b” in one revolution, maximum depth per cycle δ is reached and shifted by $d\delta$ from one cycle to the next.

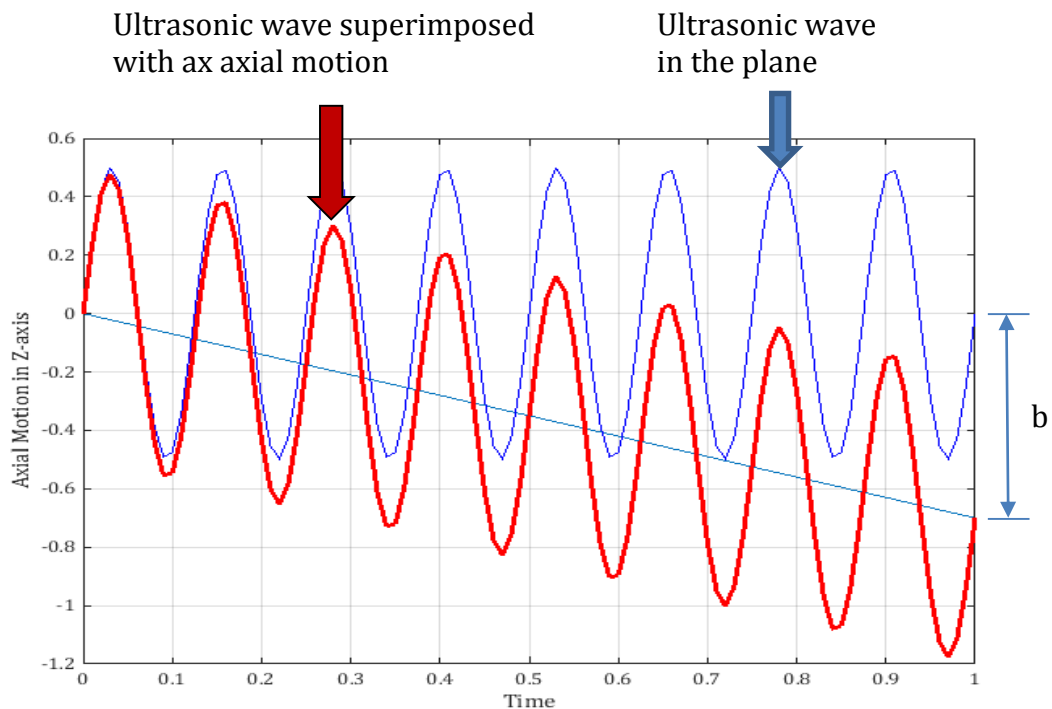


Figure 69: Rotary ultrasonic dual action of rotation in a helix path and oscillation vertically

7.1. Experiments Parameters

In order to examine the validity of this model, a series of core drilling tests were performed for three types of rock. All of the process parameters and all of the bit design parameters except for (t) and (α_o) were varied. However, it is important to note that the rotary ultrasonic system used for these tests controlled ROP and measured F.

Table 5 summarizes the values used for each parameter.

Table 5: Experiments value range for each drill bit design and process parameters

Sets	Drilling process parameters			Drill bit design parameters		
	Spindle Speed S (rpm)	Feed Rate b (mm/sec)	Ultrasonic amplitude A (μm)	Abrasive size Sa (mm)	Abrasive concentration Ca	Average drill bit size Davg (mm)
1	1500, 2500, 3500, 4500	0.3	7	0.125	100	11
2	2500	0.1, 0.3, 0.5, 0.7	7	0.125	100	11
3	2500	0.3	7	0.125	100	11
4	2500	0.3	7	0.08, 0.12, 0.16, 0.20	100	11
5	2500	0.3	7	0.125	50, 100, 150	11
6	2500	0.3	7	0.125	100	8, 11, 14
7	2500	0.3	5, 7, 9, 11	0.125	100	11
8	Establishing the K value for Travertine					
9	Establishing the K value for Marble					
10	Establishing the K value for Basalt					

7.2. Rock Type Selection

Rock types were chosen to represent a variety of strength. The three types of rocks were chosen based on their strength where the travertine (sedimentary rock type/limestone) has least strength, marble is average (metamorphic rock type), and basalt (igneous rock type) is the strongest according to data provided in the literature (Table 6).

Table 6: Mechanical properties of rock materials

Rock	UC Strength (MPa)	Tensile Strength (MPa)	Elastic Modulus (GPa)	Poisson's Ratio	Strain at Failure (%)	Point Load Index $I_{p(50)}$ (MPa)	Fracture Mode I Toughness
<i>Igneous</i>							
Granite	100 – 300	7 – 25	30 – 70	0.17	0.25	5 – 15	0.11 – 0.41
Dolerite	100 – 350	7 – 30	30 – 100	0.10 – 0.20	0.30		>0.41
Gabbro	150 – 250	7 – 30	40 – 100	0.20 – 0.35	0.30	6 – 15	>0.41
Rhyolite	80 – 160	5 – 10	10 – 50	0.2 – 0.4			
Andesite	100 – 300	5 – 15	10 – 70	0.2		10 – 15	
Basalt	100 – 350	10 – 30	40 – 80	0.1 – 0.2	0.35	9 – 15	>0.41
<i>Sedimentary</i>							
Conglomerate	30 – 230	3 – 10	10 – 90	0.10 – 0.15	0.16		
Sandstone	20 – 170	4 – 25	15 – 50	0.14	0.20	1 – 8	0.027 – 0.041
Shale	5 – 100	2 – 10	5 – 30	0.10			0.027 – 0.041
Mudstone	10 – 100	5 – 30	5 – 70	0.15	0.15	0.1 – 6	
Dolomite	20 – 120	6 – 15	30 – 70	0.15	0.17		
Limestone	30 – 250	6 – 25	20 – 70	0.30		3 – 7	0.027 – 0.041
<i>Metamorphic</i>							
Gneiss	100 – 250	7 – 20	30 – 80	0.24	0.12	5 – 15	0.11 – 0.41
Schist	70 – 150	4 – 10	5 – 60	0.15 – 0.25		5 – 10	0.005 – 0.027
Phyllite	5 – 150	6 – 20	10 – 85	0.26			
Slate	50 – 180	7 – 20	20 – 90	0.20 – 0.30	0.35	1 – 9	0.027 – 0.041
Marble	50 – 200	7 – 20	30 – 70	0.15 – 0.30	0.40	4 – 12	0.11 – 0.41
Quartzite	150 – 300	5 – 20	50 – 90	0.17	0.20	5 – 15	>0.41

7.2.1. Travertine

Travertine is a kind of limestone deposit. As groundwater travels through limestone beds, it dissolves calcium carbonate. The dissolved matter precipitates in thin layers of two crystallographically different forms, calcite and aragonite, as the mineral-saturated water encounters surface conditions. After a period of time, the minerals build up into deposits of travertine (Figure 70). (<http://geology.about.com/od/rocks/ig/sedrockindex/rocpicttravertine.htm>).



Figure 70: Natural Travertine rocks, <http://www.collecting-rocks-and-minerals.com/image-files/turkish-travertine.jpg>

7.2.2. Marble

Regional metamorphism of limestone or dolomite rock which forms marble causes their microscopic grains to combine in larger crystals. The crystal size depends on the type of marble. While it might be small in Vermont marble, it is even smaller crystals in the marble types used in buildings and sculptures. Marble colors also vary drastically from very bright white to black with a range of colors in between depending on the amount of other minerals presence as impurities (Figure 71).

(<http://geology.about.com/od/rocks/ig/metrockindex/rocpicmarble.htm>)



Figure 71: Natural marble rocks, <http://www.creativeincounters.com/wp-content/uploads/2012/03/white-marble-blocks.jpg>

7.2.3. Basalt

Basalt is the type of rock that makes up most of the world's oceanic crust. It is usually fine-grained, where the individual minerals including pyroxene, plagioclase feldspar and olivine are not visible. These minerals are visible, however, in the coarse-grained type of basalt called gabbro, a plutonic version of basalt (Figure 72 and Figure 73).



Figure 72: Basalt and lava rock, http://meteorites.wustl.edu/id/basalt_0885l.jpg

<http://geology.about.com/od/rocks/ig/igrockindex/rocpicbasalt.htm>.



Figure 73: Natural Basalt rocks,
http://farm4.staticflickr.com/3077/2517111350_051e520c92.jpg

7.3. Rock Samples

The sample dimension for each type of rock were measured and smaller samples were prepared for the materials properties tests (Figure 74, Figure 76 and Figure 78). Material properties needed for the developed mathematical model are elastic modulus (E) and Poisson's ratio (ν) that are determined from uniaxial compression strength test (UCS). Fracture toughness (K_{Ic}) and Vickers hardness (H_v) tests were also conducted where the average value of three tests were determined for each property for each type of rock. The dimensions of the samples used for each test are given in Table 7.

In order to meet the ASTM requirements for material property tests, the rock grain size is taken in consideration. The following images show the overall sample rock dimensions for each type of rock as well as close up views used to estimate the grain sizes (Figure 75, Figure 77 and Figure 79).

Table 7: Specimens dimensions and quantities for materials properties tests

Test	Quantity	Travertine	Marble	Basalt
UCS	3	1" dia x 2.5" length	1" dia x 2.5" length	2" dia x 4" length
Fracture Toughness	3	1" x 1" x 5"	1" x 1" x 10"	2" x 2" x 14"
Vickers Hardness	3	10" x 2.5"	2.5" x 6"	4" x 5"
No. of holes		480	380	280



Figure 74: Top view of travertine Rock Sample with overall dimensions of 38x60x2.5 cm



Figure 75: Side view of travertine sample close up image showing an estimated grain size and porosity level



Figure 76: Top view of marble Rock Sample with overall dimensions of 25x152x2.54 cm



Figure 77: Side view of marble sample close up image showing an estimated grain size and porosity level



Figure 78: Top view of basalt rock sample with overall dimensions of 30x58x3.8 cm



Figure 79: Side view of basalt sample close up image showing an estimated grain size and porosity level

7.4. Rocks Type and Materials Properties

The material properties have a great effect on the rate of penetration performance. This is clearly evidenced in the developed mathematical model involving elastic modulus (E), fracture toughness (K_{Ic}), Vickers hardness (H_v), and Poisson's ratio (ν). Since the types of rocks on Mars vary drastically in their materials properties from very soft to very hard, three different types of rocks are investigated in this research that covers wide range of rock strength, travertine as a soft rock, marble as a medium strength rock, and basalt as a hard rock.

7.4.1. Rock Specimens Preparation

Each slab of travertine, marble, and basalt first had specimens for materials testing removed, leaving the bulk of the material available for the core drilling test. Specifically, specimens were prepared for materials properties tests: 1) Uniaxial compression strength test (UCS) to obtain the materials properties of elastic modulus (E) and Poisson's ratio (ν), 2) Fracture toughness test (K_{Ic}), and 3) Vickers Hardness (H_v) (Table 7) and (Figure 80 through Figure 85).

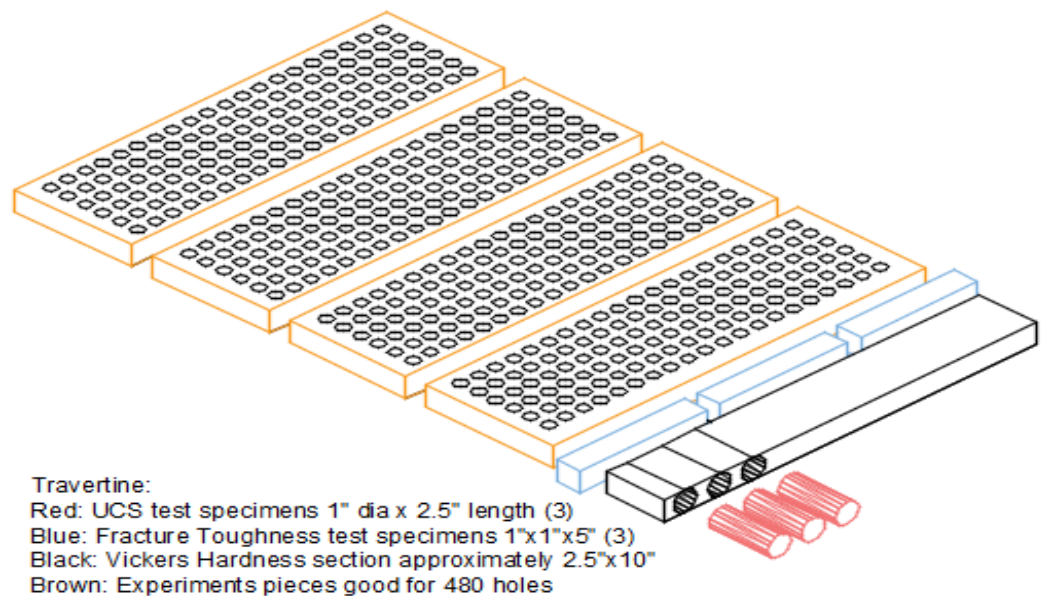


Figure 80: Property tests and experiments allocations for Travertine

Red cylindrical specimens were also used to determine the properties of elastic modulus E and Poisson's ratio ν .

Travertine Rock Samples Overall Dimensions:

$$W = 16" = 38 \text{ cm}$$

$$L = 24" = 60 \text{ cm}$$

$$H = 1" = 2.5 \text{ cm}$$



Figure 81: Travertine rock sample

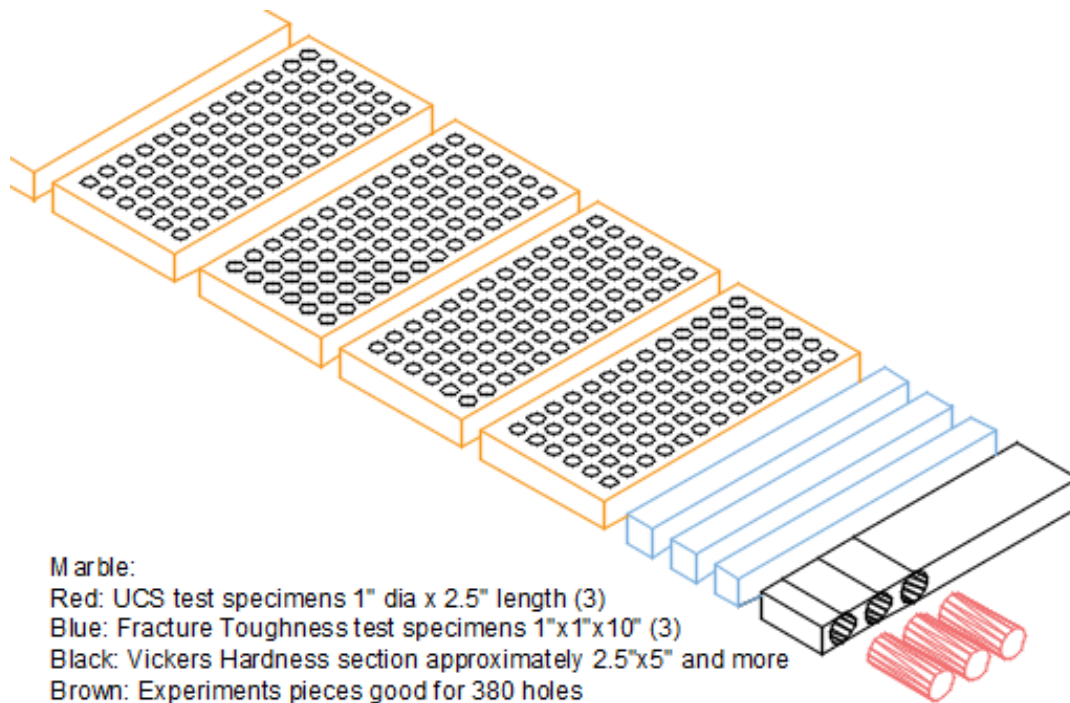


Figure 82: Property tests and experiments allocations for Marble

Red cylindrical specimens were also used to determine the properties of elastic modulus E and Poisson's ratio ν .

Marble Rock Sample Dimensions:

W = 10" = 25.4 cm

L = 60" = 152 cm

H = 1" = 2.54 cm



Figure 83: Marble rock sample

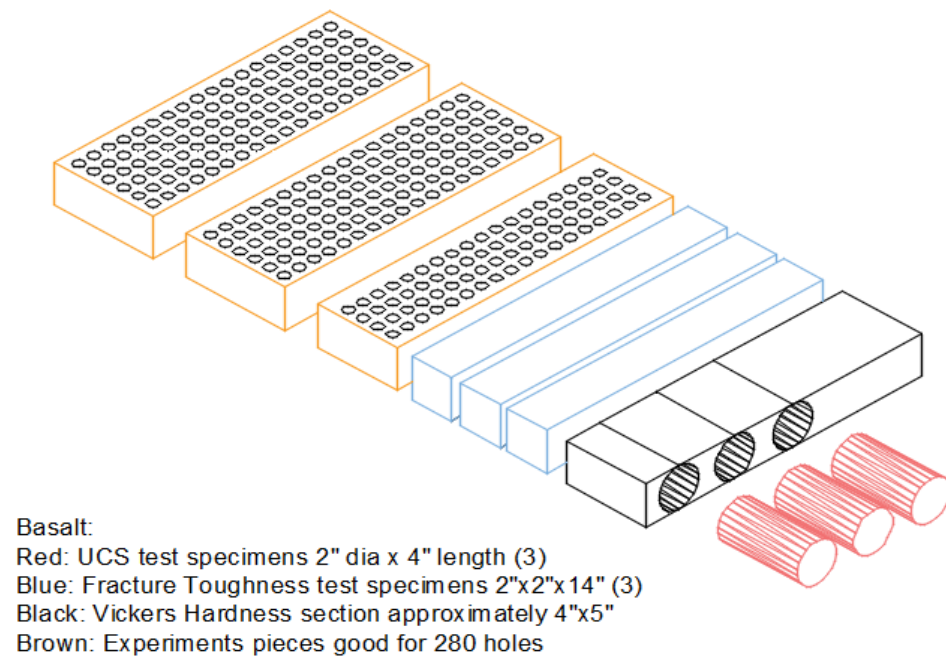


Figure 84: Property tests and experiments allocations for Basalt

Red cylindrical specimens were also used to determine the properties of elastic modulus E and Poisson's ratio ν .

Basalt Rock Sample Overall Dimensions:

$W = 12'' = 30 \text{ cm}$

$L = 23'' = 58 \text{ cm}$

$H = 1.0'' = 2.54 \text{ cm}$



Figure 85: Basalt rock sample

7.4.2. Material Property Tests

7.4.2.1. Uniaxial Compression Test

The material elastic modulus and Poisson's ratio were obtained by conducting the uniaxial compression test and calculated based on the stress / strain curve and axial and lateral strain curves respectively. ASTM standard (7012-14) was followed and the prepared specimens had length to diameter ratios between 2.0:1 and 2.5:1". Typical uniaxial compression test setup is shown in Figure 86.



Figure 86: Typical Uniaxial Compression Strength test setup (UCS), National Technical University of Athens

A. Specimens Preparation for Materials Properties Tests

The rock specimen's diameter should be about 10 times the size of the largest mineral grain (ASTM D4543). Each cylinder specimen for the three types of rocks was either 1" in diameter or larger (Figure 87, Figure 88 and Figure 89). The close up side view images of the rocks were taken aiding for an estimate of meeting such requirement since the grain size is too small compared with 1" thick slab or larger (Figure 75, Figure 77 and Figure 79). Parallel surfaces of both ends of the samples were ensured by conducting milling process on the three samples of each rock type (Figure 90).



Figure 87: Travertine specimens (3) prepared for compression test



Figure 88: Marble specimens (3) prepared for compression tests

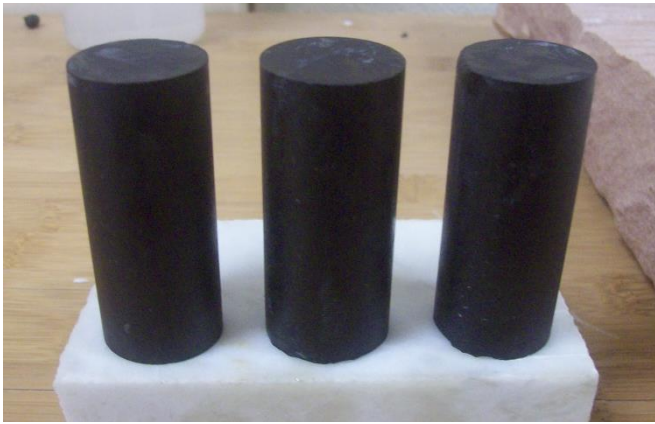


Figure 89: Basalt specimens (3) prepared for compression tests.

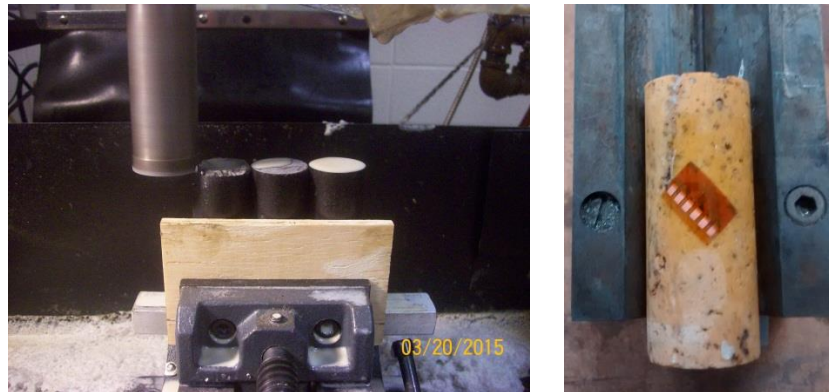


Figure 90: Milling a flat surface for basalt specimens ensuring parallel surfaces for the compression tests (left). Strain gage mounted on travertine specimen for elongation and compression strength measurements (right).

Material property tests were conducted at the Structures Laboratory of CEE at UC Berkeley (<http://www.ce.berkeley.edu/>).

The report summarizing test results including the following: According to ASTM Practice D4543, rock specimens shall be right circular cylinders. The length to diameter ratio should be from 2.0 to 2.5 with the minimum diameter of 47 mm (1-7/8"). The rock specimen's diameter should be about 10 times of the largest mineral grain. Due to limitations of the supplied raw material, the diameter of the test samples was limited to slightly less than 1-in. Table 8 lists all rock samples made available for the material tests. Figure 91 shows the specimens' number assignment. The table presents the dimensions of the samples and the length (height) to diameter ratio (Table 8) (Shakhzod Takhirov, PhD, PE, Short Report/Memo No: 2015-SL-UCB-R01.)

Table 8: List of rock samples available for the material testing

Specimens	Color	Rock material	Height(H), in	Diameter (D), in	Ratio (H/D)
Sp1, Sp2, Sp3	White	Marble	2.132	0.996	2.14
Sp4.0, Sp4, Sp5	Brown	Travertine	2.135	0.990	2.16
Sp7, Sp8, Sp9	Black	Basalt	2.140	0.992	2.16

The strains were monitored by uniaxial and rosette strain gages. The main objective of the testing program was to estimate:

- a) Ultimate compressive strength (D2938)
- b) Poisson's ratio (D3148)
- c) Young modulus (D3148).



Figure 91: Photo of test specimens

The following measurements were recorded during the tests:

- a) Compression load via a load cell in the Universal Test Machine (UTM),
- b) Axial strain via a longitudinal strain gage,
- c) Transverse strain gage via a strain gage installed in transverse direction,
- d) Displacement of the UTM's head.

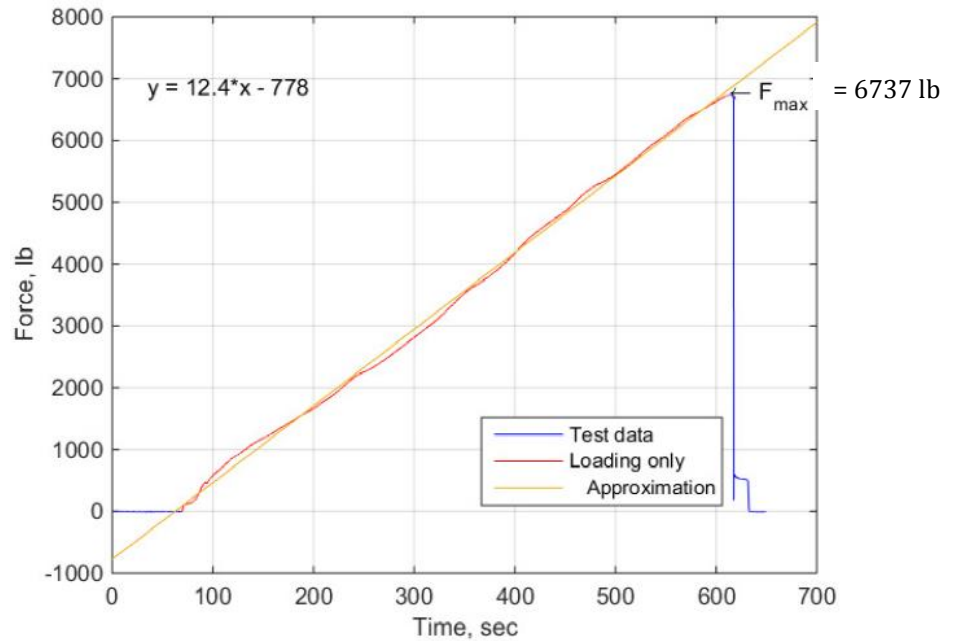


Figure 92: Loading was conducted with the same speed (test data for travertine specimen Sp4 is shown here)

The UTM was operated in force control with the load increasing at about 12 lb per second. A typical force-time curve is shown in Figure 92.

The uniaxial compressive strength (σ_u) is determined from the failure load and specimen cross section area, F_{max} , and A as (ASTM D7012).

$$\sigma_u = \frac{F_{max}}{A}$$

where:

σ_u = uniaxial compressive strength (MPa)

F_{max} = failure load (kN)

A = cross-sectional area (mm²)

The elastic modulus: is obtained from the central portion of the stress strain curve generated from the uniaxial compression test as shown below (ASTM D7012)(Figure 93):

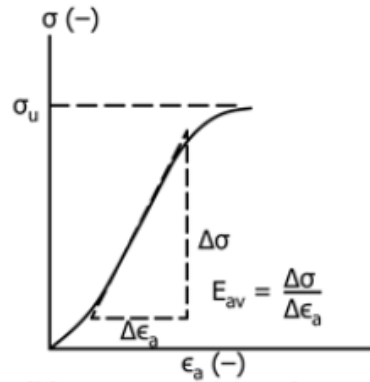


Figure 93: Average modulus of linear portion of axial stress-strain curve

A typical stress strain curve is shown in Figure 94.

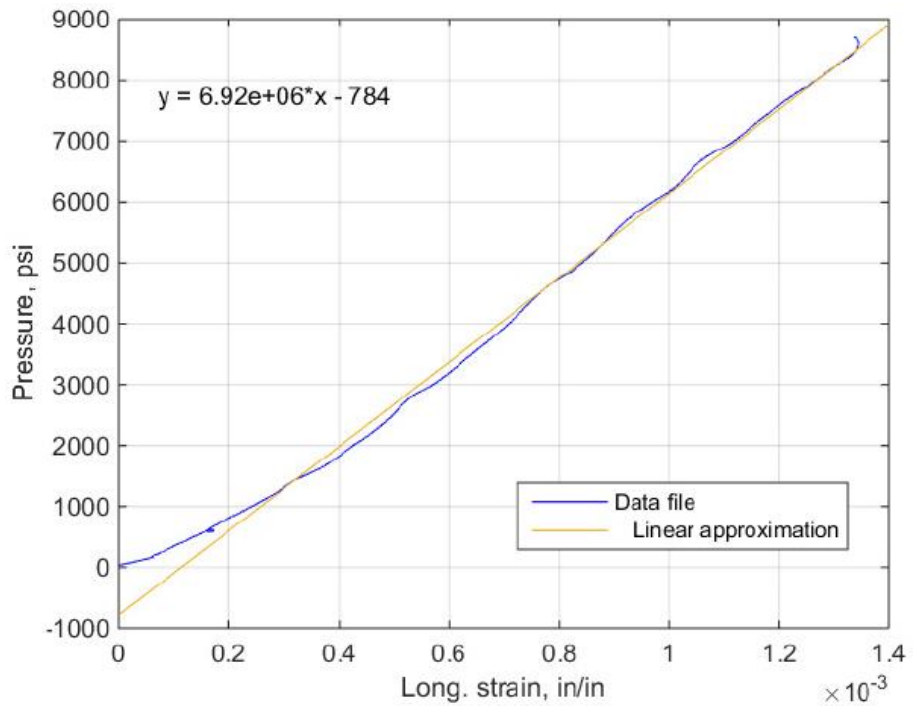


Figure 94: Travertine Young's modulus estimate (specimen Sp4 is presented as an example)

Poisson's ratio is typically calculated from the axial and lateral strain curves generated from the uniaxial compression test (ASTM D7012)(Figure 95) as:

$$v = - \frac{\text{slope of axial curve}}{\text{slope of lateral curve}}$$

$$= - \frac{E}{\text{slope of lateral curve}}$$

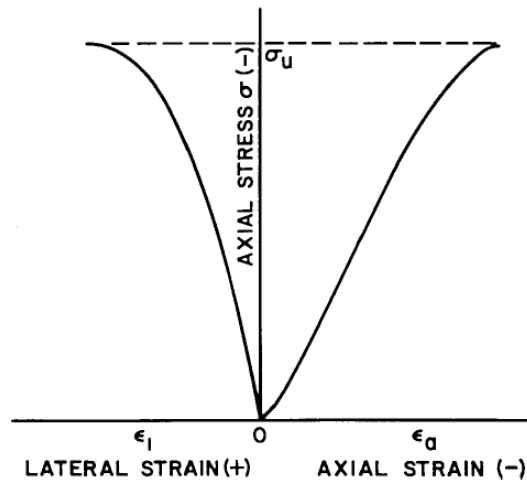


Figure 95: Format of Graphical Presentation of Data

Typical plot of Poisson’s ratio vs. stress is shown in this research is shown in Figure 96 where Poisson’s ratio was estimated as a ratio of the rock strain to longitudinal strain.

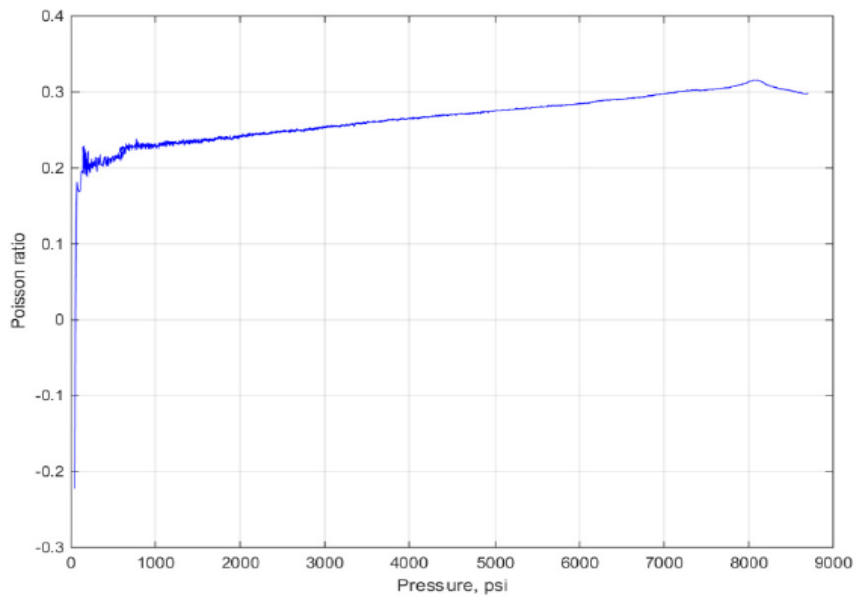


Figure 96: Travertine Poisson’s ratio (specimen Sp4 is presented as an example).

A photo of tested specimen is presented in Figure 97 and failure modes of the test specimens of Travertine, Marble, and Basalt are also presented in Figure 98, Figure 99, and Figure 100.



Figure 97: Rock specimen in UTM (spherical swivel at the bottom)



Sp4

Figure 98: Failure mode of Travertine specimen



Sp2

Figure 99: Failure mode of Marble specimen



Sp7

Figure 100: Failure mode of Basalt specimen

Table 9: A summary of test results

Specimen	Color	Load, kips	Pressure, ksi	Young modulus, E	Poisson ratio, ν
Sp1	Marble	6.48	8.38	$5.0 \cdot 10^3$	0.42
Sp2	Marble	7.22	9.34	$4.9 \cdot 10^3$	0.35
Sp4	Travertine	6.74	8.72	$6.9 \cdot 10^3$	0.28
Sp4.0	Travertine	8.45	10.93	$9.3 \cdot 10^3$	0.30
Sp7	Basalt	35.42	45.83	$10.8 \cdot 10^3$	0.32
Sp8	Basalt	34.54	44.69	$10.8 \cdot 10^3$	0.32

The detailed plots of Young's modulus and Poisson's ratio are presented in (Appendix C). The average value of the two tests of each type of rock was calculated and report as shown below (Table 10):

Table 10: Material properties average values used in this research

	Young modulus			Poisson ratio		
	Sp1	Sp2	Avg (GPa)	Sp1	Sp2	Avg
Marble	34.4	26.7	30.5	0.42	0.35	0.39
Travertine	47.7	64.3	56.0	0.28	0.30	0.29
Basalt	74.7	74.2	74.4	0.32	0.32	0.32

7.4.2.2. Vickers Hardness Test

The principle of Vickers hardness test is obtaining a hardness number that is based on a relatively small indentation made in the material surface. The Vickers hardness indenter is made of diamond with a specific geometry (Figure 102). The indenter is pressed into the test specimen surface by a very accurate applied force using a test instrument particularly designed for this purpose. While Vickers hardness testing is applied to both micro and macro-test force range, in this research the macro force range is considered as specified by ASTM standard (E384).

Macro > 9.81 to ≤ 1176.80 N (> 1 to ≤ 120 kgf)

As the diamond is pressed into the test specimen, a light microscope measures the indentation size. The macro-range indents are measured in mm and Vickers hardness is reported in GPa and based on geometry it is calculated as:

$$H_v = 0.0018544 \times \left(\frac{P_2}{d_2^2} \right)$$

Where: P_2 = force, N, and

d_2 = mean diagonal length of the indentations, mm.

Vickers Indenter:

An ideal Vickers indenter is a highly polished, pointed, and square-based pyramid shape diamond with face angle of 136°. The four faces of the indenter are equally inclined to the axis of the indenter where they meet at a sharp point (Figure 101 and Figure 102).



Figure 101: Vickers hardness diamond tip indenter,
https://upload.wikimedia.org/wikipedia/commons/d/d2/Vickers_anvil_diamonds.jpg

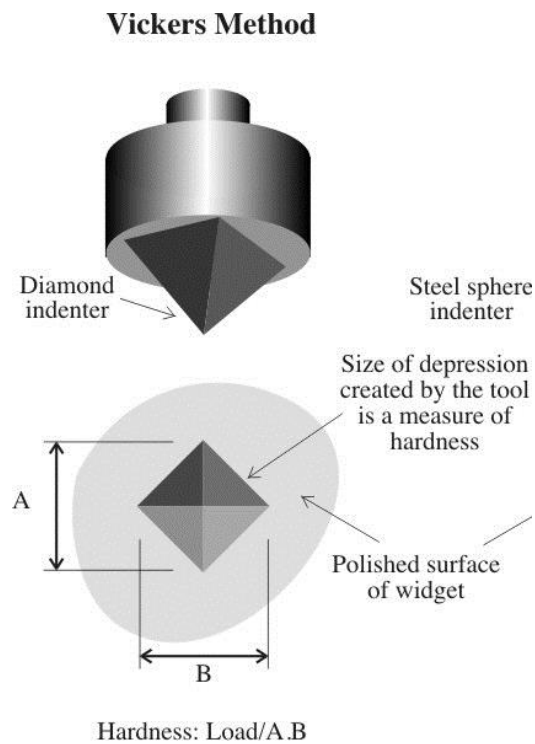


Figure 102: Vickers hardness test method, NASRUL Design
http://nasruldesign.weebly.com/uploads/7/4/1/9/7419180/8927090_orig.jpg

Vickers hardness apparatus:

The test machine used for the tests is designed to support the specimen tested and apply the controlled preselected force while measuring the movement of the indenter. See Figure 103. Equipped with a light optical microscope, the tester is capable of selecting a

desired test location to measure the size of the indentation produced by the test. The hardness testing machine has two indenters and several optical microscopes for getting a good look at the indentation. The specimen surface plane should be perpendicular to the axis of the indenter and the direction of the applied force. It is worth noting that during the entire test cycle, the test machine should be shielded from any form of vibration to ensure accurate results.



Figure 103: Vickers hardness tester, IDI lab

Vickers test specimen:

Although there is no standard shape or size to the Vickers hardness test specimen, it must conform to a few rules established by ASTM (E384). To achieve optimum accuracy of measurement, the test should be performed on a flat specimen with a polished (or suitably prepared) surface. The required surface finish quality can vary with applied forces and magnifications used where the lower the test force and smaller the indentation size the more critical is the surface preparation. Specimens shown in Figure 104 were prepared according to these standard using discs shown in Figure 105. It is also recommended to mount specimen in frames where they are secured with plaster materials as they are tested.



Figure 104: Specimens prepared for Vickers hardness tests

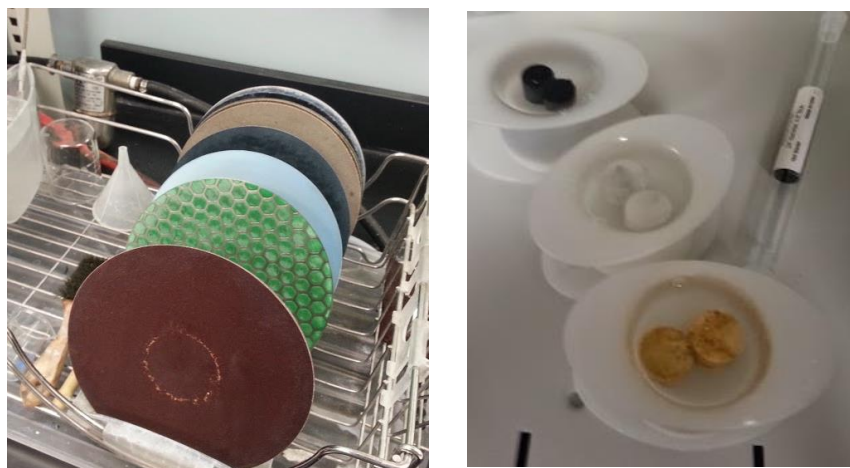


Figure 105: Discs used to polish the specimens providing very smooth surfaces (left). Casting specimens in the epoxy for Vickers hardness tests (right)

The Vickers hardness tests were conducted at two different external labs, IdiNet and Struers. The results shown in Table 11 represent the averages of the tests performed by each lab. The data for these tests is shown in Figure 106 - Figure 108.

Table 11: IDI and Struers Vickers hardness test results

	IdiNet Avg (GPa)	Struers Avg (GPa)	Average
Basalt	1.50±0.12	1.58±0.04	1.54±0.8
Marble	1.49±0.14	1.45±0.08	1.47±0.11
Travertine	1.27±0.11	1.41±0.18	1.33±0.14

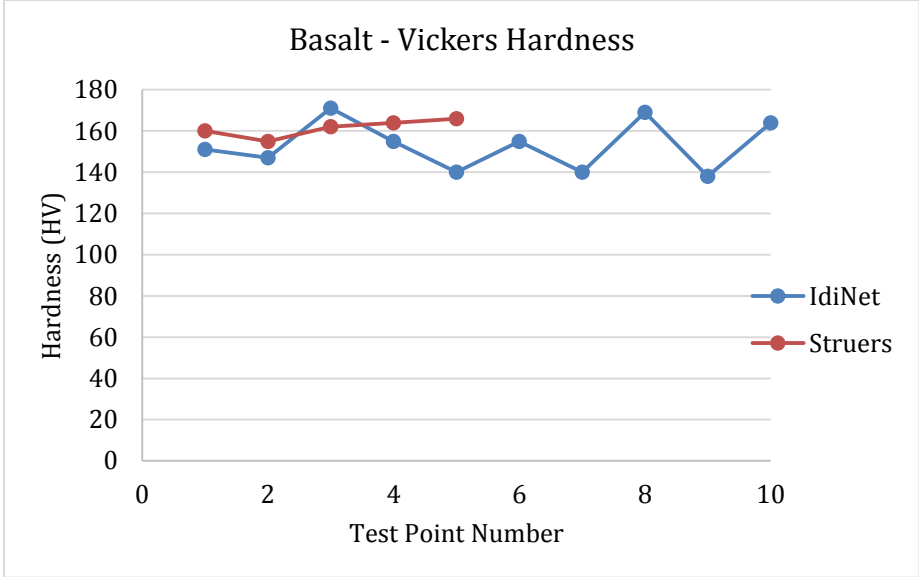


Figure 106: Basalt Vickers hardness test results

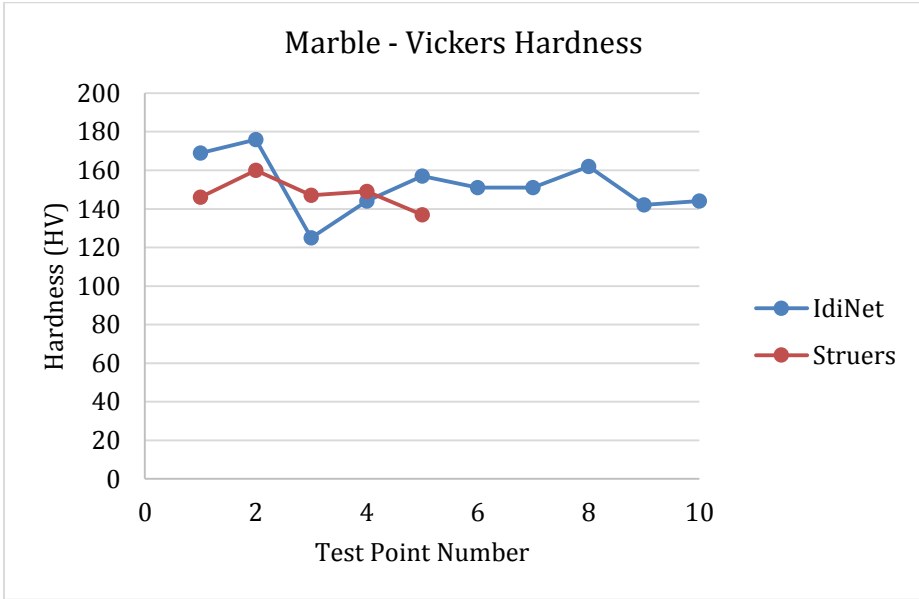


Figure 107: Marble Vickers hardness test results

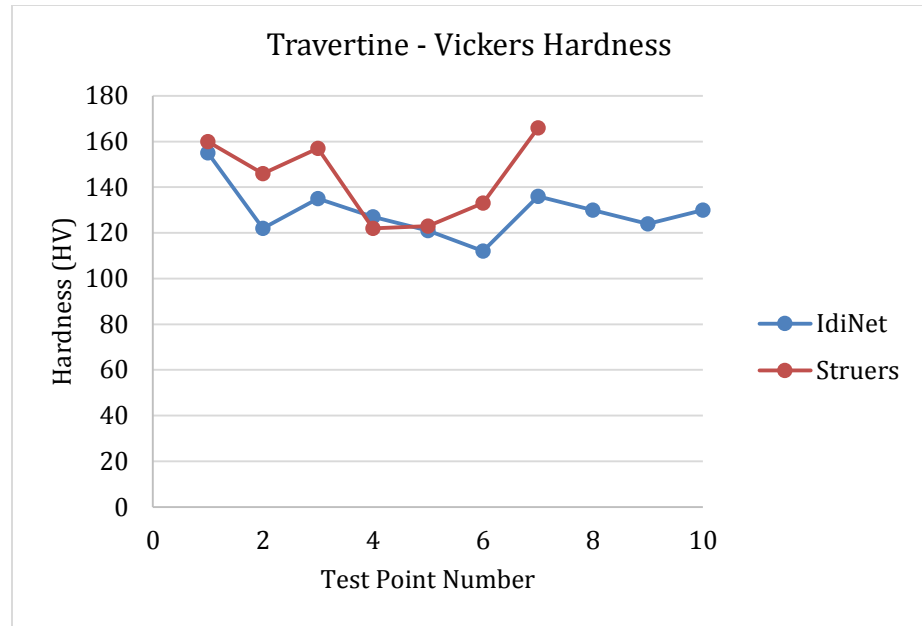


Figure 108: Travertine Vickers hardness test results

7.4.2.3. Fracture Toughness Test

The most suitable fracture toughness test for rock is reported to be the Cracked Chevron Notched Brazilian Disc (CCNBD) test (Zhao, Fowell, Roegiers, & Xu, 1994). Fracture toughness is a property that characterizes intact materials resistance to crack propagation. This test is also useful as an index for rock fragmentation processes, like crushing and tunnel boring, or used in the analysis of hydraulic or explosive fracturing and stability.

The test used in this study was applied on core specimens of rock materials where the core axis can be oriented either parallel or perpendicular to any anisotropy features such as planes of weakness. A cracked chevron notched Brazilian disc (CCNBD) specimen has a notch with a chevron “V”-shaped notch cut along the core diameter (Figure 109). One of the advantages of this test is that it only requires the recording of the maximum load in order to calculate the rock fracture toughness in mode I.

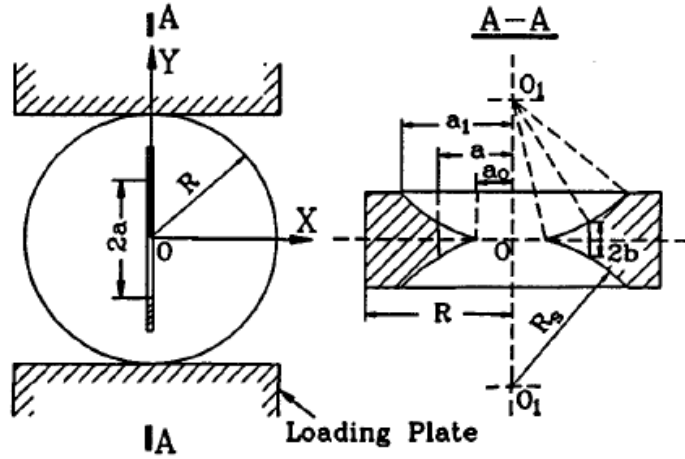


Figure 109: The CCNBD specimen geometry with recommended test fixture (Zhao et al., 1994)

The test requires that all the dimensions of the geometry should be converted into dimensionless parameters with respect to the specimen radius R or diameter D . The following table contains the definition and values of the geometrical parameters (Table 12) followed by the dimensionless expressions:

Table 12: Standard CCNBD and geometrical dimensions

Descriptions	Values
Diameter D (mm)	75.00
Thickness B (mm)	30.00
Initial chevron notched crack length a_0 (mm)	9.89
Final chevron notched crack length a_1 (mm)	24.37
Saw diameter D_s (mm)	52.00
Cutting depth h_c (mm)	16.95
Y_{min}^* (dimensionless)	0.84
a_m (mm)	19.31

$$\alpha_o = a_o/R = 0.2637$$

$$\alpha_1 = a_1/R = 0.65$$

$$\alpha_B = B/R = 0.8$$

$$\alpha_m = a_m/R = 0.5149$$

$$\alpha_s = D_s/D = 0.6933$$

The following equation is used to calculate specimen fracture toughness:

$$K_{IC} = \frac{P_{max}}{B \cdot \sqrt{D}} \cdot Y_{min}^*$$

Where

Y_{min}^* is the critical dimensionless stress intensity value for the specimen that is determined by the specimen geometry dimensions α_0 , α_1 , and α_B only.

$$Y_{min}^* = u \cdot e^{v \cdot \alpha_1}$$

Where u and v are constant determined by α_0 , and α_B only. The tabulated values of u and v are listed in Zhao et al., (1994).

Tests were conducted on one specimen each for marble and travertine rock specimens. The results are shown in Table 13 - Table 15. Basalt rock could not be tested due to the limitation of the saw available to cut through the specimen that is thicker than the other two specimens. Therefore, K_{IC} plot was generated for the basalt rock material where the fracture toughness reasonable range values were used yielding the WOB required for each K_{IC} value. The WOB value that matched or very close to the WOB from the experiment was chosen to be the K_{IC} value for Basalt (Table 15 and Figure 112). WOB vs. K_{IC} plots were also generated for marble and travertine to validate the experiment results (Figure 110, Figure 111, Table 13 and Table 14).

Table 13: Marble K_{IC} test dimensions using Brazilian disk method, (Zhao, Fowell, Roegiers, & Xu, 1994)

Marble			
Measured	[mm]	Calculated	[mm]
D1 =	76.53		
D2 =	76.84	D =	76.685
B1 =	28.58	B =	28.5575
B2 =	28.51		
B3 =	28.55	l = 2*a1	46.38
B4 =	28.59	alpha_0 =	0.26772
2*a1 side1 =	46.72	alpha_1 =	0.60481
2*a1 side 2 =	46.04	alpha_B =	0.7448
2*a0 =	20.53		
Max Load =	-1183.2	lb	
Max Load =	-5262.9	N	
u =	0.26849	From Tables in Fowell Paper	
v =	1.70066	From Tables in Fowell Paper	
Ymin =	0.75099		

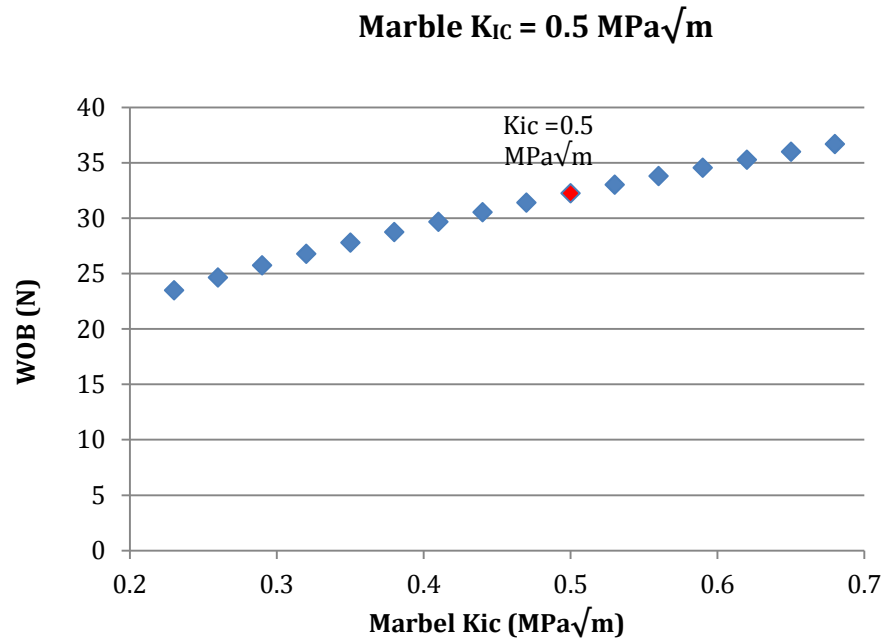


Figure 110: Marble K_{IC} value validation obtained from experiment using Brazilian disk method

Table 14: Travertine K_{IC} test dimensions using Brazilian disk method, (Zhao, Fowell, Roegiers, & Xu, 1994)

Travertine			
Measured [mm]		Calculated	[mm]
D1 =	76.87		
D2 =	76.8	D =	76.835
B1 =	29.94	B =	29.9425
B2 =	29.97		
B3 =	29.97	l =	46.295
B4 =	29.89	alpha_0 =	0.24832
2*a1 side:	46.37	alpha_1 =	0.60252
2*a1 side	46.22	alpha_B =	0.7794
2*a0 =	19.08		
Max Load	-1714.9083	lb	
Max Load	-7628.2922	N	

u = 0.26615255 From Tables in Fowell Paper

v = 1.762348 From Tables in Fowell Paper

Travertine $K_{IC} = 0.7 \text{ MPa}\sqrt{\text{m}}$

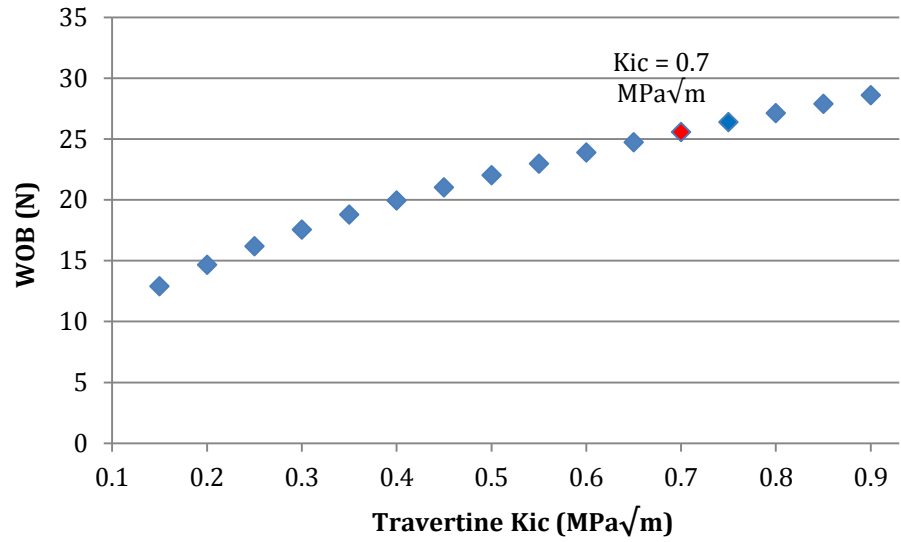


Figure 111: Travertine K_{IC} value validation obtained from experiment using Brazilian disk method

Table 15: Basalt K_{IC} test dimensions using Brazilian disk method did not yield result and analytical method was used

Basalt			
Measured [mm]		Calculated [mm]	
D1 =	77.15		
D2 =	76.92	D =	77.035
B1 =	37.83	B =	37.72
B2 =	37.74		
B3 =	37.62	l =	47.395
B4 =	37.69	alpha_0 =	0
2*a1 side:	47.37	alpha_1 =	0.61524
2*a1 side	47.42	alpha_B =	0.9793
2*a0 =	0		
Max Load	-2377.4 lb		
Max Load	-10575 N		

Basalt K_{IC} = 1.2 MPa√m ; result generated from analytical data at nominal values (Figure 112)

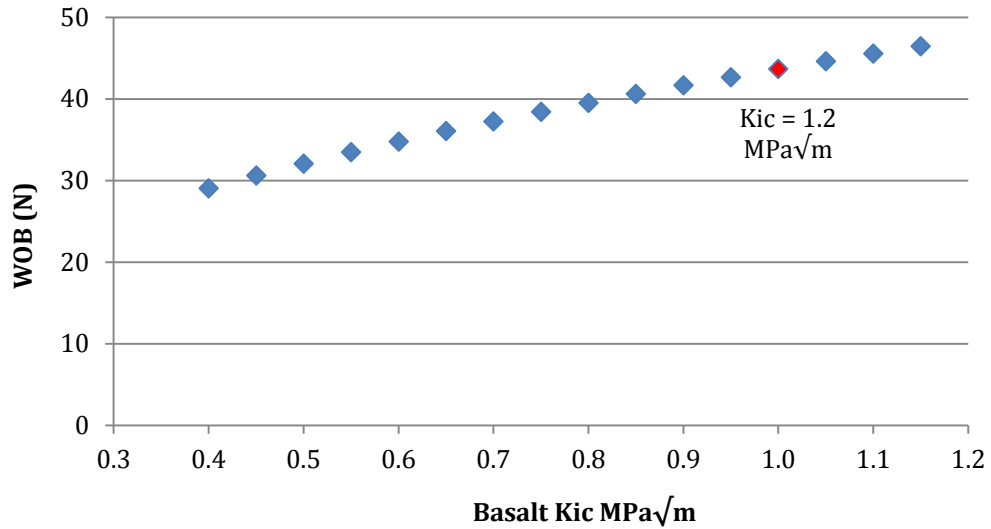


Figure 112: Basalt K_{IC} value validation

7.4.3. Material Properties Summary

Travertine, marble, and basalt rocks material properties are tested and collected as shown in the table below:

Table 16: Rocks Materials Properties Tests Summary

Rock Type	Elastic Modulus E (MPa)	Fracture Toughness K _{IC} (MPa√m)	Vickers Hardness H _v (GPa)	Poisson's Ratio ν
Basalt (Igneous)	74.4	1.2 (estimated)	1.54	0.32
Marble (Metamorphic)	31.5	0.5	1.47	0.39
Travertine (Sedimentary)	56.0	0.7	1.34	0.29

7.5. Experimental Setup

Rotary ultrasonic drilling experiments were performed using the Sonic Mill Rotary Ultrasonic Machine, Series 10 (Sonic-Mill, Albuquerque, NM, USA), located in the Industrial Engineering Laboratory at the Kansas State University (<http://catalog.k-state.edu/content.php?navoid=144&catoid=2>). The experiment setup consists of three major systems: an ultrasonic spindle system, a coolant system, and a data acquisition system.

1) Ultrasonic spindle system

The ultrasonic spindle system consists of the following components as shown in Figure 113.

- Motor speed controller: supplies the rotation motion of the core drill and the motor speed controller could be used to obtain different speeds.
- Power supply that converts 60 Hz electrical power supply to high frequency of 20 kHz AC output. This AC output is fed to the piezoelectric transducer located in the ultrasonic spindle.
- Ultrasonic spindle contains piezoelectric transducer: converts the electrical AC input received from the power supply into mechanical vibration.

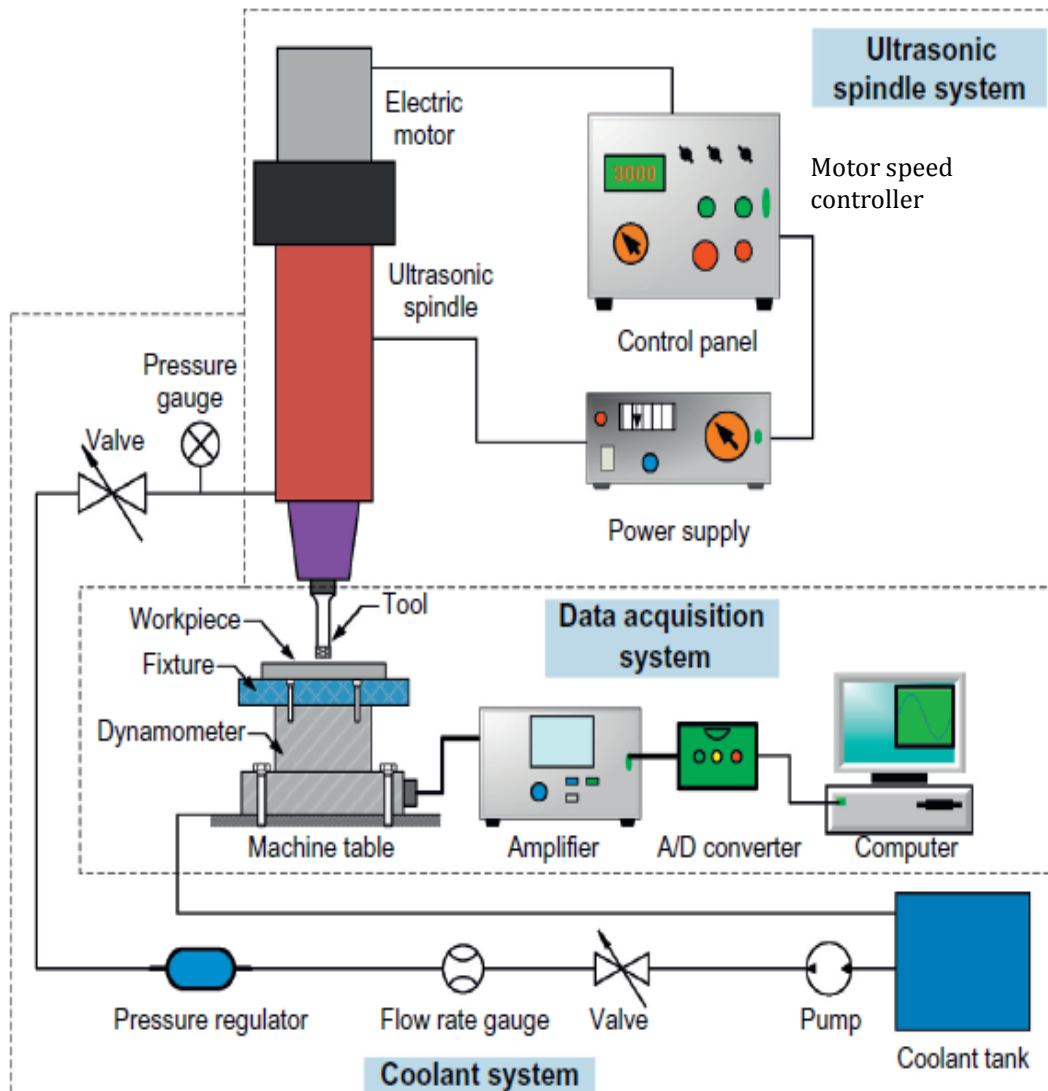


Figure 113: Schematic of Rotary Ultrasonic Machine (RUM) at KSU, (Cong et al., 2014)

- 2) The data acquisition system centers around measuring the force applied to the workpiece, or the WOB. The system consists of:
- a. A piezoelectric dynamometer (Kistler 9272) is attached to the machine table and the workpiece is mounted on top of it with fixtures. The dynamometer measures the cutting force along the feed direction (WOB) generating an electrical output voltage that is proportional to the force (Figure 114).



Figure 114: Dynamometer measuring applied force (left), ultrasonic frequency display unit by Sonic-Mill (right)

- b. A/D converter: receives the electrical signal from the dynamometer and displays it and saves it to a computer system with the help of Dynoware software (Figure 115).



Figure 115: A/D converter received signal from dynamometer of the applied force

- 3) The coolant system is activated at the beginning of each drilling test and coolant is continuously supplied to the drill bit to prevent overheating.

When performing the measurements to determine the WOB under the various testing conditions, the workpiece is placed and fastened atop Kistler 9272 piezoelectric dynamometer attached to the machine table. Cutting force sampling frequency signal is set at 1000 Hz.



Figure 116: Rotary Ultrasonic Machine (RUM) located at KSU

7.6. Ultrasonic Wave Amplitude

It is evaluated based on the drill power using a dial gage (Figure 117**Error! Reference source not found.**, a). Also, drill bit tuning length is taken in account in assessing the amplitude as shown in the image below considering the optimum value is at the multiple of an integer by half the ultrasonic wavelength (Figure 117, b). All drill bits used are in the length and amplitude values of drill bit # showing in the literature below (Cong, Pei, Mohanty, Van Vleet, & Treadwell, 2011) (Figure 119, and Figure 120).

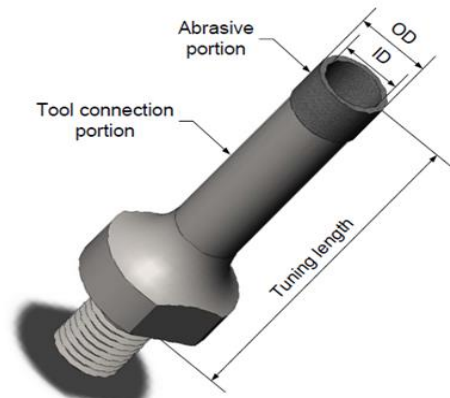


Figure 117: a) Amplitude measuring device, dial gage, b) Typical drill bit showing tuning length (Weilong Cong, 2013)

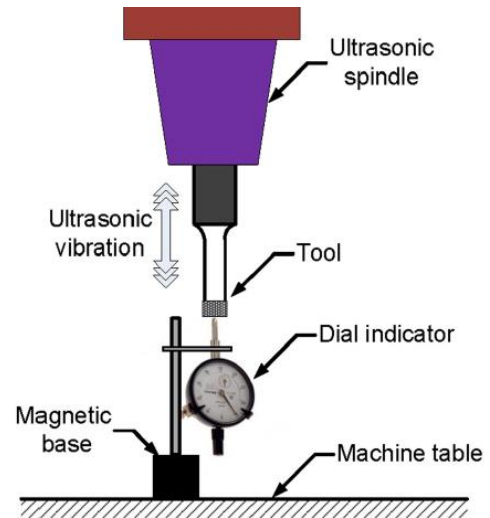


Figure 118: Dial gage placed under the drill bit and in contact with the surface as it operates and measure the wave amplitude



Figure 119: Five different tools used in the study, Cong et al, 2011

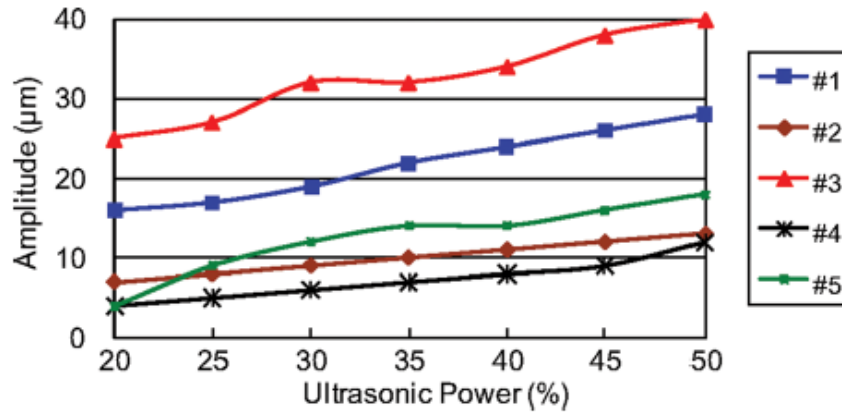


Figure 120: Effects of ultrasonic power on vibration amplitude (measure with the dial indicator method) for five tools (#1, #2, #3, #4, and #5), Cong et al, 2011.

As the Dynoware software launches, the hardware dialog between acquisition cycles window appears and it is set for A/D board multichannel amplifier type 5070 (Figure 121). Although, the A/D board is a multichannel amplifier that allows for maximum of eight (8) channels to be used, in these experiments only two channels were used. Channel 2 is used for applied force on the workpiece (WOB) as shown in Figure 122. Finally a documentation dialog appears allowing for storing document under desired title, and set up to record cutting force (Figure 123).

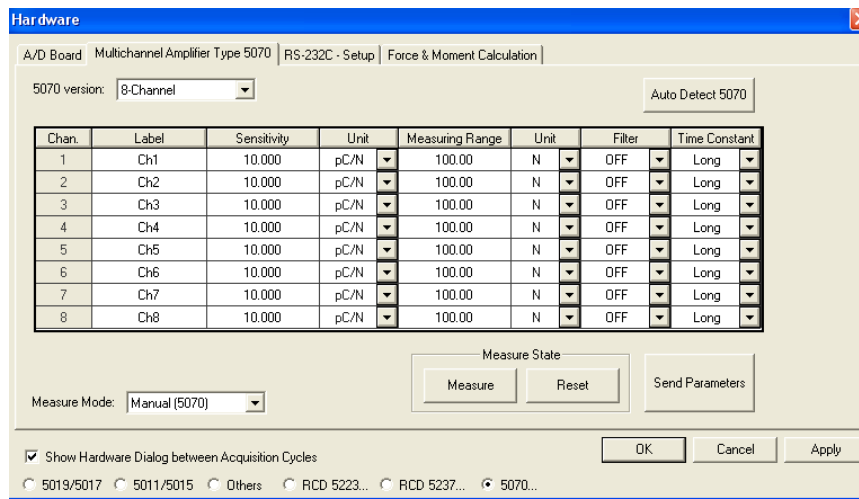


Figure 121: Hardware dialog between acquisition cycles set for A/D board multichannel amplifier type 5070

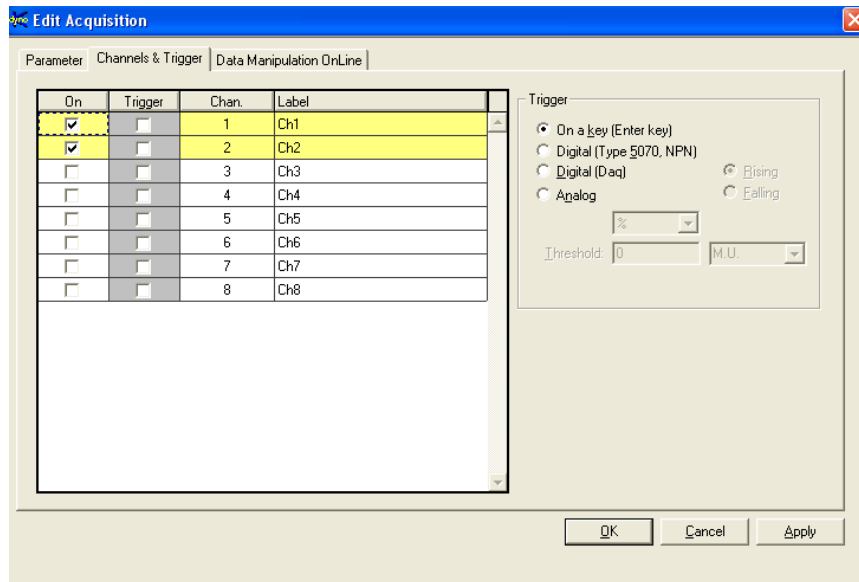


Figure 122: A/D board multichannel amplifier has Ch1 is assigned for torque and ch2 is assigned for applied force (AKA, Weight on Bit).

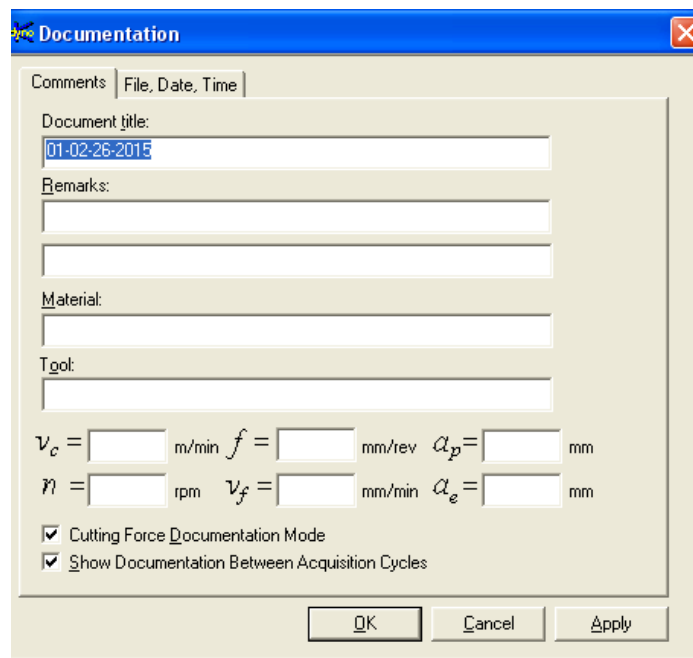


Figure 123: Documentation dialog allows for storing document under desired title, and set up to record cutting force and be displayed between acquisition cycles

Testing was performed according to the matrix specified in Table 5. All core rock samples were collected for each test, grouped and labeled with the test parameters values (Figure 124 and Figure 125).



Figure 124: Experimental core rock samples drilled at various drilling parameters



Figure 125: Rock samples drilled at various input parameters close up view showing the labeling system applied to identify each core sample.

7.7. Drill Bits

Ten core drills, three of which have same specification, with metal-bond diamond abrasive particles were provided by N.B.R. Diamond Tool Corp. (La Grangeville, NY, USA). The drill bit specifications are listed in Table 17.

Table 17: Drill bits specifications

Abrasive size Sa (mm)	Abrasive concentration Ca	Drill bit outer diameter Do (mm)	Drill bit inner diameter Di (mm)	Mesh Size
0.125	50	12	10	#100-120
0.125	100	12	10	#100-120 (3)
0.125	150	12	10	#100-120
0.080	100	12	10	#140-170
0.160	100	12	10	#80-100
0.200	100	12	10	#60-80
0.125	100	9	7	#100-120
0.125	100	15	13	#100-120

The diamond particles were provided by National Research Co. Nat-PGE. The bond between the abrasive particles and the matrix is bronze, Colmonoy #7 with a Rockwell hardness of B 92-97. The body of the drill is cold rolled seamless tubing made of 1215 steel (Figure 126).



Figure 126: Drill bits with varies design parameters

To ensure identical comparison of drill bit performance condition, the drill bit tip (cutting surface) is refreshed between each test using sharpening / dressing stick (Figure 127). The dressing process involves removing the worn out abrasive diamond particles and exposing a new surface containing new sharp diamond particles.

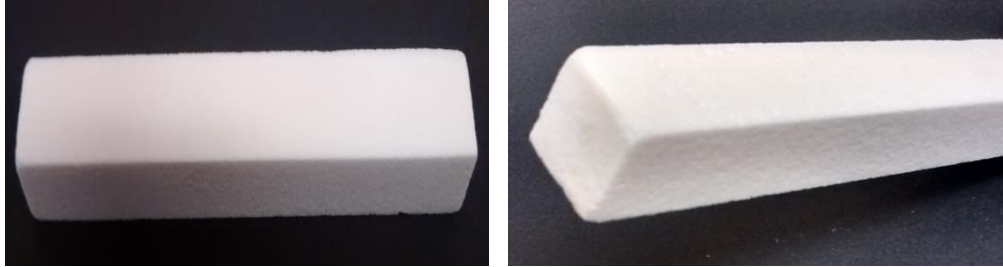


Figure 127: Sharpening (dressing) stick refreshing the core drill bit cutting surface after each test exposing a fresh layer of abrasive particles.

7.8. Core Drill Bit Design Parameters

7.8.1. Cutting Force Plots

The following are the typical plots of the cutting force vs time as the drill proceeds through the workpiece for basalt, marble and travertine (Figure 128, Figure 129, and Figure 130). In each case, the reported value is the average force (in the central portion of the drilling time).

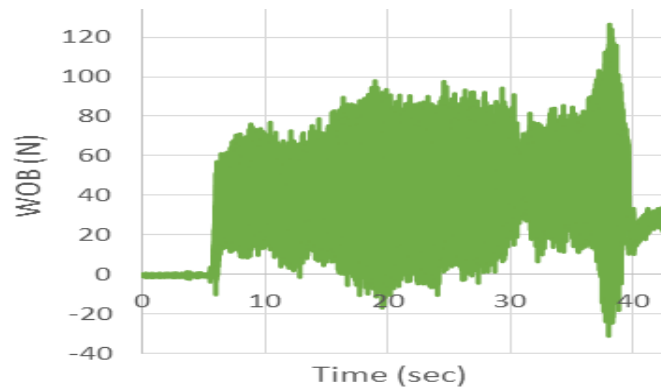


Figure 128: Typical plot of cutting force measured for travertine at a given value set of S , A , S_a , C_a , D_i , and D_o parameters

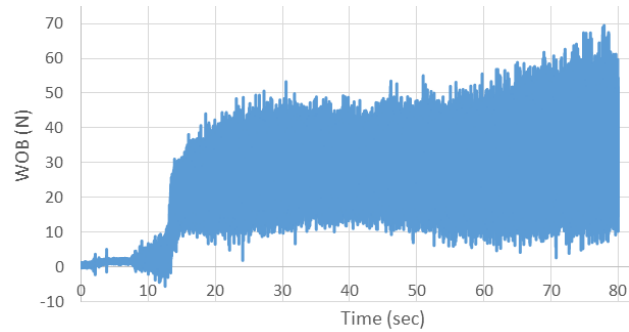


Figure 129: Typical plot of cutting force measured for marble at a given value set of S , A , S_a , C_a , D_i , and D_o parameters

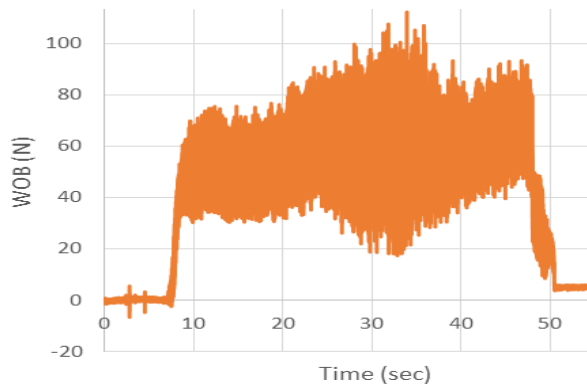


Figure 130: Typical plot of cutting force measured for basalt at a given value set of S , A , S_a , C_a , D_i , and D_o parameters

7.8.2. Core Drill Bit Outside and Inside Diameters

As the core drill bit diameters changes, the end face area changes resulting in an increase or decrease in the number of the abrasive particles taking part in cutting. Therefore, the changes of the drill bit inner and outer diameters will be related to the performance of the drill.

Three different drill bit sizes were selected to investigate the effect of the change of the bit inner and outer diameter on ROP performance. While the model shows the change of ROP as the drill bit size changes at a constant force, the experiments obtain the force required to cut through the rock sample as an output at a constant feed-rate/ROP as an input. Therefore, to validate the mathematical model, the range of average drill bit size shown in Table 5 was tested at as the rest of the listed parameter set at their listed nominal values. The results of cutting force with error bars (WOB) vs drill bit average diameter is shown in Figure 131.

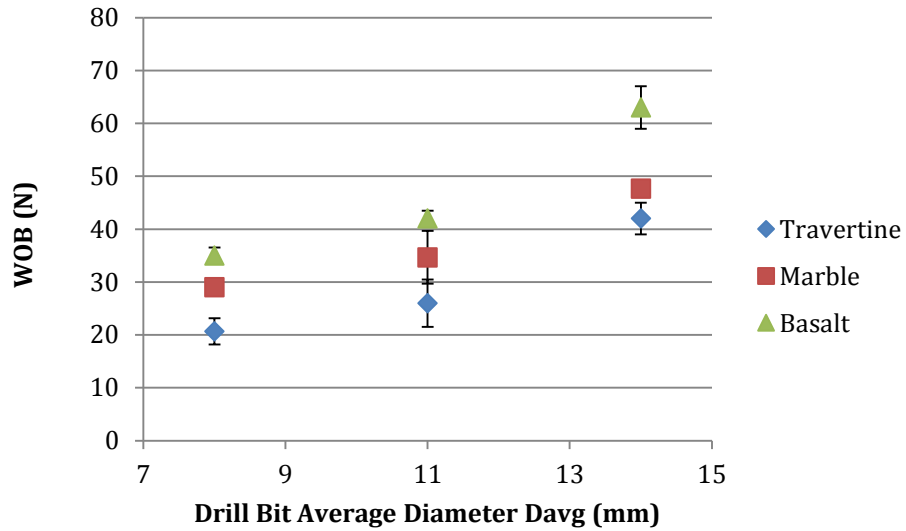


Figure 131: Experimental results of the cutting force vs drill bit average diameter

7.8.3. Abrasive Particles Concentration (C_a)

Three different abrasive particles concentrations (C_a) in the drill bit are shown in Table 5 were tested as the rest of the listed parameters were set at their listed nominal values. The results of cutting force (WOB) vs abrasive particle concentration is shown in Figure 132.

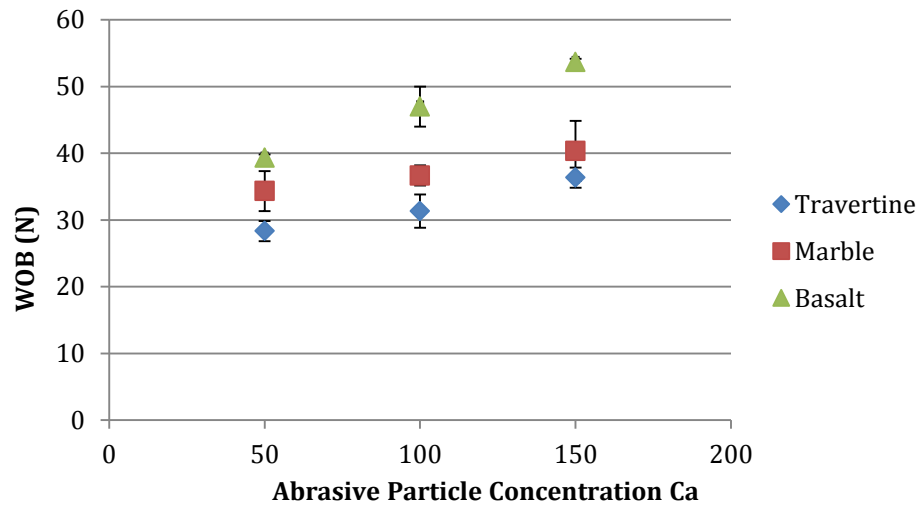


Figure 132: Experimental results of the cutting force vs cross abrasive particles concentration

7.8.4. Abrasive Particle Size (S_a)

Four different abrasive particles sizes (S_a) in the drill bit are shown in Table 5 were tested as the rest of the listed parameters were set at their listed nominal values. The results of cutting force (WOB) vs abrasive particle size is shown in (Figure 133).

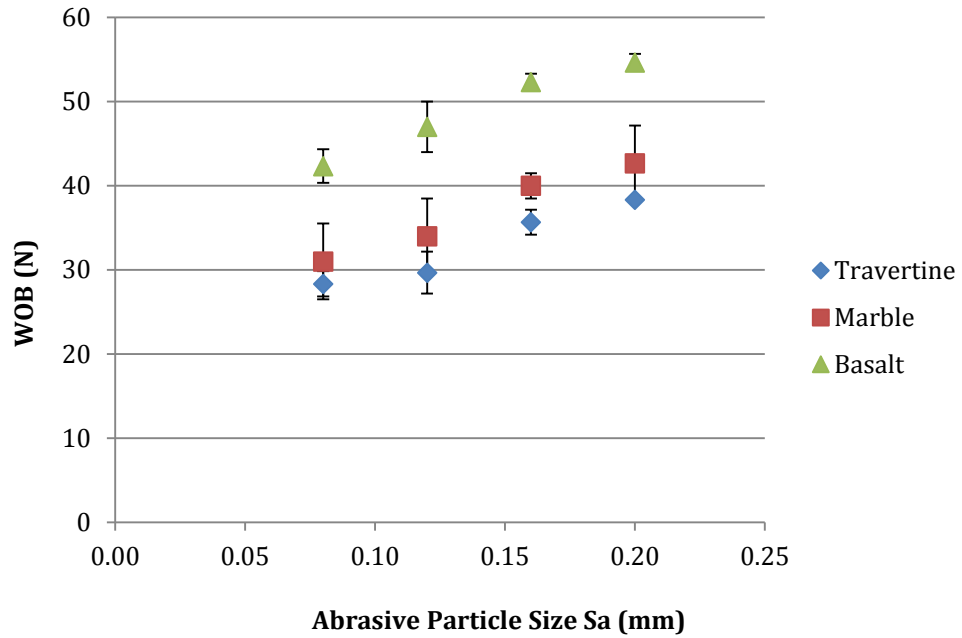


Figure 133: Experimental results of the cutting force vs cross abrasive particles size

7.9. Drill Process Parameters

7.9.1. Rate of Penetration (ROP)

Nominal drill bit size was chosen with inner diameter $D_i = 10$ mm and outer diameter $D_o = 12$ mm to use in conducting weight on bit at rates of penetration between 0.1 – 0.7 mm/s as shown in Table 5. The rest of the listed parameters were set at their listed nominal values. The results of cutting force with error bars (WOB) vs ROP are shown in Figure 134.

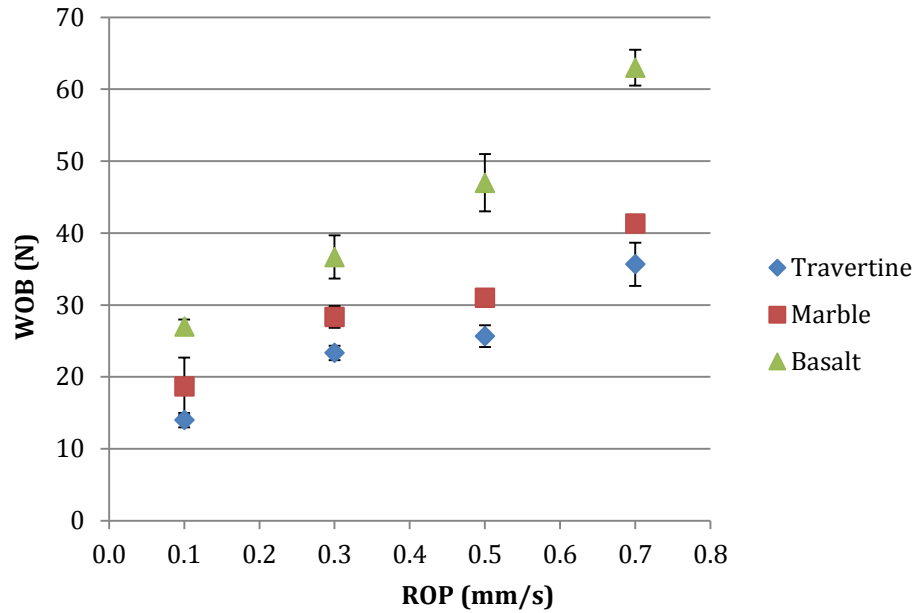


Figure 134: Experimental results of the cutting force vs ROP

7.9.2. Speed

Four different spindle speeds (S) as shown in Table 5, were tested as the rest of the listed parameters were set at their nominal values. The results of cutting force with error bars (WOB) vs spindle speed is shown in Figure 135.

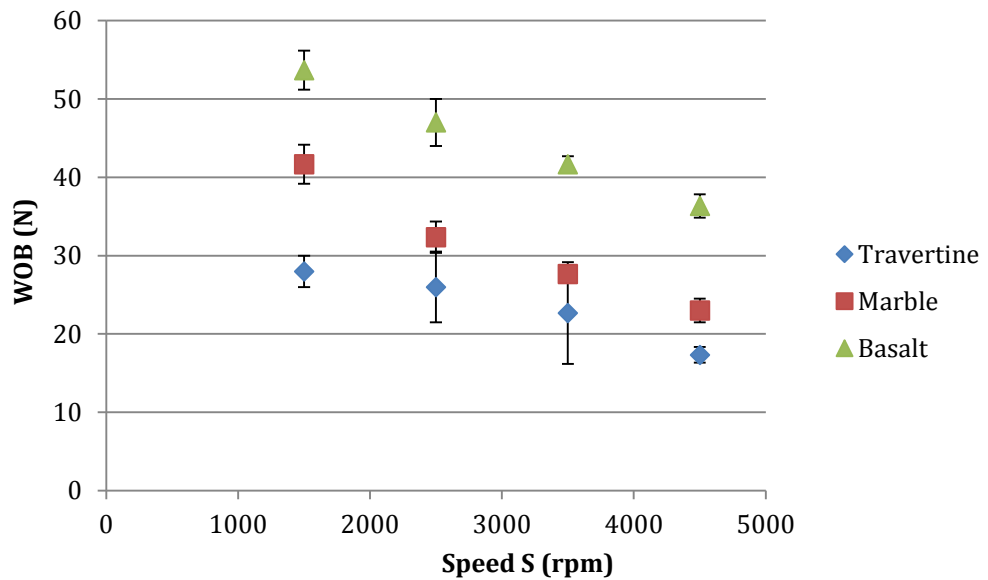


Figure 135: Experimental results of the cutting force vs Speed

7.10. Ultrasonic Wave Parameters

7.10.1. Wave Amplitude

Four different ultrasonic amplitudes (A) are shown in Table 5 were tested as the rest of the listed parameters were set at their listed nominal values. The results of cutting force (WOB) vs ultrasonic amplitude is shown in (Figure 136).

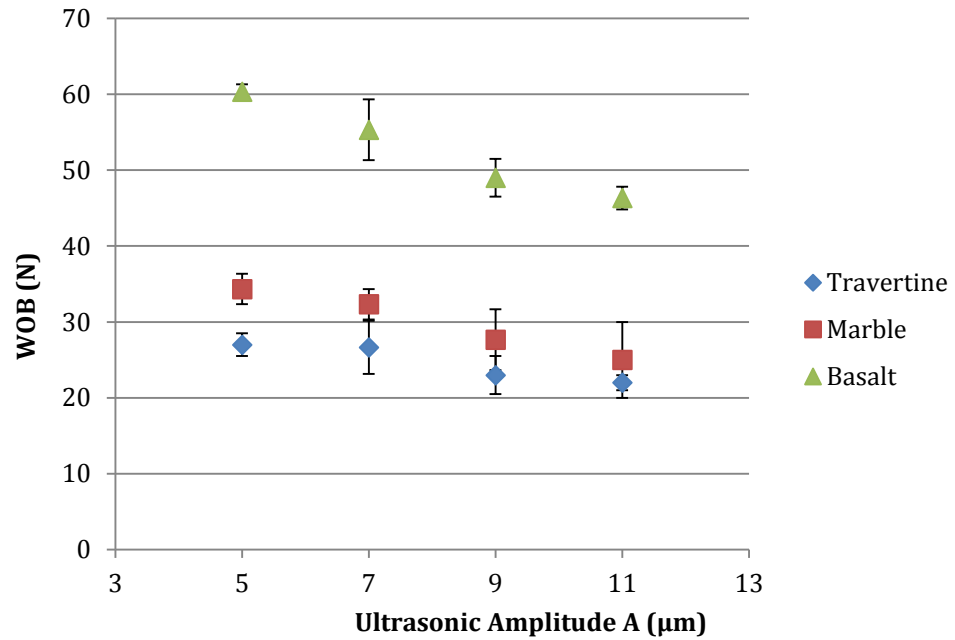


Figure 136: Experimental results of the cutting force vs ultrasonic amplitude

7.10.2. Ultrasonic Frequency

The change in frequency (f) is not investigated in this research and additional comments are presented in Appendix D.

Chapter 8

8. Mathematical Model Validation

Comparison of the input variables effect on the on WOB performance has been examined analytically and experimentally. Performance evaluations were conducted at nominal values for all parameter with the variation of one parameter at a time within acceptable range values as follow: speed $S = 2500$ rpm, abrasive particle size $S_a = 0.125$ mm, abrasive particle concentration $C_a = 100$, drill bit outside diameter $D_o = 12$ mm, drill bit inside parameter $D_i = 10$ mm, abrasive particle semi-angle $\alpha_o = 120^\circ$, ultrasonic wave amplitude $A = 7$ μ m, and ROP = 0.3 mm/s. Furthermore, materials properties were obtained from tests conducted determining elastic modulus E , Poisson's ratio ν , fracture toughness K_{IC} , and Vickers hardness H_v for each type of rock (basalt, marble and travertine).

Although, the mathematical model is developed for ROP, the experiments were conducted on a rotary ultrasonic drill machine that allows for holding the feed rate (ROP) constant while measuring the applied force (WOB). Therefore, the predicted results of ROP will not be compared to the experimental results. Instead, the force (WOB) will be calculated using the developed ROP mathematical model and compared to the applied force (WOB) measured in the experiments as each parameter vary within a reasonable range. Alternatively, the applied force (WOB) expression presented below could be used directly.

Equation 27: The mathematical model is expressed in terms of WOB in a simplified form

$$WOB = \left[\left(\frac{C_a^{1/12} (t)^{9/8} (D_{avg})^{1/8} (\tan \frac{\alpha_o}{2})^{3/4}}{G_1 S_a^{1/4}} \right) \left(\frac{(ROP) \left[\frac{\pi}{2} - \arcsin \left(1 - \frac{\delta}{A} \right) \right]^{1/8}}{S} \right) \left(\frac{H_v^{3/2} K_{IC}^{1/2} (1 - \nu^2)^{1/4}}{E^{7/8}} \right) \right]^{8/9}$$

$$\text{Where } G_1 = \frac{K C_2^2}{180 C_1^{1/8}}$$

8.1. Volume Proportionality Parameter K

K value was assumed in previous work to be independent of input variables and to be constant for a given workpiece. For a workpiece of alumina for K was found to be, $K = 0.295$ (D. Liu et. al, 2012). The mathematical model developed in Chapter 6 of this discussion also assumed a constant value for K for each type of rock. K was found to be independent of all input variables as shown in the tests' results of all experiments conducted since it vary slightly around an average value.

Figure 137, Figure 139 and Figure 141 **Error! Reference source not found.** show values of K that would be required in order to have the model match the WOB data for same test. K remained approximately unchanged, with average value of K = 1.2, 0.92, and 0.64 for marble, travertine and basalt respectively. Average K values over tested parameters with error margins are shown in Figure 138, Figure 140, and Figure 142. As discussed in Chapter 6, K was obtained as the volume proportionality between theoretical and actual volume: $V = K V_o$

8.1.1. Volume Proportionality K for Marble

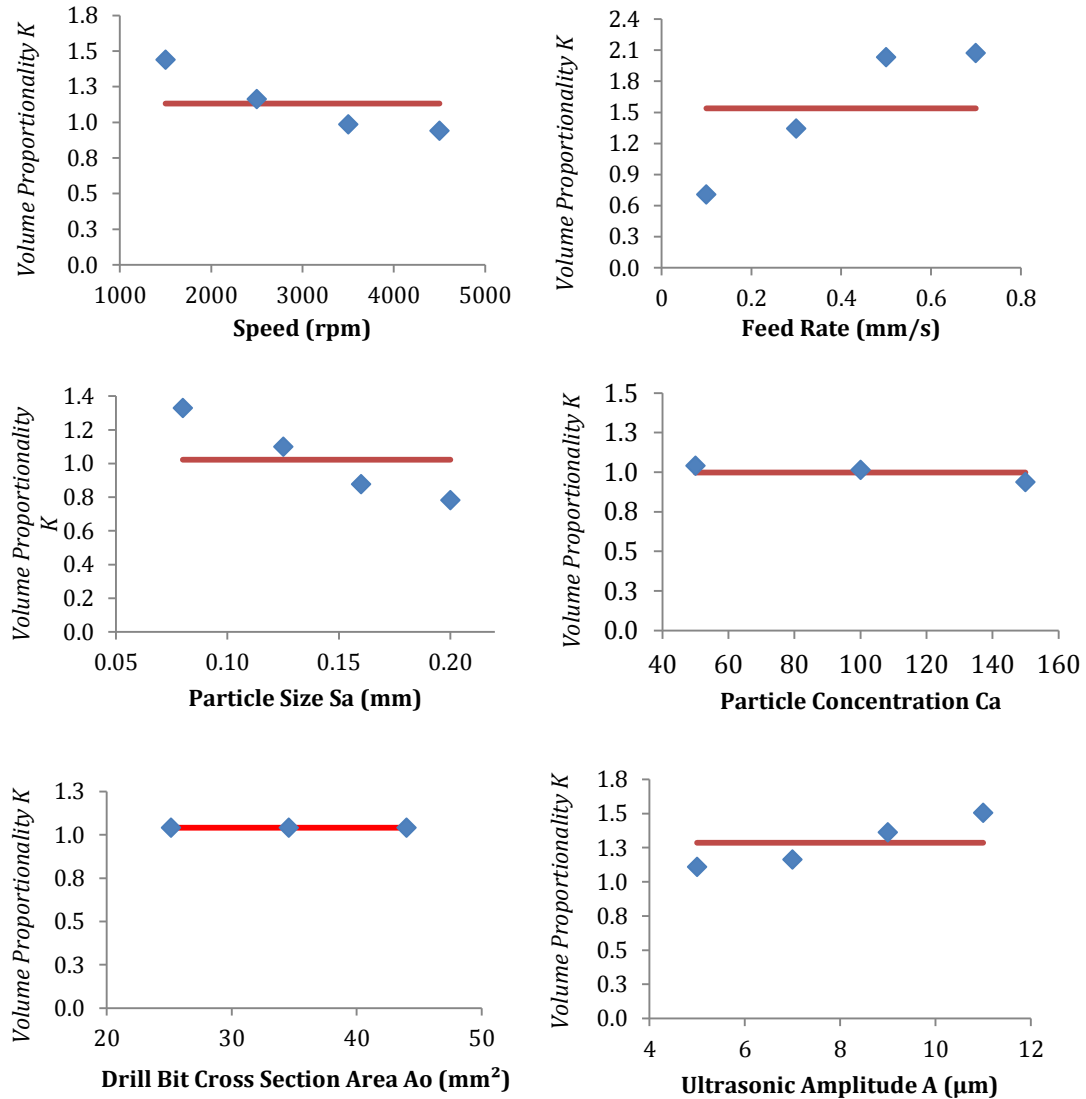


Figure 137: Volume proportionality K for marble for various parameters

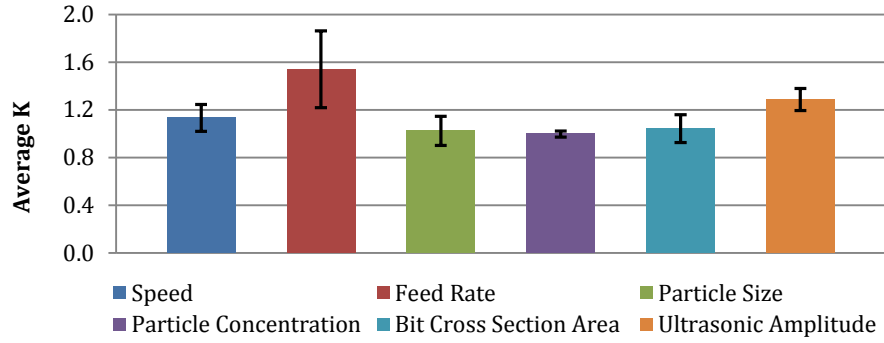


Figure 138: Average K for marble

8.1.2. Volume Proportionality K for Travertine

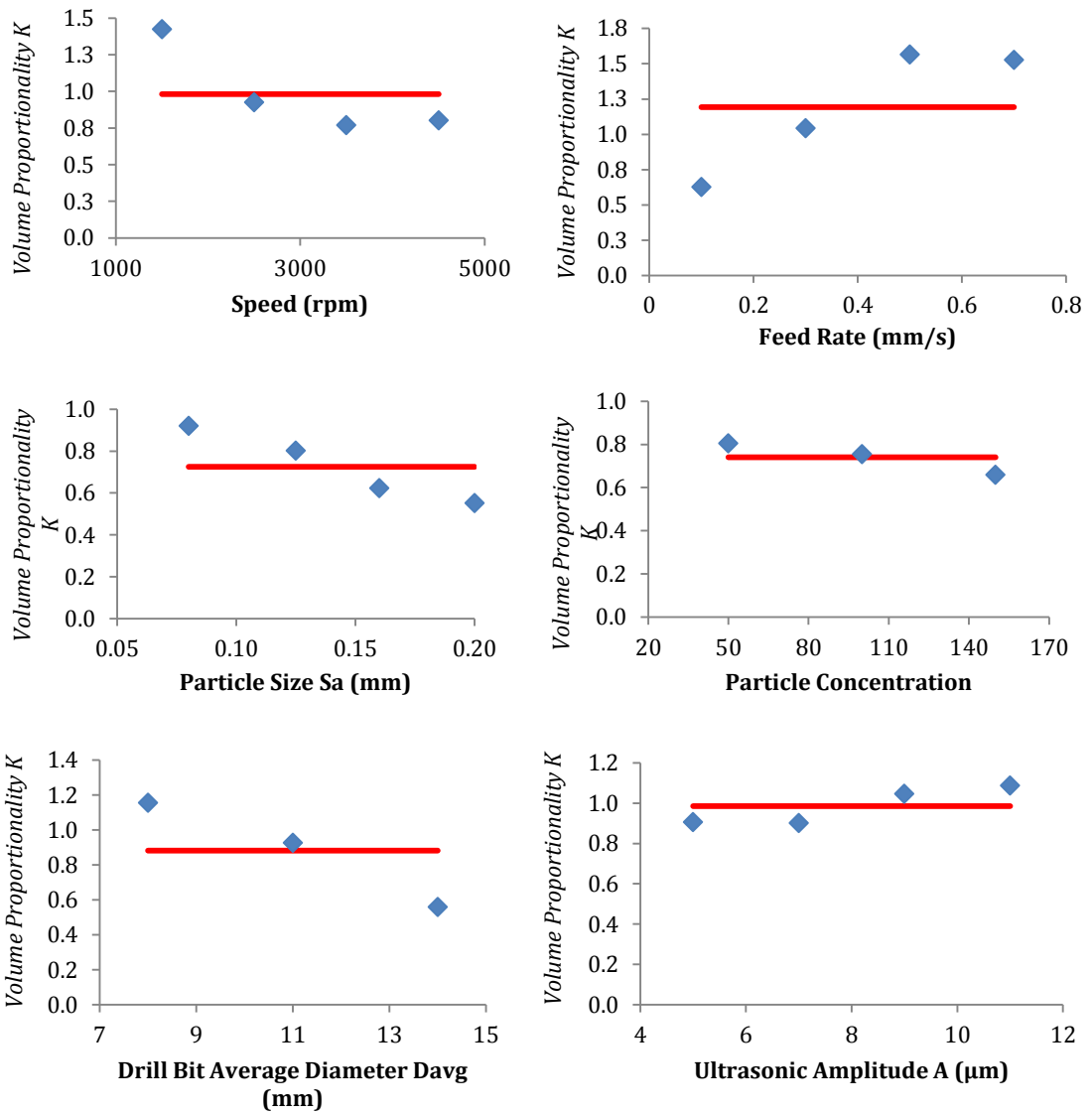


Figure 139: Volume proportionality K for travertine for various parameters

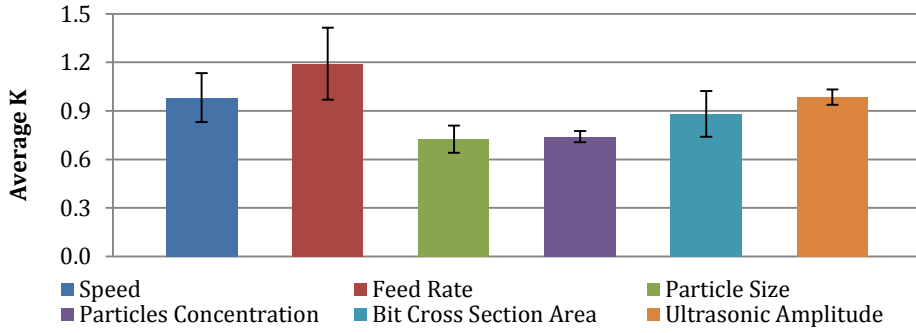


Figure 140: Average K for travertine

8.1.3. Volume Proportionality K for Basalt

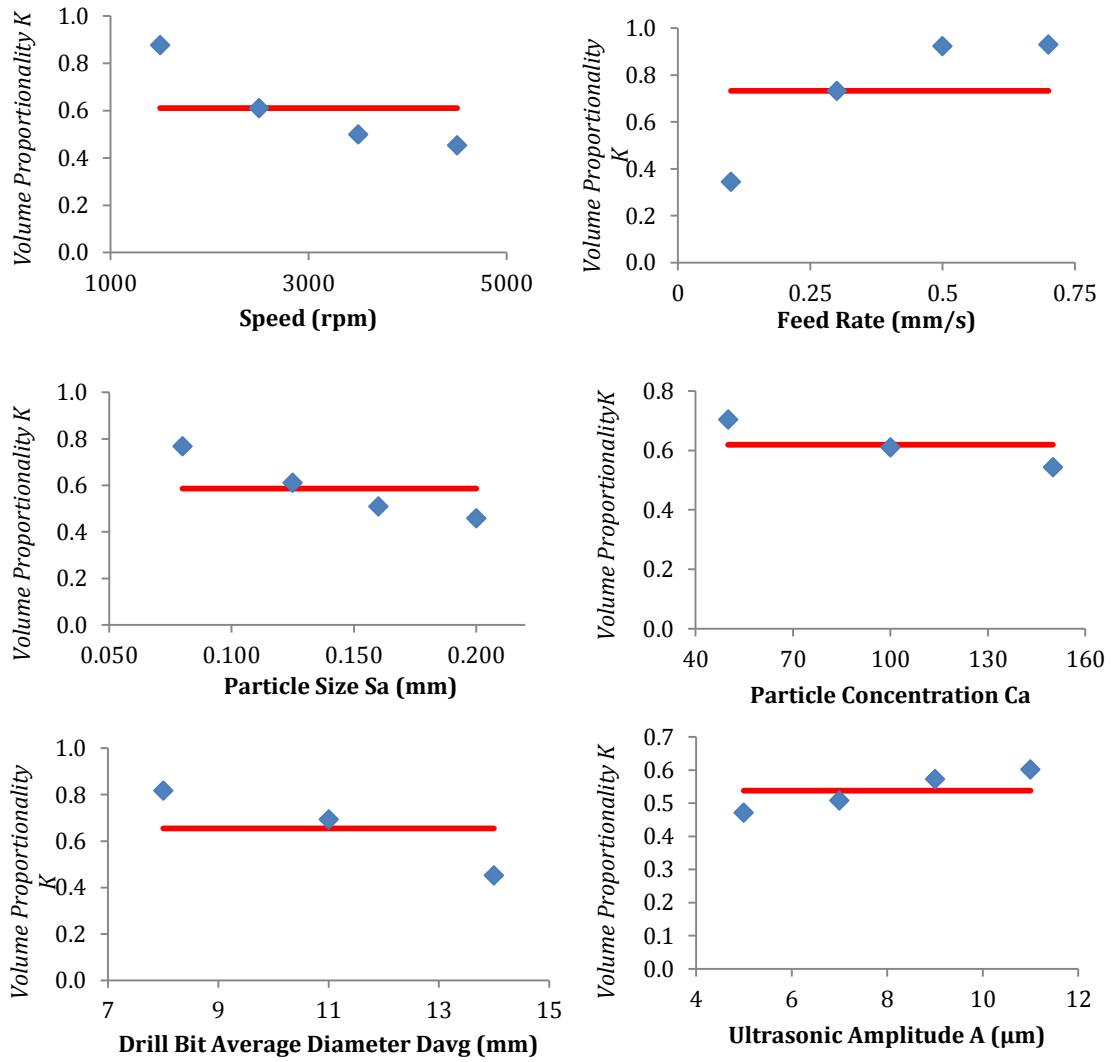


Figure 141: Volume proportionality K for Basalt for various parameters

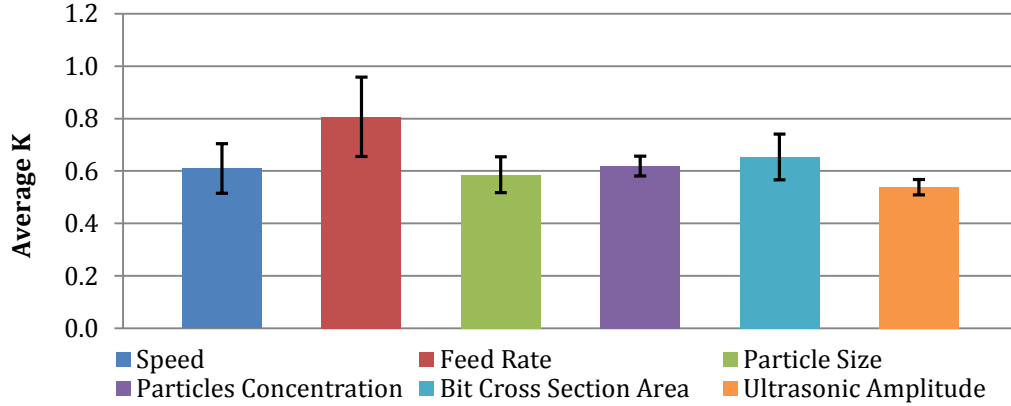


Figure 142: Average K for basalt

As shown above that K varied slightly for each workpiece, namely marble, travertine and basalt, using all data generated from experiments. The reason behind the variation is the highly probable overlapped damaged zone generated from each abrasive particle and its neighboring particles. In support of this claim the distance between abrasive particles is evaluated based on the abrasive particle size S_a , abrasive particles concentration C_a , and the number of particles N_a within the cross section area of the cutting surface A_o as follow:

Let the distance between two particles be dp

$$N_a = C_1 \left(\frac{C_a^{2/3} A_o}{S_a^2} \right)$$

$$\frac{A_o}{N_a} = \left(\frac{S_a^2}{C_1 C_a^{2/3}} \right)$$

$$d_p = \sqrt{\frac{A_o}{N_a}} = \sqrt{\frac{S_a^2}{C_1 C_a^{2/3}}} = \frac{1}{\sqrt{C_1}} \left(\frac{S_a}{C_a^{1/3}} \right)$$

The distance between two particles from center to center, dp , is compared to the two halves of the two particles that adds up to one particle size S_a . As shown in the plots Figure 143 - Figure 145 that the distance between two particles is slightly larger than the size of one particle which is a very good indication that the volume removed could possibly overlap at times. The x-axis in the three plots is set for the variation of S_a , C_a , and A_o . The overlap is expressed in terms of the volume proportionality K explained in details previously.

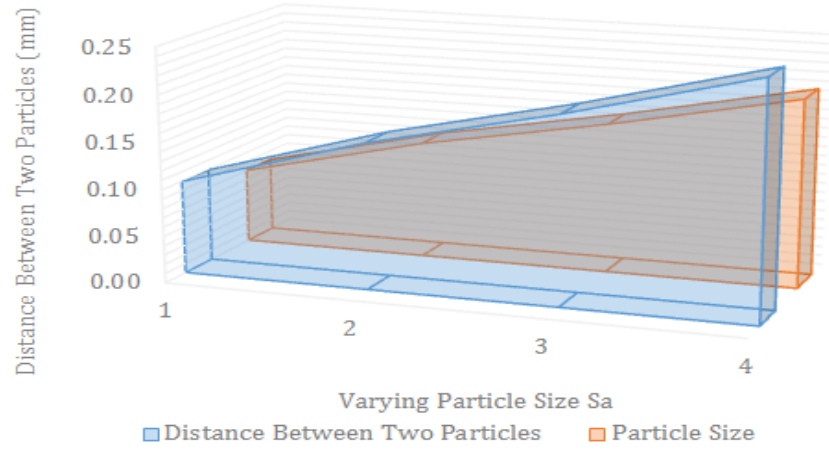


Figure 143: Distance between two particles compared to particle size as the particle size vary

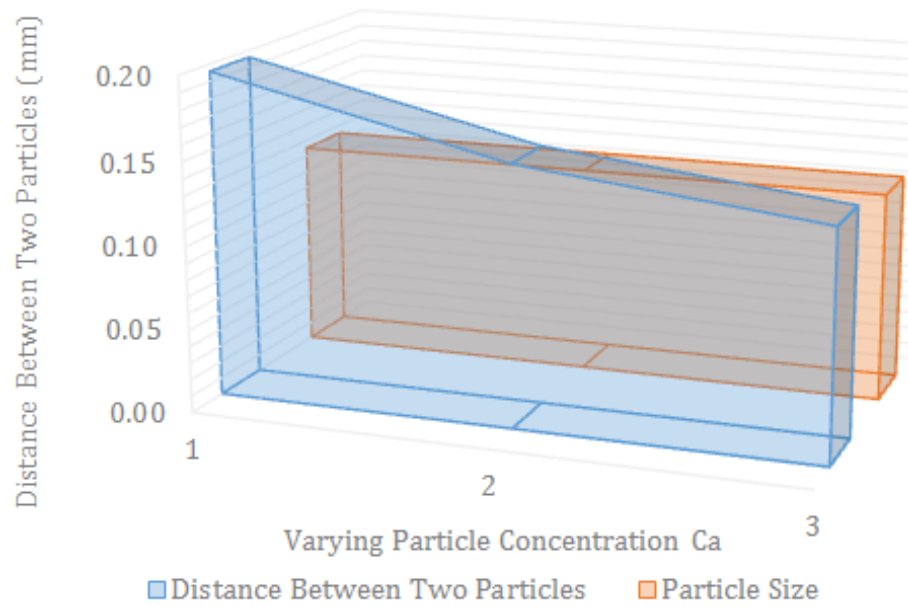


Figure 144: Distance between two particles compared to particle size as the particles concentration vary

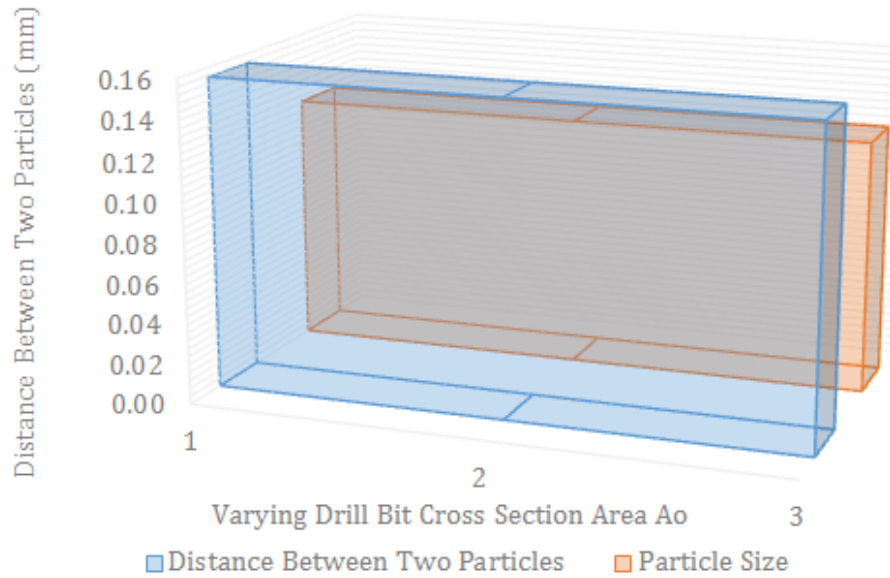


Figure 145: Distance between two particles compared to particle size as the drill bit cross section area vary

8.2. Core Drill Bit Parameters Change Effect on WOB

8.2.1. Drill Bit Outside and Inside Diameters / Drill Bit Cross Section Area (A_o)

The mathematical model developed for ROP is applied in determining the effect of the change in the drill bit outer and inner diameter (D_o and D_i) on the WOB performance. As the drill bit diameters varied, the thickness remained constant at $t = 1.0$ mm and nominal values applied to the rest of the parameters as mentioned previously predicting the effect results.

Predicted Effect:

The predicted results show that the change in the drill bit outer and inner diameters has little effect on the ROP performance. The analytical model plot below shows the slight increase in the WOB as the drill bit diameter increases for the three different types of rocks (Figure 146). Three average diameters were used: 8 mm, 11 mm and 14 mm. The predicted WOB curves are plotted in Figure 146. As shown in the mathematical model that it predicts WOB to be proportional to $(D_{avg})^{1/9}$ where little change in WOB is predicted (Equation 27).

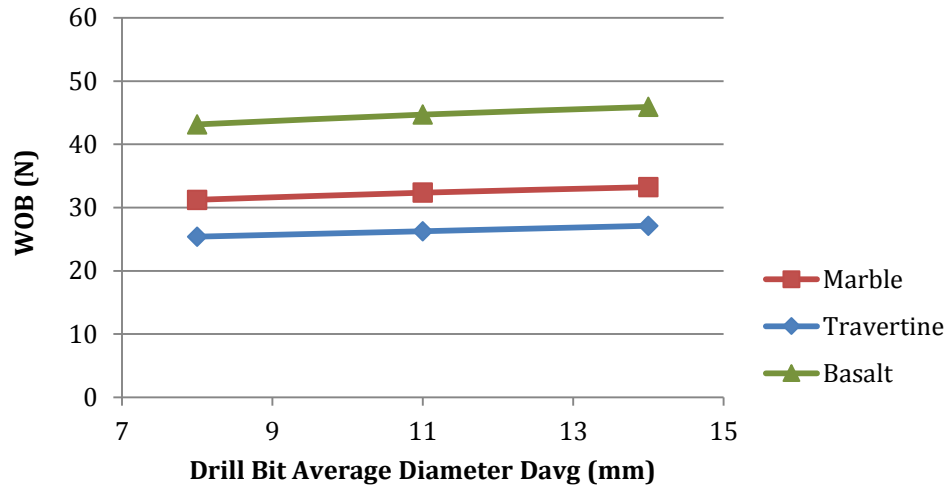


Figure 146: Predicted effect of drill bit diameters on WOB

Experimental Effect:

The experimental results show an increase in the force when the average diameter increases for the three types of rocks (Figure 147).

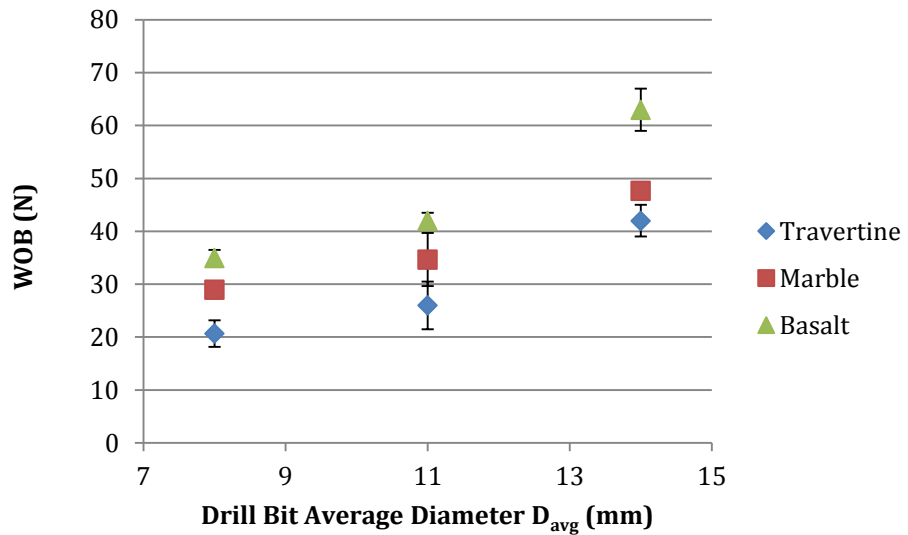


Figure 147: Experimental results of drill bit diameters on cutting force/WOB

The model captures the general trend of increasing WOB with increasing average diameter, but predicts a smaller change than is found in the data.

8.2.2. Abrasive Particles Size (S_a)

The mathematical model developed for ROP is applied in determining the effect of the change in the abrasive particle size S_a on the ROP performance. As the abrasive particle size varied between 80 – 200 μm , the nominal values applied to the rest of the parameters as mentioned previously predicting the effect results.

Predicted Effect:

The predicted results show that an increase in the abrasive particle size should cause the WOB to decrease. The model predicts WOB is proportional to $S_a^{-2/9}$ see Figure 148.

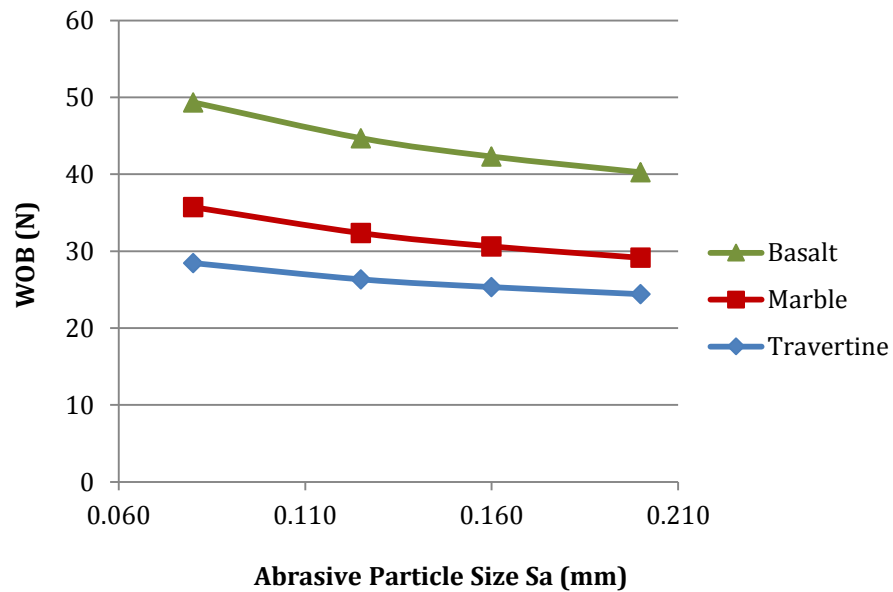


Figure 148: Predicted effect of abrasive particle size on WOB

Experimental Effect:

The experimental results show an increase in the WOB as the abrasive particle size S_a for the three types of rocks (Figure 149).

This result is different from the developed model that shows decrease in WOB as S_a increases. Therefore, the change in the abrasive particle size parameter's effect on the ROP performance is not well presented by the developed model. The model does not capture the observed effect for this parameter.

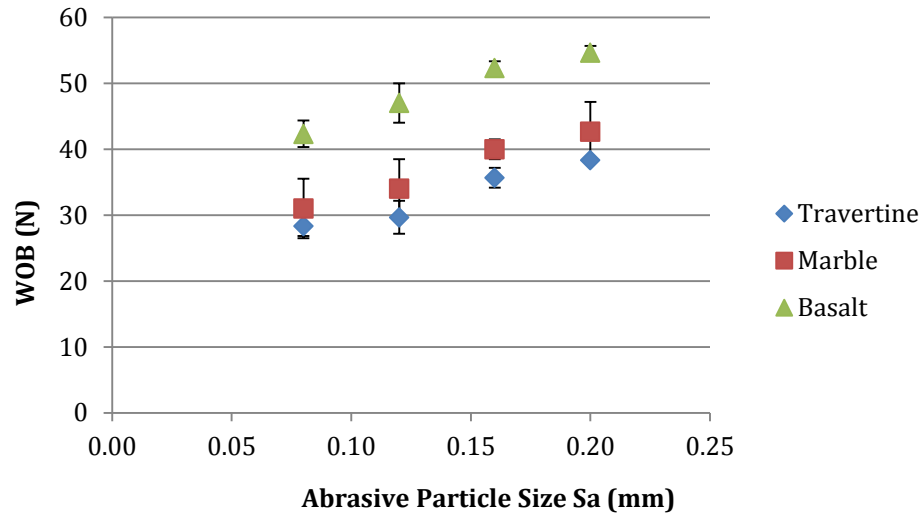


Figure 149: Experimental results of the abrasive particle size effect on cutting force/WOB

8.2.3. Abrasive Particles Concentration (C_a)

The mathematical model developed for ROP is applied in determining the effect of the change in the abrasive particle concentration C_a on the WOB applied. As the abrasive particle concentration varied between 50 and 150, the nominal values applied to the rest of the parameters as mentioned previously predicting the effect results.

Predicted Effect:

The predicted results show that the increase in the abrasive particle concentration has little effect were WOB is proportional to $C_a^{2/27}$ as shown for the three different types of rocks (Figure 150).

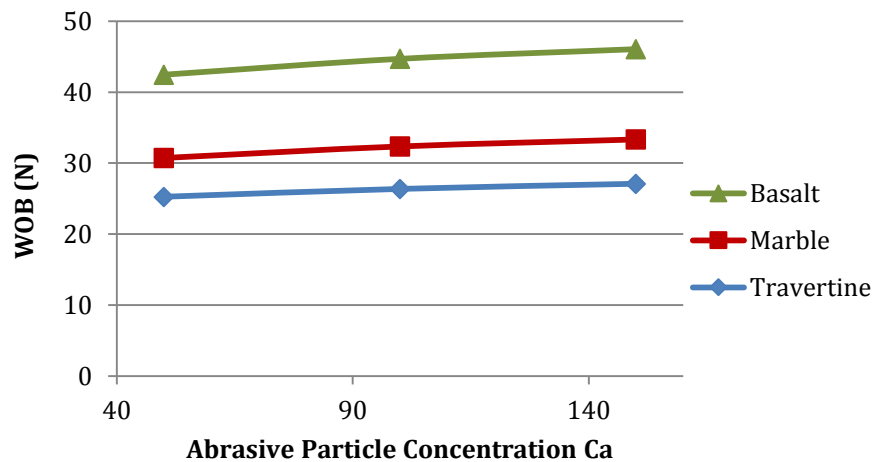


Figure 150: Predicted effect of abrasive particle concentration on WOB

Experimental Effect:

The experimental results show a moderate increase in the WOB as a result to the increase in the abrasive particle concentration for the values of 50, 100 and 150 for the three types of rocks (Figure 151).

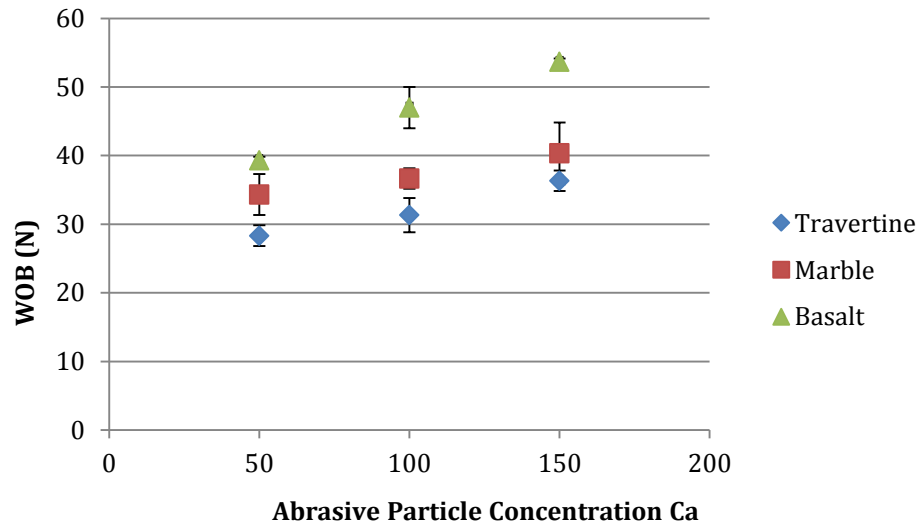


Figure 151: Experimental results of the abrasive particle concentration effect on cutting force/WOB

The model shows the same trend as the data in the performance of the abrasive particle concentration.

8.3. Process Parameter Change Effect on WOB

The effect of the process parameters such as WOB and spindle speed on the ROP performance are investigated where the predicted results are compared to the experimental results with an objective of validating the developed ROP mathematical model.

8.3.1. Rate of Penetration (ROP)

Predicted Effect:

The model predicts results show that the change in the feed rate ROP results in a significant increase in WOB as it is predicted to be proportional to $ROP^{8/9}$ as shown in Figure 152. As the applied feed rate increased from 0.1 to 0.7 mm/s the WOB increased corresponding to the rock strength.

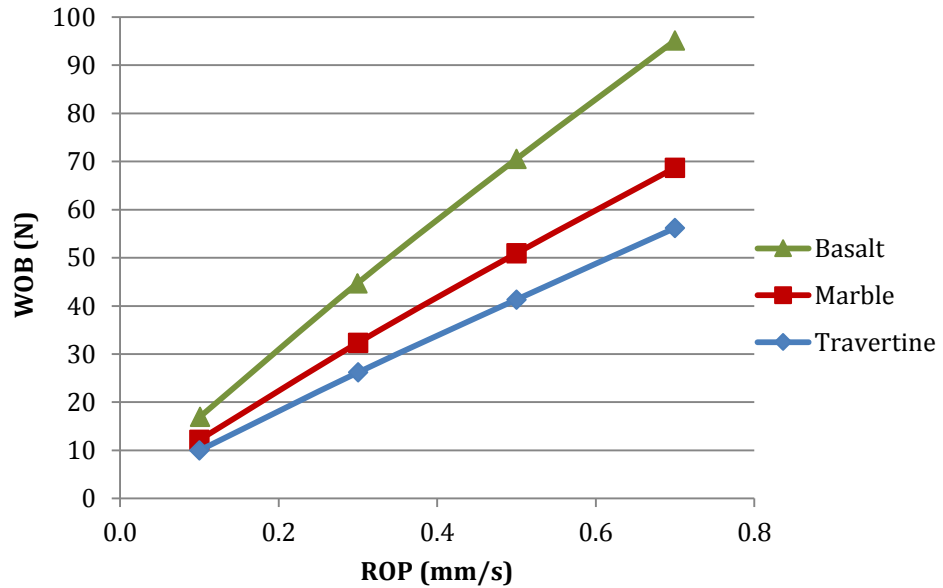


Figure 152: Predicted effect of applied force on ROP performance for basalt rock

Experimental Effect:

The experimental results show significant increase in the force applied as a result to the increase in the rate of feed rate (ROP) for the same values (0.1, 0.3, 0.5, and 0.7 mm/s) for the three types of rocks (Figure 153).

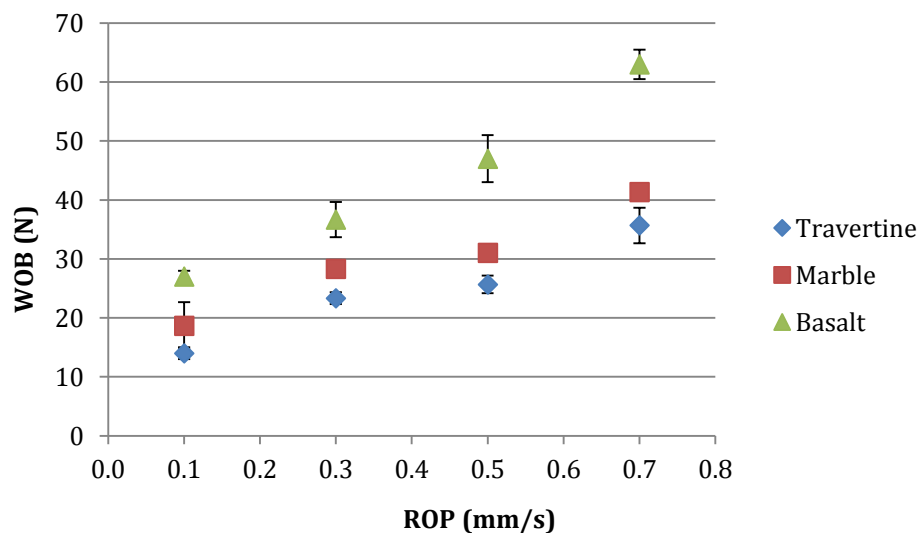


Figure 153: Experimental results of the feed rate/ROP effect on cutting force/WOB

As shown above, that the model represents the trend in the ROP performance shown in the experimental data. The difference in the slopes of

the experimental results compared with the model could be a result of the rotary ultrasonic drill machine operation that requires manual setup of the feed rate applied. The manual setup utilizes a dial gauge and a timer to specify the desired feed rate. The human error participate in this process has an effect on the slightly different resulted slopes between the model and the experiments.

8.3.2. Speed (S)

The mathematical model developed for ROP is applied in determining the effect of the change of the spindle speed on the WOB applied. As the spindle speed varied between 1500 and 4500 rpm, the nominal values applied to the rest of the parameters as mentioned previously predicting the effect results on WOB.

Predicted Effect:

The predicted results show that the increase in the spindle speed should cause significant decrease in the WOB (WOB scales as $S^{-9/8}$) for the three different types of rocks (Figure 154).

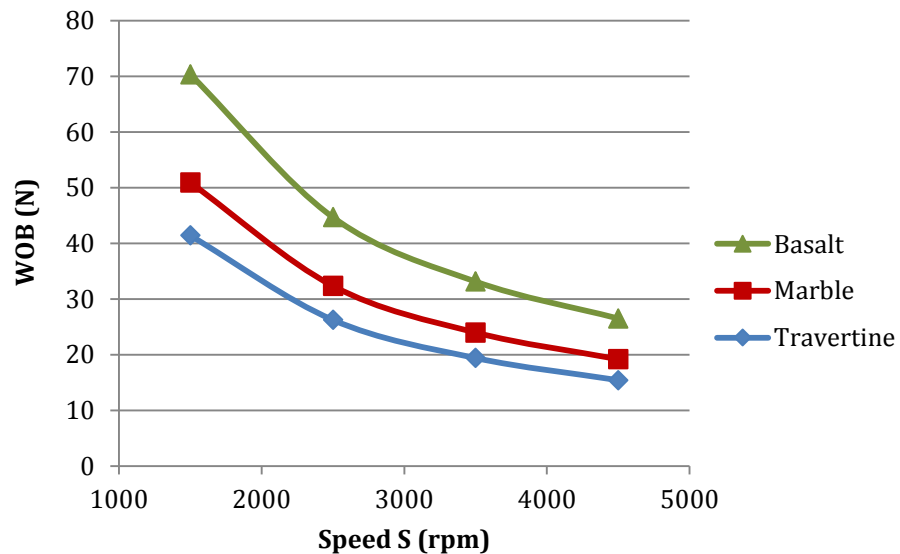


Figure 154: Predicted effect of spindle speed on WOB

Experimental Effect:

The experimental results also show significant decrease in the WOB as a result to the increase in the spindle speed for the three types of rocks (Figure 153).

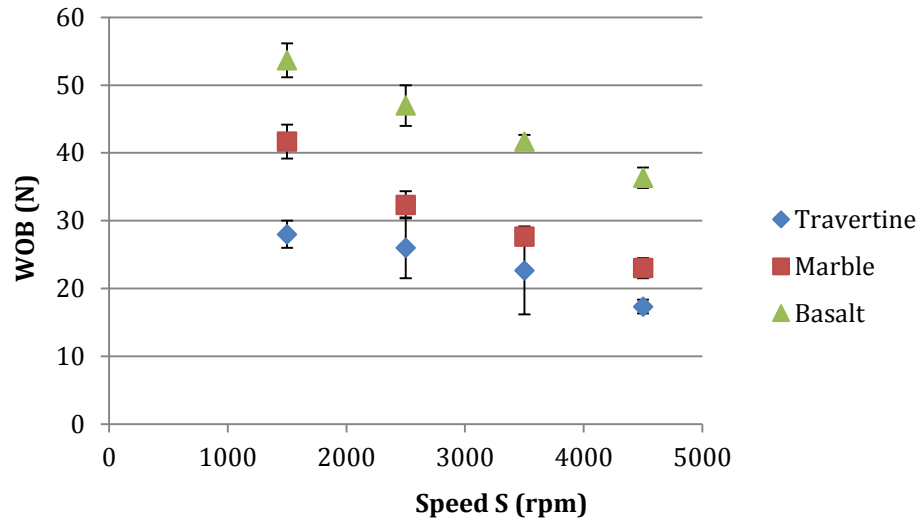


Figure 155: Experimental results of the speed effect on cutting force/WOB

These results show that the model is in general agreement with the experimental results for the spindle speed performance and its effect.

8.3.3. Ultrasonic Amplitude (A)

The effect of the ultrasonic wave parameters such as amplitude and frequency on the WOB performance are investigated where the predicted results are compared to the experimental results with the objective of validating the developed mathematical model. Furthermore, the model suggest no dependence on ultrasonic frequency f_u and only amplitude variable is considered in this study.

The mathematical model developed for ROP is applied in determining the effect of the change of the ultrasonic wave amplitude on the WOB performance. As the amplitude varied between 5 – 11 μm , the nominal values applied to the rest of the parameters as mentioned previously predicting the effect results.

Predicted Effect:

The predicted results show that the change in the ultrasonic wave amplitude should have little effect on the applied WOB for the three different types of rocks (Figure 156).

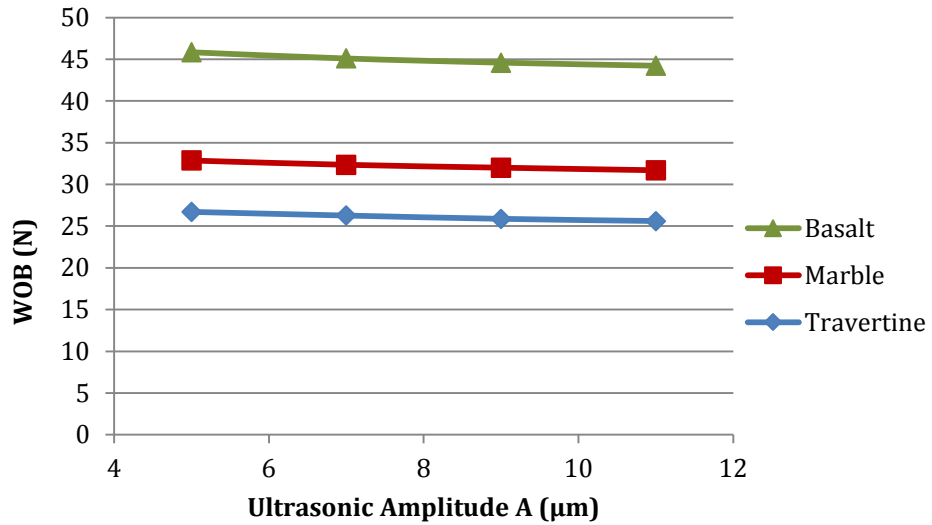


Figure 156: Predicted effect of ultrasonic wave amplitude on ROP performance for basalt rock

Experimental Effect:

The experimental results show a more substantial decrease in the force applied as a result of the increase in the ultrasonic wave amplitude also from 5 – 11 µm for the three types of rocks (Figure 157).

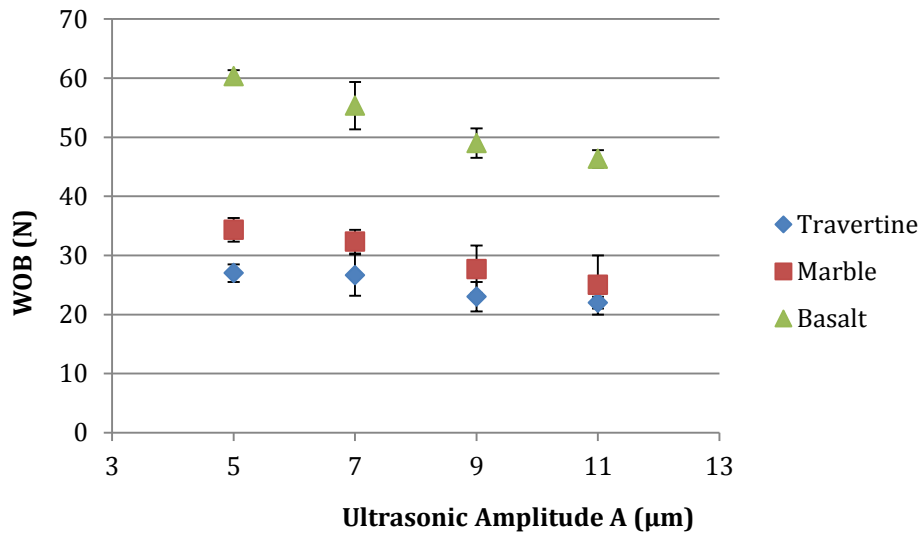


Figure 157: Experimental results of the ultrasonic wave amplitude effect on cutting force/WOB

The mathematical model results agree on the sense of the effect due to an increase in ultrasonic amplitude, but not on the magnitude.

8.4. Summary

The mathematical model showed promising results of predicting the WOB performance as the input parameters change using the same drill bit on the three different types of rocks that varied in strength. This examined further in Chapter 9.

Chapter 9

9. Conclusion and Future Work

Drilling on Mars is a huge engineering challenge. Previous research shows that drilling under simulated Martian conditions is, for many reasons, very different from drilling under terrestrial conditions. As researchers conducted their investigations under Martian conditions, they found that Mars has environmental and technological constraints and examining them led to many discoveries, which otherwise would have remained unnoticed.

9.1. Challenges of Drilling on Mars and Future Missions Requirements

Previous missions revealed that the extreme environmental condition on Mars such as low temperature, low pressure, geology variation, thermal flux, and water content impose constraints on the drilling process, as well as significant constraints on drill bit design. Also, technological constraints impose limitations on the drilling process, including such essential elements as drilling power and energy. As a result, and due to the aforementioned constraints, drilling on Mars is a challenging task and experiments are critical for thorough investigation in determining the drilling performance under Mars conditions.

The past missions to Mars revealed that the surface is totally sterilized and there is no evidence of life on the surface. Also, the results from Curiosity mission suggested the ultimate engineering challenge, which is drilling six meters deep in the red planet in search for life. This depth was determined by Curiosity scientists to ensure avoiding the effect of radiation on living organisms at lesser depths. Achieving such a depth utilizing the current drilling techniques (rotary or rotary percussive drilling) might be impossible due to their limitations. Although, rotary percussive drilling showed a much higher performance than rotary drilling alone, it has thus far been limited to a drilling depth of a few centimeters. Therefore, the search for a new drilling technique capable of reaching a greater depth than past missions, and higher rate of penetration, is critical for the success of future missions searching for life on Mars.

This research investigates rotary ultrasonic drilling as an alternative technique for use brittle materials. This approach is predicted to have a higher performance compared to currently used drilling techniques. The study presented in this dissertation focused on developing a mathematical model of the rate of penetration (ROP) using rotary ultrasonic drilling, identifying all parameters involved in drilling, and finally predicting the different parameters' effect on drilling performance. Drilling experiments on three different types of rocks that vary in strength from low strength rock such as travertine, a medium strength rock such as marble and very hard rock such as basalt were conducted. Predicted results from

the mathematical model were validated by comparing them to the experimental results.

Although there have been models of Rotary Ultrasonic Machining (RUM), they mostly focused on predicting material removal rate (MRR) or investigating material removal mechanism. A few focused on predicting the cutting force model for RUM of ductile materials. At present, no publications are available on rate of penetration model for RUM of brittle materials. Therefore, to optimize the drilling input variables, it was necessary to develop a model for ROP performance for RUM of brittle materials.

9.2. Drilling Parameters and Their Effect on Rate of Penetration Performance

The mathematical model for the rate of penetration (ROP) was developed by analyzing a single abrasive particle as the basic component of cutting by a diamond impregnated drill bit. The ROP model was derived by summing up all forces exerted by all diamond particles taking part in cutting, following earlier work involving cutting force models of variety of abrasive particles (Zhang, Zhang, & Feng, 2013).

It is important to point out the key assumptions made in developing the mathematical model: 1) All workpieces used in this study are ideal brittle materials. Therefore, the brittle fracture removal mechanism applies to the removed materials on the workpiece surface in brittle fracture mode (F. Zhang, 2004, Arif M, et al, 2011), 2) All diamond particles in a drill bit cross section are taking part in cutting, and 3) All diamond particles are rigid, with octahedral shape of the same size with equal side length for the twelve sides.

In this research a mathematical model of ROP was developed using rotary ultrasonic drilling. The model contained process parameters, drill bit design parameters, an ultrasonic parameter and material parameters. This research investigated the effect of the drilling parameters appearing in the mathematical model for ROP performance. Drilling parameters based on the drilling process such as WOB and spindle head speed, parameters based on the drill bit design such as drill bit inner and outer diameters, abrasive particle size, and abrasive particles concentration, and finally an ultrasonic parameter such as the ultrasonic amplitude are the parameters were investigated in this study. The aforementioned parameters varied within an acceptable range and the mathematical model was used to show the predicted results.

A set of experiments was conducted on three different types of rocks that varied in strength: travertine, marble and basalt. In the experiments, the same drilling parameters in the mathematical model were varied showing the effect of each one of them on the drilling performance expressed as WOB. Finally, predicted results were compared with the experimental results in the efforts of validating the mathematical model expressed previously and presented again below ([Equation 25](#)).

$$ROP = G_1 \left(\frac{S_a^{1/4}}{C_a^{1/12} (t)^{9/8} (D_{avg})^{1/8} \left(\tan \frac{\alpha_o}{2}\right)^{3/4}} \right) \left(\frac{S (WOB)^{9/8}}{\left[\frac{\pi}{2} - \arcsin\left(1 - \frac{\delta}{A}\right)\right]^{1/8}} \right) \left(\frac{E^{7/8}}{H_v^{3/2} K_{IC}^{1/2} (1 - \nu^2)^{1/4}} \right)$$

Drill bit design
Process design
Material Property

9.3. Predicted Versus Experimental Results

The rotary ultrasonic drill used in these experiments is designed to use the feed rate as an input parameter providing the applied WOB on the workpiece as the measured output parameter. Therefore, and according to the above ROP expression, the mathematical model is validated by holding ROP constant and determining the applied WOB while holding the other parameters constant at nominal values. The determined WOB from the model is compared to the cutting force obtained in the experiments. This process is repeated as one variable at a time changes determining the effect it has on the cutting force. Using the same drill bit, the drilling was conducted in cutting through three different types of rocks with varied strength. The results show general agreement with the mathematical model developed except for the abrasive particle size as it was explained previously.

The Figure 158 - Figure 160 show a set of plots for each type of rock providing a direct comparison between the model and experimental results of each input parameter. Plots were generated for each type of rock using same range of values in both model and experiments.

9.3.1. Results for Basalt

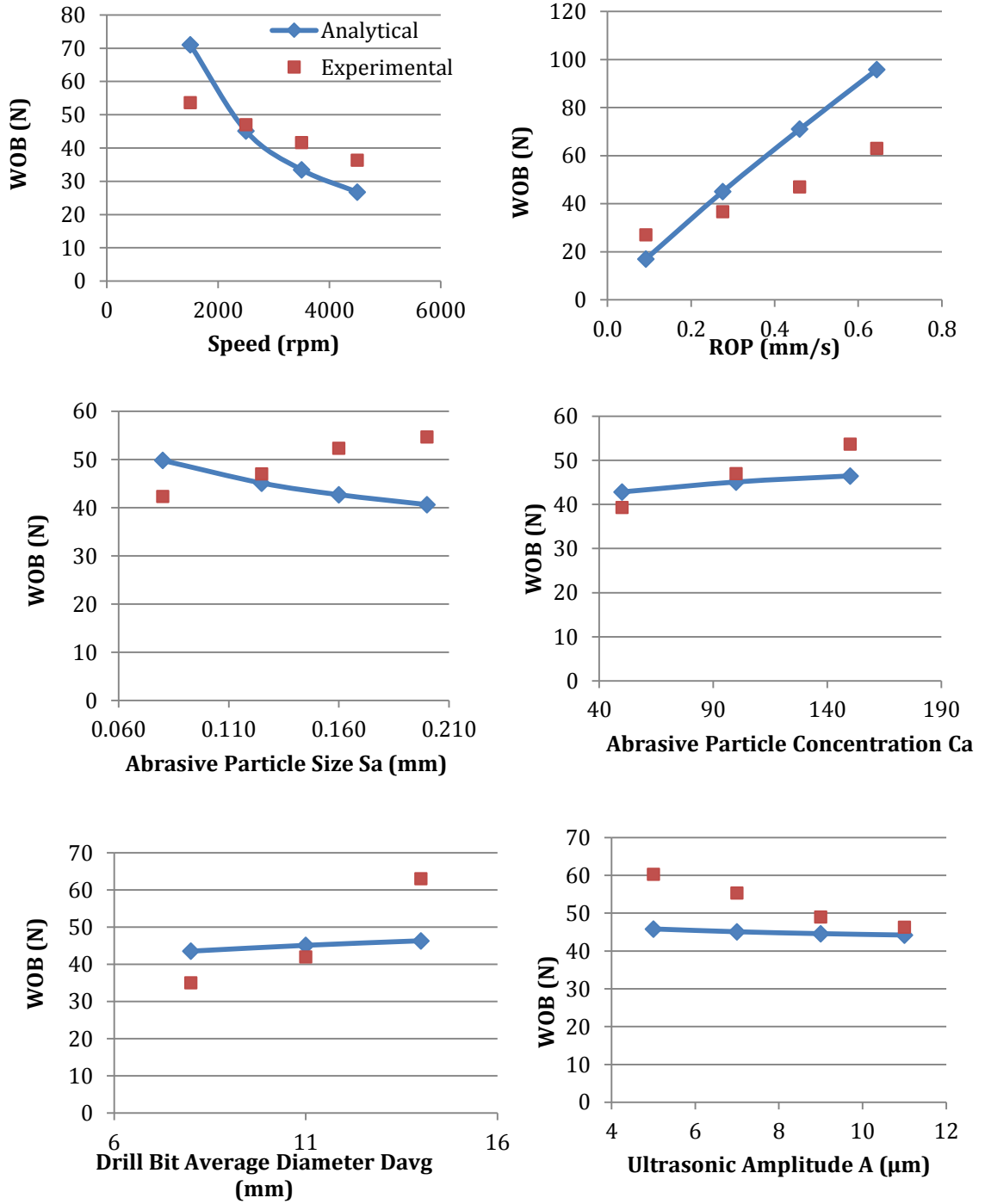


Figure 158: Mathematical model validation of RUM parameters effect on WOB performance for basalt

9.3.2. Results for Marble

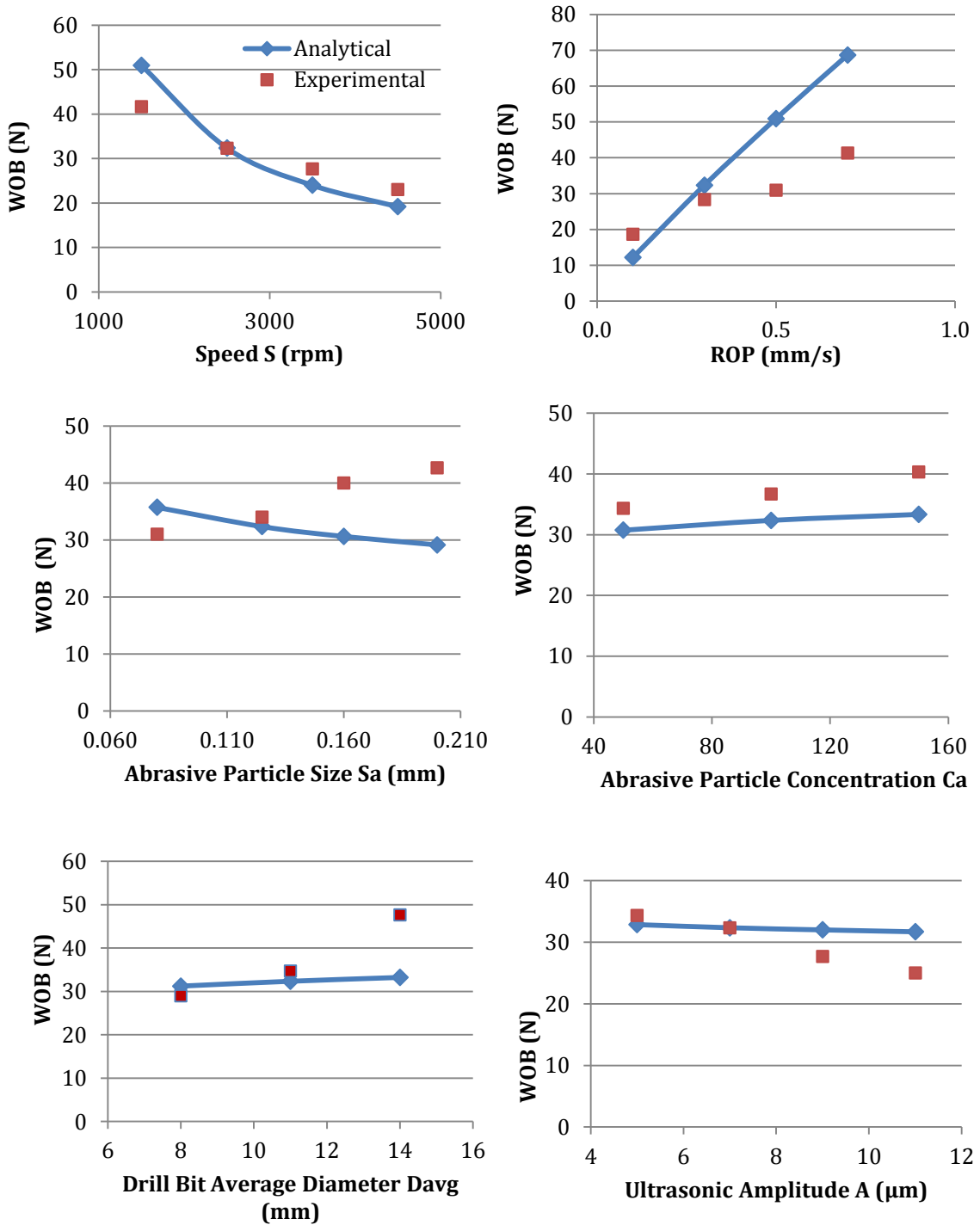


Figure 159: Mathematical model validation of RUM parameters effect on WOB performance for marble

9.3.3. Results for Travertine

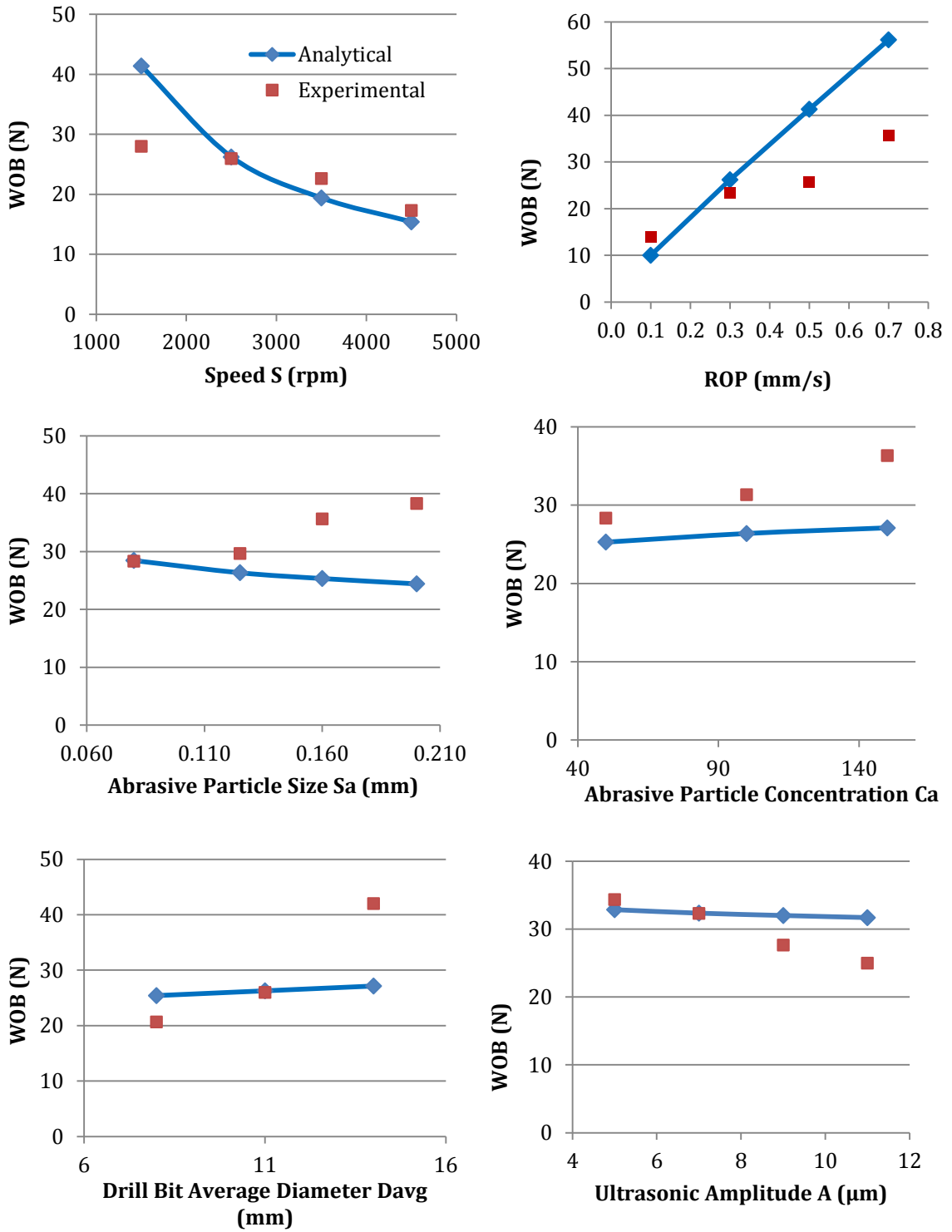


Figure 160: Mathematical model validation of RUM parameters effect on WOB performance for travertine

The model is found to agree in general with the experimental results for all input parameters performance with the exception of the abrasive particle size. Both model and experiments agree in the trends generated yet the values agree within an acceptable range of error that could be explained by the assumptions made developing the model.

9.4. Discussion

The following is a discussion of the results obtained as the following parameters were investigated:

9.4.1. Speed (S)

The predicted results agreed with experimental results showing that as the speed increased, the applied cutting force decreased. The decrease in cutting force as the speed increases while cutting through three different types of rocks was proportional to the material properties that varied in strength.

Although the model shows the same trend, it shows different values at above and below the nominal speed value of 2500 rpm. The reason for this difference is usually related to the method by which the volume proportionality K was determined. It is evident that the value of predicted speed matches the experimental results very accurately because K was determined at the nominal values of all parameters, including speed. The rest of the values, however, show a pattern of being larger of speed less the nominal and smaller for speeds that are larger than the nominal. As K remains constant for those values the WOB value drift away from the model.

9.4.2. Feed Rate / ROP

The cutting force is an output parameter in the RUM used in this research. Therefore, the feed rate is used as an input parameter where it varied showing its effect on the output parameter of the cutting force. The experimental results agreed with the predicted results showing that as the feed rate/ROP increased the cutting force increased as well linearly. The increase in cutting force as the feed rate increases while cutting through three different types of rocks varied and it is proportional to the rock strength.

Again the value of the model matches very closely the experimental results at the nominal value. The model result was lower than the experimental values at ROP lower than the nominal value and larger at ROP larger than the nominal value. Again, the reason is the use of constant value of volume

proportionality K may actually vary slightly than rather being an exact constant value as it was explained previously.

9.4.3. Particle Size (S_a)

Four sizes of the abrasive particles were used in these experiments showing the effect of the change of size on the cutting force. The experimental results showed a different trend from the results of the mathematical model. The predicted results showed that as the abrasive particle size increases, the cutting force decreases while the experiments showed an increase in cutting force. The decrease in cutting force in the model and the increase in the experimental results as the abrasive particle increases while cutting through three different types of rocks.

9.4.4. Particle Concentration (C_a)

Three different abrasive particle concentrations were used in this study. The experimental results agreed with the predicted results closely, showing that as the abrasive particles concentrations increases the cutting force also increases. The increase in cutting force as the abrasive particle concentration increases while cutting through three different types of rocks varied.

9.4.5. Drill Bit Cross Section Area (A_o)

The change in the drill bit cross section area is achieved by varying the drill bit inner and outer diameter size. Three different sizes were used in this research. The experimental results agreed with the predicted results showing that as the drill bit inner and outer diameters change, maintaining same thickness throughout the experiments, the cutting force increased linearly. The increase in cutting force as the drill bit inner and outer diameter increase while cutting through three different types of rocks varied.

9.4.6. Ultrasonic Amplitude (A)

The ultrasonic amplitude is one of the input variables of the RUM and it was easily adjusted as desired through changing the power applied to operate the drill. In this study, the ultrasonic amplitude changed showing its effect on the cutting force. The experimental results generally agreed with the predicted results showing that the increase of the ultrasonic amplitude decreases the cutting force. The decrease in cutting force as the ultrasonic amplitude increases while cutting through three different types of rocks varied.

9.5. Direction of Future Research

Although the trends of the predicted results are consistent with the experimental results with the exception of the abrasive particle size, not all parameters showed significant effects that are worth optimization. For example, the change in cutting force as a result to the change of the abrasive particle concentration, drill bit outer and inner diameters, and ultrasonic amplitude were relatively small and had very little effect on the drill performance. Therefore, the parameters that showed significant effect on the WOB performance such as the change of the spindle speed and the feed rate (ROP) are considered for future investigation of drilling input parameter optimization.

This research is significant to NASA's future missions to Mars. It provides a mathematical model of a new drilling mechanism with high potential for better performance than traditional and well known techniques of rotary and rotary percussive drilling. The data provided in this research will be utilized for comparison to other drilling techniques in the efforts of determining whether or not it has a better performance, higher ROP and better surface quality where it will be considered for the drilling mechanism of future missions to Mars.

The main goal motivating this research is to find a new drilling technique in brittle materials that is capable of achieving greater depth drilling on Mars than ever before. While previous missions drilled in a few centimeters, the latest mission revealed that it is critical to drill to the much greater depth of six meters. The current drilling technology, at the present time, is not capable of reaching such depth and new drilling mechanism ought to be investigated. This study provides a first step in this investigation by examining a new drilling technique in search for more efficient method than the conventional ones. The developed mathematical model coupled with the experimental data will be utilized to compare the drilling performance, primarily in ambient condition, to the currently drilling technique used on Mars, rotary percussive drilling. The rotary percussive drilling performance is well documented and performance comparison will be conducted in the effort to determine the most efficient drilling technique for future Mars missions and whether or not the RUM technique is the drilling method of the future space exploration.

As previously mentioned, drilling under simulated Martian conditions is significantly different from drilling under terrestrial conditions for many reasons. Therefore, it is essential to consider future research investigating drill performance using RUM under simulated Martian conditions. Rotary percussive drilling performance under simulated Martian condition is also well documented and it will be used for performance comparison with the model and data developed in this research.

The ROP mathematical model developed in this research coupled with the experimental data are significant first step in making comparison between drilling techniques determining the drilling mechanism of the future. Additional research will be conducted in optimizing the drilling input parameters under simulated

Martian condition that is capable of drilling through more variety of rock types that are closely emulating the types or rocks presence on Mars.

Conducting future experiments that ensure the consideration of all variations of the input parameters, Mars condition, process limitation, energy source, WOB limitations, and the drill bit design limitation will accurately provide reliable results and a robust model for the future drilling missions to Mars.

Chapter 10

10. Education: Activity Design Utilizing Knowledge Integration

The knowledge integration process in learning science has been investigated in numerous literature involving more than 40 case studies of middle school students (Clark & Linn, 2003; Linn & Hsi, 2000). It was concluded that students generate a repertoire of ideas about concepts they are learning as well as links between the concepts. The learner view of a concept is referred to as an “idea” and they report their ideas based on experiences. Learners also add new ideas from instruction, experience, or social interactions. This process is followed by sorting out these ideas in varied contexts, making connections between ideas on multiple levels of analysis, developing criteria for evaluating ideas, and finally formulating an increasingly linked set of views about any phenomenon.

The knowledge integration perspective capitalizes on the students pool of ideas, both individually and collectively, to stimulate science learning promoting coherent and cohesive understanding. In this chapter, knowledge integration is utilized to offer guidance to engage students in the research topic of drilling on Mars, including questions such as why and how do we drill on Mars and how do we communicate with instruments placed on Mars surface. The process helps students participate with their own ideas of what they know about planets, solar system formation, and the similarity Mars has with our planet Earth. Students will be given the opportunity to add more ideas, such as why we need to drill on Mars. Furthermore, students will learn how this goal could be achieved and why is it important, which allows them to sort out their ideas and form a coherent concept of the validity to drill on Mars (Figure 161).

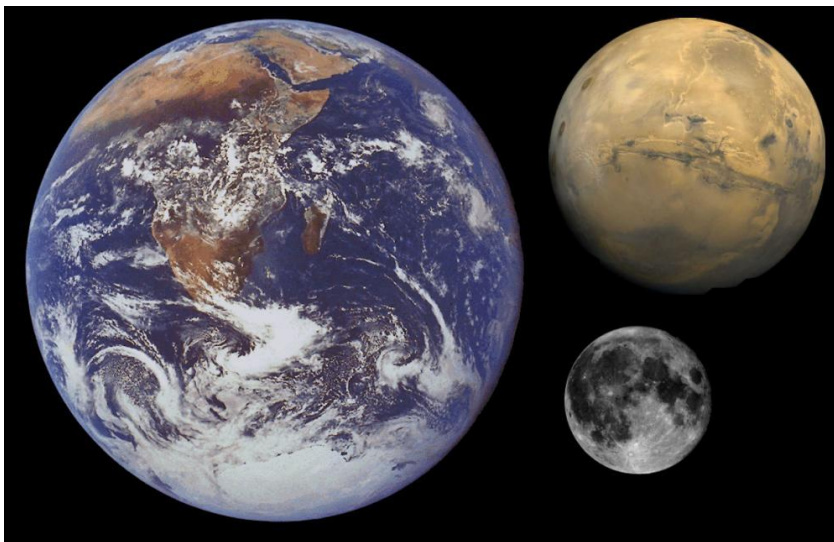


Figure 161: Size comparison between Earth, Mars and the Moon,
http://www.astro.virginia.edu/class/skrutskie/images/mars_earth_moon.jpg

10.1. Eliciting and Building on a Repertoire of Ideas

Literature shows that students in the science classroom use evidence to sort out the ideas they initially elicited. They compare, analyze, and critique various ideas whether they were their own or presented by others. Students shows the capability of generating mechanisms in order to justify the logic behind an idea they have, and they are also capable of providing evidence.

As the beginning of this activity, the students are asked a series of questions that allow them to draw from their repertoire of ideas of what they know about our solar system formation and particularly Mars with comparison to our planet Earth.

1) What do you know about our planet Earth?

This question is designed to help students share all they know about planet Earth and will be specifically guided with a series of additional questions leading to the correct answers provided. In the process, some comparisons and clues might be offered. The goal is to help students characterize the elements of “life” that makes our planet Earth habitable.

a) How did our planet Earth form?

The collisions in a giant disc-shaped cloud of materials about 4.6 billion years ago formed our early solar system as the gravity slowly gathered the gas and dust together into clumps.

b) What is the size of Earth?

Earth’s radius is 3,959 miles or 6,371 km.

c) What do you know about Earth’s layers?

The following is the detailed answer to this question:

List Earth characteristic that you know and you see in the picture. Students will be guided to think critically and share what they have learned about planet Earth’s layers: inner core, outer core, mantel and crust (Figure 163).

A new idea, Earth’s recycled crust, which is essential for life existence will be introduced. As humans deplete life resources on the Earth’s surface, it is important that the surface to be “stirred” and a new layer exposed with new resources to continue the life support process. Plate tectonics take on this role (Figure 162).

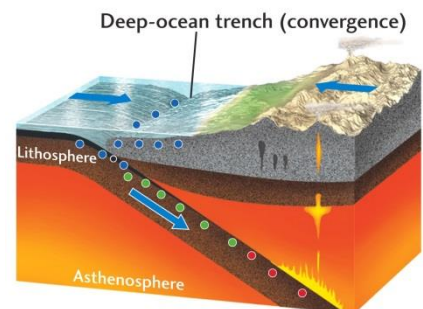


Figure 162: <http://bc.outcrop.org/images/earthquakes/press4e/figure-19-13b.jpg>

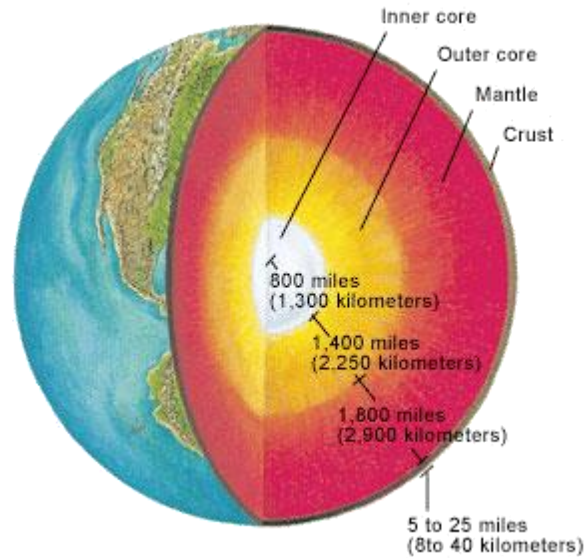


Figure 163: Earth structure, http://upload.wikimedia.org/wikipedia/en/1/1b/Earth_layers_NASA.png

d) What do you know about Earth's magnetic field?

Earth's magnetic field is generated by the motion of molten iron alloys in the Earth's outer core. The magnetic field protects Earth from the sun's charged particles of the solar wind (Figure 164).

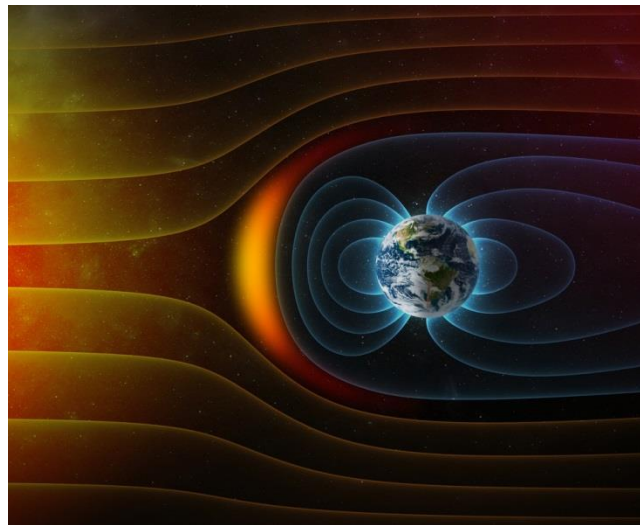


Figure 164: Earth's magnetic field, <http://www.todayifoundout.com/wp-content/uploads/2014/04/magnetic-field-earth.jpg>

2) What do you know about Mars? What are the similarities and differences between Mars and Earth?

List Mars characteristic that you know and you see in Figure 165. Students will be guided to make comparisons between the Earth and Mar's images of

layers leading to the fact that both, Earth and Mars, were formed from the same giant cloud gas and dust of the same materials. They might observe that they both have a crust and a molten metal core. However, students will be guided to also recognize the difference or be introduced to them such as: Mars does not spin and it has no magnetic field / exposed to sun's radiation. This information leads to the major take away point, which is exposure to radiation sterilizes Mars surface and eliminates all forms of life (Figure 165).

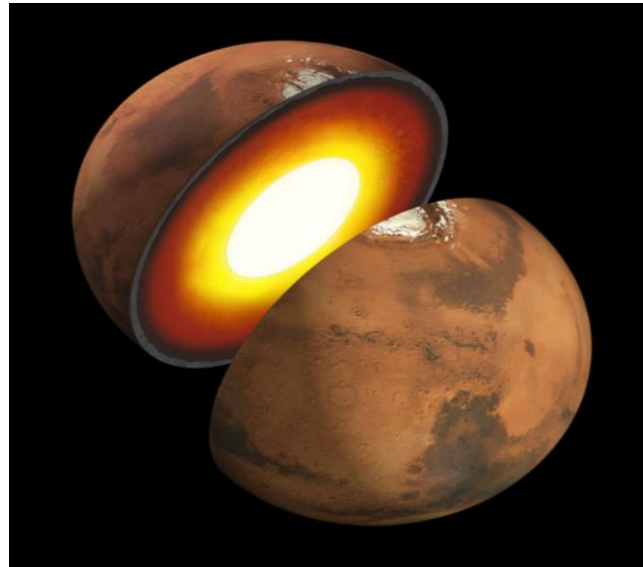


Figure 165: Planet Mars, http://i.dailymail.co.uk/i/pix/2012/08/21/article-2191399-14A3025500005DC-839_964x1035.jpg

10.2. Adding New Ideas

Knowledge integration is often provoked by instruction that adds new normative ideas. Studies show that students prefer adding ideas over distinguishing and comparing ideas. Therefore, designers need to find ideas that simulate reconsideration of the students' current views, which is an approach applied in this research activity. It was found that when students isolate the normative ideas, instead of connecting them to existing ideas, the new ideas are quickly forgotten (Eylon, & Linn, 1988). The knowledge integration perspective collectively considers these research findings in order to define pivotal cases as new ideas that are added to the students' repertoire of ideas that lead to more cohesive and normative understanding.

The characteristics of those pivotal cases are that they allow student to a) make a compelling and scientifically valid comparison between two situations, b) draw on accessible and culturally relevant contexts, such as everyday experiences, c) provide feedback that supports their efforts in developing criteria and monitoring their progress, and d) encourage students to create narrative accounts of their ideas using precise vocabulary so they are able to discuss them with others.

Based on the aforementioned characteristics, students will be asked a series of questions in order to stimulate their “added on” ideas with a relevant connections to their existing ideas of what they know about planet Earth. How they can identify the elements of life as we know it in order to compare it to Mars? Once they make this comparison, they will be able to determine the method needed to prove whether or not life existed on Mars.

- 1) What are the main features on planet Earth?

Based on what you know about the planet Earth and list all the features you see that characterize the planet and set it apart from the other planets (Figure 166).



Figure 166: Planet Earth, <http://images-gededah.in/wp-content/uploads/5517167-planet-earth-isolated.jpg>

- 2) Did water ever exist on Mars? Justify your answer?

This question is designed to point out the main element of the existence of life as we know it. In order to determine whether or not life existed on another planet, only our frame of reference of life as we know it here on Earth can apply to make this determination. Therefore, identifying “water” as the basic element for life to exist is the key point here that will guide students to try to determine whether or not water exists, or existed, on Mars in order for life also to exist.

- 3) Does water now exist on planet Mars?

Students will draw from their previous knowledge of Mars and what they know about the latest NASA’s missions. The Phoenix mission in 2008 was particularly sent to Mars in search of water and it was able to identify water’s existence in ice form. However, students will be asked if this is sufficient

evidence to conclude that life exists on Mars. This question will lead students to think of “other” elements that are required in order for life to exist.

- 4) What planet Mars would look like if it has water?

The following is the artist perspective of planet Mars if it has water. This illustration closes the gap of differences between Earth and Mars where the similarity of both planets if Mars were to have water suggests a high probability of life existence (Figure 167).

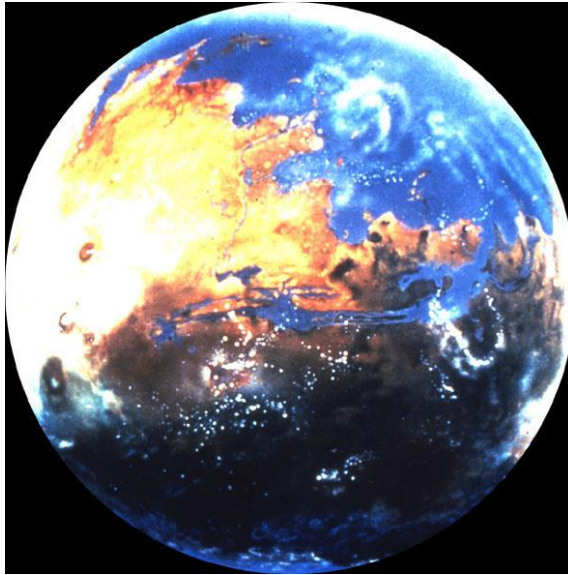


Figure 167: Artist perspective of Planet Mars if it has water,
<http://www.lpi.usra.edu/education/timeline/gallery/images/019.jpg>

- 5) List your observation of the image below and state what activities formed those channels.

This image shows gullies formed on Mars, suggesting previously existing liquid water. Students should connect the feature of this image to their knowledge of our dry rivers and water channels on Earth, which leads to creating a new idea of possible water existence on Mars in a liquid form (Figure 168).

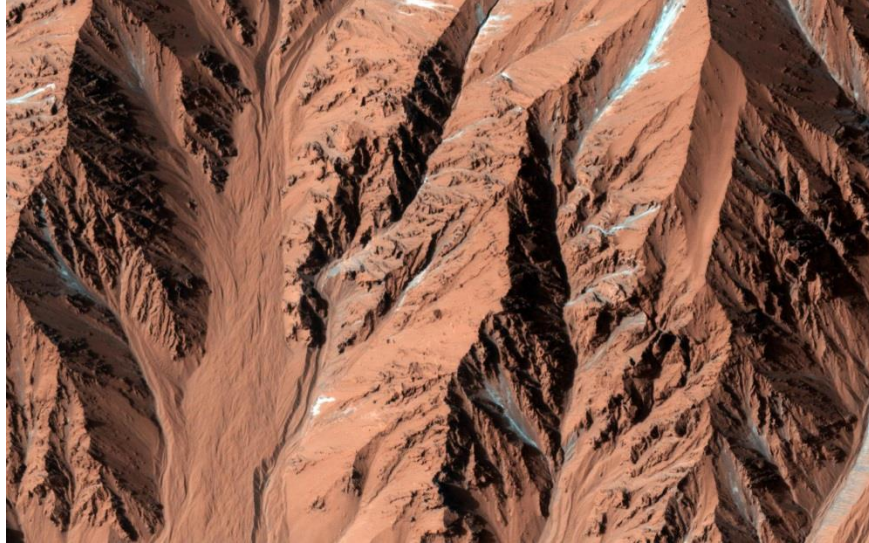


Figure 168: Gullies on Mars, <http://www.desktopexchange.net/plog-content/images/space-pictures/mars-wallpapers/fresh-crater-with-gullies.jpg>

6) What happened that may have destroyed life on Mars, had it existed?

As the students may arrive to the high probability of life existence on Mars due to the presence of water in a liquid form, as well as other critical elements such as oxygen, hydrogen and carbon, the next logical question is what destroyed life on Mars if it once existed? Note: students will learn that previous missions proved the presence of other elements that are critical for life as we know it to exist such as carbon, phosphate, oxygen, hydrogen, and nitrogen. Students, as well as scientists today, don't know the answer to such questions. However, in order to answer this question, a justification of the question's importance has to be presented in this series of questions:

- a) Since Mars and Earth are alike, could the cause of possible life destruction happen also on Earth in the future?
- b) Is it preventable? If so, how can we prevent it?

Those questions will pave the way to the importance of determining whether or not life existed on Mars in the first place before investigating what had destroyed it. It stresses the fact that this investigation of examining Mars' history is life preserving approach. The more we learn about Mars the more we may understand our own planet's future better that may be heading to the same destination of Mars. The revelation signifies the purpose of this research to answer the question, "Did life exist on Mars?"

- 7) If the surface is sterilized, where could we possibly search for life on Mars?
- a) Inside rocks: rocks provide protection to organic materials
 - b) Below the surface

Once students arrive to these two locations where organic materials might exist, the next logical question is “how to get there” that has direct and logical answer that is “drilling”. Drilling on Mars surface opens a wide door for numerous ideas that students might have not experienced before such as, how can a drill be sent to Mars?; How can we control it from Earth?; What are we searching for exactly? And many more questions likely are stemming from their rich imaginations. The focus of this activity is to introduce the students to this new outer space environment and how different it is from Earth. Tasks conducted on planet Mars are significantly different from same tasks conducted on Earth due to its extreme environment.

- 8) Let’s drill on Mars to search for life

Students’ creativity of adding on new ideas could be simulated with a series of questions such as, since previous missions were able to locate all elements of life as we know it, what form of life exactly are we looking for? This question leads to introducing students the ideas of the presence of bacteria and organic materials that are evidence of life.

- a) How do we send a drill to Mars?
- b) How do we drill remotely on Mars?

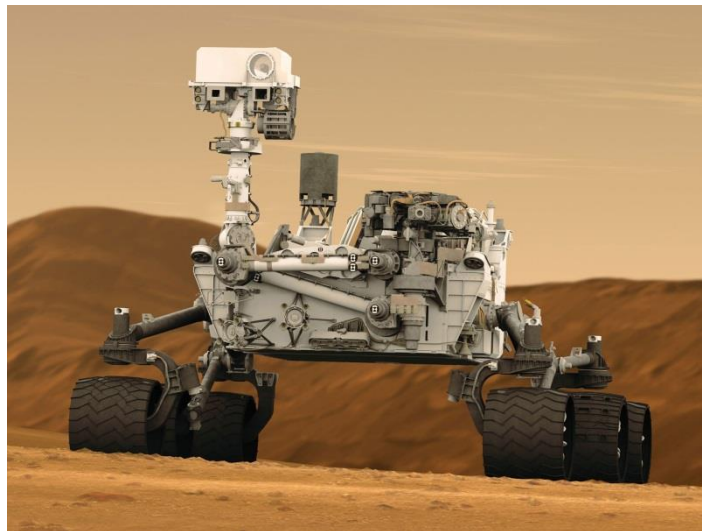


Figure 169: Mars Curiosity,
http://mars.jpl.nasa.gov/msl/images/msl20110526_MSL_Artist_Concept_PIA14165-full.jpg

While some students might have the knowledge of Rovers and Landers, this question land the opportunity to share more with them in more details the Lander and/or Rover capabilities and how they get to accomplish missions' objectives (Figure 169). Starting out with the introduction of the rover functionality and listing the components presence onboard the spacecraft and their purpose/function: camera, drill, instrumentation, electronics, sensors, and test instruments.

- c) How instruments are controlled remotely? Airplane remote control example:

A very close example that illustrates the communication system between Earth and Mars is the remote controlled airplane (Figure 170). It is a familiar object that some of the students may have even owned and they know how it works. Allowing the students to compare and contrast between the two systems will help them connect their new ideas with their existing ones. Literature shows us that taking on this approach will allow students to build a cohesive and coherent understand of how a scientific phenomenon work.



Figure 170: Remote controlled plane, <http://rc.org.uk/images/CoxEasyFlyer.jpg>

Supported by the previous example, the communication system between planet Earth and planet Mars will be further explored emphasizing on the differences between the two systems. In order to stimulate the students and get them engaged in suggesting how the system works, an illustrating image such as the one shown in Figure 171 will be presented to assist students in making inferences. The goal in this part of the activity is for the students to learn that communication takes place through satellites and there is a significant delay due to the vast distance. They will also learn that the

communication signals travel at the speed of light, which means that it will take between 3 and 22 minutes for the information to reach the other end.

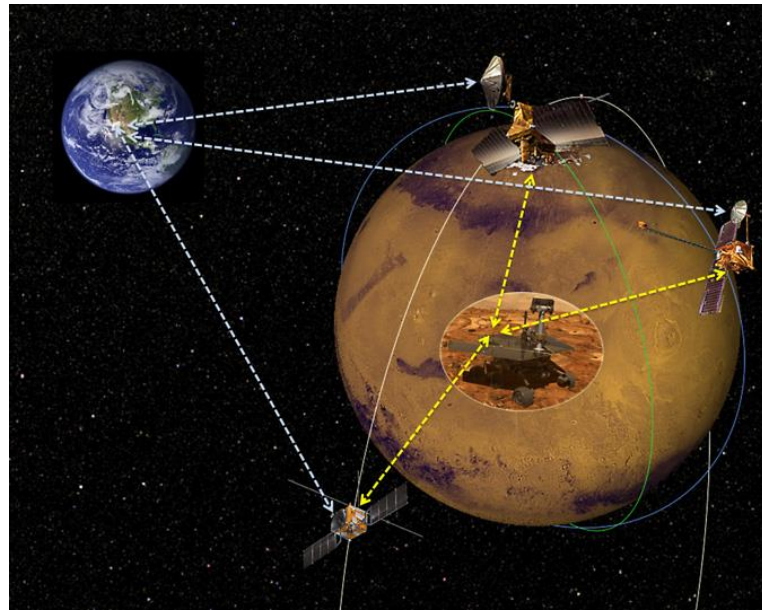


Figure 171: Communication system between Earth and Mars, <http://planete-mars.com/wp-content/uploads/2014/07/mars20140723-full.jpg>

10.3. Help Student Develop Criteria: Prediction vs. Observations

The instruction in this activity is designed to help students develop criteria to evaluate the many ideas they hold and encounter promoting cohesive understanding. Students have a variety of resources to obtain ideas from such as textbooks, internet, personal experiences, advertisements, experiments, teachers and peers. Students generally consider everything in the science text to be true. If the text is presented to them in scientific jargon, they are likely to trust it and consider it a fact. Those beliefs compel educators to discuss the limits of research methods and point out the level of uncertainty in research results. Doing so will allow the students to successfully evaluate ideas and develop criteria that combine knowledge of methods for investigation, understanding of techniques for studying difficult kinds of phenomena (such as cloning, design of new drugs, and earthquakes) and give them insight into the work of scientists. This process will help students develop criteria that integrate all their ideas to build a coherent understanding.

10.4. Sort Out Ideas

Instruction in this activity is based on helping students sort out their ideas and building strong connections between ideas, providing a foundation for future learning. As students apply their own criteria they distinguish levels of analysis, identify overlaps and gaps in their knowledge, resolve contradictions, and seek

connections (Bransford, Brown, & Cocking, 2000). Also, as they reflect, they may use their criteria to promote some ideas and demote others in the process of resolving contradictions. Students need to apply their limited energy to the most central task and monitor their progress in order to succeed. Instead, some students may resort to memorization to cope with the flood of information in science courses. They mostly memorize the information they expect on tests that is soon forgotten after taking the tests.

10.5. Develop Cohesive and Coherent Understanding of Mars Exploration

Knowledge integration provides the tools that allow students to participate, share their ideas through their life experience, and be open to new ones. It also encourages students to assess the ideas they shared or encountered and build their own criteria evaluating those ideas. As students learn about research, its limitations and level of uncertainty, they can assess the ideas they have objectively. They will be able to promote some and demote other ideas building a cohesive and coherent understanding.

Applying the above model of knowledge integration to the drilling on Mars activities will help students build a solid foundation about research, research limitation, space exploration, and elements of life as we know it, and how to communicate with other planets.

References:

- Aldrich, J., Sherrit, S., Badescu, M., Bar-Cohen, Y., Bao, X. and Chang, Z. (2006) Controller Using Extremum-Seeking to Drive Heavily Perturbed Electroactive Actuators at Resonance. NASA New Technology Report (NTR), Docket 43519, NASA.
- Arif M, Rahman M, San W, Doshi N (2011) An experimental approach to study the capability of end-milling for microcutting of glass. *Int J Adv Manuf Technol* 53(9):1063–1073
- Badescu, M., Sherrit, S., Bar-Cohen, Y., Bao, X. and Kassab, S. (2007) *Ultrasonic/Sonic Rotary-Hammer Drill (USRoHD)*. NTR Docket No. 44765, 19 December 2006. Patent application submitted 17 August 2007.
- Badescu, M., Sherrit, S., Olorunsola, A., Aldrich, J., Bao, X., Bar-Cohen, Y., Chang, Z., Doran, P.T., Fritsen, C.H., Kenig, F., McKay, C.P., Murray, A., Du, S., Peterson, T. and Song, T. (2006) Ultrasonic/sonic gopher for subsurface ice and brine sampling: analysis and fabrication challenges, and testing results. Proceedings of the SPIE Smart Structures and Materials Symposium, San Diego, CA, 27 February–2 March 2006, Paper 6171-07.
- Bao, X., Bar-Cohen, Y., Chang, Z., Dolgin, B.P., Sherrit, S., Pal, D.S., Du, S. and Peterson, T. (2003) Modeling and computer simulation of ultrasonic/sonic driller/corer (USDC). *IEEE Transactions on Ultrasonics, Ferroelectrics and Frequency, Control (UFFC)*, 50 (9), 1147–1160.
- Bao, X., Bar-Cohen, Y., Chang, Z., Sherrit, S. and Stark, R. (2004) *Ultrasonic/Sonic Impacting Penetrator (USIP)*. NASA New Technology Report (NTR), 22 December 2004, Docket No. 41666, NASA.
- Bar-Cohen, Y. (2005) *Biomimetics – Biologically Inspired Technologies*, CRC Press, Boca Raton, FL, pp. 1–527.
- Bar-Cohen, Y. and Sherrit, S. (2003) *Self-Mountable and Extractable Ultrasonic/Sonic Anchor (U/S-Anchor)*. NASA New Technology Report (NTR), 9 December 2003, Docket No. 40827, NASA.
- Bar-Cohen, Y., Randolph, J., Ritz, C., Cook, G., Bao, X. and Sherrit, S. (2002) Sample Preparation, Acquisition, Handling and Delivery (SPAHD) System using the Ultrasonic/Sonic Driller/Corer (USDC) with Interchangeable Bits. NASA New Technology Report (NTR), 1 May 2002, Docket No. 30640, NASA.
- Bar-Cohen, Y., Sherrit, S. and Herz, J.L. (2003) *Ultrasonic/Sonic Jackhammer (USJ)*. NASA New Technology Report (NTR), 31 October 2003, Docket No. 40771, NASA.

- Bar-Cohen, Y., Sherrit, S., Badescu, M., & Bao, X. (2012). Drilling, Coring, and Sampling Using Piezoelectric Actuated Mechanisms: From the USDC to a Piezo-Rotary-Hammer Drill. *Earth and Space 2012*, (818). Retrieved from <http://ascelibrary.org/doi/abs/10.1061/9780784412190.041>
- Bar-Cohen, Y., Sherrit, S., Bao, X., Badescu, M., Aldrich, J. and Chang, Z. (2007) Ultrasonic/sonic driller/corer (USDC) as a subsurface sampler and sensors platform for planetary exploration applications. Proceedings of the NASA Science and Technology Conference (NSTC-07), University of Maryland Conference Center, 19–21 June 2007.
- Bar-Cohen, Y., Sherrit, S., Dolgin, B., Peterson, T., Pal, D. and Kroh, J. (2005) *Smart-Ultrasonic/Sonic Driller/Corer*. NASA New Technology Report (NTR), 30 August 1999, Docket No. 20856; US Patent 6,863,136, 8 March 2005
- Bar-Cohen, Y., Sherrit, S., et al. (2001) Ultrasonic/sonic drilling/coring (USDC) for planetary applications. SPIE Smart Structures, Newport Beach, CA, 5–8 March 2001, Paper 4327-55.
- Bar-Cohen, Yoseph, Zacny, Kris (2008). Drilling in Extreme Environments, WILEY-VCH Verlag GmbH & Co. KGaA
- Batako, A.D., Babitsky, V.I. and Halliwell, N.A. (2004) Modeling of vibro-impact penetration of self-exciting percussive–rotary drill bit. *Journal of Sound and Vibration*, 271, 209–225. Bean, A.L., Conrad, C. Jr, and Gordon, R.F. (1970) Crew observations. In: Apollo 12 Preliminary Science Report (ed. A.J. Calio et al.), pp. 29–38.
- Bransford, J. D., Brown, A. L., & Cocking, R. R. (Eds.). (2000). *How People Learn: Brain, Mind, Experience, and School*. Washington, DC: National Research Council.
- Briggs, G. and Gross, A. (2002) Technical challenges of drilling on Mars. AIAA Aerospace Sciences Meeting and Exhibit, 40th, Reno, NV, 14–17 January 2002, 2002, AIAA-2002-469, American Institute of Aeronautics and Astronautics.
- Bruno, B. M., Han, G., & Honeger, C. (2005). Advanced Simulation Technology for Combined Percussion and Rotary Drilling and Cuttings Transport, 5–8.
- Chang, Z., Sherrit, S., Bao, X. and Bar-Cohen, Y. (2004) *Design and analysis of ultrasonic horn for USDC (ultrasonic/sonic driller/corer)*. SPIE Smart Structures and Materials Symposium, San Diego, CA, 15–18 March 2004, Paper 5387-58.
- Chenglong Zhang, Jianfu Zhang, Pingfa Feng (2013) *Mathematical model for cutting force in rotary ultrasonic face milling of brittle materials*, *Int J Adv Manuf Technol* (2013) 69:161–170
- Clark, D. B., & Linn, M. C. (2003). Scaffolding knowledge integration through curricular depth. *Journal of Learning Sciences*, 12(4), 451-494.

Cong, W. L., Pei, Z. J., Mohanty, N., Van Vleet, E., & Treadwell, C. (2011). Vibration Amplitude in Rotary Ultrasonic Machining: A Novel Measurement Method and Effects of Process Variables. *Journal of Manufacturing Science and Engineering*, 133(June 2011), 034501. doi:10.1115/1.4004133

Dolgin, B., Sherrit, S., Bar-Cohen, Y., Askins, S., Sigel, D., Bao, X. and Chang, Z. (2001b) *Ultrasonic/Sonic Vibrating/Rotating Tool*. NASA New Technology Report (NTR), 5 September 2001, Docket No. 30370.

Dolgin, B., Sherrit, S., Bar-Cohen, Y., Rainen, R., Askins, S., Sigel, D., Bickler, D., Carson, J., Dawson, S., Bao, X., Chang, Z. and Peterson, T. (2001a) *Ultrasonic Rock Abrasion Tool (URAT)*. NASA New Technology Report (NTR), 12 October 2001, Docket No. 30403.

ESA, *Mars Express* (2006)

Eylon, B. S., & Linn, M. C. (1988). Learning and instruction: An examination of four research perspectives in science education. *Review of Educational Research*, 58(3), 251–301.

Fang FZ, Zhang GX (2004) An experimental study of optical glass machining. *Int J Adv Manuf Technol* 23(3):155–160

Fracture toughness test:

http://www.tunnelling.metal.ntua.gr/uploads/images/23/dokimithlipsis_s.jpg

Griffith, A. A., *Phil. Trans. Roy. Soc. Lond.* A221 (1920) 163.

Han, G., & Bruno, M. (n.d.). Technology Assessment for Fundamental Research on Percussion Drilling: Improved Rock Mechanics Analysis, Advanced Simulation Technology, and Full-. *Netl.doe.gov*. Retrieved from <http://www.netl.doe.gov/kmd/cds/disk17/C - Drilling Completion Stimulation/NT41999 Technology Assessment.pdf>

Honeybee Robotics, Honeybee On Mars: <http://www.honeybeerobotics.com/about-us/mars/>

<http://www.mitutoyo.co.uk/media/catalog/product/cache/1/thumbnail/9df78eab33525d08d6e5fb8d27136e95/h/v/hv-aav504.jpg>

Lawn & Swain (1975), *Microfracture Beneath Point Indentations in Brittle Solids*, *Journal of Materials Science* 10 113-122

Lawn B. and R. Wilshaw, Review indentation fracture: principles and applications, *Journal of Materials Science* 10 (1975) 1049–1081

Lawn B., R. Wilshaw, Review indentation fracture: principles and applications, *Journal of Materials Science* 10 (1975) 1049–1081.

Lawn B., *J. Mater. Sci.* 10 (1975) 469

Lawn B., A.G. Evans, D.B. Marshall, Elastic/plastic indentation damage in ceramics: the median/radial crack system, *Journal of the American Ceramic Society* 63 (9–10) (1980) 574–581.

Mars 2020 SDT Report, *Mars 2020 Science Definition Team Final Report, July 1, 2013*

Mars Exploration Program Analysis Group (MEPAG) Report, *Scientific Goals, Objectives, Investigations, and Priorities*, (2001)

Mars Exploration Rovers, JPL

http://mars.nasa.gov/mer/mission/spacecraft_instrument.html

Marshall D.B., Lawn B.R., A.G. Evans, Elastic/plastic indentation damage in ceramics: the lateral crack system, *Journal of the American Ceramic Society* 65 (11) (1982) 561–566.

Maurer, W.C. (1968) *Novel Drilling Techniques*, Pergamon Press, New York

MEPAG E2E-iSAG (2011) Planning for Mars Returned Sample Science: Final report of the MSR End-to-End International Science Analysis Group (E2E-iSAG), 101 pp., posted December, 2011, by the Mars Exploration Program Analysis Group (MEPAG) at <http://mepag.jpl.nasa.gov/reports/>.

MEPAG JSWG (2012) Report of the 2018 Joint Mars Rover Mission Joint Science Working Group (JWSG), 93 pp., posted March, 2012, by the Mars Exploration Program Analysis Group (MEPAG) at <http://mepag.jpl.nasa.gov/reports/>.

MEPAG ND-SAG (2008). Science Priorities for Mars Sample Return, Unpublished white paper, 73 p., posted March 2008 by the Mars Exploration Program Analysis Group (MEPAG) at <http://mepag.jpl.nasa.gov/reports/ndsag.html>.

Mitchell, D., *Berkeley SSL* (1999)

NASA Mars Exploration, <http://mars.nasa.gov/programmissions/missions/past/viking/>

Ostojic P., R. McPherson, A review of indentation of fracture: its development, principles and limitations, *International Journal of Fracture* 33 (1987) 297–312.

Paulsen, G., Zacny, K., McKay, C., Shiraishi, L., Kriechbaum, K., Glass, B., ... Maksymuk, M. (2010). Rotary-Percussive Deep Drill for Planetary Applications. *Earth and Space 2010*, 1423–1436. doi:10.1061/41096(366)128

Phoenix Mars Mission, (2008), <http://phoenix.lpl.arizona.edu/>

Phoenix Mars Mission: <http://phoenix.lpl.arizona.edu/phases.php>

Review Indentation Fractures - Principles and Applications.pdf,
<http://www.msel.nist.gov/lawn/Publications/Papers.BRL/PapersBRL.1975/JMS%2010%201049%201975.pdf>.

Samuel, G.R., Percussion Drilling...Is it a Lost Technique? A Review, *Society of Petroleum Engineers Paper No. 35240, the Permian Basin Oil & Gas Recovery Conference, Midland, Texas, March 1996*.

Sherrit, S., Askins, S. a, Gradziol, M., Dolgin, B. P., Bao, X., Chang, Z., & Bar-Cohen, Y. (2002). Novel horn designs for ultrasonic/sonic cleaning welding, soldering, cutting and drilling. *Proceedings of SPIE, 4701*(March 2002), 353. doi:10.1117/12.474671

Sherrit, S., Askins, S.A., Gradziel, M., Dolgin, B.P., Bar-Cohen, Y., Bao, X. and Cheng, Z. (2001) *Novel ultrasonic horns for power ultrasonics*. NASA New Technology Report (NTR), Docket No. 30489 (6 December 2001). NASA Technical Briefs, 27 (4), 54–55

Sherrit, S., Bar-Cohen, Y., Bao, X., Chang, Z., Blake, D. and Bryson, C. (2003) *Ultrasonic/sonic rock powdering sampler and delivery tool*. NASA New Technology Report (NTR), Docket No. 40564 (13 August 2003).

Sherrit, S., Bar-Cohen, Y., Dolgin, B., Bao, X. and Chang, Z. (2002) *Ultrasonic crusher for crushing, milling, and powdering*. NASA New Technology Report (NTR), Docket No. 30682 (21 June 2002).

Sims, M.R., Sykes, J., Stevenson, T., Wiercigroch, M., Parnell, J. and Hole, M. (2002) *Design of an ultrasonic rock corer for use in planetary missions*. Final Report, December 2002. Final report of contract No. 16222/02/NL/PA. ESTEC, European Space Agency, Noordwijk.

Smithsonian National Air and Space Museum
http://airandspace.si.edu/exhibitions/exploring-the-planets/online/mars/viking_lab.html#view

Terralog Technologies Inc (USA), Vibration/Ultrasonic waves

Vickers hardness diamond tip indenter:

[http://upload.wikimedia.org/wikipedia/commons/d/d2/Vickers anvil diamonds.jpg](http://upload.wikimedia.org/wikipedia/commons/d/d2/Vickers_anvil_diamonds.jpg)

Vickers hardness tester:

Zacny, K. a. (2005). Enhancing cuttings removal with gas blasts while drilling on Mars.

Journal of Geophysical Research, 110(E4), E04002. doi:10.1029/2004JE002340

Zacny, K. A., & Cooper, G. A. (2005). Mars, 1–16. doi:10.1555/mars.2005.1.0

Zacny, K., & Cooper, G. (2005). Investigation of the performance of a coring bit in frozen mud under Martian conditions of low temperature and pressure. *Journal of Geophysical Research: ...*, 1–8. Retrieved from

<http://onlinelibrary.wiley.com/doi/10.1029/2004JE002341/full>

Zacny, K., & Cooper, G. (2006). Considerations, constraints and strategies for drilling on Mars. *Planetary and Space Science*, 54(4), 345–356. doi:10.1016/j.pss.2005.12.003

Zacny, K., Bar-Cohen, Y., Boucher, D., Brennan, M., Briggs, G., Cooper, G., Davis, K., Dolgin, B., Glaser, D., Glass, B., Gorevan, S., Guerrero, J., Paulsen, G., Stanley, S. and Stoker, C.

(2008b) Drilling systems for extraterrestrial subsurface exploration. *Astrobiology*, 8 (3), 665–706, DOI:10.1089/ast.2007.0179.

Zacny, K., Bar-cohen, Y., Davis, K., Coste, P., Paulsen, G., Sherrit, S., ... Wakabayashi, S.

(2009). *Extraterrestrial Drilling and Excavation*.

Zancy K., PhD thesis *Mars Drilling - An Investigation and Development of Techniques for Drilling Exploratory Boreholes on Mars*, UC Berkeley, (2005)

Zhang, C., Zhang, J., & Feng, P. (2013). Mathematical model for cutting force in rotary ultrasonic face milling of brittle materials. *The International Journal of Advanced Manufacturing Technology*, 69(1-4), 161–170. doi:10.1007/s00170-013-5004-z

Zhao, X. L., Fowell, R. J., Roegiers, J.-C., & Xu, C. (1994). Rock fracture-toughness determination by the Brazilian test, by H. Guo, N.I. Aziz, L.C. Schmidt. *Engineering Geology*, 38(1994), 181–184. doi:10.1016/0013-7952(94)90033-7

11. Appendix A

Mathematical Model Development

Determining the effect of the ultrasonic amplitude (A), cutting force (F) known as Weight on Bit (WOB), and Speed (s) on Rate of Penetration (ROP) taking the following steps:

- 1) Establishing a relationship between the cutting force (F) and the maximum depth (δ) into the workpiece.
- 2) Estimate the actual volume (V) of the materials removed by one abrasive particle, as the basic component in cutting forces, during one ultrasonic cycle.
- 3) Estimate the cutting force model (F) by summing the effect of all active abrasive particles in sample core drilling.
- 4) Determine the effect of amplitude (A), cutting force/WOB (F), and speed (s) on ROP.

Rate of Penetration Expression Derivation

$$ROP = \frac{N_a}{A_o} f_u \cdot \left(\frac{K}{3} L_s C_L C_h \right)$$

$$N_a = C_1 \left(\frac{C_a^{2/3} A_o}{S_a^2} \right); \quad C_1 = \left(\frac{3 \times 0.88 \times 10^{-3}}{100 \sqrt{2} \rho} \right)^{2/3} = 0.03 \quad ; \quad A_o = \frac{\pi(D_o^2 - D_i^2)}{4}$$

$$L_s = \left[\left(\frac{\pi S(D_o + D_i)}{120} \right)^2 + b^2 \right]^{1/2} \frac{1}{\pi f_u} \left[\frac{\pi}{2} - \arcsin \left(1 - \frac{\delta}{A} \right) \right]$$

$$C_L C_h = \frac{C_2^2}{\left(\tan \frac{\alpha_o}{2} \right)^{3/4}} \left(\frac{E^{7/8}}{H_v^{3/2} K_{IC}^{1/2} (1 - \nu^2)^{1/4}} \right) (F_n)^{9/8}$$

$$\text{Let } Q = \left(\frac{E^{7/8}}{H_v^{3/2} K_{IC}^{1/2} (1 - \nu^2)^{1/4}} \right)$$

$$C_L C_h = \frac{C_2^2}{\left(\tan \frac{\alpha_o}{2} \right)^{3/4}} Q (F_n)^{9/8}$$

$$F_n = \frac{\pi F}{N_a \left[\frac{\pi}{2} - \arcsin \left(1 - \frac{\delta}{A} \right) \right]}$$

$$ROP = \frac{N_a}{A_o} f_u \cdot \frac{K}{3} \left(\left[\left(\frac{D_o + D_i}{4} \right)^2 \left(\frac{2\pi S}{60} \right)^2 + ROP^2 \right]^{1/2} \frac{1}{\pi f_u} \left[\frac{\pi}{2} - \arcsin \left(1 - \frac{\delta}{A} \right) \right] \right) \left(\frac{C_2^2}{\left(\tan \frac{\alpha_o}{2} \right)^{3/4}} Q (F_n)^{9/8} \right)$$

$$ROP = \frac{K}{3} \left(\left[\left(\frac{D_o + D_i}{4} \right)^2 \left(\frac{2\pi S}{60} \right)^2 + ROP^2 \right]^{1/2} \left[\frac{\pi}{2} - \arcsin \left(1 - \frac{\delta}{A} \right) \right] \right) \left(\frac{N_a}{\pi A_o} \frac{C_2^2}{\left(\tan \frac{\alpha_o}{2} \right)^{3/4}} Q (F_n)^{9/8} \right)$$

$$ROP = \frac{K}{3} \left(\left[\left(\frac{D_o + D_i}{4} \right)^2 \left(\frac{2\pi S}{60} \right)^2 + ROP^2 \right]^{1/2} \left[\frac{\pi}{2} - \arcsin \left(1 - \frac{\delta}{A} \right) \right] \right) \left(\frac{N_a}{\pi A_o} \frac{C_2^2}{\left(\tan \frac{\alpha_o}{2} \right)^{3/4}} Q \left(\frac{\pi F}{N_a \left[\frac{\pi}{2} - \arcsin \left(1 - \frac{\delta}{A} \right) \right]} \right)^{9/8} \right)$$

$$ROP = \frac{C_2^2 K}{3} \left(\left[\left(\frac{D_o + D_i}{4} \right)^2 \left(\frac{2\pi S}{60} \right)^2 + ROP^2 \right]^{1/2} \right) \left(\frac{(\pi)^{9/8} Q}{\pi A_o \left(\tan \frac{\alpha_o}{2} \right)^{3/4}} \left(\frac{1}{N_a \left[\frac{\pi}{2} - \arcsin \left(1 - \frac{\delta}{A} \right) \right]} \right)^{1/8} (F)^{9/8} \right)$$

$$ROP = \frac{C_2^2 K}{3} \left(\left[\left(\frac{\pi S (D_o + D_i)}{120} \right)^2 \right. \right. \\ \left. \left. + ROP^2 \right]^{1/2} \left(\frac{Q}{A_o \left(\tan \frac{\alpha_o}{2} \right)^{3/4}} \left(\frac{\pi}{C_1 \left(\frac{C_a^{2/3} A_o}{S_a^2} \right) \left[\frac{\pi}{2} - \arcsin \left(1 - \frac{\delta}{A} \right) \right]} \right)^{1/8} (F)^{9/8} \right) \right)$$

$$ROP = \frac{C_2^2 K}{3} \left(\frac{1}{C_1} \right)^{1/8} \left(\left[\left(\frac{\pi S (D_o + D_i)}{120} \right)^2 \right. \right. \\ \left. \left. + ROP^2 \right]^{1/2} \left(\frac{Q}{\left(\tan \frac{\alpha_o}{2} \right)^{3/4}} \left(\frac{\pi S_a^2}{C_a^{2/3} A_o \left[\frac{\pi}{2} - \arcsin \left(1 - \frac{\delta}{A} \right) \right]} \right)^{1/8} (F)^{9/8} \right) \right)$$

$$ROP \\ = \frac{C_2^2 K}{3} \left(\frac{1}{C_1} \right)^{1/8} \left(\left[\left(\frac{\pi S (D_o + D_i)}{120} \right)^2 \right. \right. \\ \left. \left. + ROP^2 \right]^{1/2} \left(\frac{Q}{\left(\tan \frac{\alpha_o}{2} \right)^{3/4}} \left(\frac{\pi S_a^2}{C_a^{2/3} \left(\frac{\pi (D_o^2 - D_i^2)}{4} \right)^9 \left[\frac{\pi}{2} - \arcsin \left(1 - \frac{\delta}{A} \right) \right]} \right)^{1/8} (F)^{9/8} \right) \right)$$

$$ROP \\ = \frac{C_2^2 K}{3 \pi} \left(\frac{4^9}{C_1} \right)^{1/8} \left(\left[\left(\frac{\pi S (D_o + D_i)}{120} \right)^2 \right. \right. \\ \left. \left. + ROP^2 \right]^{1/2} \left(\frac{Q}{\left(\tan \frac{\alpha_o}{2} \right)^{3/4}} \left(\frac{S_a^2}{C_a^{2/3} (D_o^2 - D_i^2)^9 \left[\frac{\pi}{2} - \arcsin \left(1 - \frac{\delta}{A} \right) \right]} \right)^{1/8} (F)^{9/8} \right) \right)$$

$$ROP = \frac{C_2^2 K \left(\frac{4^9}{C_1}\right)^{1/8} \left(\left[\left(\frac{\pi S (D_o + D_i)}{120} \right)^2 + ROP^2 \right]^{1/2} \right) \left(\frac{Q (F)^{9/8}}{(\tan \frac{\alpha_o}{2})^{3/4}} \left(\frac{S_a^2}{C_a^{2/3} (D_o^2 - D_i^2)^9 \left[\frac{\pi}{2} - \arcsin \left(1 - \frac{\delta}{A} \right) \right]} \right)^{1/8} \right)}$$

Let $G = \frac{C_2^2 K \left(\frac{4^9}{C_1}\right)^{1/8}$; $C1 = 0.03$, $C2 = 0.226$, and $K = 0.3$

$$ROP = \left(\left[\left(\frac{\pi S (D_o + D_i)}{120} \right)^2 + ROP^2 \right]^{1/2} \right) \left(\frac{G Q (F)^{9/8} S_a^{1/4}}{(\tan \frac{\alpha_o}{2})^{3/4} (C_a^{2/3} (D_o^2 - D_i^2)^9 \left[\frac{\pi}{2} - \arcsin \left(1 - \frac{\delta}{A} \right) \right])^{1/8}} \right)$$

$$ROP \left(\frac{(\tan \frac{\alpha_o}{2})^{3/4} (C_a^{2/3} (D_o^2 - D_i^2)^9 \left[\frac{\pi}{2} - \arcsin \left(1 - \frac{\delta}{A} \right) \right])^{1/8}}{G Q (F)^{9/8} S_a^{1/4}} \right) = \left[\left(\frac{\pi S (D_o + D_i)}{120} \right)^2 + ROP^2 \right]^{1/2}$$

Square both sides:

$$ROP^2 \left(\frac{(\tan \frac{\alpha_o}{2})^{3/4} (C_a^{2/3} (D_o^2 - D_i^2)^9 \left[\frac{\pi}{2} - \arcsin \left(1 - \frac{\delta}{A} \right) \right])^{1/8}}{G Q (F)^{9/8} S_a^{1/4}} \right)^2 = \left(\frac{\pi S (D_o + D_i)}{120} \right)^2 + ROP^2$$

Combine like terms

$$ROP^2 \left[\left(\frac{(\tan \frac{\alpha_o}{2})^{3/4} (C_a^{2/3} (D_o^2 - D_i^2)^9 \left[\frac{\pi}{2} - \arcsin \left(1 - \frac{\delta}{A} \right) \right])^{1/8}}{G Q (F)^{9/8} S_a^{1/4}} \right)^2 - 1 \right] = \left(\frac{\pi S (D_o + D_i)}{120} \right)^2$$

Solve for ROP

$$ROP = \frac{\pi S (D_o + D_i)}{120 \sqrt{\left(\frac{\left(\tan \frac{\alpha_o}{2} \right)^{3/4} \left(C_a^{2/3} (D_o^2 - D_i^2)^9 \left[\frac{\pi}{2} - \arcsin \left(1 - \frac{\delta}{A} \right) \right]^{1/8} \right)^2}{G Q (F)^{9/8} S_a^{1/4}} \right) - 1}$$

$$ROP = \frac{\pi S (D_o + D_i)}{120 \sqrt{\left(\frac{\left(\tan \frac{\alpha_o}{2} \right)^{3/2} C_a^{1/6} (D_o^2 - D_i^2)^{9/4} \left[\frac{\pi}{2} - \arcsin \left(1 - \frac{\delta}{A} \right) \right]^{1/4}}{G^2 Q^2 (F)^{9/4} S_a^{1/2}} \right) - 1}$$

$$ROP = \frac{\pi S (D_o + D_i)}{120 \sqrt{\left(\frac{\left(\tan \frac{\alpha_o}{2} \right)^{3/2} C_a^{1/6} (D_o^2 - D_i^2)^{9/4} \left[\frac{\pi}{2} - \arcsin \left(1 - \frac{\delta}{A} \right) \right]^{1/4}}{G^2 \left(\frac{E^{7/8}}{H_v^{3/2} K_{IC}^{1/2} (1 - \nu^2)^{1/4}} \right)^2 (F)^{9/4} S_a^{1/2}} \right) - 1}$$

$$ROP = \frac{\pi S (D_o + D_i)}{120 \sqrt{\left(\frac{\left(\tan \frac{\alpha_o}{2} \right)^{3/2} C_a^{1/6} (D_o^2 - D_i^2)^{9/4} \left[\frac{\pi}{2} - \arcsin \left(1 - \frac{\delta}{A} \right) \right]^{1/4}}{G^2 \left(\frac{E^{7/4}}{H_v^3 K_{IC} (1 - \nu^2)^{1/2}} \right) (F)^{9/4} S_a^{1/2}} \right) - 1}$$

Where $G = \left(\frac{3\pi C_1^{1/8}}{4^{9/8} K C_2^2} \right)$

Let

$$\gamma = G^2 \left(\frac{C_a^{1/6} (D_o^2 - D_i^2)^{9/4} \left(\tan \frac{\alpha_o}{2} \right)^{3/2} \left[\frac{\pi}{2} - \arcsin \left(1 - \frac{\delta}{A} \right) \right]^{1/4}}{S_a^{1/2} \left(\frac{E^{7/4}}{H_v^3 K_{IC} (1 - \nu^2)^{1/2}} \right) (F)^{9/4}} \right) = \varphi$$

Where Φ is a large number

Then

$$120 \sqrt{G^2 \left(\frac{C_a^{1/6} (D_o^2 - D_i^2)^{9/4} \left(\tan \frac{\alpha_o}{2} \right)^{3/2} \left[\frac{\pi}{2} - \arcsin \left(1 - \frac{\delta}{A} \right) \right]^{1/4}}{S_a^{1/2} \left(\frac{E^{7/4}}{H_v^3 K_{IC} (1 - \nu^2)^{1/2}} \right) (F)^{9/4}} \right)} - 1 = 120 \sqrt{\gamma - 1} = \varphi$$

$$\sqrt{\gamma - 1} = \frac{\varphi}{120}$$

$$\gamma = \left(\frac{\varphi}{120} \right)^2 + 1$$

Since Φ is a large number, then $\gamma \gg 1$

Therefore, the ROP expression can be simplified as follow;

$$ROP = \frac{\pi S (D_o + D_i)}{\sqrt{120 \sqrt{G^2 \left(\frac{C_a^{1/6} (D_o^2 - D_i^2)^{9/4} \left(\tan \frac{\alpha_o}{2} \right)^{3/2} \left[\frac{\pi}{2} - \arcsin \left(1 - \frac{\delta}{A} \right) \right]^{1/4}}{S_a^{1/2} \left(\frac{E^{7/4}}{H_v^3 K_{IC} (1 - \nu^2)^{1/2}} \right) (F)^{9/4}} \right)}}$$

$$\text{Let } D_{avg} = \frac{D_o + D_i}{2} \quad ; \text{ then } D_o + D_i = 2D_{avg}$$

$$\text{Also, } D_o^2 - D_i^2 = (D_o + D_i)(D_o - D_i)$$

$$\text{Let the thickness } t = \frac{(D_o - D_i)}{2}$$

$$D_o^2 - D_i^2 = (2D_{avg})(2t)$$

$$D_o^2 - D_i^2 = 4 t D_{avg}$$

Substituting the values of $(D_o + D_i)$ and $(D_o^2 - D_i^2)$ in the above equation yield the final ROP expression as follow:

$$ROP = \frac{\pi S (D_o + D_i)}{120 G \left(\frac{C_a^{1/6} (D_o^2 - D_i^2)^{9/4} \left(\tan \frac{\alpha_o}{2} \right)^{3/2} \left[\frac{\pi}{2} - \arcsin \left(1 - \frac{\delta}{A} \right) \right]^{1/4}}{S_a^{1/2} \left(\frac{E^{7/4}}{H_v^3 K_{IC} (1 - \nu^2)^{1/2}} \right) (F)^{9/4}} \right)^{1/2}}$$

$$ROP = \frac{\pi S (D_o + D_i)}{120 G \left(\frac{C_a^{1/12} (D_o^2 - D_i^2)^{9/8} \left(\tan \frac{\alpha_o}{2} \right)^{3/4} \left[\frac{\pi}{2} - \arcsin \left(1 - \frac{\delta}{A} \right) \right]^{1/8}}{S_a^{1/4} \left(\frac{E^{7/8}}{H_v^{3/2} K_{IC}^{1/2} (1 - \nu^2)^{1/4}} \right) (F)^{9/8}} \right)}$$

$$ROP = \frac{\pi S (D_o + D_i) S_a^{1/4} (F)^{9/8}}{120 G C_a^{1/12} (D_o^2 - D_i^2)^{9/8} \left(\tan \frac{\alpha_o}{2} \right)^{3/4} \left[\frac{\pi}{2} - \arcsin \left(1 - \frac{\delta}{A} \right) \right]^{1/8}} \left(\frac{E^{7/8}}{H_v^{3/2} K_{IC}^{1/2} (1 - \nu^2)^{1/4}} \right)$$

$$ROP = \frac{\pi S (2 D_{avg}) S_a^{1/4} (F)^{9/8}}{120 G C_a^{1/12} (4 t D_{avg})^{9/8} \left(\tan \frac{\alpha_o}{2} \right)^{3/4} \left[\frac{\pi}{2} - \arcsin \left(1 - \frac{\delta}{A} \right) \right]^{1/8}} \left(\frac{E^{7/8}}{H_v^{3/2} K_{IC}^{1/2} (1 - \nu^2)^{1/4}} \right)$$

$$ROP = \frac{\pi S S_a^{1/4} (F)^{9/8}}{60 (4)^{9/8} G C_a^{1/12} (t)^{9/8} (D_{avg})^{1/8} \left(\tan \frac{\alpha_o}{2} \right)^{3/4} \left[\frac{\pi}{2} - \arcsin \left(1 - \frac{\delta}{A} \right) \right]^{1/8}} \left(\frac{E^{7/8}}{H_v^{3/2} K_{IC}^{1/2} (1 - \nu^2)^{1/4}} \right)$$

Let

$$G_1 = \frac{\pi}{60 (4)^{9/8} G}; \quad \text{Where} \quad G = \left(\frac{3\pi C_1^{1/8}}{4^{9/8} K C_2^2} \right)$$

Then

$$G_1 = \frac{\pi}{60 (4)^{9/8} \left(\frac{3\pi C_1^{1/8}}{4^{9/8} K C_2^2} \right)}$$

$$G_1 = \frac{K C_2^2}{180 C_1^{1/8}}$$

Then

$$ROP = \frac{G_1 S S_a^{1/4} (F)^{9/8}}{C_a^{1/12} (t)^{9/8} (D_{avg})^{1/8} \left(\tan \frac{\alpha_o}{2}\right)^{3/4} \left[\frac{\pi}{2} - \arcsin\left(1 - \frac{\delta}{A}\right)\right]^{1/8}} \left(\frac{E^{7/8}}{H_v^{3/2} K_{IC}^{1/2} (1 - \nu^2)^{1/4}} \right)$$

12. Appendix B

Vickers Hardness Indentation Area Derivation

$$A_s = \frac{1}{2} 4 e h = 2 e h \quad (1)$$

$$\sin(45^\circ) = \frac{e}{d} = \frac{\sqrt{2}}{2}$$

$$e = \frac{\sqrt{2}}{2} d \quad (2)$$

$$h^2 = \left(\frac{e}{2}\right)^2 + \delta^2$$

$$h^2 = \left(\frac{\sqrt{2}d}{4}\right)^2 + \delta^2$$

$$h^2 = \frac{d^2}{8} + \delta^2$$

$$\tan\left(\frac{\alpha_o}{2}\right) = \frac{d/2}{\delta}$$

$$d = 2 \tan\left(\frac{\alpha_o}{2}\right) \delta \quad (3)$$

Then

$$h^2 = \frac{\left(2 \tan\left(\frac{\alpha_o}{2}\right) \delta\right)^2}{8} + \delta^2 = \delta^2 \left(\frac{\left(\tan\left(\frac{\alpha_o}{2}\right)\right)^2}{2} + 1\right)$$

$$h^2 = \frac{\delta^2}{2} \left(\left[\tan\left(\frac{\alpha_o}{2}\right)\right]^2 + 2\right)$$

$$h = \frac{\delta}{\sqrt{2}} \sqrt{\left[\tan\left(\frac{\alpha_o}{2}\right)\right]^2 + 2} \quad (4)$$

Substitute (2), (3) and (4) in (1)

$$A_s = 2 b h$$

$$A_s = 2 \left(\frac{\sqrt{2}}{2} d \right) \left(\frac{\delta}{\sqrt{2}} \sqrt{\left[\tan\left(\frac{\alpha_o}{2}\right) \right]^2 + 2} \right)$$

$$A_s = 2 \left(\frac{\sqrt{2}}{2} 2 \tan\left(\frac{\alpha_o}{2}\right) \delta \right) \left(\frac{\delta}{\sqrt{2}} \sqrt{\left[\tan\left(\frac{\alpha_o}{2}\right) \right]^2 + 2} \right)$$

$$A_s = \left(2 \tan\left(\frac{\alpha_o}{2}\right) \sqrt{\left[\tan\left(\frac{\alpha_o}{2}\right) \right]^2 + 2} \right) \delta^2$$

ROP derivation simplification:

$$ROP = \frac{K}{3} \frac{N_a}{A_o} \left(\frac{S(D_o + D_i)}{120} \right) \left[\frac{\pi}{2} - \arcsin\left(1 - \frac{\delta}{A}\right) \right] \frac{C_2^2}{\left(\tan\frac{\alpha_o}{2}\right)^{3/4}} (Q) \left(\frac{\pi F}{N_a \left[\frac{\pi}{2} - \arcsin\left(1 - \frac{\delta}{A}\right) \right]} \right)^{9/8}$$

$$ROP = \left(\frac{K C_2^2 \pi^{9/8}}{360} \right) \left(\frac{S(D_o + D_i)}{\left(\tan\frac{\alpha_o}{2}\right)^{3/4}} \right) (Q) \frac{F^{9/8}}{A_o N_a^{1/8} \left[\frac{\pi}{2} - \arcsin\left(1 - \frac{\delta}{A}\right) \right]^{1/8}}$$

$$ROP = \left(\frac{K C_2^2 \pi^{9/8}}{360 C_1^{1/8}} \right) \left(\frac{S(D_o + D_i)}{\left(\tan\frac{\alpha_o}{2}\right)^{3/4}} \right) (Q) \frac{F^{9/8}}{A_o \left(\frac{C_a^{2/3} A_o}{S_a^2} \right)^{1/8} \left[\frac{\pi}{2} - \arcsin\left(1 - \frac{\delta}{A}\right) \right]^{1/8}}$$

$$ROP = \left(\frac{K C_2^2 \pi^{9/8}}{360 C_1^{1/8}} \right) \left(\frac{S(D_o + D_i)}{\left(\tan\frac{\alpha_o}{2}\right)^{3/4}} \right) (Q) \frac{S_a^{1/4} F^{9/8}}{A_o^{9/8} C_a^{1/12} \left[\frac{\pi}{2} - \arcsin\left(1 - \frac{\delta}{A}\right) \right]^{1/8}}$$

$$A_o = \frac{\pi(D_o^2 - D_i^2)}{4}$$

$$ROP = \left(\frac{K C_2^2 \pi^{9/8}}{360 C_1^{1/8}} \right) \left(\frac{S(D_o + D_i)}{\left(\tan\frac{\alpha_o}{2}\right)^{3/4}} \right) (Q) \frac{S_a^{1/4} F^{9/8}}{\left(\frac{\pi(D_o^2 - D_i^2)}{4} \right)^{9/8} C_a^{1/12} \left[\frac{\pi}{2} - \arcsin\left(1 - \frac{\delta}{A}\right) \right]^{1/8}}$$

13. Appendix C

Plots of the material properties Young's modulus and Poisson's ratio for three types of rocks: marble, travertine, and basalt for two specimens each:

Marble test plots of Sp1 Young modulus and Poisson ratio:

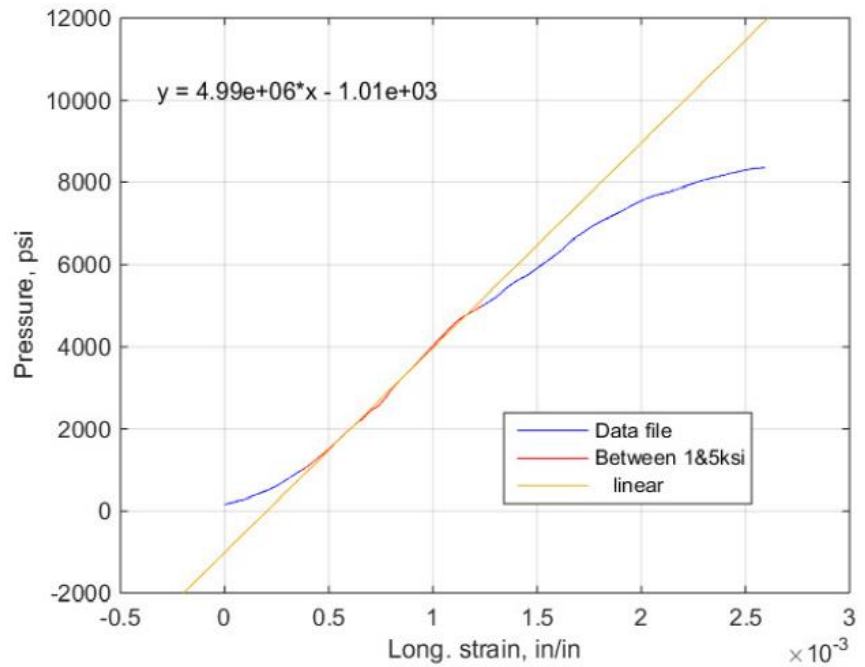


Figure 172: Marble Sp1 Young modulus

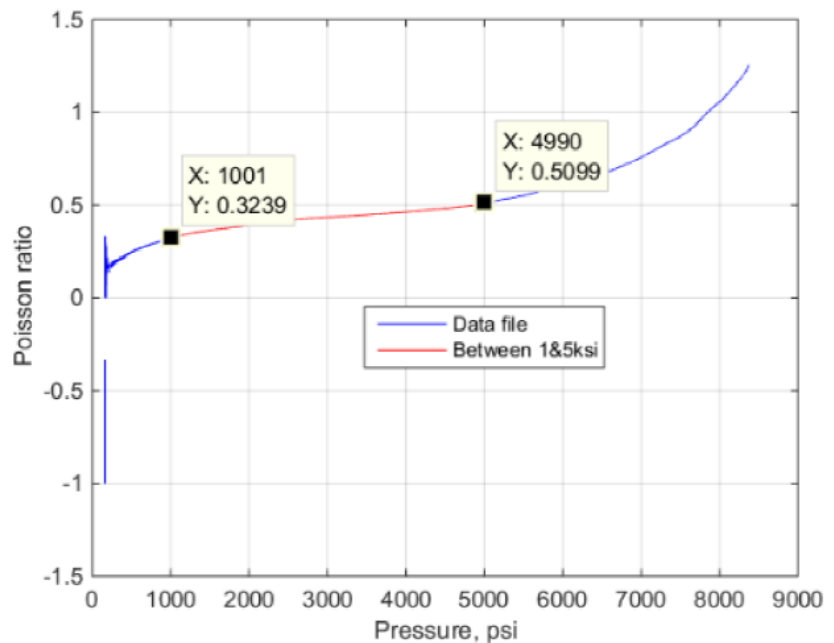


Figure 173: Marble Sp1 Poisson ratio

Marble test plots of Sp2 Young modulus and Poisson ratio:

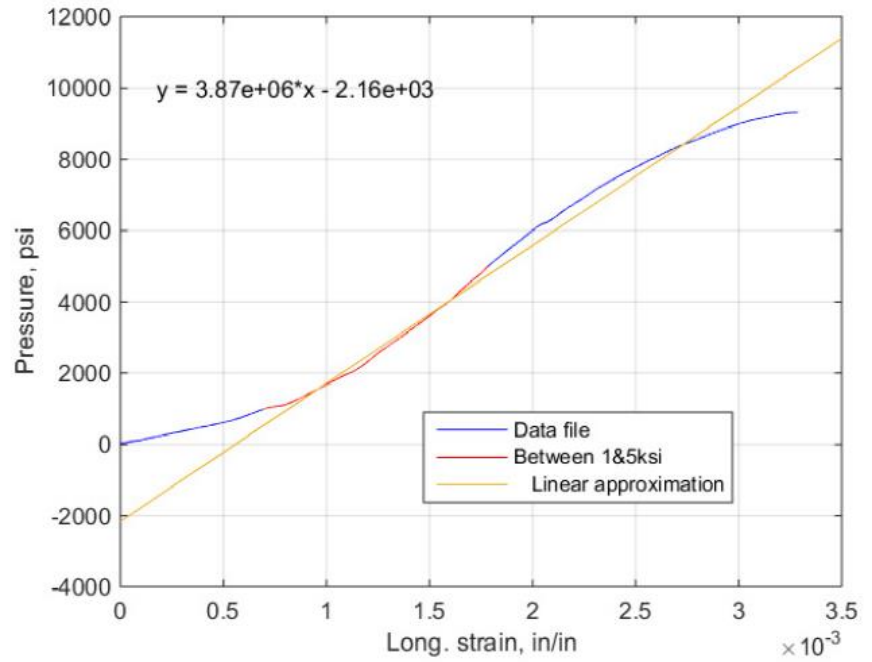


Figure 174: Marble Sp2 Young modulus

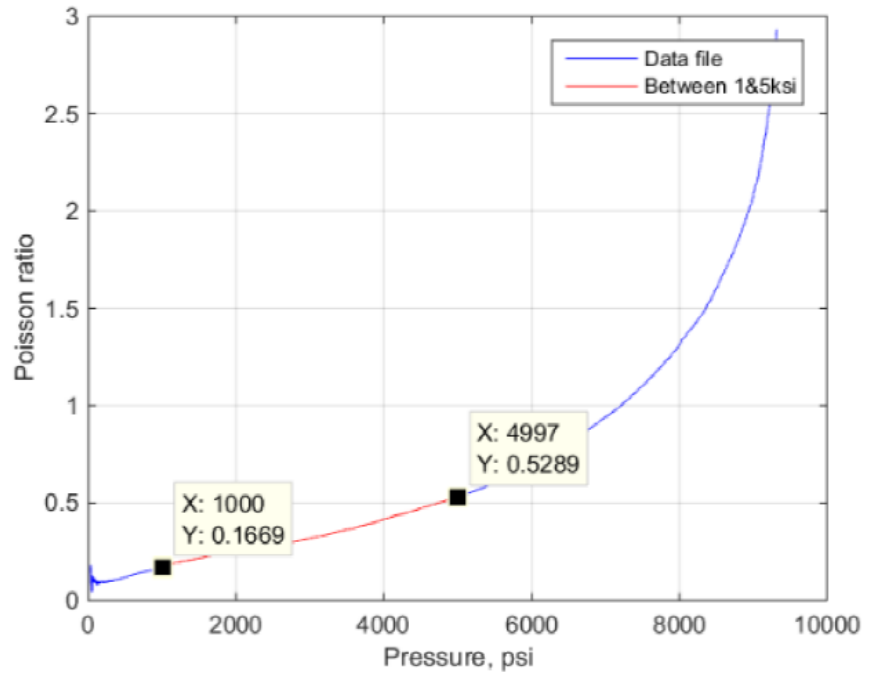


Figure 175: Marble Sp2 Poisson ratio

Travertine test plots of Sp4 Young modulus and Poisson ratio:

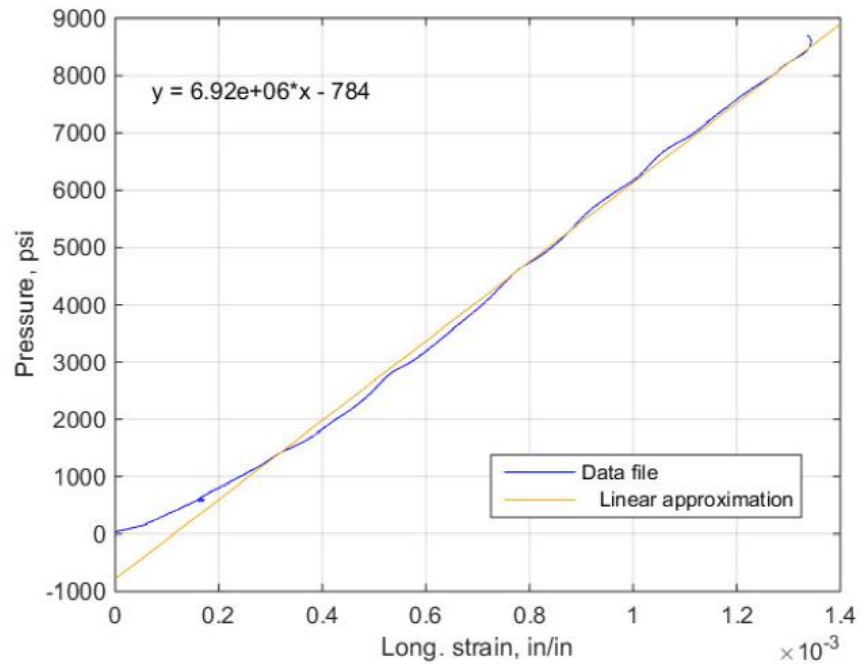


Figure 176: Travertine Sp4 Young modulus

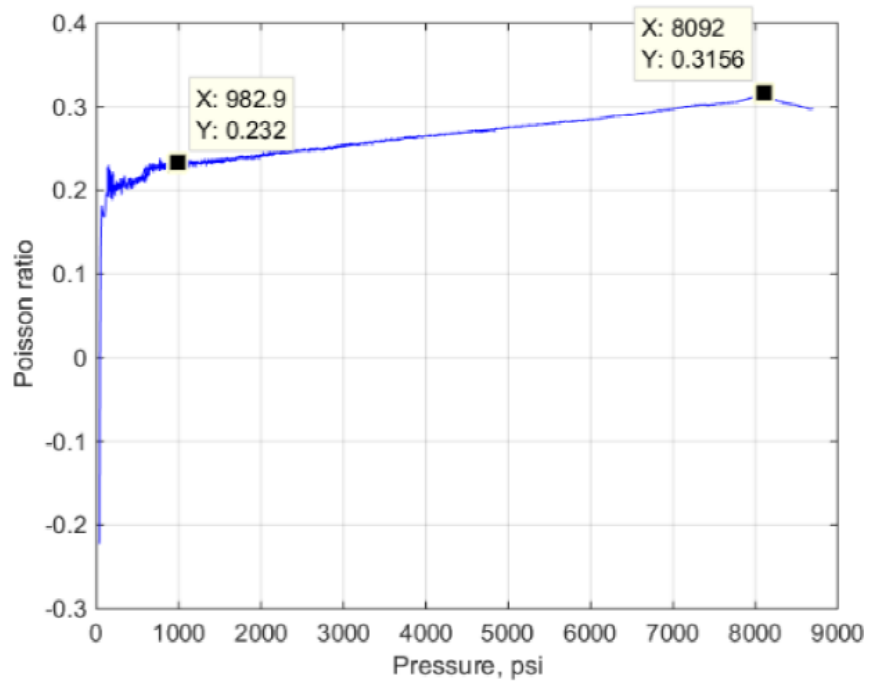


Figure 177: Travertine Sp4 Poisson ratio

Travertine test plots of Sp4.0 Young modulus and Poisson ratio:

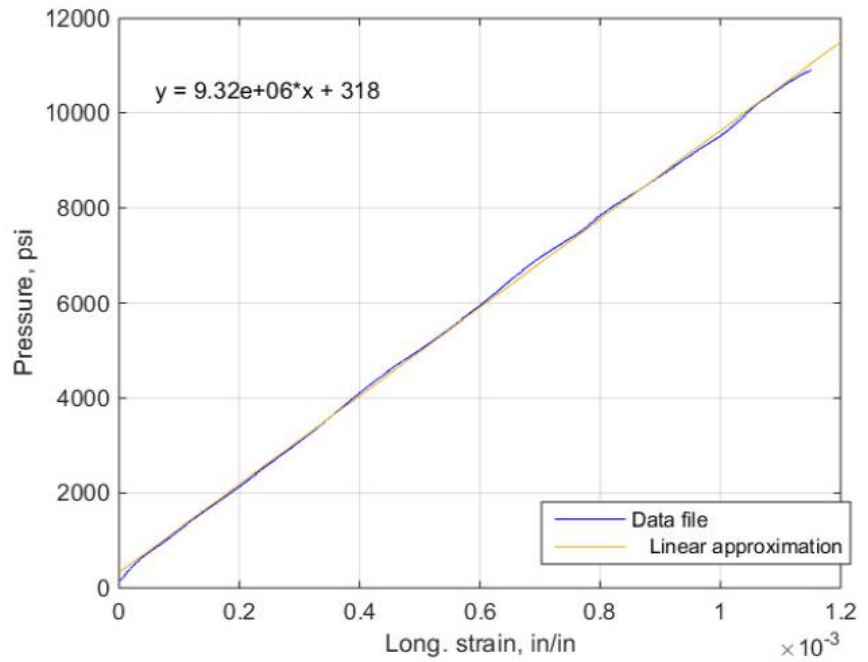


Figure 178: Travertine Sp4.0 Young modulus

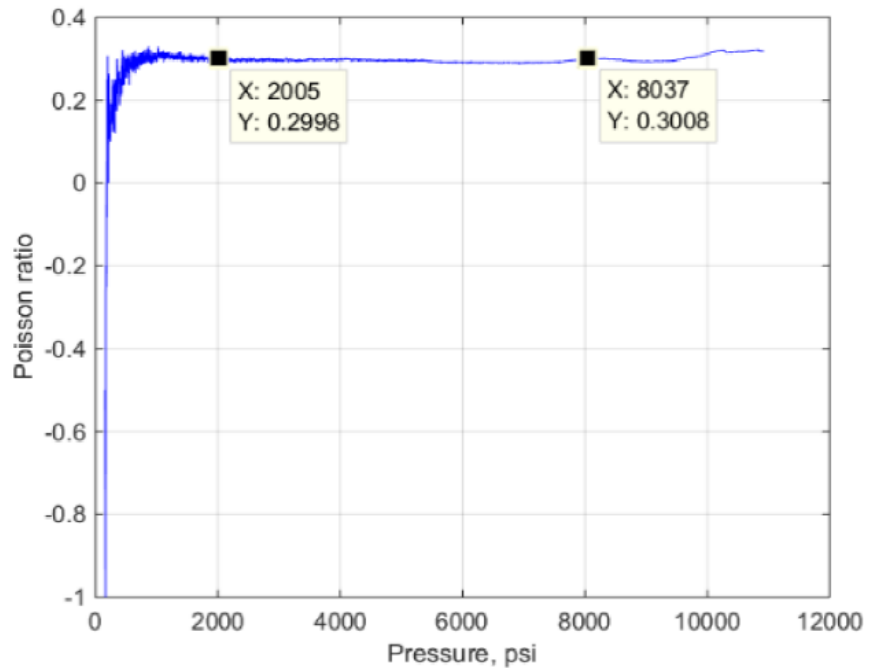


Figure 179: Travertine Sp4.0 Poisson ratio

Basalt test plots of Sp7 Young modulus and Poisson ratio:

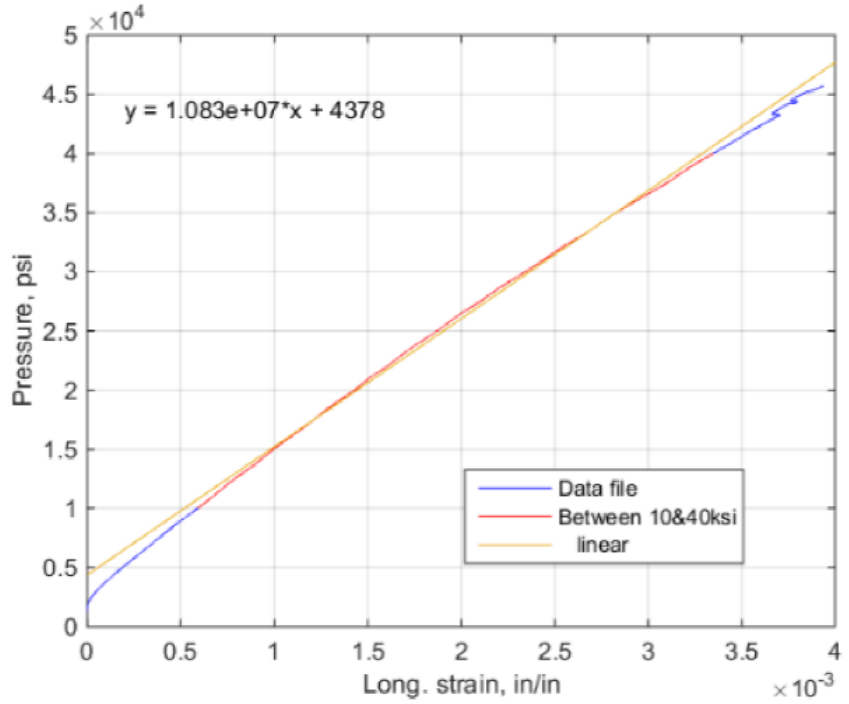


Figure 180: Basalt Sp7 Young modulus

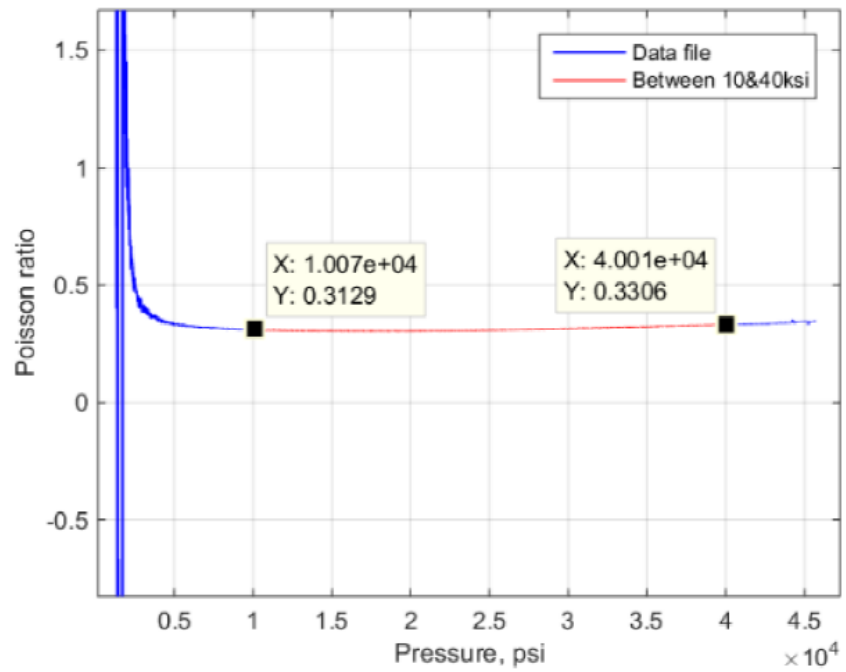


Figure 181: Basalt Sp7 Poisson ratio

Basalt test plots of Sp8 Young modulus and Poisson ratio:

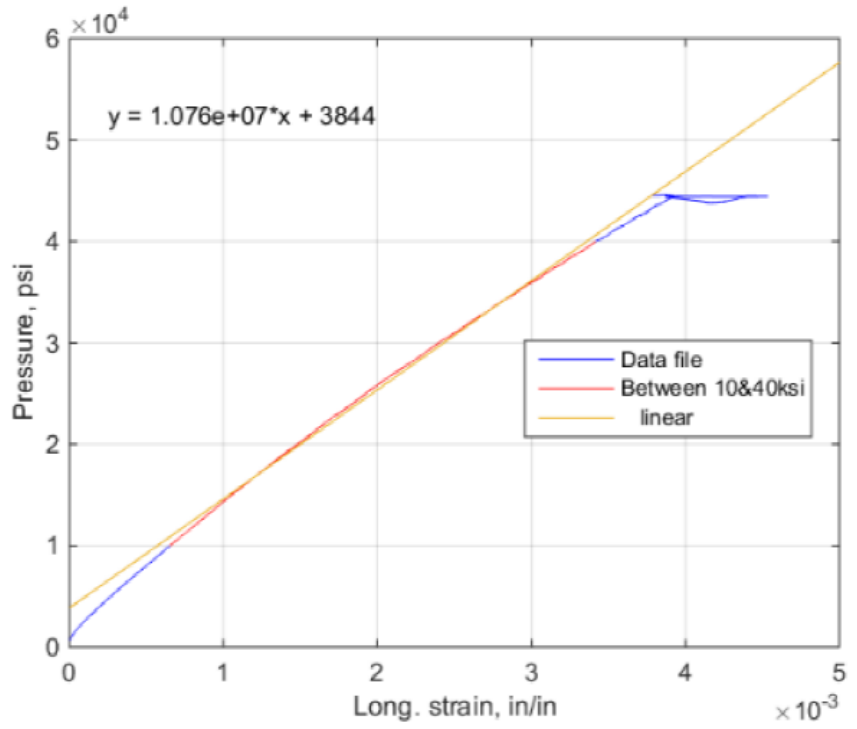


Figure 182: Basalt Sp8 Young modulus

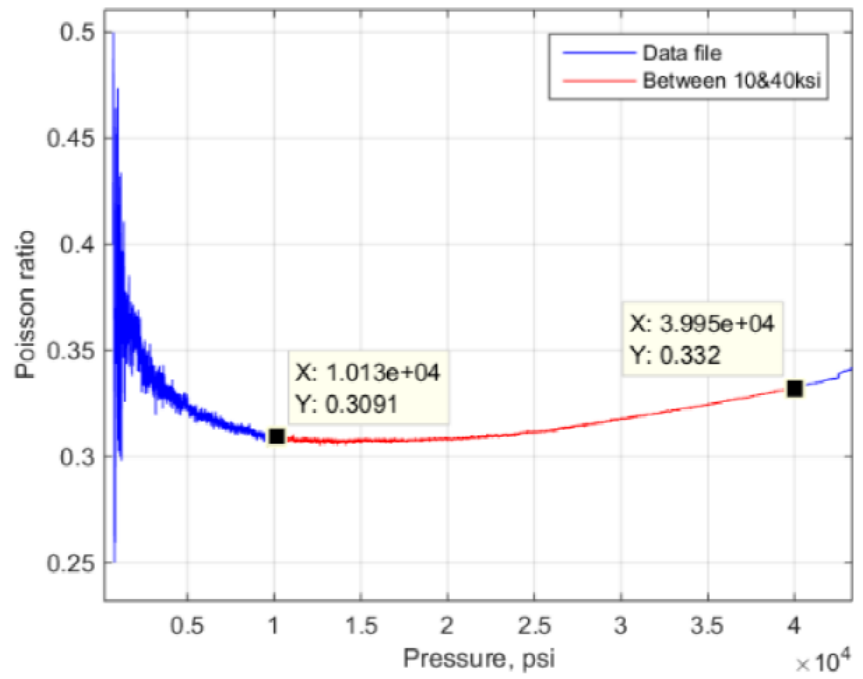


Figure 183: Basalt Sp8 Poisson ratio

14. Appendix D

Wave Frequency

The change in frequency (f) shows that did not have an effect on the rate of penetration performance. As shown in the figure below, the effective time of the frequency in blue is equal to the two effective times of the double frequency in red. As a result, the increase in frequency only divides the time to smaller equal fractions that are the product of the frequency times the effective time fraction (**Error! Reference source not found.**).

Figure 184: Change of frequency has no effect on the effective time and ROP performance

Let $f_1 = 100$ Hz, and $f_2 = 200$ Hz

Then $f_2 = 2 f_1$

If we can prove that the effective time of f_1 equals twice the effective time of f_2 , then the change of frequency has no effect on the rate of penetration performance. To prove this concept, the expression of the effective time (Δt) is simplified in terms of the frequency as follow:

$$\text{Let } X = \frac{1}{\pi} \left[\frac{\pi}{2} - \arcsin \left(1 - \frac{\delta}{A} \right) \right]$$

$$\text{Then } \Delta t = \frac{1}{\pi f_u} \left[\frac{\pi}{2} - \arcsin \left(1 - \frac{\delta}{A} \right) \right]$$

$$\text{And } \Delta t_1 = \frac{1}{f_{u1}} [X] \quad \text{and} \quad \Delta t_2 = \frac{1}{f_{u2}} [X]$$

$$\Delta t_1 = \frac{1}{100} [X] \quad \text{and} \quad \Delta t_2 = \frac{1}{200} [X]$$

$$\text{Finally } X = 100 \Delta t_1 = 200 \Delta t_2$$

$$\text{And } \Delta t_1 = 2 \Delta t_2$$